

Phase Stabilisation of Nb-Si-Ti Alloys via Elemental Additions and Post-Processing

ADAM JOHN SAM ALLEN (MCHEM)

Department of Engineering

A Thesis Submitted to

THE UNIVERSITY OF LEICESTER

For the Degree of

DOCTOR OF PHILOSOPHY

Abstract

Efficiency is a primary concern of the commercial aerospace sector, both in terms of environmental factors and financial incentive. One way to improve engine efficiency is to increase the turbine entry temperature of the engine, but this is currently limited by the material of choice, nickel superalloys. Nb-Si alloys have the potential to replace current turbine materials with a combination of a Nb₅Si₃ silicide phase providing strength and a Nb_{ss} solid solution matrix increasing overall toughness.

There are, however, problems with this alloy system that must be overcome if they are to become a viable replacement. One such difficulty observed is in promoting the optimal α -Nb₅Si₃, with long (100 h), energy consuming (1500°C) heat treatments often being required. This work explored ways to promote the formation of α -Nb₅Si₃ and suppressing β/γ -Nb₅Si₃ phases using elemental additions and novel processing techniques such as additive manufacturing and hot isostatic pressing. Additive manufacturing was implemented due to its flexible nature and lack of mould requirement. Hot isostatic pressing was used to successfully consolidate porosity after formation of Nb-Si alloys.

Comparison of rapid solidification from additive manufacturing to other manufacturing techniques showed the formation of alternate phases to the literature, suggesting that novel processing techniques influence promoted phases. Elemental addition of Cr, Hf, Ti, Zr, Y and Ta were used to control phase evolution. Additions of Hf displayed Hafnia inclusions at all stages of production. Addition of Cr in high concentrations promoted α -Nb₅Si₃, but also produced the unexpected cubic C15 Laves phase over the hexagonal C14 phase.

Ti_{ss} was noted in some alloys when phase transitions occurred during post-processing, although after long heat treatments these were reduced. High levels of Zr showed promotion of γ -Nb₅Si₃, whilst low concentrations allowed for α -Nb₅Si₃ formation. Additions of Ta helped to promote α -Nb₅Si₃ during the formation stage and helped reduce β -Nb₅Si₃ after short post-processing heat treatments (5 h), potentially opening faster heat treatment routes.

Acknowledgements

I dedicate this thesis to my daughter Mia and my parents (Donna and Dave Allen) who have always provided me with love, understanding and support throughout my PhD. You encouraged me to better myself and become the first Allen to pursue a PhD. I would like to thank my partner Claudia for letting me ignore her whilst I got this finished. Thank you Reece for getting cancer and scoring me an extra two months extension. Tyler, you were there. Good job.

I really wish to thank Ben for proof reading my thesis, fixing my English and essentially learning engineering. I promise I was not discouraged when you asked one week before hand in: "What is a eutectic anyway?"

I am thankful and wish to acknowledge my supervisors Prof. Hong Dong and Dr Rob Thornton for their guidance and encouragement to become a better researcher. I am grateful for the opportunities to travel that you have provided, both to see production of samples in Xian, China and training provided in Caen.

Myself and my team (A.C. Douglas, L.M. Feitosa and H. Qian) wish to acknowledge Rolls-Royce plc., EPSRC CDT in Innovative Metal Processing and CNPq/Brazil for their financial contribution. The project was also sponsored by NWPU to cover the experimental costs in China. Without the financial support of each organisation I would have never met such a great team.

I would like to thank Dr D. Weston for his support in XRD and general analysis of data despite not being my supervisor. I wish to thank the Geology Analytical Team (C. Haidon and Dr T. Knott) for their support and many conversations, especially the training and support on all things X-ray. I wish to acknowledge the Advanced Microscopy Facility, University of Leicester for their access to their technical equipment and I am indebted to the support staff for their help, (V. Patel, G. Clark and A. Frost) I promised I wouldn't break anything.

To my friends I've been ignoring for the past year. Sorry, I'm free now.

Thank you people, you know who you are. If you aren't mentioned, sorry, the page is short.

P.S.

Thanks IceFrog for making Dota 2, the only way to relax by getting angrier.

List of Conference Publications/Presentations

[1] L.M. Feitosa, A. Allen, A. Douglas, H. Qian, H.B. Dong. Microstructure Evolution of the Nb-18Si-24Ti-5Cr-5Al-2Mo Alloy Produced via Laser Additive Manufacturing METAL 2017, Conference Proceedings p. 1615-1618. ISBN: 978-80-87294-79-6

[2] A.C. Douglas, A. Allen, H. Qian, L.M. Feitosa, H.B. Dong, X. Lin, W. Huang. Laser additive manufacturing of niobium silicide-based composites, in Proceedings of “Beyond Nickel-Based Superalloys II”, ECI Symposium Series, Cambridge, 2016. Oral Presentation.

[3] L.M. Feitosa, A. Allen, A. Douglas, H. Qian, H.B. Dong. Microstructure evolution of the Nb-18Si-24Ti-5Cr-5Al-2Mo alloy produced via laser additive manufacturing, in Proceedings of “Metal 2017”, Brno, 2017. Oral Presentation.

[4] L.M. Feitosa, A. Allen, H. Qian, A. Douglas, H.B. Dong, X. Lin, W. Huang. Analysis of the solidification behaviour of Nb-Si-Ti alloys produced by Laser Additive Manufacturing, in Proceedings of the “5th Decennial International Conference on Solidification Processing”, Old Windsor, 2017. Oral Presentation.

[5] L.M. Feitosa, A. Allen, A. Douglas, H. Qian, H.B. Dong. Thermal Analysis Validation of the Solidification Sequence of a High Chromium Niobium-Based Alloy Produced via Additive Manufacturing, in Proceedings of “Recent Applications of Thermal Analysis and Calorimetry”, Belfast, 2018. Oral Presentation.

Contents

Abstract.....	I
Contents.....	IV
1 Introduction	1
1.1 Context	1
1.2 History	1
1.3 Current Materials	3
1.4 Aim and Objectives.....	4
2 Literature Review	5
2.1 Introduction.....	5
2.2 Ongoing Material Research	5
2.2.1 Ceramic Matrix Composites	5
2.2.2 Mo–Si–B Alloys.....	6
2.2.3 Pt Group Alloys.....	7
2.2.4 Niobium Silicide’s	8
2.2.5 Summary	8
2.3 Introduction to Nb-Si alloys	10
2.4 Future Challenges of Nb-Si Alloy Development	12
2.4.1 Low Temperature Mechanical Properties	13
2.4.2 Oxidation Resistance	15
2.4.3 High Temperature Reactivity.....	17
2.4.4 Summary	23
3 Experimental Methods.....	24
3.1 Introduction.....	24
3.2 Construction and Post-Processing	24
3.2.1 Powder preparation	25
3.2.2 Laser Parameters (Direct Laser Deposition)	27
3.2.3 Hot Isostatic Pressing (HIP)	29
3.2.4 Heat Treatment.....	30
3.3 Analysis Methods.....	31
3.3.1 Sample Preparation.....	31
3.3.2 Volume Fraction Calculations.....	32
3.3.3 Scanning Electron Microscopes.....	32
3.3.4 X-Ray Diffraction	33
3.3.5 X-ray Computed Tomography (X-ray CT).....	33
3.4 Rietveld Refinement.....	34

3.4.1	Intensity Factors.....	34
3.4.2	R_{wp} , R_{exp} and Goodness of Fit	35
3.4.3	Factors Affecting Peak Position and Shape	36
3.5	Calibration of X-ray Diffractometer	37
3.5.1	Refinement of NIST Standard Reference Material (SRM).....	38
3.5.2	Acquisition of Corundum Data	38
3.5.3	Removal of Diffractogram Features	41
3.6	Principles of X-ray CT Set-up.....	42
4	Effects of Cr and Hf additions on Phase Evolution in Direct Laser Melting of Nb-Si Alloys.....	46
4.1	Introduction.....	46
4.2	Nb-15Si-22Ti-14Cr-2Al-2Hf-2V (14Cr).....	48
4.3	Nb-15Si-22Ti-2Cr-2Al-2Hf-2V (2Cr).....	58
4.4	Nb-22Si-26Ti-2Al-6Cr-3Hf (6Cr)	65
4.5	Evaluation of Elemental Additions of Chromium and Hafnium	72
5	Effects of Mo additions on Phase Evolution in Direct Laser Melting of Nb-Si Alloys	73
5.1	Introduction.....	73
5.2	Nb-18Si-24Ti-5Cr-5Al-2Mo (2Mo)	74
5.3	Evaluation of Elemental Additions.....	84
6	Effects of Zr and Y Additions in 4 th Generation Nb-Si Alloys.....	85
6.1	Introduction.....	85
6.2	Nb-18Si-24Ti-5Cr-5Al-2Mo-5Zr-0.4Y (CoZy5).....	87
6.3	Nb-18Si-24Ti-5Cr-5Al-2Mo-1Zr-0.08Y (CoZy1).....	97
6.4	Evaluation of Elemental Additions.....	106
7	Effects of Ta Additions in 4 th Generation Nb-Si Alloys.....	107
7.1	Chapter Introduction	107
7.2	Nb-18Si-24Ti-5Cr-5Al-2Mo-5Zr-0.4Y-2Ta (TCoZy5).....	108
7.3	Nb-18Si-24Ti-5Cr-5Al-2Mo-1Zr-0.08Y-2Ta (TCoZy1).....	118
7.4	Evaluation of Elemental Additions.....	127
8	Effects of Hot Isostatic Pressing on Direct Laser Melted Nb-Si Alloys	128
8.1	Chapter Introduction	128
8.2	Densification of Laser Additive Manufactured Nb-Si-Ti-(2,14)Cr Alloys During Hot Isostatic Pressing 129	
8.3	Phase Transformation of Alloys During Hot Isostatic Pressing.....	137
8.4	Evaluation on the Effect of Hot Isostatic Pressing	143
9	Overall Conclusion and Future Work	144
	References	147

List of Acronyms

GE	General Electric
SLA	Stereolithography
FDM	Fused Deposition Modelling
SLS	Selective Laser Sintering
DLM	Direct Laser Melting
CS	Cold Spray
SEM	Secondary Electron Microscopy
BSE	Back Scattered Electron Imaging
W_{max}	Work Delivered
Q_h	Quantity of Heat Input
T_h	Operational Temperature
T_c	External Temperature
TET	Turbine Entrance Temperature
MHI	Mitsubishi Heavy Industries
CMS	Ceramic Metal Composites
CFRC	Ceramic-Fibre-Reinforced-Ceramic
T_m	Melting Point
Nb _{ss}	Niobium Solid Solution
(α, β, γ) Nb ₅ Si ₃	(α, β, γ) Niobium Silicide
BCC	Body Centred Cubic
HCP	Hexagonal Close Packed
OFZ	Optical Floating Zone Method
VAM	Vacuum Arc-Melting
EB	Electron-Beam
PVD	Physical Vapour Deposition
VAM	Vacuum-Arc-Melting
AF	As-Formed
HIP	Hot Isostatic Pressing
HT	Heat Treatment
AM	Additive Manufacturing
LAM	Laser Additive Manufacturing
XRD	X-ray Diffraction
X-ray CT	X-ray Computer Tomography
DLF	Direct Laser Fabrication
DLD	Direct Laser Deposition
NWPU	North-Western Polytechnical University
EDS	Energy Dispersive X-ray Spectroscopy
COD	Crystallographic Open Database
MAUD	Material Analysis Using Diffraction
I	Intensities
S_F	Beam Intensity
V_i	Phase Cell Volume

V_f	Volume Fraction
S	Scale Factor
L_k	Lorentz-Polarisation Factor
F_K	Structure Factor
K	Peak Number
S_i	Profile Function
P_k	Grain Orientation (Texture)
GOF	Goodness of Fit
A	Absorption Factor
bkg	Modelled Background Intensity
R_{wp}	Weighted Pattern
R_{exp}	Expected Value
N	Number of Data Points
P	Number of Refined Parameters
C	Constraints
NIST	National Institute of Standards and Technology
SRM	Standard Reference Material
EPS	Effective Pixel Size
DPP	Detector Pixel Pitch
GM	Geometric Magnification
MSS	Minimum Spot Size
MSP	Minimum Spot Power
HPR	Highest Power Requirements
14Cr	Nb-15Si-22Ti-14Cr-2Al-2Hf-2V
2Cr	Nb-15Si-22Ti-2Cr-2Al-2Hf-2V
6Cr	Nb-22Si-26Ti-2Al-6Cr-3Hf
2Mo	Nb-18Si-24Ti-5Al-5Cr-2Mo
CoZy1	Nb-18Si-24Ti-5Al-5Cr-2Mo-1Zr-0.08Y
CoZy5	Nb-18Si-24Ti-5Al-5Cr-2Mo-5Zr-0.4Y
TCoZy1	Nb-18Si-24Ti-5Al-5Cr-2Mo-1Zr-0.08Y-2Ta
TCoZy5	Nb-18Si-24Ti-5Al-5Cr-2Mo-5Zr-0.4Y-2Ta
$D_{Ti/Nb}$	Diffusion Rates Ti / Nb

1 Introduction

1.1 Context

The gas turbine industry is dominated by four major companies; Rolls-Royce, Snecma, General Electric, and Pratt and Whitney. These companies own the majority share in a worldwide industry worth \$40.5 billion as of 2009, an increase of 13% from 2008.^[1] If these companies are to stay at the forefront of this market it is imperative that the engines they produce have either the greatest performance, most reliability or lowest cost on the market.

1.2 History

Whilst the principles of gas turbines have been known since the 18th century^[2], it wasn't until 1937 when Frank Whittle demonstrated the first working turbojet that the work of gas turbines could finally get off the ground.^[3] Since the original design, the jet engine has undergone a number of iterations, ultimately adapting from its original and bulky centripetal compressor to a thinner, longer axial design, increasing the efficiency of the engines overall. Some areas still see use of the centripetal engine where space is a limiting factor, such as helicopter engines.

With performance being an important quality, it is important to calculate correctly, a common method to determine the efficiency(η) of an engine is the Carnot equation (**1**).

$$\eta = \frac{W_{max}}{Q_h} = \frac{(T_h - T_c)}{T_h} \quad (1)$$

This shows is the mechanical work delivered (W_{max}), the quantity of heat input to the system (Q_h), the operational temperature (T_h) and the external temperature (T_c). As can be seen from the equation (**1**), one of the ways companies are able to increase efficiency is to increase the temperature in which the hot section of the engine operates. Most engines are limited in their efficiency and very few reach 60% efficiency, one of the most efficient is General Electric's 7HA.02 gas turbine which only has an efficiency of 61%.^[4] In all engines the hottest point is adjacent to the fuel ignition, and is referred to as the turbine entrance temperature (TET). Originally turbine blades were made from steel but were unable to reach high temperatures and had very short service lives.^[5]

Since then the materials of choice have been nickel superalloys, which are able to operate at a much higher TET. **Figure 1** shows that since the 1940s the engine operating temperature has increased by over 800°C, with Mitsubishi Heavy Industries (MHI) achieving a TET of 1600°C in

2011.^[6] It is important to recognise that this temperature milestone was reached using blades constructed from 4th generation superalloys. The melting temperature of these alloys are $\sim 1350^{\circ}\text{C}$, over 200°C lower than its reported operating temperature.^[7]

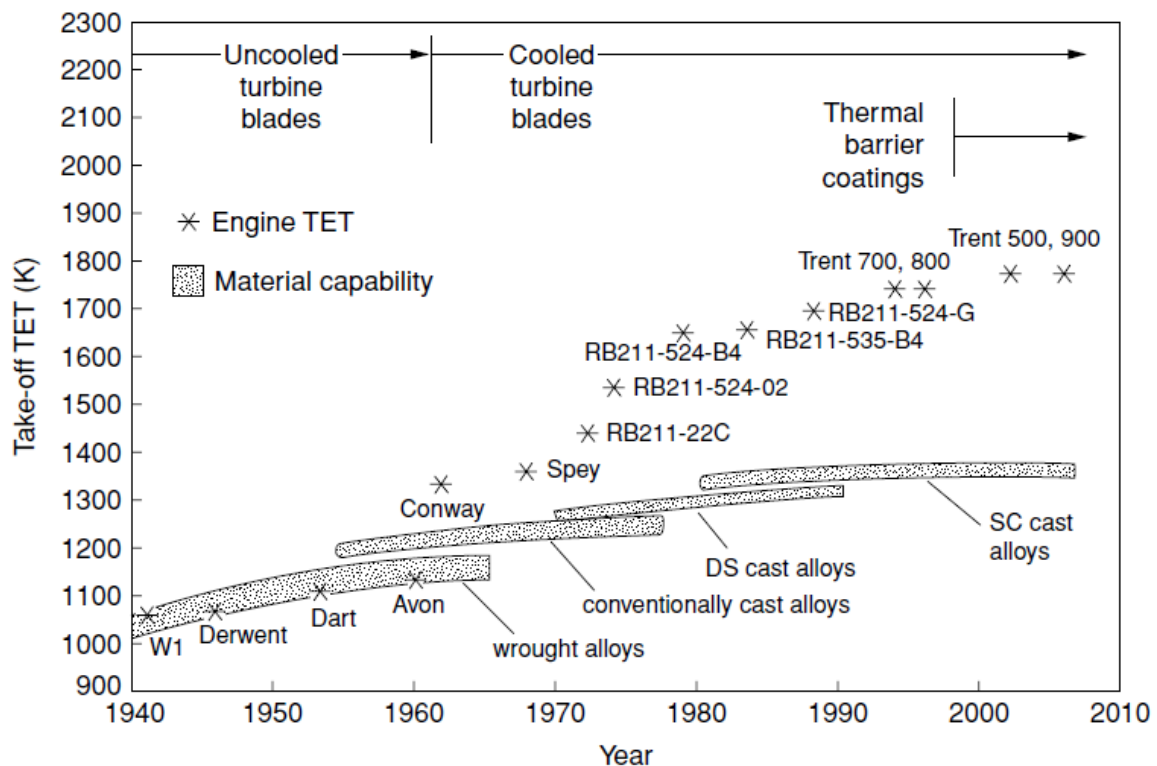


Figure 1: Evolution of the turbine entry temperature (TET) capability of Rolls-Royce's civil aero engines, from 1940 to the present day.^[8]

The increase in TET has been achieved through a combination of processing methods, design changes and thermal barrier coatings, including the addition of cooling channels within the blade. This increase in TET has plateaued and it is commonly understood that nickel superalloys as a material are approaching the peak of their performance. Therefore an alternative is required if these temperature barriers are to be breached.^[7, 9]

This document will focus on the recent development of materials for use in gas turbines with a focus on niobium silicide's as a replacement for nickel superalloys. There will be a focus on alloy design to reduce formation defects and promote ideal phase characteristics. Some fundamental issues will also be discussed as there are still many issues to address before this material can be implemented on a large scale.

1.3 Current Materials

When high temperature environments are needed, specialist materials are required to fulfil a wide range of tasks. **Figure 2** depicts some of the components that can be found in service, and attention will be drawn to the rotating components; both the compressor and turbine blades.

The diagram below shows a titanium alloy being implemented in the fan blade and compressor sections. An example of a common wrought alloy is Ti-6Al-4V which is made through super-plastic forming and diffusion bonding. However, other materials are being developed, for example advanced engine models use carbon fibre to lower weight.^[10]

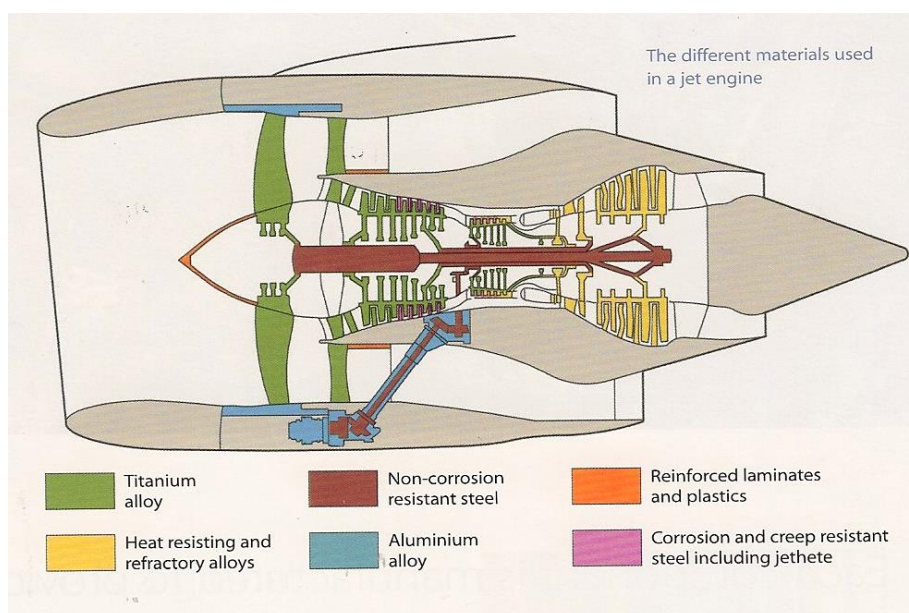


Figure 2: A generalised diagram of the materials used in a gas turbine engine.^[11]

Low pressure compressor blades are typically constructed from similar titanium alloys as they are resistant to corrosion, have an excellent balance of low density and strength. These are, however, only useful at lower temperatures, as their effective strength is lost above 600°C. This means they are not able to be used in hotter areas of the engine, where they are thereby replaced with nickel superalloys.

Steel is often used as the shaft where compressor and turbine blades are attached due to its good strength, can be easily made to different requirements and heat treated to promote specific characteristics. Super CMV is often used to produce 3 interconnected shafts which allow you to run different turbines and compressors independently.^[12]

As has been stated before, nickel superalloys have undergone a great amount of development, but it is likely they have reached their pinnacle. Finding the correct alloy composition is largely a balancing act of multiple factors. Attempts to increase the melting point, whilst possible, lead to an increase of both temperature and density. High density materials undergo high stresses when in operation, requiring more reinforcement to the central axel. This increases the weight of the engine and reduces the alloys desirability.

Further increases in TET are unlikely from nickel, as seen in **Figure 1** the majority of the increases can be attributed to blade design and thermal barrier coatings, future development is likely to be focused on increasing process efficiency.^[13]

1.4 Aim and Objectives

The desire to increase the efficiency of gas turbine engines has led to the research and development of new materials to push the boundaries further.

There is a world-wide effort to replace nickel superalloys, with some materials having the potential to meet these demands. The overall objectives of this thesis can be seen below:

1. Identify appropriate material to replace Ni superalloys.
2. Establish desired microstructure to produce ideal mechanical, oxidation resistance and high temperature properties.
3. Identify suitable manufacturing technique for novel material.
4. Reproduce literature material using alternative manufacturing technique to provide comparison.
5. Iteratively improve material to produce novel material composition/alloy.

Some of the proposed materials include ceramic metal composites (CMS's), Mo-Si-B alloys, Pt group materials and Nb-Si alloys, the pros and cons of each material will be discussed in 2.2. The latter has great potential, and the majority of this thesis will focus upon the advances in niobium silicide's for high temperature applications. Traditional manufacturing techniques may not be suitable to produce Nb-Si alloys and will be discussed in 2.4.3 with Chapter 8 will discuss the post processing techniques applied during manufacturing. Chapter 4 and 5 will compare alloys produced via additive manufacturing to other manufacturing methods, and iterative improvements to the alloy system will be discussed in Chapters 6 and 7.

2 Literature Review

2.1 Introduction

A review of the literature surrounding the topic of gas turbine blades was performed, focused on novel materials aimed at replacing the current nickel superalloys. A brief introduction to Nb-Si alloys, describing the known phase diagram and crystal structures as well as their comparison to other materials discussed in **section 2.2**. The final section of the literature review will discuss the challenges that need to be overcome before Nb-Si alloys can be implemented into gas turbine engines.

2.2 Ongoing Material Research

There are many potential materials that could be used to replace nickel superalloys, each of them has their benefits and shortcomings. Processing techniques are designed for current nickel superalloys. The sections below will discuss many of the new materials and manufacturing methods being researched

2.2.1 Ceramic Matrix Composites

CMCs belong to a subgroup of composite materials consisting of ceramic fibres embedded in a ceramic matrix, this forms a ceramic-fibre-reinforced-ceramic (CFRC) material. CMCs being used in gas turbines have some advantages over metal designs. A lot of the early research has focussed on stationary components within the engine and started in the combustion chamber, as opposed to the turbine sections. CMC's can be used to line the combustion chamber give a few notable advantages; firstly, CMC's such as OXIPOL (an oxide CMC based on polymers) have a higher temperature capability ($T_m \sim 2000^\circ\text{C}$) and thus allows firing temperature to be increased without affecting the materials properties adversely. Secondly, the air which is usually syphoned off from the compressor to cool the combustion chamber may be saved and thus used for useful work in the turbine, or to be used to burn the fuel more effectively and thus reduce harmful NO_x emissions.^[14] Thirdly, if the combustion chamber is cooled it may cause incomplete combustion to occur near the wall (see **Figure 3**). If a CMC is used then the wall may be hotter and reduce the chance of flame quenching.^[15]

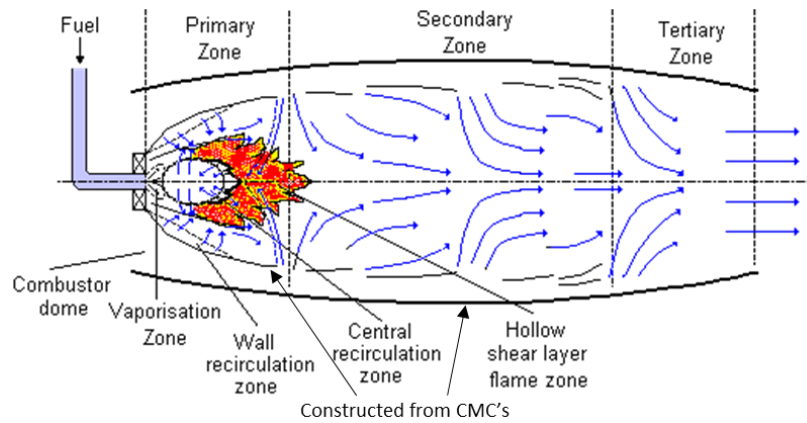


Figure 3: Cross sectional view of a combustion chamber in a gas turbine engine.^[16]

General Electric have made a push towards developing CMCs to be placed in multiple sections of the turbine, publishing multiple patents for their use.^[17-19] They have also announced their first successful testing of a CMC in a rotating turbine blade.^[20] The blade weighs one third that of a conventional nickel blade and requires no air cooling, another efficiency boost to this material. This material was later integrated into the GE9X engine, one of the world first CMC containing engines.

To compete with nickel superalloys, more work is required to lower manufacturing cost of this route. Additionally, cost reduction in the fibers and more use of protective coatings will increase competitiveness.^[21]

Silicon carbide composites have the potential to be used at extremely high temperatures in a gas turbine, exhibiting both high temperature strength and durability. In dry air they have superb oxidation resistance, but in moisture (a side product of the combustion reaction) a silica scale is produced on the turbine blades surface which reacts further to form silicon hydroxide products at around 1300°C. Coatings are being developed for SiC materials to resist moisture and many have made advances, however they do suffer from other shortcomings; including cost and a suitable manufacturing method.^[22, 23] Typically CMC's are usually batch developed using over 50 separate steps including melt infiltration of Si into a carbon matrix to produce complex turbine blades.^[24]

2.2.2 Mo–Si–B Alloys

Molybdenum silicide's share many of the same potential advantages as niobium silicides for the future of high temperature application materials. Early studies however have shown that the intermetallic phases in isolation are not yet suitable. MoSi₂, which is the major constituent,

has excellent oxygen resistance up to 1700°C, but at temperatures greater than 1200°C it suffers from very high creep deformation.^[25] In spite of this drawback, Mo₃Si₅ oxidises very quickly at high temperatures but maintains a low creep rate. In an attempt to alleviate the negative properties, a ternary system has been developed which includes small amounts of boron (0.8- 1.9 wt. %)^[26]. This produces a glassy borosilicate layer on the surface which aids oxidation resistance. A study has also implemented this material as a surface coating to niobium silicide in-situ composites, details of which are discussed later in this review.^[27] A single crystal monolith created from MoSi₂ has been tested at low oxidation temperatures and boasts a continuous oxide scale on the surface. This scale - free from cracks - limited the further oxidation and is expected to be controlled by diffusion of the ions through the layers.^[28] One aspect of these materials which limits their viability is density. This is an important factor which needs to be considered in order to obtain higher propulsive efficiencies. As the density of Mo-Si in these alloys is ~9.5 g.cm⁻³, not only are they significantly higher than niobium silicide materials at ~7g.cm⁻³, they are also more dense than the existing nickel superalloys which are 9.2 g.cm⁻³ placing them at a significant disadvantage.^[29-31]

2.2.3 Pt Group Alloys

Platinum group materials have the potential for high temperature applications. These consist of alloys based on Ru, Rh, Pd, Os, Ir and Pt as the predominate element. In contrast to the refractory metals, the platinum group metals have exceptional oxidation and chemical resistance. Some of the metals in this group, whilst having these excellent resistive properties, have very undesirable strength aspects associated with them in their pure form. However, alloying them with elements such as zirconium and hafnium in the case of an iridium alloy have been shown greatly improve this.^[32] While these materials may potentially be used in temperatures above 2000°C (Ir-Nb for example), it is unlikely that they will meet the demands of the gas turbine industry. Their densities vary greatly (11.9 g.cm⁻³ – 22.57 g.cm⁻³) but are all higher than the average nickel superalloy of ~9.2 g.cm⁻³.^[33-35] One other major setback is the cost. These turbine blades would contain some of the most expensive metals in the world, further reducing the likelihood of their implementation. Other industries such as space exploration (where budgets are less constrained) may however see a benefit from materials being constructed this way. Again however, the density will remain a major concern.

2.2.4 Niobium Silicide's

Niobium silicide's (Nb-Si) are one of the more promising material possibilities. They consist of a 2-phase in-situ region containing a niobium solid solution (Nb_{ss}) as well as an intermetallic Nb₅Si₃. Having initially been considered more than 15 years ago, recent papers have shown some compositions to have similar creep and oxidation resistance as second generation nickel superalloys.^[36-40] These systems have the potential to fulfil both requirements of lower density and higher TET. Their density is lower than nickel superalloys allows (~7 g.cm⁻³ compared to ~9.2 g.cm⁻³). The lower density results in lower stresses on the blade as seen in (2) where σ is the stress experienced by a blade of radius r with a density of ρ , rotating at ω .

$$\sigma = \rho \cdot r \cdot \omega^2 \quad (2)$$

As the blade experiences less stress, the amount of reinforcement on the blade can be reduced leading to further weight reductions. This, along with the higher TET result in an increase of overall propulsive efficiency and fuel cost reduction^[33, 40, 41]

2.2.5 Summary

Of the materials discussed in this section, Nb-Si alloys have the greatest potential and will be the main focus of this thesis. A broad comparison table of the previous references can be seen in **Figure 4**. Unlike CMCs, Nb-Si alloys can form complex shapes, they are less dense than Mo-Si-B alloys and unlike Pt materials, can be produced at a relatively low cost. With current knowledge they are comparable with second generation nickel superalloys, and improved production methods and alloy understanding, they may one day surpass superalloys, allowing for lighter, more efficient engines in the future.

Figure 4 : Summary table of materials research compared to Ni superalloys, the legend can be seen below

	CMC	Mo-Si-B	Ni superalloys	Nb-Si	Pt group
Melting Point					
Density					
Cost					
Workability					
Oxidation Resistance					
Tensile Strength					

- Better properties than Ni superalloys
- Worse properties than Ni superalloys
- Comparable properties than Ni superalloys
- Base Line
- No Data

2.3 Introduction to Nb-Si alloys

The binary phase diagram for niobium silicide can be seen in **Figure 5**. Nb and Si both have a higher solidus temperature than nickel superalloys with a eutectic noted at 1880°C with 18.2at.% Si, consisting of Nb₃Si and a Nb solid solution (Nb_{ss}). These two phases share similar qualities with the Mo-Si systems; the former intermetallic provides good strength up to 1500°C where the latter provides room temperature toughness.^[42] The alloy also retains some long term morphological and chemical stability at increased temperatures, making them desirable for use in high temperature applications.^[7, 40]

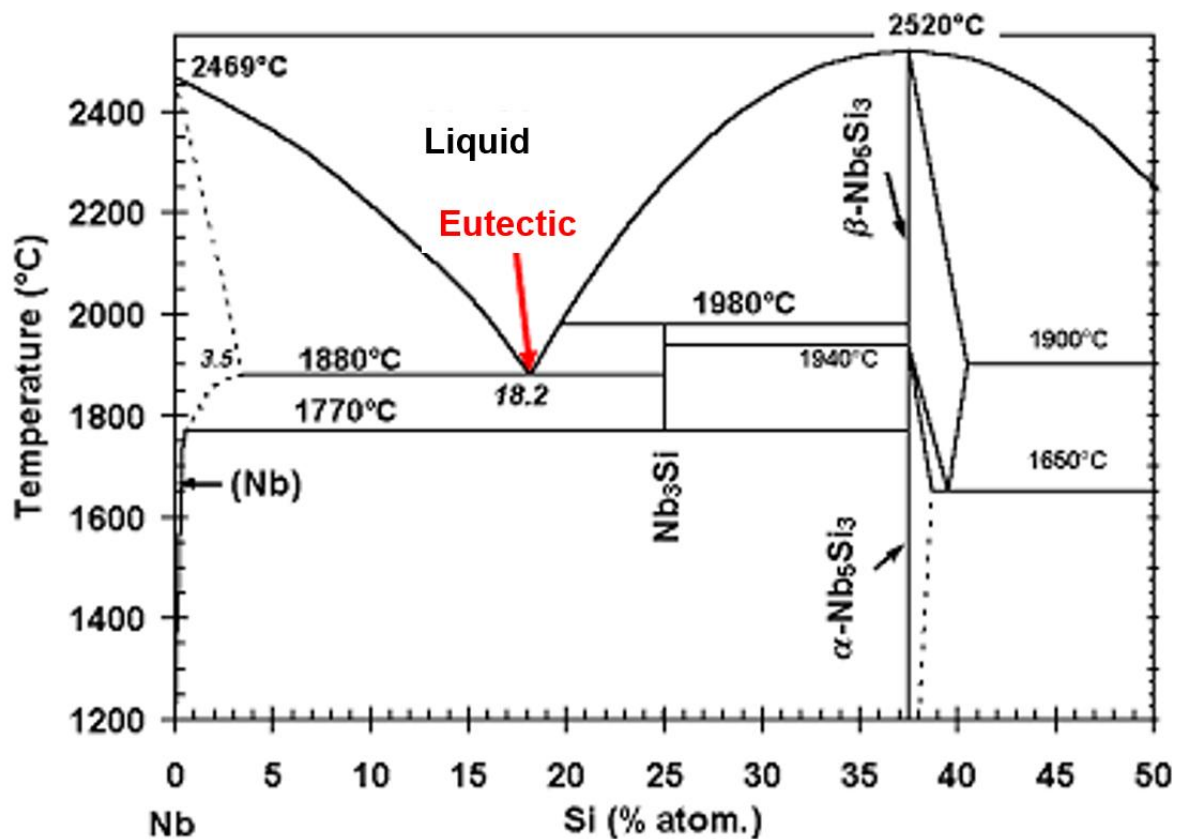
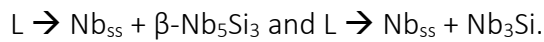


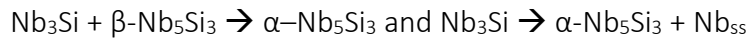
Figure 5: The Nb-Si phase diagram with the eutectic of interest labelled in red.^[43]

Crystallographic data for the niobium rich Nb-Si binary alloys shows a few different phases, the most important and desired phases are the body centred cubic (BCC) Nb solid solution (Nb_{ss}) and α-Nb₅Si₃, both are stable at low temperatures. Other phases include Nb₃Si and β-Nb₅Si₃ which are both metastable and are noted to form through a variety of peritectoid and eutectoid transformations, depending on the processing technique used.

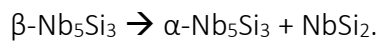
The most notable reactions include the metastable eutectic reactions:



Both metastable phases are known to interact to produce $\alpha\text{-Nb}_5\text{Si}_3$, these include the peritectoid reactions:



As well as the eutectoid reaction:



A hexagonal crystal system for $\gamma\text{-Nb}_5\text{Si}_3$ also exists and Bewlay has shown it to be stabilised by hafnium (>12.5at.%), Ti or small amounts of carbon, although it is detrimental to creep properties for the material and as such is largely avoided.^[44, 45]

Whilst crystallographic information on all these phases is known, as seen in **Table 1**, the binary phase diagram is considered largely incomplete. For instance, the location and relationship of $\gamma\text{-Nb}_5\text{Si}_3$ on the Nb-Si binary diagram is debated.^[46] Much experimental data is missing to reinforce predicted trends, with alloyed elements such as Ti, Zr and Hf creating an even larger uncertainty in models.

Table 1: Table of crystallographic information on important Nb-Si binary phases.

Phase Name	Crystal system	Theoretical Density	Crystal Lattice Parameters (Å)		Space group
			a	c	
Nb_{ss}	Cubic	8.56	3.286	--	Im3m
$\alpha\text{-Nb}_5\text{Si}_3$	Tetragonal	7.10	6.570	11.884	I4/mcm
$\beta\text{-Nb}_5\text{Si}_3$	Tetragonal	7.15	10.018	5.072	I4/mcm
$\gamma\text{-Nb}_5\text{Si}_3$	Hexagonal	7.00	7.536	5.249	P63/mcm
Nb₃Si	Tetragonal	7.53	10.224	5.189	P4 ₂ /n
NbSi₂	Hexagonal	5.72	4.7974	6.5923	P6222

Using the Nb-Si binary system as a template, multiple experiments have been conducted to improve the problems listed above. Many elements have been implemented to understand trends, the most common being titanium, chromium, hafnium and aluminium.

2.4 Future Challenges of Nb-Si Alloy Development

The problems for Nb-Si alloys can be seen in **Figure 6**. Oxidation resistance is unique as under a high temperature oxygen environment, a phenomenon known as “peeling” occurs. This is where the material disintegrates into smaller particles and flakes from the surface, resulting in a non-protective oxide coating. This remains one of the main issues facing industrial use of niobium silicide’s, and various elements have been implemented to try and alleviate the issues. It comes at a price however, as many elements compromise the high temperature mechanical properties - finding a suitable alloy which provides an adequate amount of oxidation resistance without sacrificing mechanical performance is vital. To produce most aerofoils, industry often employs the Bridgman casting method, as the moulds currently used in nickel superalloy production are not sufficient to cope with the high temperature required, and suitable alternatives are required.

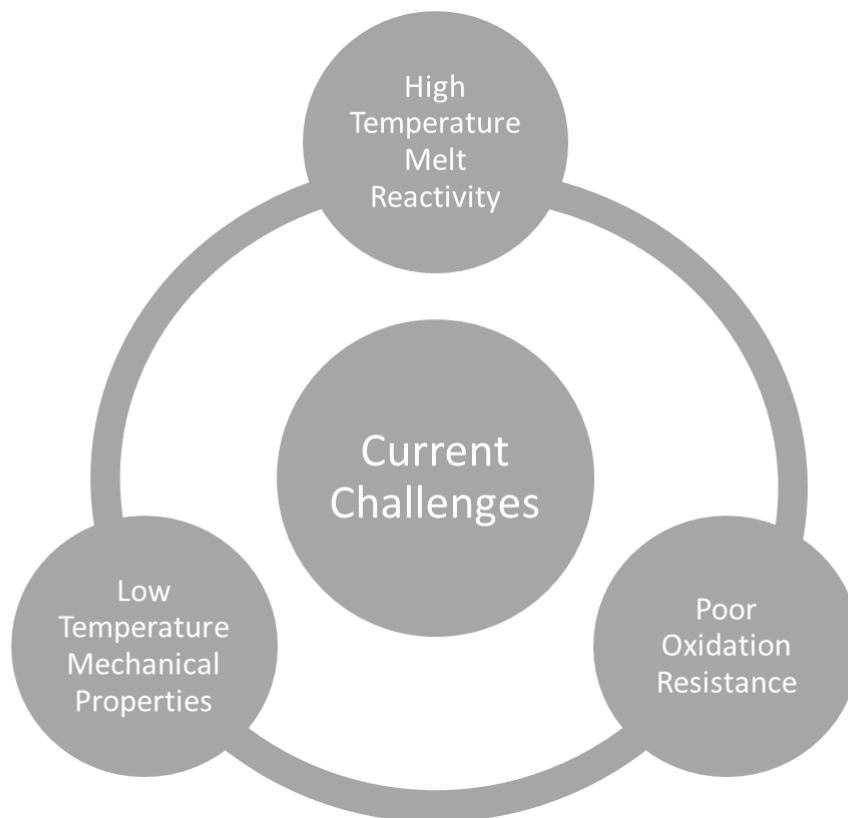


Figure 6: Diagram showing the three main problems in Nb-Si alloy development

2.4.1 Low Temperature Mechanical Properties

One of the requirements for Nb-Si alloys is to have mechanical properties comparable with nickel superalloys. Creep, tensile strength and fracture toughness mechanisms are all important concepts in determining how blades will interact in the harsh environments of a jet turbine engine. The production of Nb-Si alloys presents many challenges, for instance increasing mechanical properties invariably reduces oxidation properties. This section discusses some of the possible mechanical properties using Nb-Si alloys.

Fracture Toughness (K_{Ic})

Toughness is an important property when considering Nb-Si alloys for service in the turbine industry. Complex relationships between Nb_{ss} and Nb_5Si_3 boundaries control the relationship, through a combination of ductile rupture and interface separation.^[47] Toughness in the binary system can be seen in **Figure 7**. Altering Si content enables toughness to be controlled, with 18-22% Si providing a 48% increase in fracture toughness due to alterations in the microstructure parameters. Undercooling promotes a fine eutectic scale which also provides increased toughness compared to arc melted alloys.^[48]

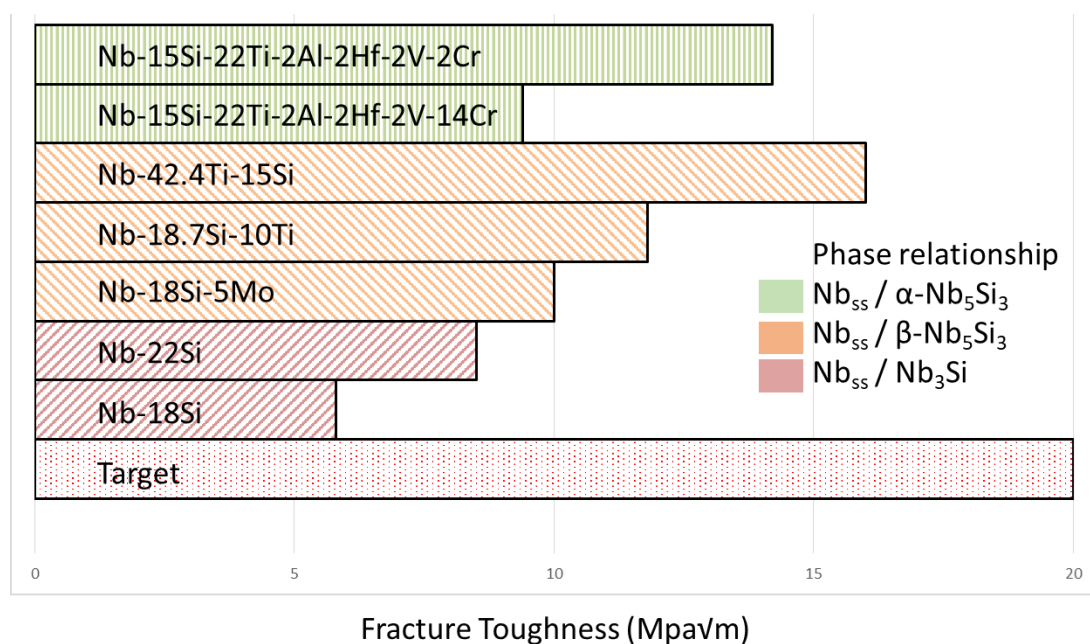


Figure 7: Fracture toughness of Nb-Si alloys[7, 9, 49-51]

New generations of alloys are usually based on the Nb-Si-Ti system of alloys, Nobuaki Sekido (2006) investigated the differences in the binary and ternary systems. Whilst increases in Si improve fracture toughness, it suggests that in non-lamella type eutectoid microstructures the

Nb_{ss} does not greatly improve K_Q. The addition of Ti, directional solidification and annealing process enhance dislocation mobility and plastic flow in the Nb_{ss} phase, this helped decompose the Nb₃Si phase to produce a lamellar structure of Nb_{ss}/Nb₅Si₃. The Nb_{ss} is coarsened as a result of this process and it is commonly known that the coarsening of ductile grains (Nb_{ss} in this case) can increase K_Q.^{[53] [49]}

Other elements have been shown to suppress the formation of Nb₃Si and promote β-Nb₅Si₃. The addition of gallium, shown to partition to Nb_{ss}, has caused this as well as an increase in fracture toughness up to 24 MPa√m. The paper by S. Kashyap (2011) describes the alteration of the microstructure due to both the addition of gallium but also the method of suction casting used, producing an ultrafine eutectic.^[48]

Stabilising the low temperature α-Nb₅Si₃ shows potential increases in fracture toughness, 14Cr has reduced toughness due to the Nb_{ss}/Nb₅Si₃/Laves ternary phase system developed. Laves phases are known for their high hardness values and produce brittle fracture points within this material (along with Nb₅Si₃), with Nb_{ss} exhibiting plastic deformation. Hf/yttria inclusions are also noted at each stage of development, giving potential crack propagation sites through debonding from matrix or cracking themselves.^[54]

Tensile Strength of Nb-Si Based Alloys

Work on the tensile strength of Nb-Si alloys has developed values, competing with Ni superalloys at 1200°C, however, superalloys still outmatch silicide's at lower temperatures (702 MPa for superalloys versus 260 MPa at 300 K for Nb-Si).^[55-57] Investigations into the effects of various elemental additions on tensile strength have revealed high temperature improvements with Ti and Al. Vanadium, with its low melting point reduces high temperature strength of Nb-Si alloys.^[50]

Creep Resistance

Of the relatively small number of studies previously conducted, few have focused on creep resistance in Nb-Si. The future goal for creep properties is 1% creep in 125 h at 1473 K.^[58] This will be achieved through careful balance of Nb_{ss}/Nb₅Si₃. The high creep properties are provided by the silicide, through the tetragonal silicide α / β. An undesired hexagonal silicide also exists but is avoided due to its poor creep properties, though these will be discussed in detail later in

this document.^[59] The main creep mechanism between 1200°C – 1400°C determined by Subramaniam is Nabarro-Herring. Other structures such as Nb₃Si and NbSi₂ have been investigated, but dislocation movements and inferior creep properties leave them inferior to Nickel superalloys.^[55] The creep exponents for Nb and Nb₅Si₃ have been determined as ≈6 and ≈1 respectively.^[60, 61] The volume % of Nb₅Si₃ must be balanced to not reduce the toughness properties that the Nb_{ss} provides.

2.4.2 Oxidation Resistance

The oxidation resistance of Nb-Si alloys is generally poor. Whilst some alloys may have good resistance, it often at the sacrifice of mechanical properties. Very few experiments provide both oxidation resistance and creep/toughness properties.^[46] This section will investigate current research focused on corrosion resistance, including elemental additions and coatings.

The most significant disadvantage is pesting which was mentioned briefly in **section 2.4**. Whilst the exact mechanism is unknown, some evidence suggests it propagates through pre-existing cracks or pores, intergranular oxidation and grain boundary hardening.^[28] Different phases within the Nb-Si system react differently, for example the resistance of NbSi₂ shows a tendency to pest when pores and cracks are present. Both the Nb_{ss} and Nb₃Si intermetallic have been observed exhibiting this phenomena, decaying into powders after 24 h.^[62]

Table 2: Table comparing oxidation resistance across a varied alloy composition

Alloy	Experiment Temperature (°C)	Recession Rates (µm.h ⁻¹)	Processing Method
Nickel superalloys ^[63]	1200	23	Investment casting
Target	1200	25	--
Nb-10 at.% Si ^[63]	1200	225	Arc-melting
Silicide coating ^[64]	1250	22	Arc-melting, Molten Salt
4 th Generation Nb-Si-Ti ^[46]	1200	40.2	Directional Solidification

Oxidation on both polycrystalline and single crystal materials follows a linear rate law suggesting that the rate of oxidation is dependent upon a surface-reaction step or gas diffusion.^[65] The Nb-Si system produces an oxide layer at elevated temperatures, consisting of

Nb₂O₅ with small amounts of SiO₂, all in the form of a loose scale. Due to the multiple allotropes the oxide may adopt, some of the scales are larger than the surrounding crystals and do not adhere to the surface, exposing any material underneath. Microstructural evidence confirms that oxidation rate is limited by the reaction rate of oxygen with the niobium solid solution and intrinsically the exposure of the Nb_{ss} to the atmosphere.^[46] The grain boundaries which are present in the polycrystalline material serve to increase this exposure area, dramatically increasing oxidation rate through oxygen diffusion paths.^[66]

Elemental additions can improve oxidation resistance, with 4th generation Nb-Si alloys often containing Ti, Al and Cr. The addition of Ti and Al greatly reduces pesting, whilst Cr can form Laves phases; oxygen resistant phases with unique mechanical properties.^[50, 67]

Work on silicide coatings for Nb_{ss}/Nb₅Si₃ alloys has also been developed.^[27, 64, 68] Multiple coatings have been attempted based on Ti-Al-Si or Ti-Al-Cr. Whilst not achieving long term resistance, these coatings do show a potential protection path.^[69-71] Other developments include a Si-Ge glassy coating developed in Beijing University. Through a combination of GeO₂ and SiO₂ surface deposits, a mass gain of 5.42 mg.cm⁻² has been achieved at 1250°C after 100 h.^[68] Molten salt coatings of Cr₂O₃, SiO₂ and Al₂O₃ have also shown promising results. The mass gain of the oxide coating was recorded as 1.77 mg.cm⁻² over 80 h compared to an uncoated samples gain of 34.34 mg.cm⁻² after 50 h (overall oxide resistance of ~22 μg.cm⁻².h⁻¹).^[64] TiO₂ inclusions formed within the molten salt continuous layer, increasing in concentration over time. Eventually TiO₂ became detrimental due to rapid diffusion of Ti and O₂ through the layer, which must be controlled to prevent the scale becoming a failing point in oxidation resistance.

Other glassy coatings include borosilicate's containing Mo, Si and B. The development of continuous glass coverage has led to mass gain of only 1.28 mg.cm⁻² over 100 h at 1250°C. A dense coating of MoSi₂ deposits on the surface, reacting with oxygen to produce a silica glass. The addition of boride lowers the viscosity of the silica, allowing a more uniform coverage. At increased temperatures MoO₃ begins to evaporate, exposing B₂O₃ which reacts to seal any cracks.^[72]

2.4.3 High Temperature Reactivity

There are many contributing factors involved in making commercially successful Nb-Si aerofoils. These alloys have been successfully created using a variety of processing methods ranging from optical floating zone method (OFZ), vacuum arc-melting (VAM) and directional solidification. The following section will be dedicated to some of the common processing techniques and their current progress with respect to oxidation resistance, low temperature mechanical properties and the capability to be constructed into useful components, an important factor for a processing method to become industrially viable.

Physical Vapour Deposition (PVD)

PVD is an unusual method which uses a type of vacuum deposition to deposit thin layers of material on a work piece as seen in **Figure 8**.^[38] This process has shown that a variety of materials can be produced using both electron-beam (EB) and magnetron sputter deposition. Components are created by sputter, depositing alternate layers of metal and intermetallic. This method is time intensive and unfeasible for industrial manufacture, with typical deposition times of $\sim 0.2 \mu\text{m}\cdot\text{min}^{-1}$. It may however provide a practical way of adding coatings on the surface of the blades (including inside air channels). General Electric have been researching this particular method and have employed it to produce disk shaped micro-laminates of Nb-Ti-Hf-Si up to $\sim 1 \text{ mm}$ thick.^[73] It may be that EB-PVD will provide part of the solution, allowing the control of thickness, microstructure and chemical properties of any given blades coating.

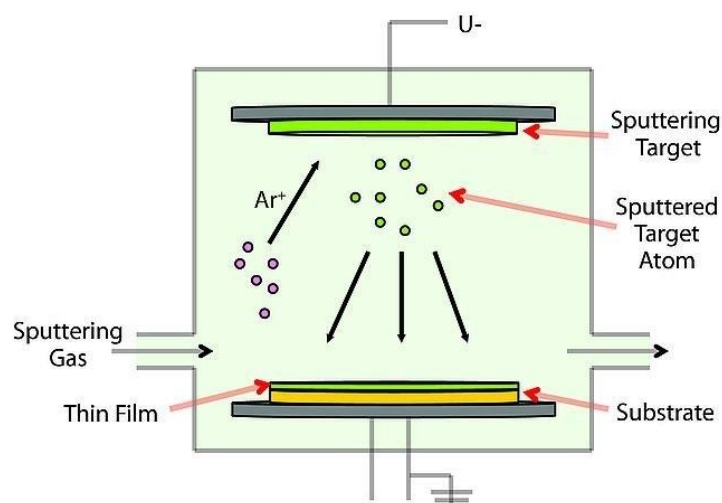


Figure 8: Schematic diagram of physical vapour deposition machine. A coating is heated to a vapour which deposits on the surface of a component.^[74]

Optical Floating Zone Melting (OFZ)

The optical floating zone is a method to purify crystals commonly used in the computer industry to create high purity semiconductors. A narrow section of impure crystal is melted, and a floating molten zone created and moved along the crystal, any impurities move along the crystal through the melt, leaving a purer metal solidifying in its wake, the schematic diagram can be seen in **Figure 9**. This method works based on the principle that the ratio of impurities in the solid phase to the liquid phase is less than one. This ensures that impurities will diffuse into the liquid phase at the solid-liquid boundary. The slow movement of the molten zone ensures that impurities stay within this section, moving through the crystal, and are moved to the end of the sample. Wide diameter samples may be produced, controlled using the electromagnetic-levitation effect. The actual specimen size is limited by the compromise between the hot zone dimension and the liquid surface tension. Single crystal monoliths have been constructed using this method with a pure Nb-Si alloy, where a much greater oxidation resistance is achieved due to lack of cracks and pores and lack of peeling at medium ranged temperatures.^[28] The examples that Zhang provides, however, show the single crystal monoliths being constructed at a very slow $1.39 \text{ mm}\cdot\text{s}^{-1}$ with other sources quoting even slower rates.^[75] With current technology, this construction rate has no feasible potential upscaling.

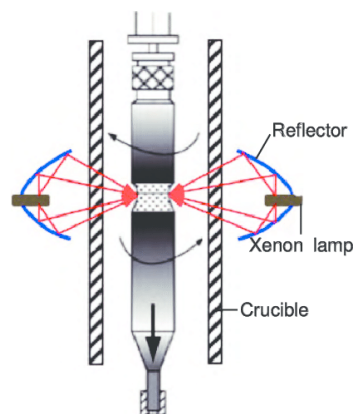


Figure 9: Shows a schematic diagram of an optical floating zone furnace, reflectors focus the lamp to a focused point producing a melting zone.^[76]

Extrusion

Possible fabrication methods include extrusion, involving the heating of canned ingots, in induction furnaces to temperatures in the range of 1400°C - 1600°C before being pushed/pulled through heated tool-steel dies maintained at 260°C as seen in **Figure 10**. These can be further machined into required shapes - turbine blades/engine section stators etc. Little work has been performed on the forging of components at the time of writing. The extrusion process has been shown to create directionally solidified microstructures parallel to the extrusion direction and the Nb₅Si₃ volume can be controlled by manipulating the silicon concentration.^[77]

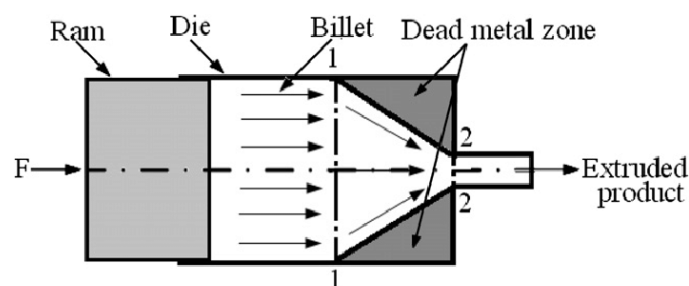


Figure 10: Shows a schematic representation of the extrusion process.^[78]

Czochralski method

The Czochralski method is another directionally solidifying technique often used to create single crystals, where samples are melted multiple times encouraging homogeneity within the alloy, this can be seen in diagram **Figure 11**. The melt is cooled at a controlled rate, and a seed crystal acts to encourage directional growth. Growth rates are consistent with low defect crystals produced in industry with rates between 0.5 mm.min⁻¹ - 15 mm.min⁻¹ and samples have been produced with lengths larger than 100 mm and diameters ~15 mm.^[7]

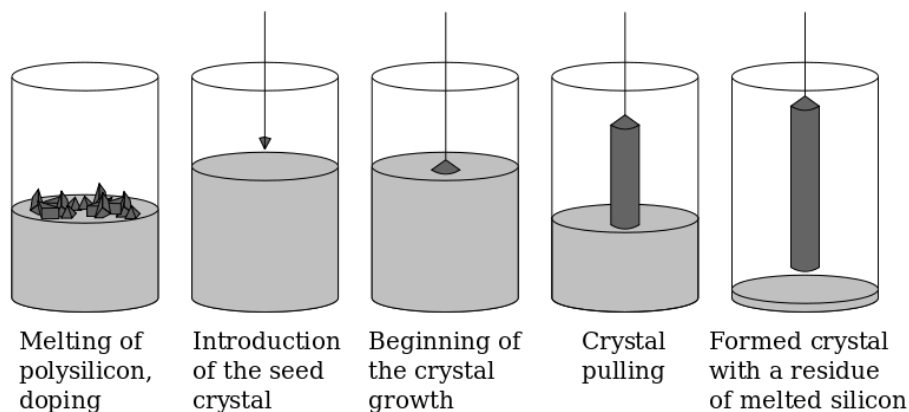


Figure 11: Formation of single crystal monolith via Czochralski method.

developed using this method as the temperature ceramics require for Nickel are lower than what is required for Nb-Si alloys. As noted in **section 2.3**, the eutectic point of Nb-Si alloys is 1915°C, this temperature is beyond the design parameters of superalloy moulds, resulting in undesired melt/mould reactions. The reactivity results from the oxygen content of the ceramic, reacting with alloy melts, forming brittle niobium oxide layers.

Thermodynamic studies have been performed and yttria (Y_2O_3) has been suggested as one of the more stable ceramics.^[81] It is not inert, and therefore diffuses into the melt, resulting in inclusions seen in **Figure 13**. These inclusions have been shown to react with Hf (a common addition to Nb-Si alloys) forming HfO_2 .^[82] The noted inclusions have a lower density than the melt, causing them to float, lowering overall inclusion concentration.

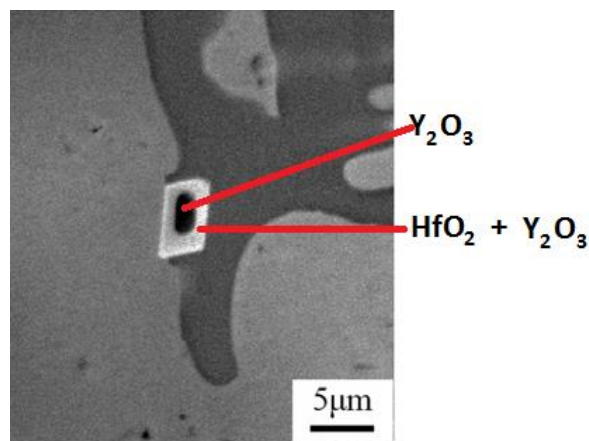


Figure 13: Backscattered electron micrograph of metal-mould interface in 0.1 Y alloy showing yttria reacting with hafnium at the metal mould interface^[82]

Hot Isostatic Pressing (HIP)

HIP is an adaptable process. It can be used as a near net-shape manufacturing process, and also as a post-processing technique to reduce the porosity of fabricated materials. It is used to improve mechanical properties of many alloy mixtures, some plastics and glasses.^[83]

High temperature and pressures are applied to sealed degassed cans containing alloy powders or pre-fabricated samples. The combination of temperature/pressure consolidates materials, fusing them together, through a combination of plastic deformation, diffusion bonding and creep mechanisms.

HIP is becoming more common as a near net-shape manufacturing technique as the high cost of using powders can be outweighed by cheap and simple manufacturing procedures. The use

of HIP to create Nb-Si alloys has been researched by Dicks and it may be a viable processing technique^[9]. Other researchers have successfully used this method, although they were slightly more complex and involved a pre-alloyed material ingot which is then used as the precursor material.^[84]

Additive Manufacturing (AM)

The term additive manufacturing encapsulates many techniques for material fabrication, including; stereolithography (SLA), fused deposition modelling (FDM), selective laser sintering (SLS), direct laser melting (DLM), cold spray (CS) and others.^[85-90]

Additive manufacturing has been tested to establish efficiency and plausibility of near net-shape processing on an industrial scale.^[85] Companies such as GE use AM to streamline production, creating a single bespoke material to replace the almost 20 individual components originally hand joined.^[10] DLM is one type of additive manufacturing process which builds a material layer-by-layer, directly depositing powders in a melt pool. A focused laser beam is directed at a Ti base plate and used to form this melt pool onto which powders are deposited. These then melt and re-solidify as the beam scans over each section, building a 3-dimensional material. It can create walled objects with microstructures comparable with traditional casting. A thermal history develops due to thermal differences along its axis, for example, a titanium substrate is often employed, and this is in direct contact with the base of any fabrication and acts as a heat sink, forming a thermal gradient.

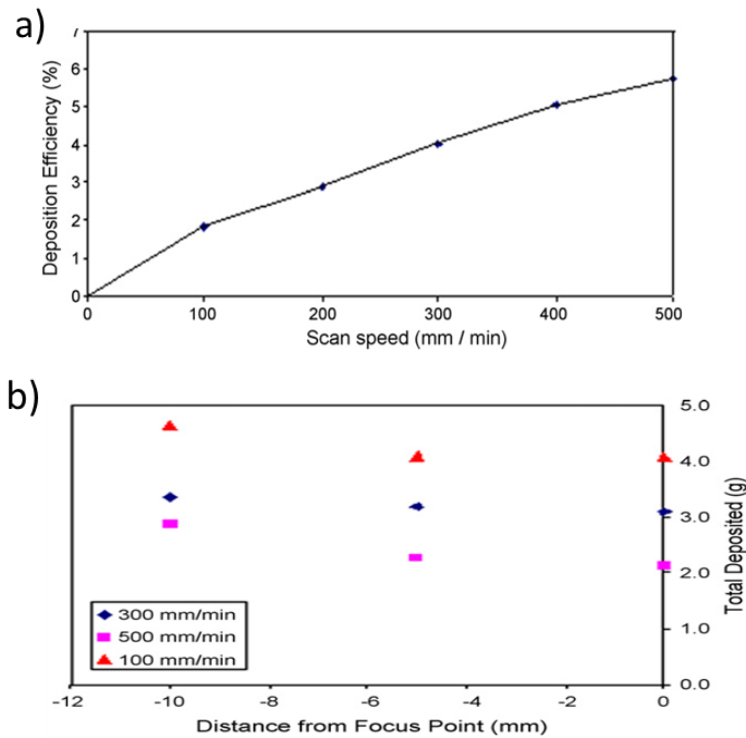


Figure 14: Graphs showing a) Deposition efficiency of DLF processing as a function of scan speed and b) Total material deposited as a function of distance from focal point, for three different scan speeds^[85]

The effectiveness of DLM is dependent on multiple factors, some are illustrated in Figure 14. Process efficiency can be determined by beam power, spot size and scan speed control, the latter presenting the highest efficiency improvement.^[85] Overall construction speed has been shown up to 500 mm.min⁻¹, this is relatively fast compared with the Czochralski method, however, it is likely that these systems won't be fully implemented until further research in process performance, mechanical and oxidation properties have been established.

2.4.4 Summary

This section of the thesis has discussed the current challenges that remain to be overcome in Nb-Si alloys. A balance of properties is required in order to develop a material to replace nickel superalloys. These properties can be chosen by understanding microstructural impacts of each phase and targeting the desired phase combination. The mechanical and oxidation properties of multiple phase combinations have been considered throughout sections 2.4.1 and 2.4.2. These phase combinations will also be affected by the production method used, as discussed DLM is the process used over the others considered due to the high melt reactivity of Nb-Si alloys, simplifying construction.

3 Experimental Methods

3.1 Introduction

The following section will discuss the production and analysis of Nb-Si alloys used in this thesis. Samples were constructed using LAM and post processing was performed using HIP and heat treatment. A combination of back scattered electron images (BEI), X-ray diffraction (XRD) and X-ray CT was performed, and these techniques will be discussed here along with Rietveld modelling used to calculate crystal sizes from collected XRD data.

3.2 Construction and Post-Processing

Near net-shape manufacturing is a novel method to process powdered metal feedstock. The main processing method used in this experiment is Direct Laser Fabrication (DLF), a schematic diagram of which is presented in **Figure 15 a)** and DLF machine that was used in **b)**.

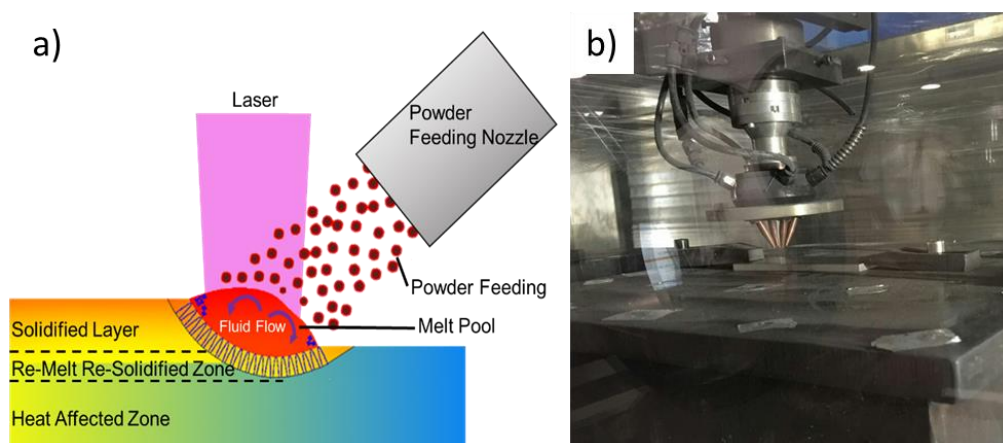


Figure 15: a) Schematic diagram of the deposition of material via direct laser fabrication b) LSF-SI600A direct deposition laser used during experimental

The main advantage of this method over casting is the lack of cast or mould. As mentioned previously in **section 2.3**, Nb-Si-Ti alloys have a higher solidus temperature than conventional nickel superalloys, as a result Limin Ma (2012) has shown interaction between Nb-Si-Ti melt and the mould wall.^[82] DLF removes the required mould and allows complex near net-shape components. DLF does have its disadvantages however, Dicks has shown that deposition efficiency may vary depending on scan speed and laser focus.^[85] Increasing scan speed may increase deposition efficiency, but loss of material can be observed and material near the walls of structures may only partially melt. After construction, samples were HIPped to both reduce porosity and to enhance the samples microstructure. Post-HIP, samples were heat treated to

reduce internal stresses induced during hot isostatic pressing and to finalise phase changes. Not all samples experienced the same post processing and **Figure 16** below shows the construction route each sample.

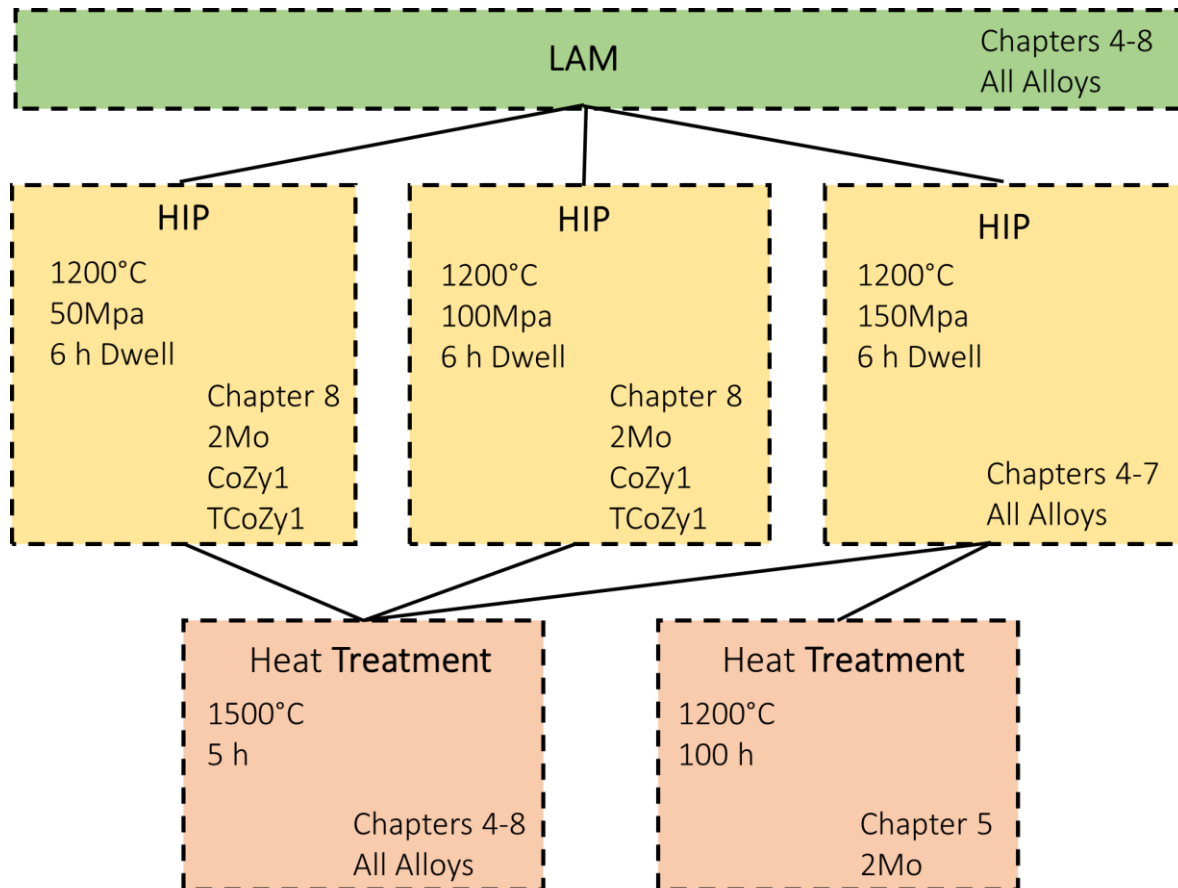


Figure 16: Diagram showing the route each sample took during construction

3.2.1 Powder preparation

Alloys for DLM were prepared and built at Northwestern Polytechnical University, Xi'an, China (NWPU). Samples were created with a 3 kW LSF-SI600A laser in a custom housing unit under protective argon atmosphere. Elemental powders of Nb, Si, Ti, Al, Cr, Hf, V, Mo, Zr, Y and Ta were prepared to 200 mesh (~ 74 μm) and obtained from NWPU. Respective alloys were measured out with individual elemental powders in an electric balance before drying for 3h at 120°C under Ar and ground in MITR YXQM-0.4 L ball mill (see **Figure 17**) for 2 h. The milling balls used were steel, samples were analysed using X-ray Fluorescence to determine if Fe traces were present. No solvents were used in preparation of powders.



Figure 17: Ball mill used to grind powders to even size

Powders were filtered to 200 mesh ($\sim 74 \mu\text{m}$) using a mesh screen and then added into DPSF-2 containers seen in **Figure 18**, argon was used to feed powders into the system.



Figure 18: DPSF-2 container (highlighted) used to store powder before processing

3.2.2 Laser Parameters (Direct Laser Deposition)

A 3 kW LSF-SI600A laser was used to produce cuboidal structures as these allowed easily repeatable objects for analysis, images of constructed test pieces can be seen below in **Figure 19 a)**, a demonstration blade can also be seen in **b)**.

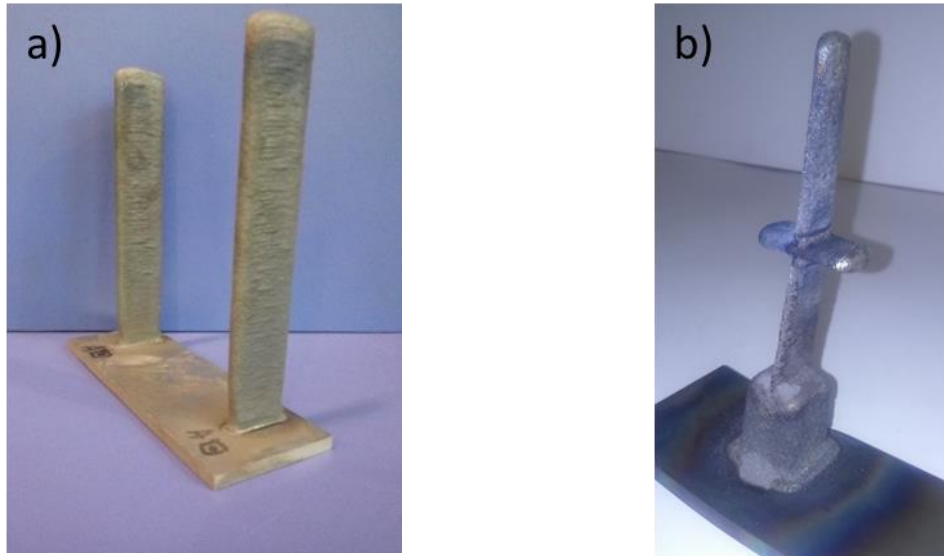


Figure 19 : Images of a) constructed samples and b) demonstration blades

Fabrication occurred under an argon atmosphere ($O_2 < 100$ ppm) using a clear bag to provide a protective enclosure. A melt pool was created on a titanium baseplate using a semiconductor laser (power = 3 kW, spot diameter = 6 mm). Powder was blown at constant flow rate of 6 $L \cdot min^{-1}$, with a mean particle size of 74 μm , through four nozzles at either pole directed at 45° towards the laser beam, the laser working distance was 15 mm. The substrate focal point remained as constant as possible (some deviation occurred during construction but was corrected for), a continuous scan speed of 900 $mm \cdot min^{-1}$ was used. The layer thickness was 30 μm and sample fabrication occurred in one continuous process with 30% overlap on each run.

The scan pattern used throughout the experiment was the cross-snake. After the initial layer is deposited in both x+ and x- direction, a second layer is deposited in y+ and y- direction, this aims to reduce the thermal stress through the material. A Schematic can be seen in **Figure 20**.

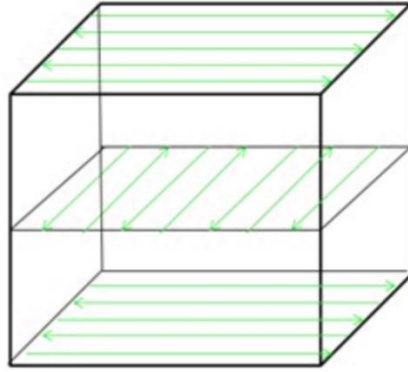


Figure 20: Schematic layout of cross-snake scanning pattern

Multiple alloys have been created using DLM, and alloy compositions were based on previous studies and are discussed in each relevant chapter. The goal was to create samples based on previous work to show replicability, later chapters discuss alloys designed by the group at the University of Leicester. Alloys chosen can be observed in **Table 3**.

Table 3: Compositions chosen for DLM (values in at.%)

Alloy	Nb	Si	Ti	Cr	Al	Hf	V	Mo	Zr	Y	Ta	Ref
14Cr	Bal	15	22	14	2	2	2	--	--	--	--	[50]
2Cr	Bal	15	22	2	2	2	2	--	--	--	--	[50]
6Cr	Bal	15	22	6	2	3	--	--	--	--	--	[85]
2Mo	Bal	18	24	5	5	--	--	2	--	--	--	[46]
CoZy1	Bal	18	24	5	5	--	--	2	1	0.08	--	--
CoZy5	Bal	18	24	5	5	--	--	2	5	0.40	--	--
TCoZy1	Bal	18	24	5	5	--	--	2	1	0.08	2	--
TCoZy5	Bal	18	24	5	5	--	--	2	5	0.40	2	--

3.2.3 Hot Isostatic Pressing (HIP)

During solidification of DLF materials porosity was noted in the form of round porosity seen in **Figure 21**. In a typical component this porosity can serve as stress concentration points leading to failure of the sample.

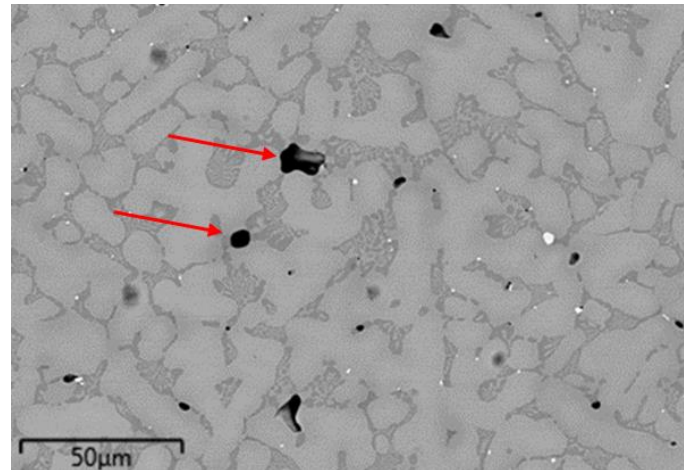


Figure 21: Shows formation of gaseous porosity in Nb-Si-Ti alloys

As part of the post-processing scheme, DLF structures underwent a hot isostatic pressing treatment to reduce this porosity. HIPping involves placing samples in a high temperature (usually $<0.8 T_m$), high pressure environment. Ar was used to provide isostatic pressure, although He may also be used. This is aimed at lowering internal porosity and reducing the residual stress resulting from solidification contraction, as represented in **Figure 22**.

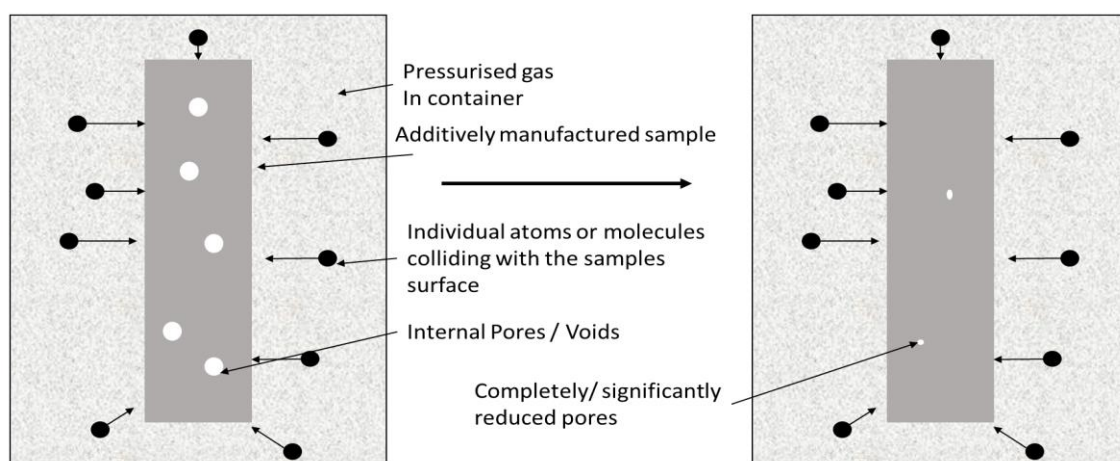


Figure 22: Shows the generalised mechanism for HIP^[91]

Samples were removed from the titanium base plates prior to the HIP experiments, an EPSI model V0 15197 from the University of Birmingham, shown in **Figure 23**, was used for all experiments.^[92]



Figure 23: Shows the HIP equipment used during experiments^[92]

Three HIP experiments were performed to observe the relationship between pressure and porosity closure. The parameters for the experiments may be seen in **Table 4**.

Table 4: Parameters used during HIP experiments

Parameter	Value
Temperature	1200°C
Dwell	6 h
Heating/Cooling rate	10°C.min ⁻¹
Pressure	50 / 100 / 150 MPa

3.2.4 Heat Treatment

The second stage in post-processing was a heat treatment stage to encourage equilibrium conditions and produce the desired end phase established in phase diagrams. A horizontal tube furnace from Elite Furnaces (model number TSH16/50/180) was used. Heat treatment was performed for 5 h at 1500°C under argon atmosphere to prevent oxidation of alloys. A picture of the furnace is seen in **Figure 24** for reference.



Figure 24: Shows tube furnace used for heat treatment of Nb-Si-Ti alloys

Heat treatments encourage solid state diffusion close to the liquid temperature, promoting a thermodynamic equilibrium state. Parameters such as temperature, cooling time etc. may be altered to promote the required properties of phases, i.e. iron's martensitic transformation or evolution of γ/γ' in Ni-superalloys.

A second heat treatment was performed at 1200°C for 100 h. This was only performed on 2Mo to observe the effects of lower temperature on phase evolution.

3.3 Analysis Methods

3.3.1 Sample Preparation

Samples were prepared for characterisation by a series of cutting, grinding and polishing. Samples were cut into ~4 mm thick samples using both ATM Brilliant 220 precision cutter and the company EDM precision technologies Ltd. They were then mounted in conductive Bakelite™ in a Struers CitoPress. Using a Saphir 520, samples were ground using 80, 240, 600, 900, 1200 grit SiC paper before being polished using diamond paste of 6, 3 and 1 μm .

A schematic diagram can be seen in **Figure 25** which describes the area observed during SEM analysis. This area was chosen as provided the most stable cooling areas i.e. was not affected by the heat sink effect of the base plate or the areas that experienced less heating (from fewer passes of the laser beam).

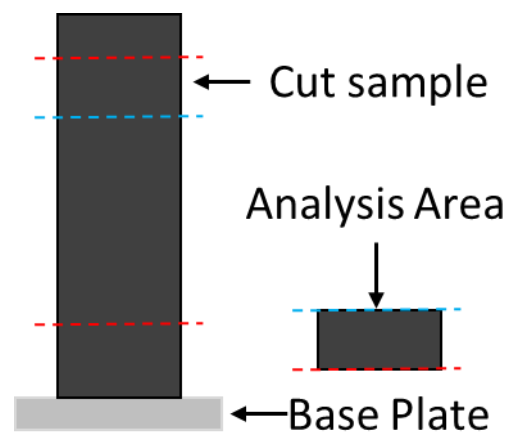


Figure 25: Schematic of analysis area of test pieces

3.3.2 Volume Fraction Calculations

Three methods were possible for volume fraction calculation and each have their pros and cons. Image analysis of a series of back scattered electron images can provide close analysis of the microstructure and allows smaller porosity to be estimated (in this thesis, at least three images were analysed at different points on the microstructure and the volume fractions averaged). X-ray CT may be used to calculate porosity on an entire sample. It is limited by the detector size on the instrument. This method was performed in conjunction with BSE image analysis in section **8.2**. Another method is to calculate it using XRD and modelling the volume fraction using Rietveld refinement. This calculates a volume fraction over a much wider area giving a better average of the phases present, it isn't able to observe porosity however. This method was used for volume fraction analysis throughout the rest of the thesis, with standard deviation for the model being listed in the appendix. Further information on each method can be seen in **section 3.3.53, 3.3.54 and 3.3.5** respectively.

3.3.3 Scanning Electron Microscopes

Scanning electron microscopy (SEM) was performed using Quanta FEG 650 by FEI with 20 kV accelerating voltage and a relative spot size of 5. Secondary electron and back-scattered electron images were obtained using a R580 and DBS 1005713 detector respectively. EDS point analysis was obtained over a range of three spots to give an average of sample.

An X-Max 20 by Oxford Instruments was used for Energy Dispersive X-ray Spectroscopy (EDS) analysis using the same parameters as previously mentioned. EDS was collected using INCA software to calculate elemental composition. Collection time for spectra was 120 s live time.

3.3.4 X-Ray Diffraction

All phase identification was performed using a Bruker D8 Advance Powder Diffractometer with DaVinci, equipped with a LynxEye Position Sensitive Detector in a flat plate (Bragg-Brentano) 2 θ configuration. A CuK α source was used with a Ni-K β filter. The initial 2 θ angular range used was 4° to 90° using a 250 mm goniometer, with a 0.01° 2 θ step size and a 0.5 s count time per step. Information regarding crystallographic structures obtained from the Crystallographic Open Database (COD), individual data files and origins are credited in **Table 5**.^[93]

Table 5: List of phases attempted in models

Phase	Space Group	Source
Corundum	R-3C:H	Lutterotti (1990) ^[94]
Nb₅₅	Im-3m	Badenet <i>al.</i> (1983) ^[95]
α-Nb₅Si₃	I4-mcm	Partheet <i>al.</i> (1955) ^[96]
β-Nb₅Si₃	I4-mcm	Aronsson (1955) ^[97]
γ-Nb₅Si₃	P63-mcm	Schachneret <i>al.</i> (1954) ^[98]
Cub-Nb₃Si	Pm-3m	Galassoet <i>al.</i> (1963) ^[99]
Tet-Nb₃Si	P42-ni2	Waterstrat (1975) ^[100]
NbSi₂	P62-22	Kubiaket <i>al.</i> (1972) ^[101]
C14-Cr₂Nb	P63-mmc	Laveset <i>al.</i> (1939) ^[102]
C15-Cr₂Nb	Fd-3m	Kornilov (1965) ^[103]
HfO₂	Fm-3m	Wyckoff (1963) ^[104]
HfO₂	P121-c1	Whittleet <i>al.</i> (2006) ^[105]

3.3.5 X-ray Computed Tomography (X-ray CT)

X-ray CT combines many x-ray images (of different orientations) of an object to produce a tomographic image. Each slice of an x-ray image allows non-invasive inspection of an object. Data was collected using a Nikon XT H 225, with a tungsten filament used for each sample and Varian 2520Dx detector with pixel size 127 μ m. X-ray CT is a unique analysis technique, in that parameters are usually bespoke for each sample.

3.4 Rietveld Refinement

Rietveld refinement was used to model several functions including the volume fractions used in this document, modelled parameters are compared to experimental X-ray diffractograms until an accurate “fit” is achieved. Functions begin simple and with each iteration, more complex parameters are introduced and refined. A brief introduction to Rietveld refinement will provide the reader with basic concepts, while further reading is provided by Dr L. Lutterotti and Chateigner.^[106, 107] Many programs may be used to perform Rietveld refinement, the experiments used MAUD (Material Analysis Using Diffraction) to perform modelling of collected XRD data. An annual MAUD school, hosted in Caen, provided much of the knowledge for this program.^[108]

3.4.1 Intensity Factors

MAUD uses a non-linear least-squared algorithm seen in equations (3) and (4), to fit a residual function S, the function is allowed to vary and allows the crystal structure to be refined on the dataset, I_n^{calc} and I_n^{exp} are the intensities at n , of modelled and experimental pattern respectively. Each pattern is “refined” over a set of iterations, often called a cycle.^[108]

$$S = \sum_n w_n (I_n^{exp} - I_n^{calc})^2 \quad (3)$$

Where by $w_i =$

$$w_n = \frac{1}{I_n^{exp}} \quad (4)$$

The intensity of a simple modelled pattern with one crystal phase can be determined in (5), parameters will be defined here and described in further detail in their own section.

$$I_i^{calc} = S_F \sum_{j=1}^{Nphases} \frac{f_j}{V_j^2} \sum_{k=1}^{Npeaks} L_k |F_{k,j}|^2 S_j (2\theta_i - 2\theta_{k,j}) P_{k,j} A_j + bkg_i \quad (5)$$

Where: S_F is the beam intensity, dependent upon measurements. V_j and f_j are phase cell volume and volume fraction respectively, these influence S which is the overall scale factor and must be modelled for each data set.

L_k is the Lorentz-Polarisation factor and depends on the instrument-geometry. Instrument geometry, monochromator and detector are all considered factors to determine using a standard reference. K is a peak number describing a set of Miller indices (h, k, l).

F_k is the structure factor of a peak number K and relates the scattering from each atom with a unit cell. This factors in the multiplicity of reflections, as well as the influence on temperature and atomic vibrations within a crystal lattice. Only X-rays were modelled in this thesis, so temperature factors were not defined. Neutron scattering would have allowed accurate measurements of these displacements but was beyond the scope of this thesis.

S_j is the profile function, and this affects peak shape, based on the sample and instrument. Different profile functions can be fitted, Gaussian function was used, with 'gaussianity' calculated using a reference sample discussed in **section 3.5**.

P_k describes the preferred orientation of grains (texture). In samples containing texture the relative intensities of X-rays differ depending on the Bragg angle plane. In a sample without texture, crystals would be randomly orientated and thus have no preference to any one plane. Samples may be prepared to help reduce texture (if desired), which is usual for powder samples and typical in geological samples. Samples in this thesis were not powdered samples and so texture is likely due to the effective 'directional solidification' of laser additive manufacturing (LAM). Samples will be considered case by case in regard to texture and further details will be present in relevant sections. A standard corundum reference material was used to calibrate texture. Whilst this sample is not ideal, an acceptable goodness of fit (GOF) was achieved.

A is the absorption factor and is affected by both beam intensity and sample absorption. bkg describes the modelled background intensity; a polynomial is used in this experiment, but many others exist.

3.4.2 R_{wp} , R_{exp} and Goodness of Fit

The quality of a refinement in this thesis will use the values of R_{wp} and R_{exp} to calculate a (GOF). The successfulness of a modelled fit is based on the relationship:

$$GOF = \frac{R_{wp}}{R_{exp}} \quad (6)$$

Where R_{wp} is the 'weighted pattern' and is the value that is minimised during refinement, and R_{exp} is the expected value of R_{wp} after refinement. R_{wp} does not depend on the absolute values of intensities but is affected by to the ratio of signal/noise. With high background noise, low values are easily obtained and more complex diffractograms with multiple sharp peaks reduce

the chances of a good fit. Over each cycle, modelled peaks are assessed by inspecting R_{wp} factor, calculated in (7), throughout a set of refinements. The aim is to reduce the value to align calculated and experimental values.

$$R_{wp} = \left[\frac{\sum w_n (I_n^{exp} - I_n^{calc})^2}{\sum w_n (I_n^{exp})^2} \right]^{1/2} \quad (7)$$

R_{exp} describes the minimum obtainable value of R_{wp} over a given number of refined parameters and is calculated by (8). N , P and C are the number of data points, number of refined parameters, and the constraints in the refinement respectively.

$$R_{exp} = \left[\frac{N - P + C}{\sum w_n (I_n^{exp})^2} \right]^{1/2} \quad (8)$$

3.4.3 Factors Affecting Peak Position and Shape Sample Height Displacement

An adequate X-ray diffraction requires that samples are sufficiently prepared, the sample holders used require precise setup to achieve accurate results. Any variation in sample height produces a shift of $\Delta\theta$ in the 2θ positions of recorded patterns. Samples were adhered to holders on a level surface to ensure no accidental displacement. This is more difficult with constructed test pieces where larger holders were required. As a result, interference was detected at low 2θ due to a combination of the beam leaving the sample area and increased air scattering. This can be observed in **Figure 26**. Due to this interference, angles less than $2\theta=20$ were not considered. This simplified peak fits, as little information was lost compared to the corrected noise.

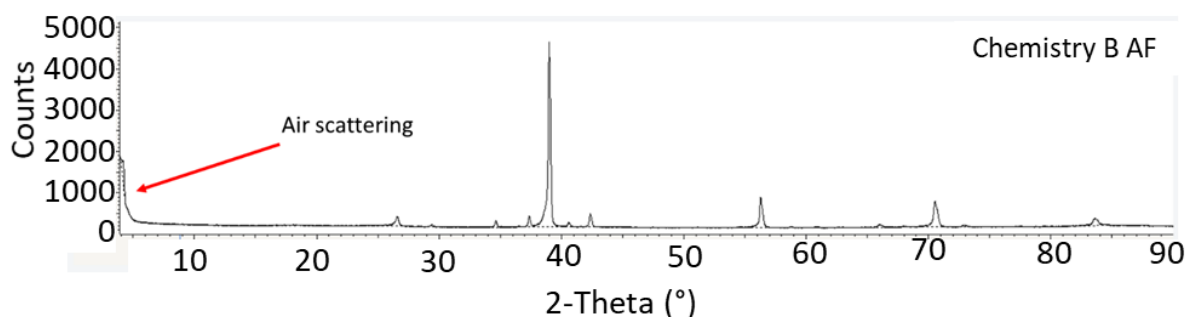


Figure 26: Example X-ray diffractogram, displaying low angle noise

2 θ Theta offset

Peak positions may be offset due to instrument misalignment, which will be calculated using a standard reference material and is discussed later in this document. A corundum scan was performed each time a set of data was taken to ensure erroneous results due to misalignments were avoided.

Strain

Strain inside the material can change lattice parameters which may shift positions of peaks.^[109] Hot isostatic pressing was used to consolidate samples, the increased pressure of which and subsequent effects on crystal structure will be discussed within the thesis in more detail.

Crystallite size

Lattice parameters will not be absolute for each crystallite present and a distribution will be calculated, with large distribution in parameters presenting as peak broadening. This broadening will be characteristic of solid solution phases (such as Nb_{ss}), where crystallites will be homogenous over a system but may contain micro-segregation of elements, slightly altering lattice parameters.^[110]

Instrumental broadening

Peak shape may also be influenced by the instrument used, factors such as geometrical configuration, sollers and beam characteristics. To model beam influences, peak asymmetry, full-width-at-half-maximum (FWHM) and line broadening, samples are characterised according to the NIST standard discussed in **section 3.5**.

3.5 Calibration of X-ray Diffractometer

Section 3.4 discussed the basic parameters that affect the x-ray diffractogram pattern including instrument and sample contributions. These two factors may interfere with Rietveld refinement, and in order to begin processing samples it is important to account for any instrument broadening. This requires that the instrument be “defined” using a standard reference material (SRM).^[111] Materials with minimum line broadening are required, these properties require low microstrain and large crystallite size. Standard reference materials can be obtained from the national institute of standards and technology (NIST) accompanied by a

certificate of the samples microstrain and crystallite size. Using this standard, it is possible to fit a Rietveld refinement. The Caglioti equation (9) is used to help define any asymmetry in the Gaussian fraction of the instrument, from this the instrumental line broadening contributions can be accounted for.

$$H = (U. \tan^2\theta + V. \tan\theta + W)^{1/2} \quad (9)$$

3.5.1 Refinement of NIST Standard Reference Material (SRM)

Many SRMs exist, each with benefits and drawbacks. The SRM used for these experiments is the 1976b Al₂O₃ (Corundum) structure and is a sample primarily used for peak position determination rather than line shapes.^[112] This sample is not ideal but due to constraining factors it was not possible to use LaB₆ – usually used to calibrate line position and line shape.^[113] Although not ideal, the NIST certificate states that the sample contains a reduced level of microstrain although it contains a “slight but discernible level of Gaussian microstrain broadening”.^[112] It does however state that the sample has an “essential absence of crystallite size broadening” and can be used to obtain an approximation for the instrument profile function. It is for this reason that the corundum SRM was used in this material.

As a result of manufacturing methods, 1976b is known to have some texturing properties, this is from the pressing of the sintered platelets to form the compact, the lattice parameters for this material can be seen below in **Table 6**.

Table 6: NIST certified lattice parameters for 1976b standard reference material

Lattice Parameter	Value (Å)
a	4.759137
c	12.99337

3.5.2 Acquisition of Corundum Data

Observation of the overall corundum peaks in **Figure 27 a)** shows many diffraction peaks along the sample. Without closer inspection the sample peaks appear very sharp (Lorentzian) with few gaussian qualities, suggesting little affect from the instrument. Closer inspection of individual peaks shows that each K α peak has a neighbouring K α_2 peak seen in **Figure 27 b)**. Features can also be seen on either side of peaks and are labelled. In order to perform Rietveld analysis, these features must be identified or attempted to be modelled.

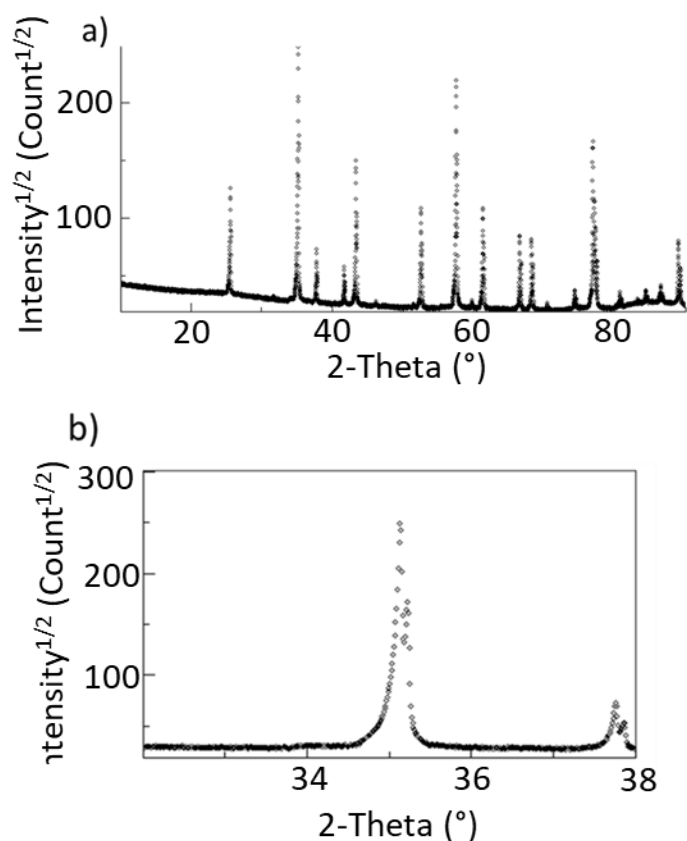


Figure 27 : Diffraction of 1976b corundum at a) Full spectrum and b) 32° to 37.5°

When modelling is first attempted under instrument standard conditions an imperfect fit is reached. The plotted model can be seen in **Figure 28** and the values for R_{wp} and R_{exp} (11.343 and 2.978 respectively) result in a GOF of 3.809. For reference, a “good fit” for a medium complicated sample is ~ 2 .^[107]

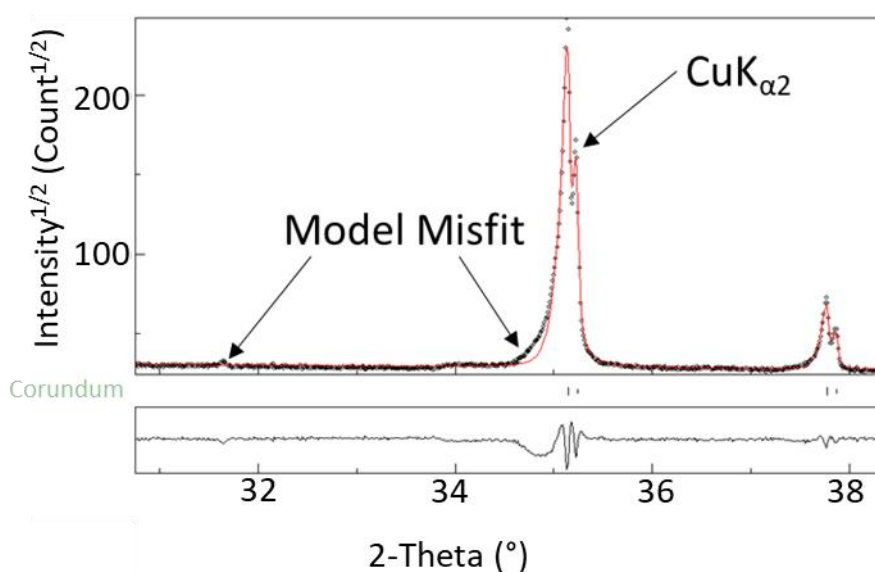


Figure 28 : Diffraction of 1976b corundum at modelled using Rietveld analysis in Maud

This fit for a reference sample is not high enough and is caused by the features noted above.

There are two possible reasons that these features are produced:

- 1) Crystallographic impurities on the corundum sample
- 2) Instrumental parameter error.

The certificate with the SRM states it does not contain crystallographic impurities.^[112] The reason most likely for the feature is instrumental, and the following sections will attempt to remove these features.

Removal of Diffractogram Features

The observation in **Figure 27** has been modelled using MAUD (version 2.8) and the corundum.cif file by Lutterotti and Scardi from COD.^[93, 94, 114] Some assumptions were made prior to modelling and refinement was performed in the following order:

Refinement order:

- 1) Background function (5th degree polynomial)
- 2) Intensity Scale
- 3) Asymmetric_0 and 1
- 4) Caglioti U, V, W
- 5) Gaussian_0 and 1

Assumptions made for the SRM were a nominally chosen crystallite size of 3 μm , an absence of crystallite size broadening and that the Bruker D8 data assumed the wavelength of Cu $K_{\alpha 1}$ and Cu $K_{\alpha 2}$ was 1.5405 Å and 1.54439 Å respectively.

As previously stated in **section 3.5.2**, the corundum modelled contains a texture, this requires modelling to fully complete the equipment defining. As a detailed knowledge of texture analysis was not required to complete the project, assistance from Prof. D. Chateigner and Prof L Lutterotti was sought. Several texture models have been attempted previously by Watkinson EJ. (2017) and information on these models can be found here:^[115]

Standard functions (Lutteroti 2007)^[116]

Spherical Harmonics (Chateigner 2013)^[117]

Arbitrary texture (Fong 2013)^[118]

For this thesis, an arbitrary texture model was applied.

3.6 Principles of X-ray CT Set-up

The setup aim for each X-ray CT scan is to produce an overall image with a contrast ratio of 6:1 i.e. the background is 6 times brighter than target. Quality of CT data depends on many parameters, including sample density, exposure time and beam current. Below is a generalised set up to produce desired images, initial parameters are listed in **Table 7** with further details after.

Table 7: Arbitrary values for initial set up

Feature	Value
Voltage	40 kV
Power	7 W
Exposure	500 ms

Set up procedures:

- 1) Centre sample (ensure sample is in view during a 360° rotation)
- 2) Calculate spot size (discussed below)
- 3) Set minimum grey value of sample as 10 k
 - a. Increase grey value by increasing kV of X-ray beam
- 4) Set maximum grey value of background to 40 k
 - a. Increase exposure to increase object and background grey value
- 5) Add filters as required
 - a. Incremental increases of filters
- 6) Perform shading correction to change ratio of grey values from 4:1 to 6:1
 - a. If banding is visible, then return to step 2

Spot size

The spot size of the X-ray CT is determined by either the power or the current used during experimentation. It is therefore important to choose a spot size that is lower than the effective pixel size (EPS) of the sample being analysed. The EPS shares a relationship with the detector pixel pitch and geometric magnification of the sample as such:

$$EPS = \frac{DPP}{GM} \quad (10)$$

The detector pixel pitch is given as 127 from the instrument's manual.^[119]

An example of geometric magnification is shown in **Figure 29** and is calculated as follows:

$$GM = \frac{\text{source to detector distance } (x)}{\text{source to sample distance } (y)} \quad (11)$$

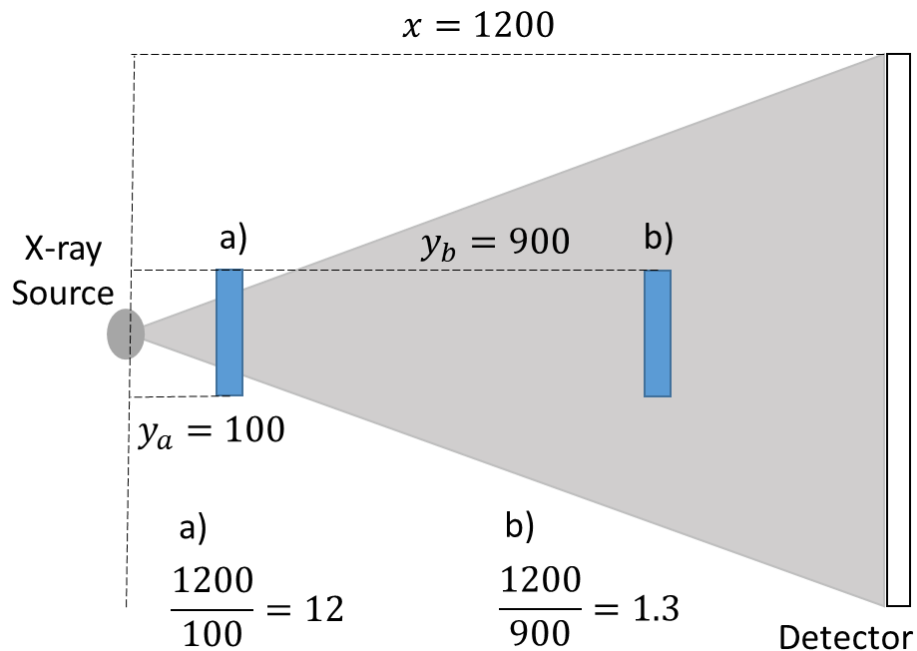


Figure 29: Example of geometric magnification of two different samples

The minimum spot size (MSS) of the source is 3 μm with a minimum spot power (MSP) of 7 W. Spot size increases by $\sim 1 \mu\text{m}$ every 1 W after the minimum. This may also be considered when calculating the highest power requirements (HPR).

$$EPS - MSS = HPR \quad (12)$$

$$HPR + MSP = W \quad (13)$$

For example:

A sample has an EPS of 16 μm and therefore the highest possible spot size/power increase is:

$$16 \mu\text{m} - 3 \mu\text{m} = 13 \mu\text{m}$$

As the minimum spot size has a power of 7 W the highest power increase may be added to produce the required power of that sample:

$$13 \text{ W} + 7 \text{ W} = 20 \text{ W}$$

Shading correction

It was previously mentioned that a background to object brightness ratio of 6:1 was required for a good scan. The instrument used contains a Varian 2520Dx detector which becomes saturated after a grey value of 40 k, which produces banding during the initial set up and disturbs data collection. To improve sample analysis a shading correction is used. This is an average image of the X-ray beam under different grey values and without a target object. During analysis, three grey values were used with a frame averaging of 256 times.

Filters

Filters are added in step 5 to improve the ratio of background to object. These help optimise grey values (see **Figure 30**) as well as reducing beam hardening.

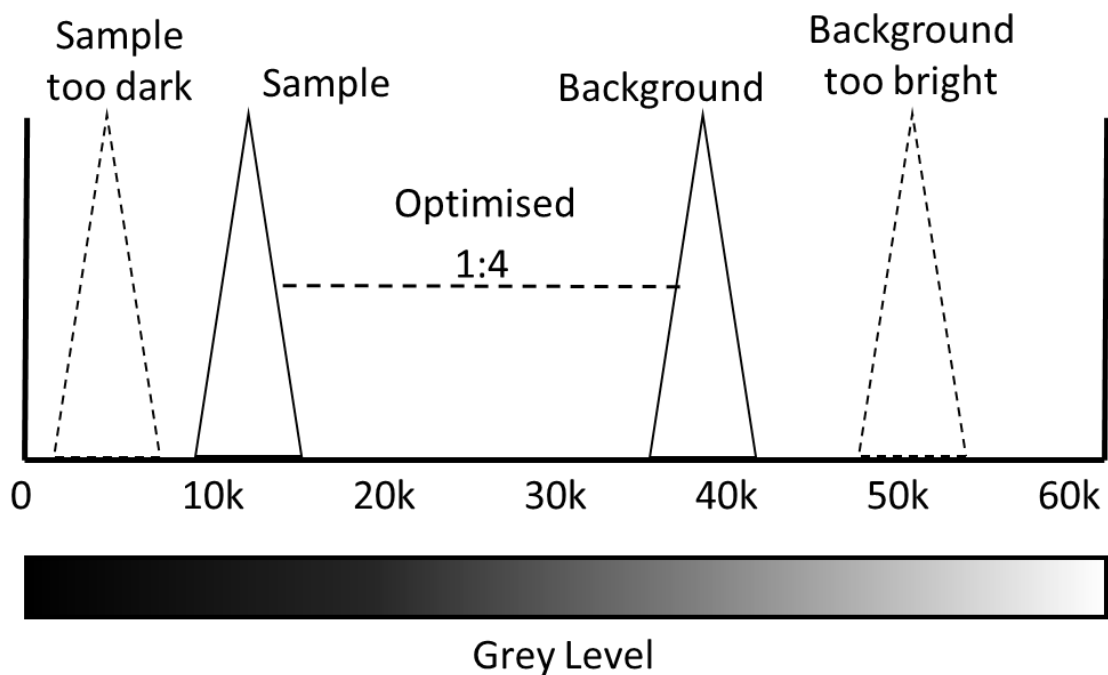


Figure 30: Demonstration of grey level optimisation

Beam hardening is the result of lower energy x-rays being absorbed by the surface of a scanned object resulting in a lower detected signal (as seen in **Figure 31 a**)). It gives the appearance of a higher density boundary on the material, resulting in a cupping formation seen in **Figure 31 b**). During analysis Cu was used as the default filter and increased incrementally, in some occasion's Sn was used which absorbs ~3x more x-rays than Cu but reduces signal.

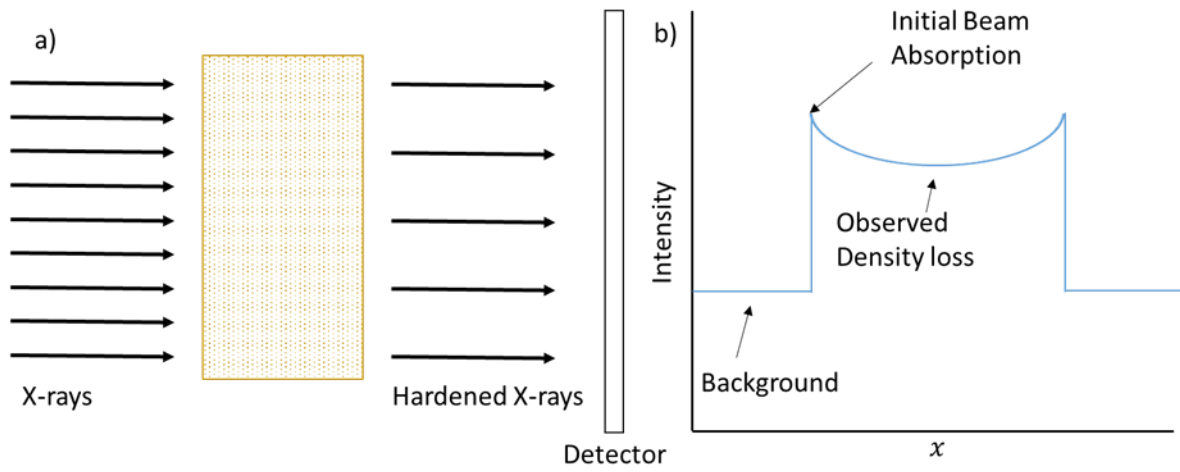


Figure 31 : An example of a) Sample showing beam hardening b) Histogram of cupping over scanned area

4 Effects of Cr and Hf additions on Phase Evolution in Direct Laser Melting of Nb-Si Alloys

4.1 Introduction

Using the Nb-Si binary system as a template there have been multiple experiments performed to improve the problems listed in **section 2.4**. Many elements have been implemented to understand trends, the most common of which are titanium, chromium, aluminium and hafnium.

Titanium has been one of the most used alloying elements in the Nb-Si system, showing good solubility at low temperatures, becoming completely soluble in niobium at temperatures above 882°C.^[120] The other common phase, Nb₅Si₃ also has high solubility, but at a higher temperature of 1200°C. It is promoted in the presence of Ti.^[44]

Studies by Bewlay have observed the stabilising effect of titanium in the Nb₃Si phase at low temperatures and its ability to prevent pesting. The addition of titanium lowers the solidus and liquidus temperature for the Nb_{ss} + Nb₃Si. This is controlled so the eutectic remains above 1700°C to ensure strength during high temperature applications. Excess Ti <25 at.%, may lead to the formation of Ti₅Si₃ which is detrimental for creep properties.^[38] Despite this, the effect of preventing the pesting anomaly means that it is still a desirable material to add to an alloy mix. It has been suggested that ways to reduce the TiO₂ content would help increase its high temperature stability.^[64] Increased levels of Ti have also been shown to affect γ -Nb₅Si₃ stabilisation, its actual influence on the microstructure is still unclear and the position of γ -Nb₅Si₃ on phase diagrams is also unclear.

Cr additions help to improve oxidation resistance, although the mechanism is still under debate.^[7, 50] With a high at.% Cr a Cr₂M Laves phase is produced establishing a ternary system of Nb_{ss}/Nb₅Si₃/Cr₂Nb. It has been found in alloys containing >5 % Cr and it is this phase in which the oxidation resistance is attributed to, although high volume fraction of Laves phase has shown to reduce plastic deformation properties of materials.^[121]

Aluminium serves two purposes, to increase both the oxidation resistance and the mechanical properties. The Nb₃Si phase is less favourable with aluminium present in the intermetallic phase and will decompose at lower temperatures into the solid solution and Nb₅Si₃ phase.^[122]

Small quantities are deemed useful, but the formation of Nb₃Al phases occur above 5 at.% of Al which decreases the materials creep resistance, for this reason, all alloys in this thesis contain ≤5% Al.^[50]

Hafnium has shown to dissolve in both Nb_{ss} and Nb₅Si₃, causing the crystal lattice to expand in both cases. The lattice increases are attributed to differences in relative atomic radii of Hf, Nb and Si; 1.56 Å, 1.43 Å and 1.17 Å respectively. This increases the coarsening effect of the material which in turn helps with high temperature creep resistance but also lowers the strength of the sample. Zhao has shown that Hf prefers to substitute at Nb sites in the intermetallic phase rather than the Nb-solid solution,^[44] this greatly effects the stabilisation of Nb₅Si₃ and promotes the formation of γ-Nb₅Si₃ which remains stable at 1500°C.^[51] In another paper, Zhao has determined that alloys with Hf concentrations above 10 at.% produce Hf₂Si and Hf₅Si₃.^[123] Bewlay on the other hand has linked Hf to stabilising the Ti₅Si₃ phase discussed above, the presence of which has been noted as unfavourable for creep behaviour.^[38] Other suggestions include the idea that Hf helps oxidation resistance by the formation of HfO₂.^[124] This compound reduces the oxidation of niobium as it is has a lower energy of formation than Nb₂O₅, which is the spallation material found on regular niobium silicide samples. This has consequences to oxide inclusions however, as discussed in **section 2.4.2**.

Vanadium dissolves preferentially into the Nb_{ss} phase and provides a low temperature yield strength increase. However, due to the lower melting temperature of vanadium it decreases the high temperature strength.^[120]

The following chemistries: Nb-15Si-22Ti-14Cr-2Al-2Hf-2V (14Cr), Nb-15Si-22Ti-2Cr-2Al-2Hf-2V (2Cr), Nb-22Si-26Ti-2Al-6Cr-3Hf (6Cr) were analysed using a series of SEM, EDS and XRD at each stage of processing. This enabled monitoring of phase formation / transformation. SEM was used to visually analyse the microstructure of each chemistry. However, phases were difficult to distinguish using only SEM, and so EDS and XRD were implemented to assist with phase characterisation. Most chemistries were previously produced using arc-melting, though Nb-22Si-26Ti-2Al-6Cr-3Hf has a similar chemistry to others in this series and was produced using direct laser fabrication. These choices allowed for a start point, which could then be further expanded into the alloy choices discussed in **6** and **Chapter 7**.

4.2 Nb-15Si-22Ti-14Cr-2Al-2Hf-2V (14Cr)

Songming Zhang (2015) previously showed that this elemental composition forms a three-phase alloy of Nb_{ss}, α -Nb₅Si₃ and C15-Cr₂Nb Laves phase. The Nb-Ti-Cr ternary diagram seen in **Figure 32** is used to show the suspected phases found in thermodynamic equilibrium. The chemistries discussed below will be Nb-Si-Ti ternary diagrams, the high Cr concentration will have a significant effect on microstructure however and thus requires further inspection.^[30, 50]

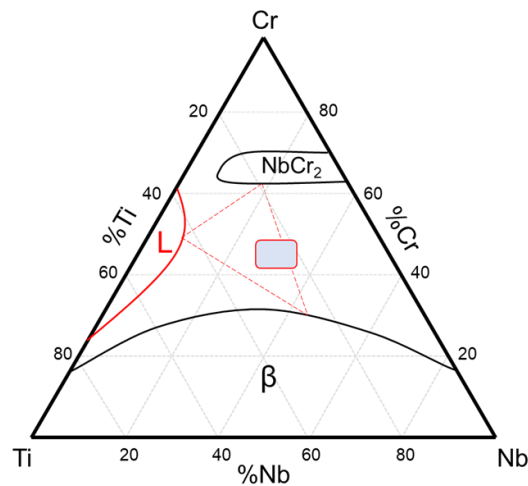


Figure 32: Ternary diagram of Nb-Ti-Cr^[125]

On review of **Figure 33**, the low magnification image shows an almost equal distribution of all three of the main phases with small amounts of a fourth distributed evenly. Porosity is noted throughout the sample and some areas of concentrated Nb are also observed, which is the result of poor mixing on construction. The high magnification image shows a light phase, likely the primary Niobium solid solution with two other grey phases.

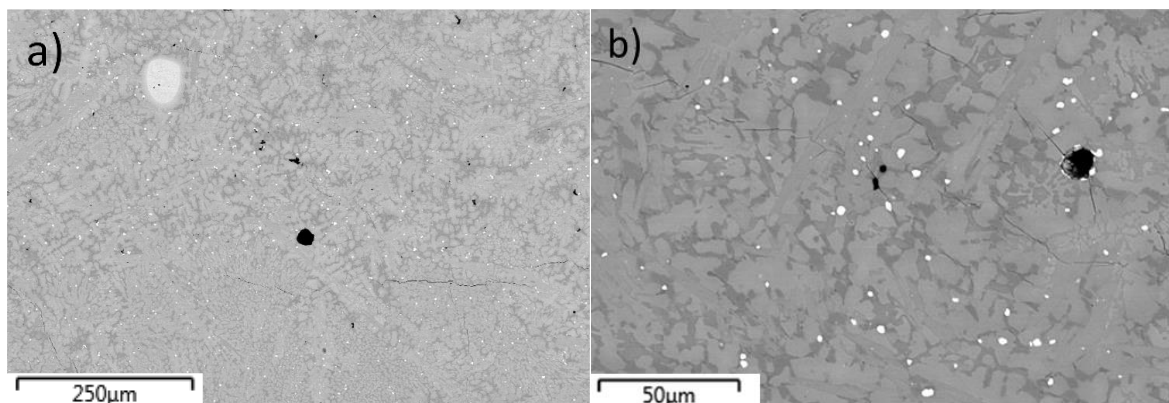


Figure 33: BEI image of Nb-15Si-22Ti-14Cr-2Al-2Hf-2V at a) Low and b) High magnification, images located in the centre of sample

White hafnia inclusions are also noted in **Figure 33 b)**, Hafnium has been noted by Limin Ma (2012) to act as an oxygen scrubber which the EDS appears to confirm. Titanium and aluminium are known for their highly reactive nature so oxides of these should be expected.

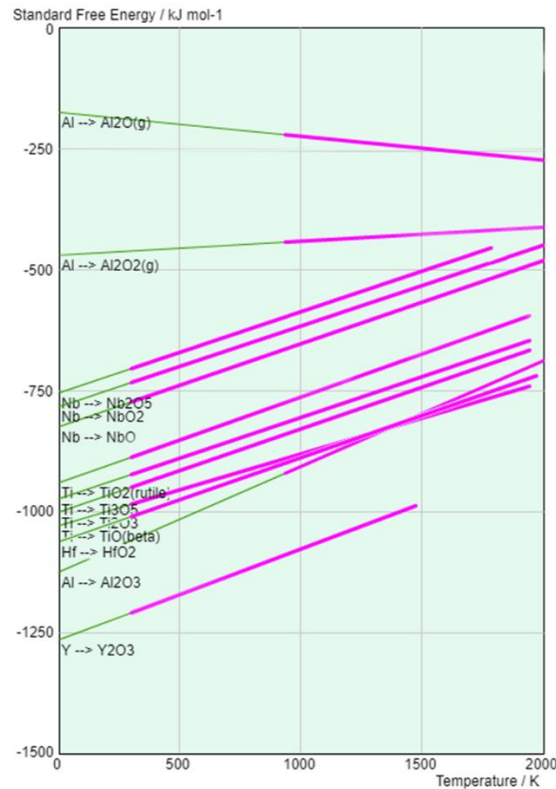


Figure 34: Ellingham diagram of oxide formation with elements found in Nb-15Si-22Ti-14Cr-2Al-2Hf-2V^[126]

Figure 34 presents the Ellingham diagram of the elements used in 14Cr. Hf sits below the other elements at high temperatures, this stability suggests that Hf does act as an oxygen getter in this sample. This presents a problem as oxide inclusions in materials usually negatively affects any mechanical properties and act as crack initiation sites.

Using EDS, it is possible to part-identify the remaining darker phases using their elemental compositions, this can be seen in **Table 8**. With this information, the lightest phase can be confirmed as (Nb, Ti)_{ss}. The second lightest phase suggests Nb₅Si₃ or Nb₃Si from the lower percentage of Nb but the high Si content. The darkest phase contains the highest Cr at 52.1%, this is likely expelled from the Nb₅Si₃ phase at the later stages of the reaction. The high Cr suggests that the Cr₂Nb phase is formed, discussed by Songming Zhang (2015).^[50]

Table 8: Element distribution in phases for Nb-15Si-22Ti-14Cr-2Al-2Hf-2V, all values in at.% unless otherwise stated

	Nb	Si	Ti	Al	Cr	Hf	V	O	Volume Fraction (%)
Nb _{ss}	54.89		26.89	1.07	13.98	0.58	2.59	--	56.38
Nb ₅ Si ₃	26.06	24.68	28.79	0.48	16	2.47	1.77	--	20.94
Cr ₂ Nb	14.84	5.78	19.55	--	52.1	3.09	4.65	--	21.28
HfO ₂	--	--	1.28	--	0.66	34.00	--	64.06	1.40

Nb₅Si₃ and Nb_{ss}, are difficult to distinguish by BEI contrast alone, **Figure 35** highlights the difference in phases using EDS. **a)** Observes a map of Si (purple) **b)** shows only Cr (green). The original BEI is added for comparison in **c)**.

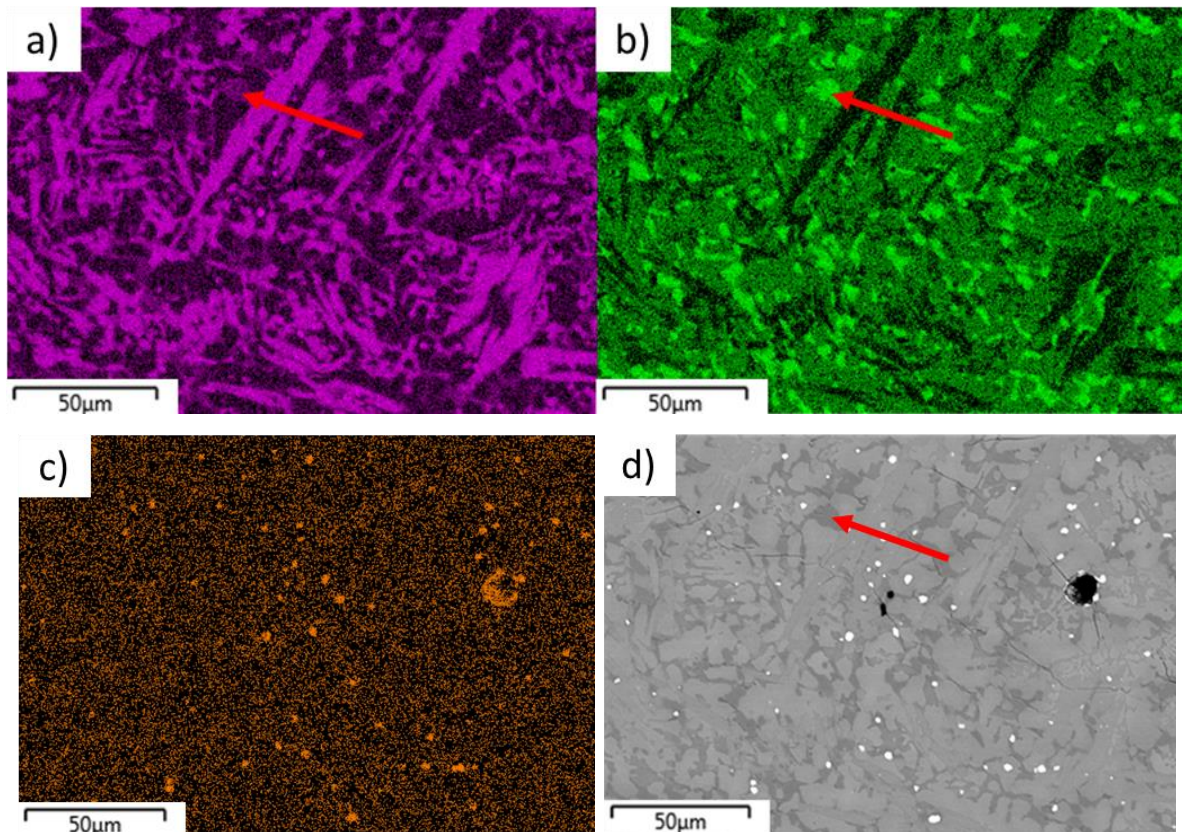


Figure 35: EDS Map image of a) Si, b) Cr, c) Hf and d) BEI image. Arrows indicate Laves phase with low Si concentration

The crystal structure of these phases cannot be identified using only SEM and EDS analysis. As mentioned in **section 2.3**, Nb₅Si₃ can appear in multiple phases (α , β and γ) and whilst Zhang mentions a C15 Laves phase being formed, two others exist which are also present.^[50, 127, 128] The crystal structures that are predicted from ternary diagrams can be found in **Table 9**.

Table 9: Possible crystal structures suggested by ternary diagram

Phase	Crystal Structure	Space Group Number
α -Nb ₅ Si ₃	Tetragonal	I4/mcm
β -Nb ₅ Si ₃	Tetragonal	I4/mcm
γ -Nb ₅ Si ₃	Hexagonal	P63/mcm
C15	Cubic	Fd-3m
C14	Hexagonal	P6 ₃ /mmc
C36	Hexagonal	P6 ₃ /mmc

The EDS data is cross-referenced with the X-ray diffractogram in order to estimate the crystal structure of the observed BEI images. **Figure 36** shows the diffractogram with a number of phases. The Laves phase was modelled as the cubic C15 form of Cr₂Nb, C14 was noted in the paper by Zhang but could not be identified in the diffractogram. The Nb₅Si₃ phase suggests a both α - and γ -silicide's are formed.^[129]

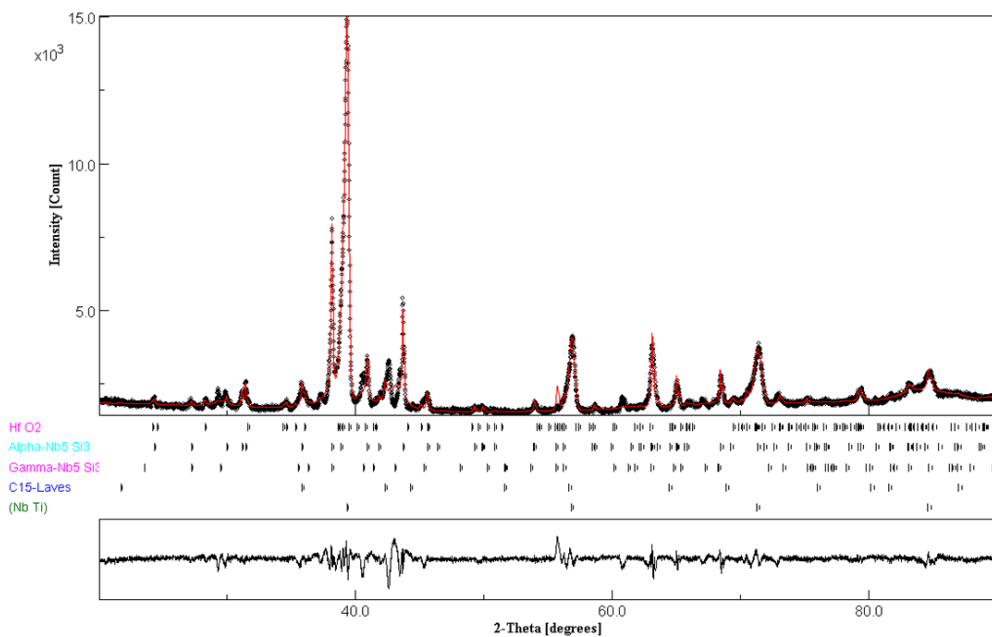


Figure 36: X-ray diffractogram of as-formed Nb-15Si-22Ti-14Cr-2Al-2Hf-2V

Porosity is noted in **Figure 33**, hot isostatic pressing (HIP) was performed to densify the material as detailed in **8**. All subsequent materials will undergo this process after formation unless otherwise stated. **Figure 37** shows the **a)** low and **b)** high magnification images of the post-HIP material.

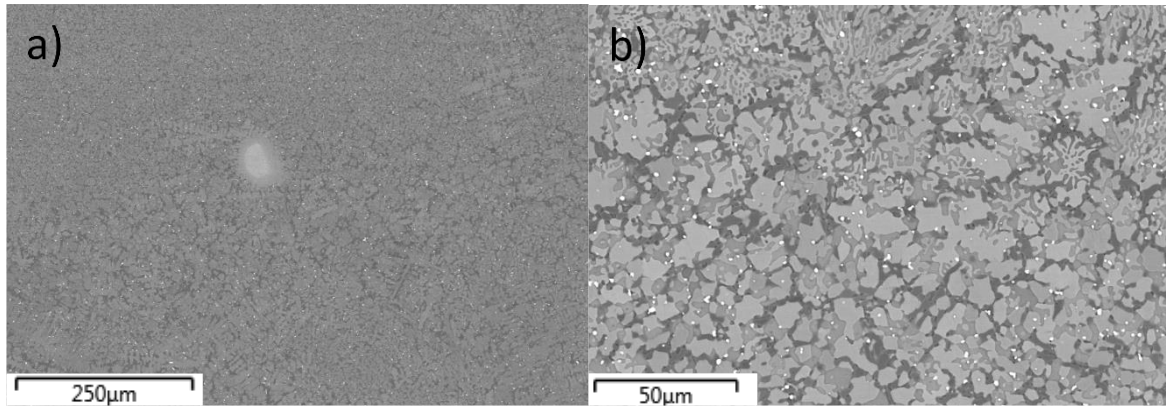


Figure 37: BEI image of Nb-15Si-22Ti-14Cr-2Al-2Hf-2V post-HIP at a) Low and b) High magnification. Image was taken at centre of sample

Table 10 shows the elemental distribution in different phases as a result of diffusion during hot isostatic pressing.

Table 10: Possible crystal structures suggested by ternary diagrams

	Nb	Si	Ti	Al	Cr	Hf	V	O	Volume Fraction (%)
Nb_{ss}	58.78	--	28.36	--	9.63	0.75	2.48	--	61.18
Nb₅Si₃	30.2	33.05	29.62	--	2.12	3.86	1.17	--	17.74
Cr₂Nb	25.25	8.27	12.91	0.24	47.56	1.96	3.82	--	14.49
HfO₂	--	--	1.16	--	0.71	31.4	0.16	66.58	4.07
Nb₃Si	--	--	--	--	--	--	--	--	2.52

After HIP the phases show many changes in composition, most notably for the higher concentration elements which had not reached equilibrium during formation. For convenience, highlights from Table 8 and Table 10 have been consolidated in the table below. Nb₃Si was noted in the diffractogram in Figure 38 but was not observed in BEI images.

Table 11: Comparison of volume fraction % at as-formed and HIP elemental processing stages

	Nb		Si		Ti		Cr	
	AF	HIP	AF	HIP	AF	HIP	AF	HIP
Nb _{ss}	42.88	58.08	14.09	--	24.68	27.58	14.01	9.75
Nb ₅ Si ₃	29.19	39.61	21.80	23.27	33.71	27.37	9.18	4.72
Cr ₂ Nb	26.58	25.07	6.76	9.21	35.62	12.98	24.18	46.78

A loss of Si from the Nb_{ss} suggests that the original cooling during laser additive manufacturing was rapid, forcing Si into an undesirable phase and thus trapping it interstitially, similar to martensite formation. A post-HIP segregation has been set up, observing no Si in the solid solution. Diffusion of Cr between Laves phase and Nb_{ss} shows a preference to form Cr₂Nb.

From **Table 11** it is clear there is a shift in Ti concentration from the Laves phase and increasing in the solid solution, HfO₂ remains largely unchanged as it is a very stable oxide although the volume fraction does increase from diffusion of Hf from the Laves phase, unlikely to react at the temperatures used in HIP, preventing reactions from Ti or Al occurring.

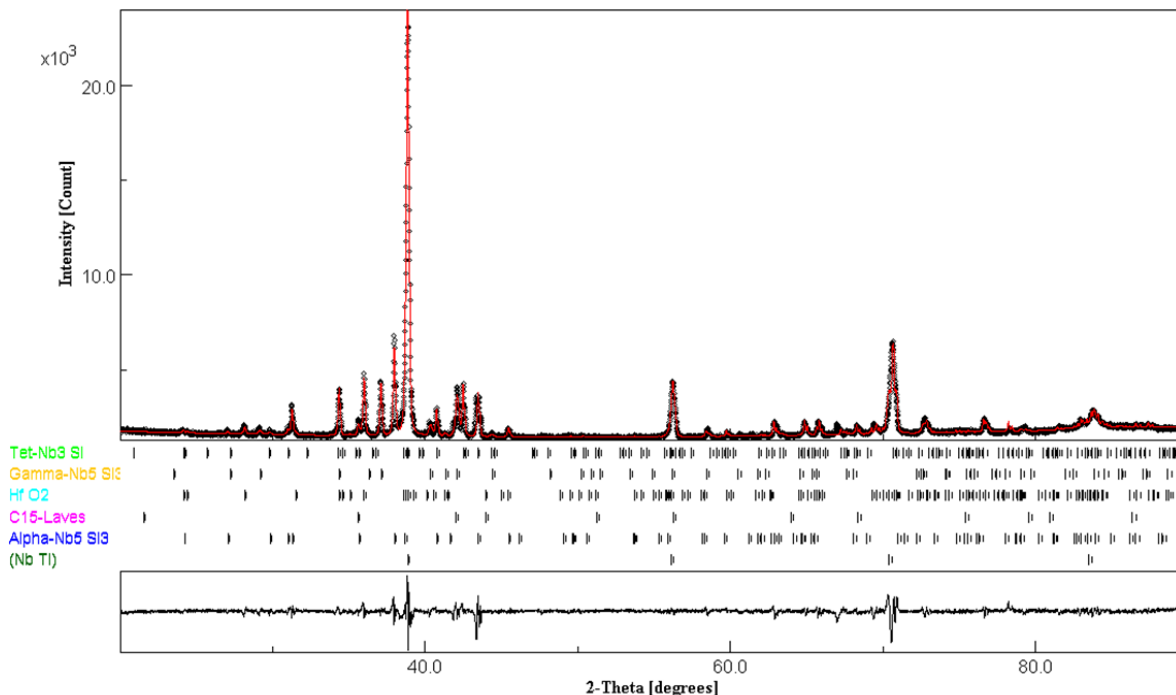


Figure 38: X- ray diffractogram of as-formed Nb-15Si-22Ti-14Cr-2Al-2Hf-2V

The diffractogram in **Figure 38** suggests the formation of trace amounts of Nb₃Si (~2%) although it is not detected in the BEI images. The remaining fractions remain similar to observed in the as-formed sample although a reduction of 7% Laves phase is noted.

The BEI images of Nb-15Si-22Ti-14Cr-2Al-2Hf-2V after heat treatment (5 hr, 1500°C) are presented in **Figure 39 a)**. The microstructure shows significant coarsening compared to previous processes. A contrast in the image can be observed due to the coarsening of each phase over the heat treatment stages. The increase in volume fraction of HfO₂ also effects the contrast, as this is non-conductive an increase of charge will be noted around these areas increasing its brightness whilst increasing the surrounding phase contrast. The increase in HfO₂ volume fraction is likely due to either ingassing of the material or potential oxygen within the chamber during heat-treatment. This can either originate from residual oxygen remaining in the chamber after being purged or from the trace concentration of O₂ within the Ar gas supply.

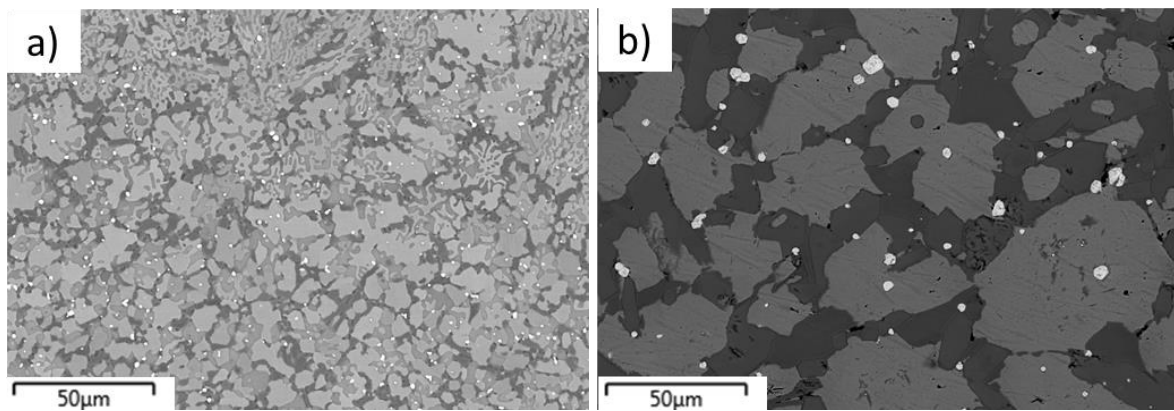


Figure 39: BEI image of Nb-15Si-22Ti-14Cr-2Al-2Hf-2V at a) Post-HIP and b) Post-HT, image located in the centre of sample

The microstructure inspected in **Figure 39 b)** shows the morphology has changed with absence of the small, thin phases observed previously. The phases can be easily distinguished using EDS seen in **Figure 40**, with **a)** presenting regions of Nb_{ss} along with the outlines of HfO₂ in **b)**. A regular morphology of Cr₂Nb and Nb₅Si₃ may be observed in **c)** and **d)**, presenting a mixture of semi-regular shaped hexagonal and tetragonal silicides. Close analysis will observe Cr concentrations on the Nb₅Si₃ phase boundaries.

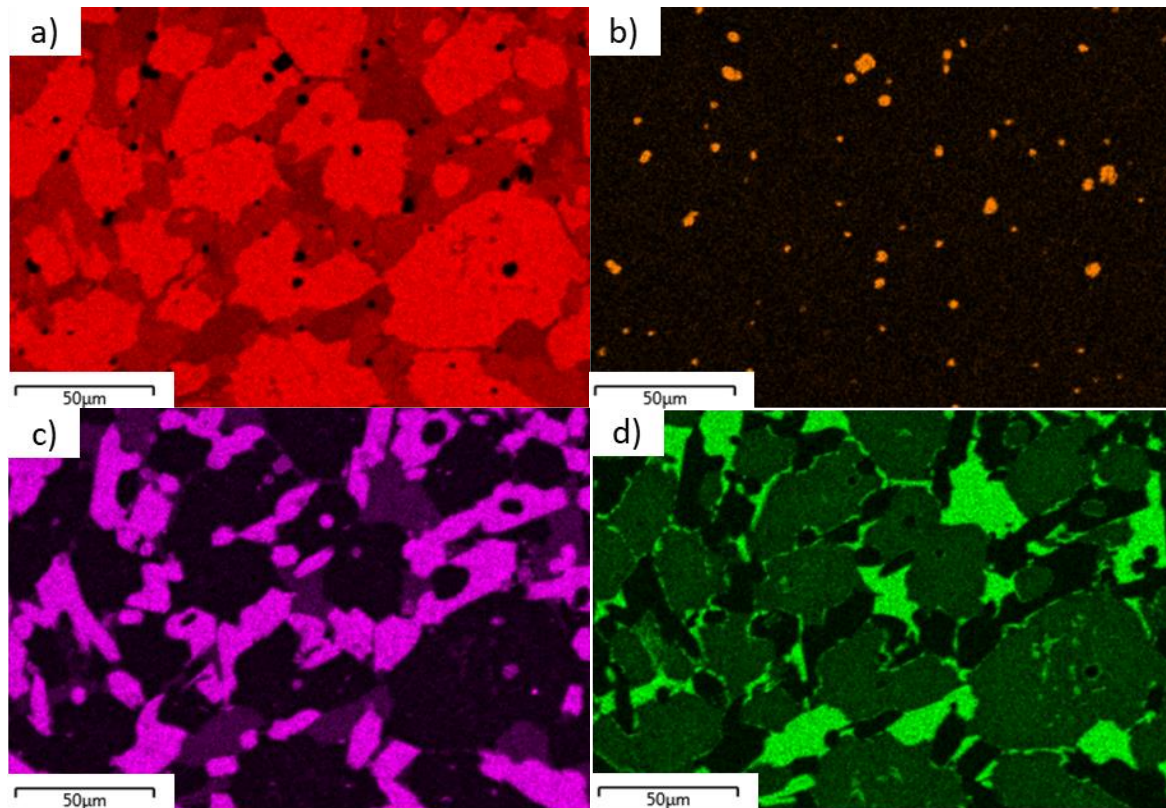


Figure 40: EDS map of Nb-15Si-22Ti-14Cr-2Al-2Hf-2V post-HT at the centre of sample highlighting
a) Nb, b) Hf, c) Cr, d) Si

The silicides appear to have formed within the Laves phase in some areas (highlighted). It would be highly unlikely that any diffusion process would cause this to occur and is thus likely that local melting has occurred as discussed by Feitosa L. (2018).^[54] The composition of each element can be seen in Table 12.

Table 12: Element distribution in phases for Nb-15Si-22Ti-14Cr-2Al-2Hf-2V post-HT, all values in at.% unless otherwise stated

	Nb	Si	Ti	Al	Cr	Hf	V	O	Volume Fraction (%)
Nb _{SS}	59.09	1.42	24.16	0.68	11.99	0.15	2.54	--	46.55
Nb ₅ Si ₃	36.59	35.32	24.01	0.39	1.99	0.69	1.01	--	26.51
Cr ₂ Nb	28.31	10.56	10.42	0.29	47.01	0.23	3.20	--	8.45
HfO ₂	--	--	--	--	--	33.27	0.34	63.31	6.06
Nb ₃ Si	--	--	--	--	--	--	--	--	12.43

Figure 41 shows a comparison of each phase at each stage of production for ease of the reader. A steady decline in Laves phase is noted as Nb₃Si concentrations increase alongside the decrease of Nb_{SS}.

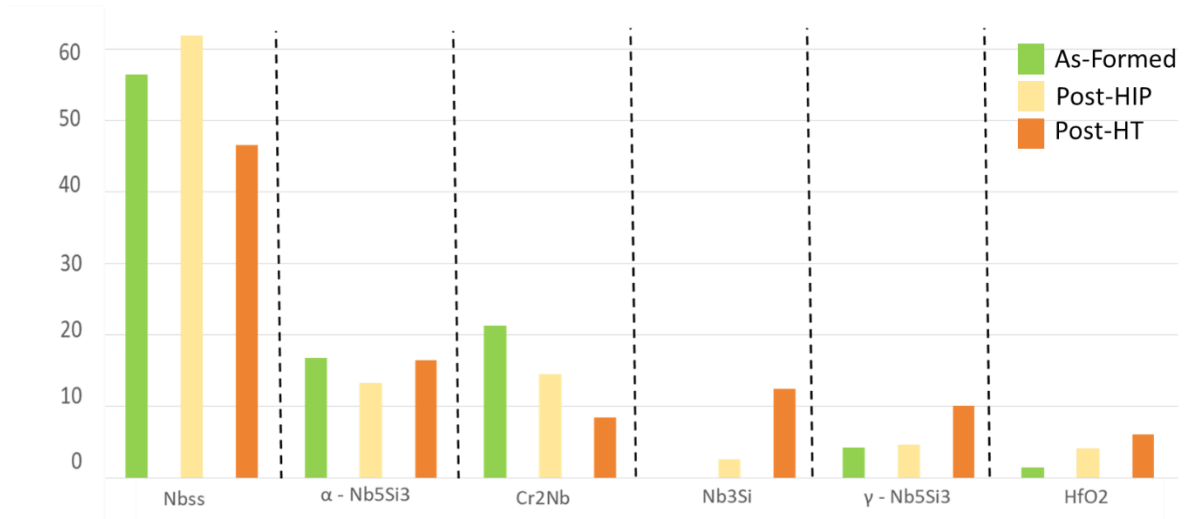


Figure 41: Comparison graph of phases in 14Cr at each stage of production

The regular shaped hexagonal and tetragonal Si concentrations suggest that multiple phases have been formed through the HT process. When modelling the diffractogram in Figure 42, it suggests that quantities of γ -Nb₅Si₃ are indeed present, along with α -Nb₅Si₃. The volume fraction of Nb₃Si increased greatly at a loss of Nb_{ss}. The HfO₂ observed in all formations can be identified at this stage as monoclinic. As stated before, HfO₂ is a very stable compound. Some increase is noted in its volume fraction during post-processing which can be attributed to the decreases of Hf observed in all other phases. Ta foil was not used to protect samples so reaction with residual oxygen is likely the cause of this increase.

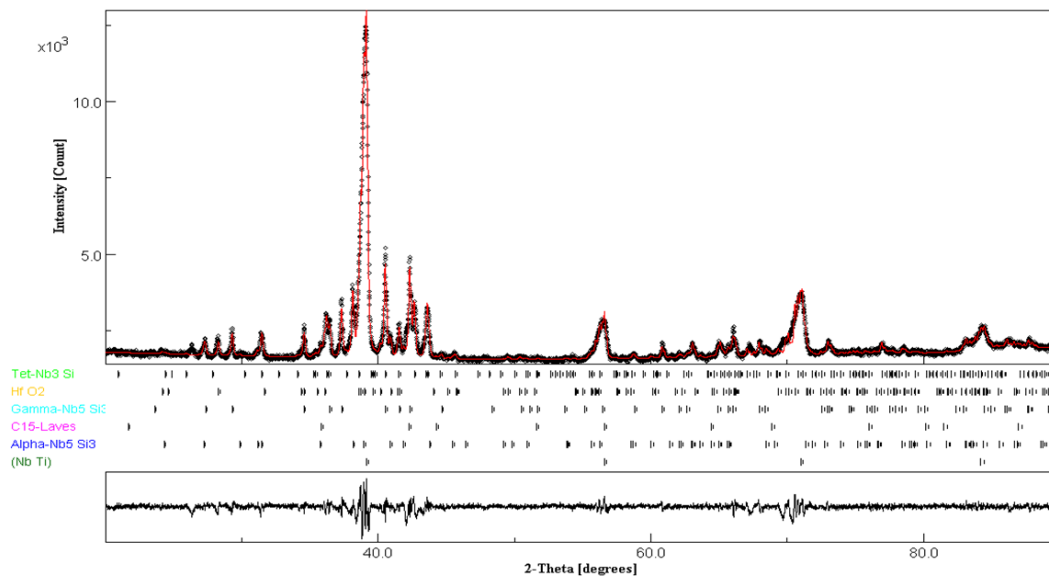


Figure 42: X-ray diffractogram of post-HT Nb-15Si-22Ti-14Cr-2Al-2Hf-2V modelled using MAUD

The presence of the C15 Laves phase throughout each step of processing is unexpected as silicon usually stabilises the C14 Laves phase by lowering electron density. The presence of Si should have destabilised the formation of C15 as discussed by Songming Zhang (2015).^[50] Although the typical Laves phase consists of Cr₂Nb, EDS analysis through each step has presented with both substitutional and interstitial atoms within the phase. The recorded elemental concentration is observed in **Table 13** presents diminished Si and Cr content in the as-formed sample before equilibrating during post-processing. This altered chemistry likely lowered the valence electron concentration within the system and thus promoted C15 over C14 during formation. The reason a transformation was not observed during post-processing is unknown, models were attempted to identify the C14 Laves phase but were not adequate.

Table 13: Element concentration of Laves phases observed at each processing step

	Nb	Si	Ti	Al	Cr	Hf	V
Zhang (2015)	23.70	10.90	15.70	0.60	42.40	3.20	3.50
As-Formed	26.58	6.76	35.62	0.32	24.18	1.98	4.56
Post-HIP	25.07	9.21	12.98	0.28	46.78	1.94	3.76
Post-HT	28.31	10.56	10.42	0.29	47.01	0.23	3.20

4.3 Nb-15Si-22Ti-2Cr-2Al-2Hf-2V (2Cr)

The alloy discussed previously contains higher Cr % and significantly less Nb, producing markedly different microstructure with an absence of the Laves phase noted. The low-resolution BEI image in **Figure 43 a)** shows the equal distribution of a dendritic phase Nb_{ss} . A eutectic may be observed between the dendrite formations formed from the remaining melt during solidification in **b)**, this was expected from work by Zhang showing $Nb_{ss} / \alpha-Nb_5Si_3$ phases.^[50] The low Cr % suggests that the C15 Laves phase may not have formed.

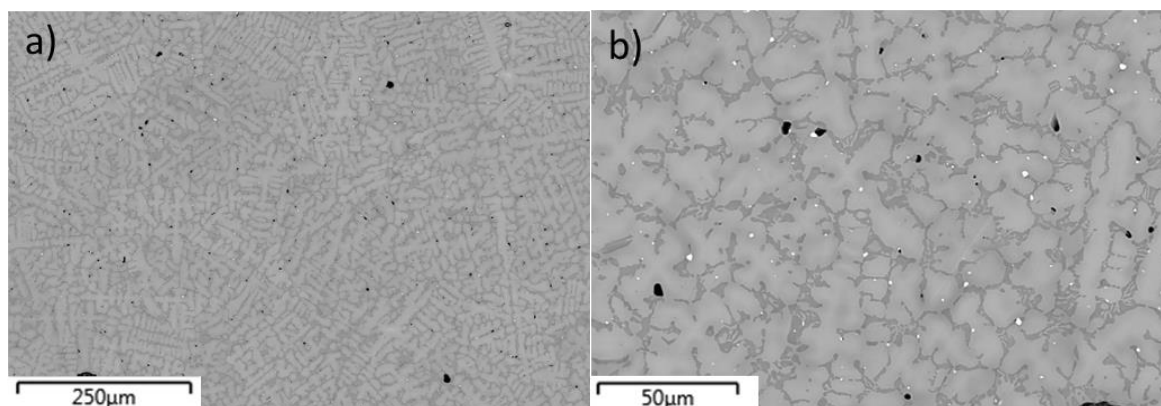


Figure 43: BEI of Nb-15Si-22Ti-2Cr-2Al-2Hf-2V as-formed at a) Low and b) High magnification.

Figure 44 presents the Nb-Si-Ti ternary diagram and suggests that a main Nb_{ss} along with Nb_5Si_3 is formed. The BEI images show a light (Nb_{ss}) phase along with the fine Nb_5Si_3 eutectic between dendrites. Additional information using XRD and EDS analysis techniques seen below also confirm this. As with the chemistry discussed above, the Hf content is high enough to act as an oxygen sink, producing residual HfO_2 which is likely formed during early solidification.

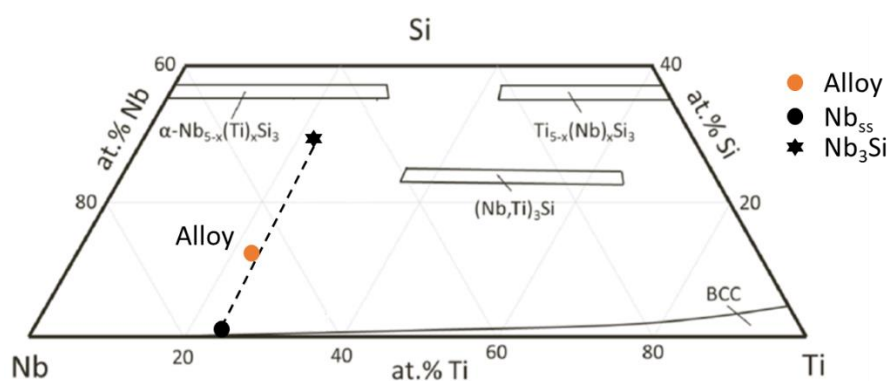


Figure 44: Ternary diagram of Nb-Si-Ti along with indicated Nb_3Si and Nb_{ss} phases

Initial analysis of the XRD pattern in **Figure 45** show large peaks associated with Nb_{ss} with smaller peaks representing HfO_2 and Nb_3Si . A shift in peak position of Nb_{ss} and slight

broadening at (1,1,0) is observed. Using a combination of the BEI and EDS, a distribution of solutes can be seen within the phase. Additions of lighter elements such as Ti and Cr shift the peaks towards the lower 2θ angle. The BEI suggests this is uneven, with shadows of grey at the edges of a lighter coloured core, this indicates an increased concentration of Nb at the core with Ti tending towards the edges.

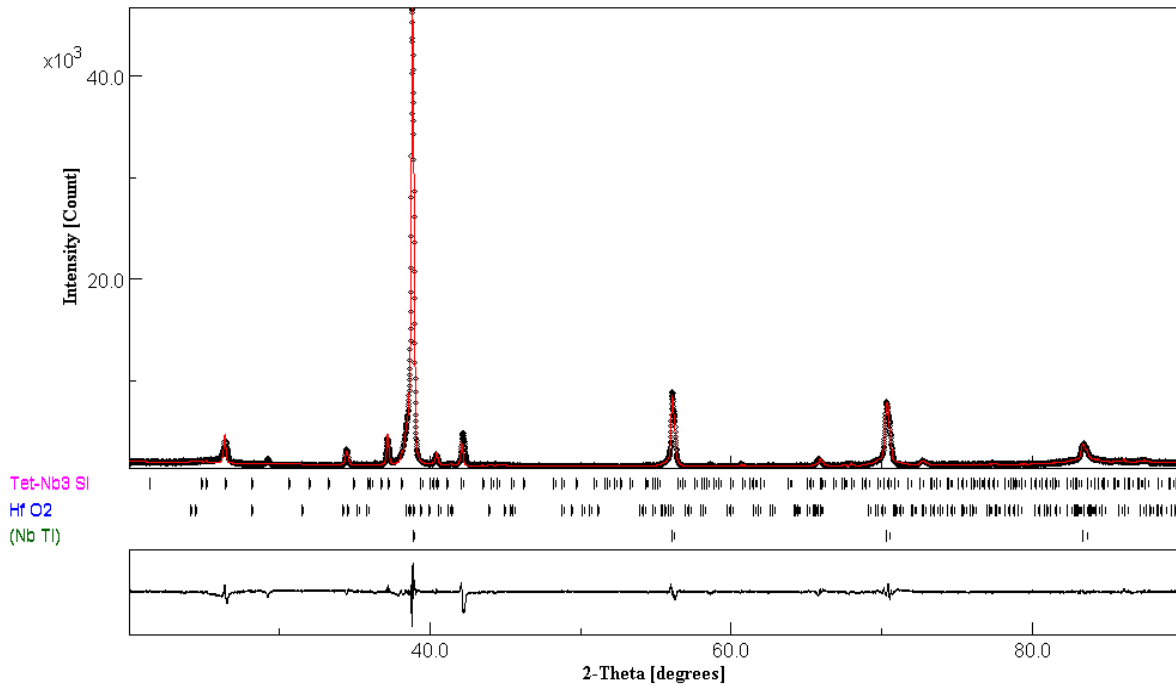


Figure 45: X-ray diffractogram of as-formed Nb-15Si-22Ti-2Cr-2Al-2Hf-2V

Table 14 shows the volume fraction of each phase present calculated using both image analysis and quantitative analysis of the diffractogram in Figure 45.

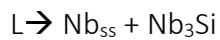
Table 14: Showing element and volume distribution for each phase in Nb-15Si-22Ti-2Cr-2Al-2Hf-2V as-formed, all values in at.% unless otherwise stated

	Nb	Si	Ti	Al	Cr	Hf	V	O	Volume Fraction (%)
Nb _{SS}	68	--	23.79	2.52	1.94	1.46	2.24	--	90.95
Nb ₃ Si	35.77	33.66	23.85	1.53	0.57	3.58	1.03	--	8.82
HfO ₂	5.37	--	3.53	--	0.4	27.46	0.31	62.93	0.25

The XRD model suggests the presence of Nb₃Si, which could be the result of low Cr content or production methods. K. Zelenitsas (2005) discussed the stabilising effects of Nb₅Si₃ with additions of Cr by breaking down Nb₃Si via the peritectoid reaction $\text{Nb}_3\text{Si} \rightarrow \alpha\text{-Nb}_5\text{Si}_3 + \text{Nb}_{\text{SS}}$.^[130] Zhang et al created the same chemistry using arc-melting with directional solidification and

showed a binary system of $Nb_{ss}/\alpha-Nb_5Si_3$ both before and after heat treatments. This alludes towards the rapid solidification of DLM preventing the decomposition of Nb_3Si to form the Nb_{ss}/Nb_5Si_3 binary observed by Zhang.

The solidification route for this alloy has been discussed by Feitosa L. (2018) and the evidence presented suggests an alternative pathway.^[125] The work concludes the presence of Nb_3Si but does discover any Nb_5Si_3 present. For this reason, it is suggested that the solidification route be altered to:



Early stages of solidification include hafnia formations, which are a result of interaction between Hf in the melt pool and residual oxygen. These inclusions likely acted as nucleation points for dendrite growth, commensurate with findings from Feitosa L. (2018) and Songming Zhang (2015).^[50, 125]

A morphology change occurs during the first stages of post-processing seen in **Figure 46** with coarsening of the interdendritic eutectic. Paired with this, the high temperature and pressure diffusion has promoted homogeneity in the Nb_{ss} phase resulting in an even contrast.

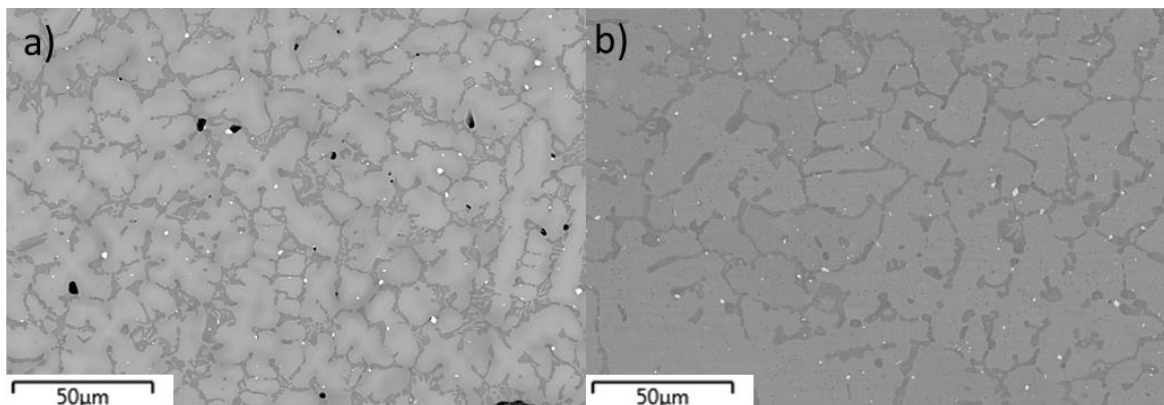


Figure 46: BEI image of Nb-15Si-22Ti-2Cr-2Al-2Hf-2V showing a) as-formed b) post-HIP

The diffractograms of Nb-15Si-22Ti-2Cr-2Al-2Hf-2V post-HIP in **Figure 47** reveals the presence of $\gamma-Nb_5Si_3$ as well as the previously noted phases.

The peritectoid reaction of $\text{Nb}_3\text{Si} \rightarrow \gamma\text{-Nb}_5\text{Si}_3 + \text{Nb}_{\text{ss}}$ is likely the cause of the new silicide phase with the excess Ti and Hf content and low Cr. The hexagonal Nb_5Si_3 is promoted over the $\alpha\text{-Nb}_5\text{Si}_3$ phase expected by conventional reaction path agreed by most.^[129]

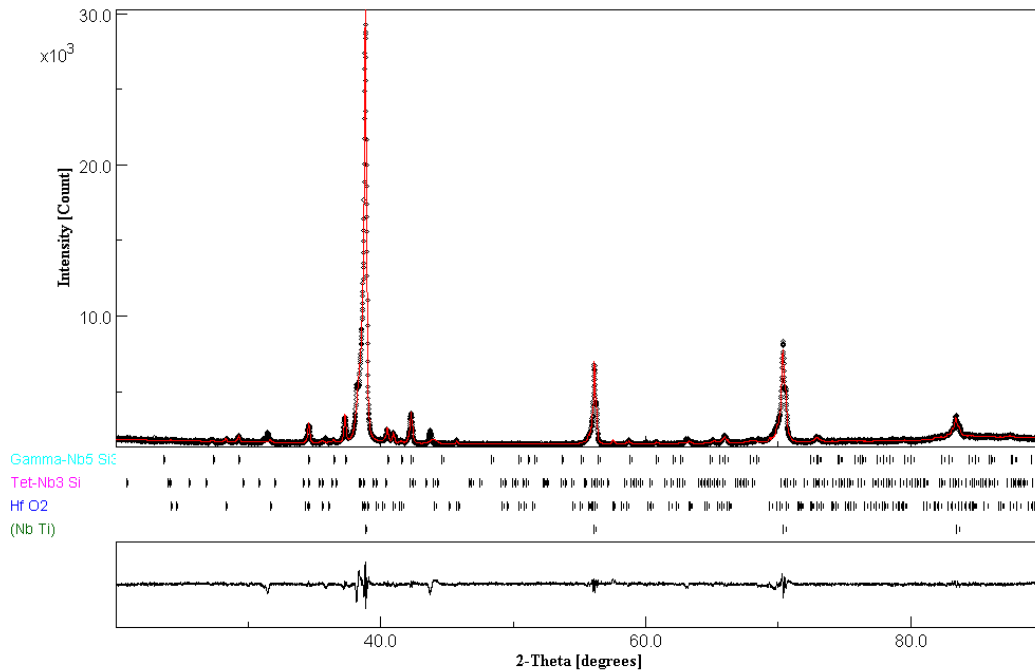


Figure 47: X-ray diffractograms of Nb-15Si-22Ti-2Cr-2Al-2Hf-2V post-HIP

A small shift in peak position and broadening of the Nb_{ss} is noted. This suggests both an expulsion of heavy elements or intake of lighter elements such as Ti and Al. This is evident in the XRD volume fraction modelling in **Table 15** of the same phase, which shows a decrease in Nb and an increase of the noted elements. Hafnia also shares similar peaks with Nb_{ss} . Expansion in the lattice of HfO_2 and increased volume fraction is modelled, and so appears as broadening of the Nb_{ss} peak at 56.13° (2,0,0) and 70.37° (2,1,1).

Table 15: Showing element and volume distribution for each phase in Nb-15Si-22Ti-2Cr-2Al-2Hf-2V post-HIP, all values in at.% unless otherwise stated

	Nb	Si	Ti	Al	Cr	Hf	V	O	Volume Fraction %
Nb_{ss}	63.13	0.91	27.52	2.74	2.25	1.16	2.56	--	76.07
$\text{Nb}_5\text{Si}_3/\text{Nb}_3\text{Si}$	36.09	33.84	24.26	1.17	0.34	3.3	1.13	--	21.01
HfO_2	2.89	2.89	1.57	0.79	0.01	28.86	0.17	62.76	2.92

Continued microsegregation of Cr is noted in the above table, with the same quantity noted in the as-formed and post-HIP samples, this is a very low concentration of Cr in the silicide phase (compared to 14Cr), along with the 3% Hf promoted the formation of γ -Nb₅Si₃

It was previously mentioned that the Nb_{ss} phase showed anisotropy when originally constructed. During hot isostatic pressing bulk diffusion has occurred with the high concentration of Nb moving more evenly throughout the material. Ti has a good solubility in Nb₅Si₃ and is also concentrated on the phase boundaries, allowing for both bulk and grain boundary diffusion to occur. This diffusion between both Nb_{ss} and both silicide phases results in the transformation of dendrite morphology to cellular.

The backscattered electron image of Nb-15Si-22Ti-2Cr-2Al-2Hf-2V post-HT may be seen in **Figure 48**. It presents a dendritic microstructure, similar to previous stages, with further coarsening of the silicide as well as more HfO₂.

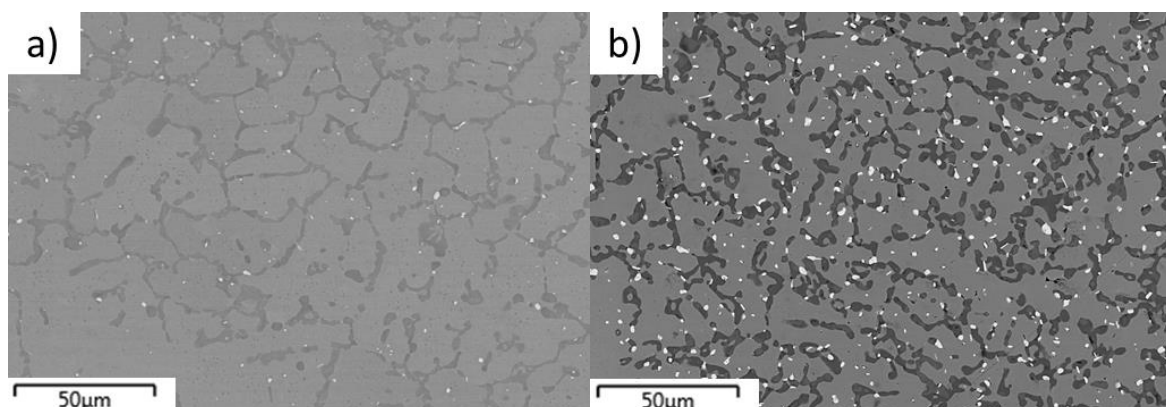


Figure 48: BEI image of Nb-15Si-22Ti-2Cr-2Al-2Hf-2V post-HT, showing a) Post-HIP b) Post-HT

The diffractogram shows very little change in phases, a shift of Nb_{ss} to a higher 2θ suggests that the matrix relaxed post-HT, reducing its lattice size, this could either be due to relaxation from stress induced from the HIP process or diffusion of smaller elements into the matrix (or larger atoms out).

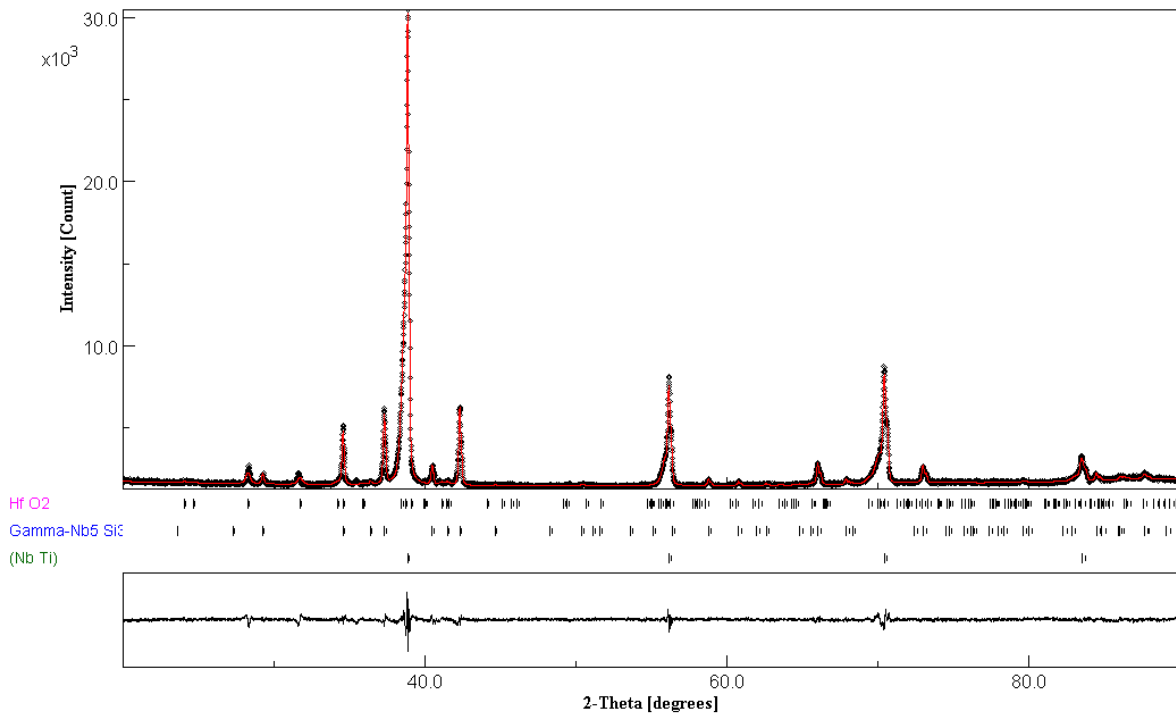


Figure 49: X-ray diffractograms of Nb-15Si-22Ti-2Cr-2Al-2Hf-2V post-HT at 1500°C for 5 h

Table 16 displays the elements calculated in each phase via EDS analysis, it presents a loss of Hf from the matrix, likely forming HfO_2 , this reduction in larger atoms explains the observed shift of Nb_{ss} . The volume fraction of HfO_2 is larger than was observed post-HIP, this may be due to Hf in the solid solution reacting with residual oxygen in the chamber, acting as an oxygen sink protecting the niobium matrix.

Table 16: Showing element and volume distribution for each phase in Nb-15Si-22Ti-2Cr-2Al-2Hf-2V post-HT, all values in at.% unless otherwise stated

	Nb	Si	Ti	Al	Cr	Hf	V	O	Volume Fraction %
Nb_{ss}	64.98	1.08	25.56	2.46	2.89	0.35	2.70	--	80.35
Nb_5Si_3	36.09	33.62	25.94	1.51	0.44	1.22	1.17	--	12.90
HfO_2	7.10	4.67	3.52	0.00	0.00	26.93	0.00	56.22	6.75

The remaining elements are similar as observed in the as-formed sample, meaning it was in thermodynamic equilibrium on construction. Further breakdown of Nb_3Si through the peritectoid reaction $\text{Nb}_3\text{Si} \rightarrow \alpha\text{-Nb}_5\text{Si}_3 + \text{Nb}_{ss}$ is noted, similarly to the post-HIP sample. A breakdown of phase transformation can be seen in Figure 50. The change in Cr content

between 2 and 14Cr shows a markedly different microstructure. The reduction from 14 at.% to 2 at.% notes the absence of the Laves phase as well as the formation of α -Nb₅Si₃.

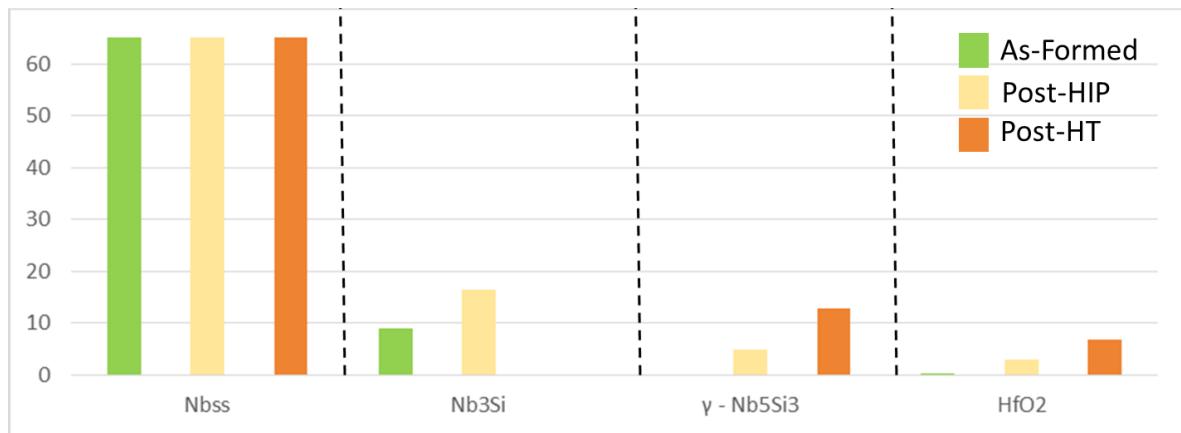


Figure 50: Comparison graph of phases in 2Cr at each stage of production

Original work by Zhang produced this binary microstructure of Nb_{ss} / α -Nb₅Si₃. The choice to create these samples using DLM has radically altered the cooling, producing the metastable γ -Nb₅Si₃ instead. The transformation from γ - \rightarrow α -silicide was not observed in these experiments, possibly due to the low kinetic speed of transformation. Processing route is the key difference between both processes, and therefore it may be important to consider different construction parameters in order to promote α -Nb₅Si₃, but it is out of the scope of this PhD. In Nb-15Si-22Ti-2Al-2Hf-2V-14Cr the large amount of Cr helped to stabilise the tetragonal silicide in both DLM and arc furnace samples.

Hafnia and yttria oxide inclusions were noted in the work by Zhang. Whilst yttria oxides may have originated from mould interactions with the melt pool, these are absent due to process differences. HfO₂ is noted in large quantities, however, throughout the microstructures displayed in **Figure 43** and **Figure 46** It was discussed in the **section 2.4.3** that yttria/hafnia inclusions may float on a melt pool, essentially partitioning the inclusions to the top of the mould during directional solidification.^[82] The rapid solidification prevented this from occurring and inclusions were essentially trapped where they were produced. This is significant as the distribution of HfO₂ throughout the matrix disrupts expected mechanical properties. Ductility and toughness will be hindered as the oxide will act as crack initiator sites or de-bond themselves from the matrix interface propagating cracks.

4.4 Nb-22Si-26Ti-2Al-6Cr-3Hf (6Cr)

Unlike the alloys previously examined, the chemistry explored here contains more Si, Ti and Cr, compensating with less Nb and Hf, and a complete removal of V. This results in a very non-uniform microstructure as seen in **Figure 51 a)**. When examined closely in **b)**, equal distributions of light and multiple dark phases can be seen. The light phase is likely the Nb_{ss} , the other darker phases may be Nb_5Si_3 and the Laves phase observed in 14Cr.

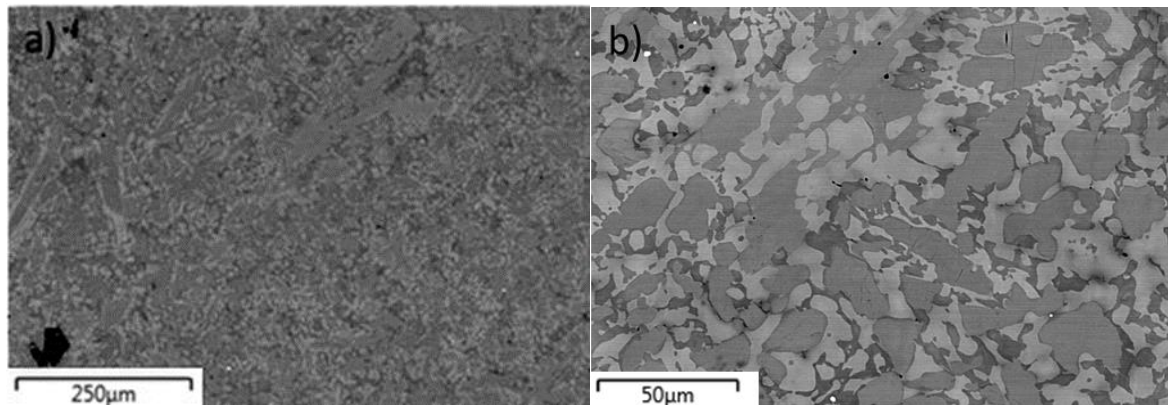


Figure 51: BEI of Nb-22Si-26Ti-6Cr-2Al-3Hf as-formed at a) Low and b) High magnification

Using the ternary diagram seen in **Figure 52**, Nb_5Si_3 and Nb_{ss} are the logical phases. Whilst this alloy has a large amount of Cr, analysis of EDS in **Figure 53** suggests that a Laves phase has not formed.

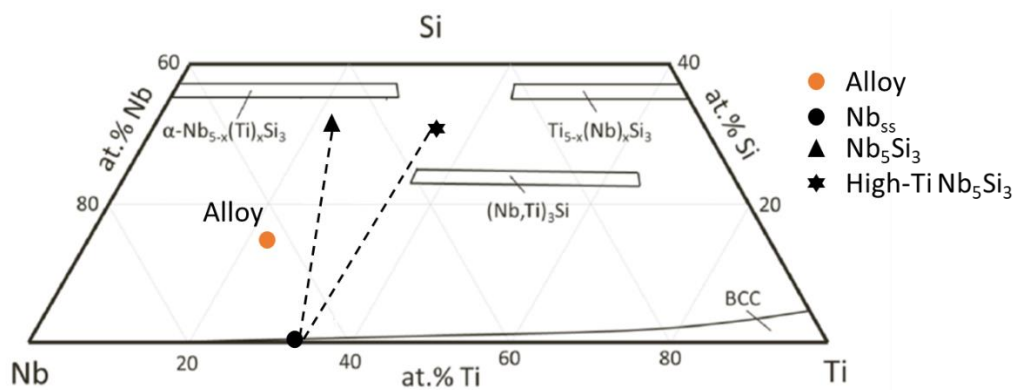


Figure 52: Ternary phase diagram of Nb-Si-Ti with respective phases plotted

The high concentrations of Cr present in 14Cr typically produced two distinguishable phases in the Si map (presented below), one phase of silicon present in Nb_{ss} and one in Nb_5Si_3 . Conversely, map presented in 6Cr shows two contrasting phases, suggesting the lack of laves phase.

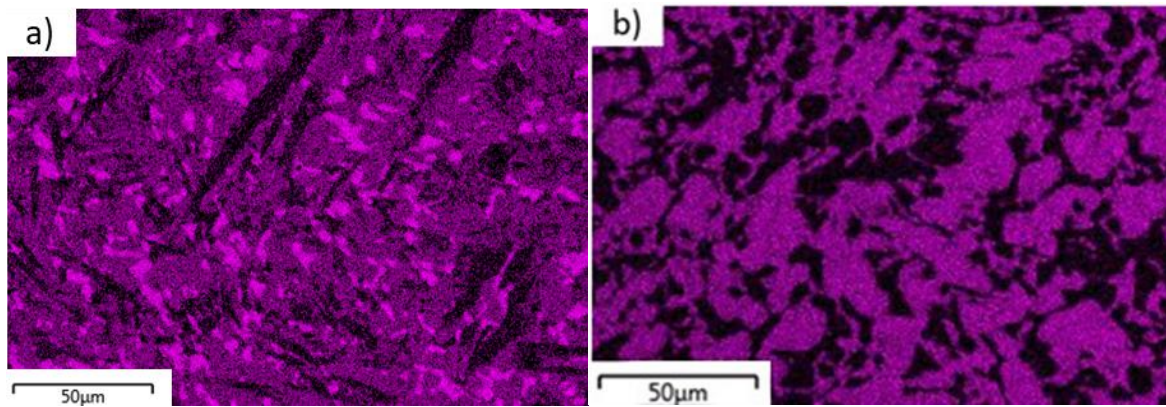


Figure 53: EDS Map image of Cr in a) 14Cr and b) 6Cr

As with the previously discussed chemistries, Hf is contained within the samples, although in lower concentration. As a result, HfO_2 may still be seen, although at a significantly lower volume %.

When examining the diffractograms of this sample (Figure 54), it can be seen that like 2Cr, both solid solution and silicide are observed. In contrast to the previously discussed chemistry, both the $\gamma\text{-Nb}_5\text{Si}_3$ and $\beta\text{-Nb}_5\text{Si}_3$ are present. Unlike 14Cr, the lower Cr content suppresses the formation of any high chromium C15 Laves phase. Feitosa L. (2018) has noted its presence in low concentration but these were not observed in either the microstructure or diffractogram of this sample.^[125]

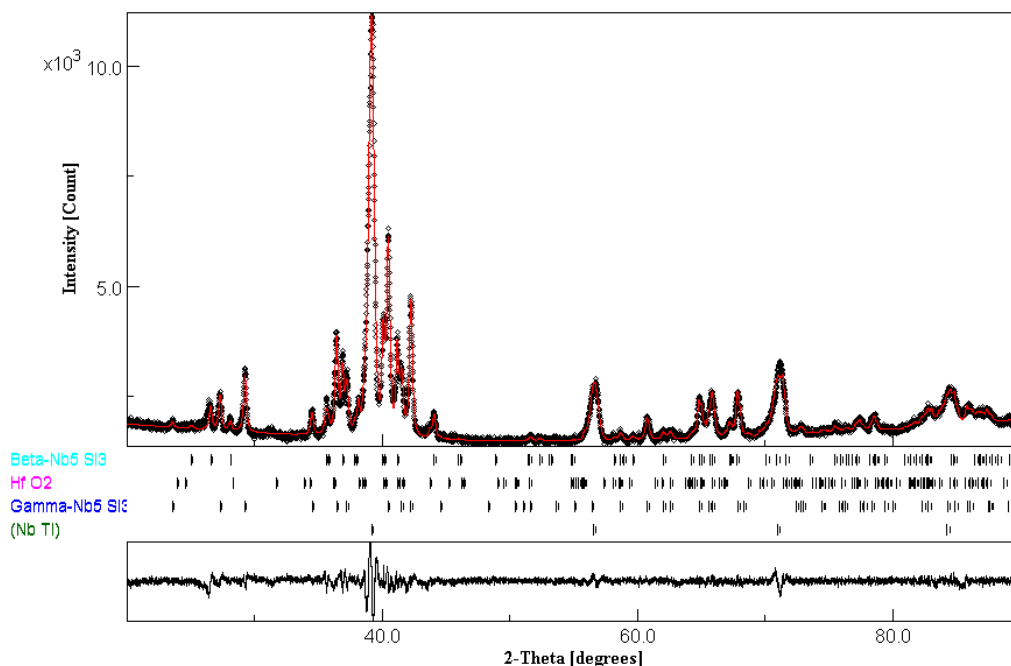


Figure 54: X-ray diffractograms of as-formed Nb-15Si-22Ti-6Cr-2Al-3Hf, modelled using MAUD

When comparing the Nb_{ss} (1,1,0) peak it is noted that a shift of 0.48° has occurred between 2Cr and 6Cr. This displacement suggests one of two things:

- 1) The sample was not originally placed flush with sample holder during scan resulting in Z axis misalignment.
- 2) A chemistry difference exists between the two phases resulting in an overall shift

Table 17: Showing element distribution in phases

	Nb	Si	Ti	Al	Cr	Hf	O	XRD
Nb _{ss}	50.85	2.17	32.48	2.15	11.03	1.32	--	23.31
γ-Nb ₅ Si ₃	33.43	36.41	24.90	0.84	0.75	3.67	--	47.32
β-Nb ₅ Si ₃	45.78	--	36.90	2.35	13.73	1.24	--	27.63
HfO ₂	0.85	0.40	0.30	0.82	0.43	31.1	66.1	1.74

Whilst reason 1 is possible, results from both the modelled diffractogram and post-processing evidence suggest that the alignment was adequate. Using EDS analysis in **Table 17** the concentration of Nb in the alloys discussed so far can be compared in **Figure 55**. A trend is observed with the lattice constant a is proportional to niobium concentration. The concentration of Ti within the matrix appears to be less important with higher concentrations noted in 6Cr. As titanium has a smaller radius, substitution over Nb would decrease the lattice constant observed in Nb_{ss}. Cr also shows segregation to the solid solution over the silicide, with a similar atomic radius to Ti it also reduces lattice size. All this leads to the observed shift in θ .

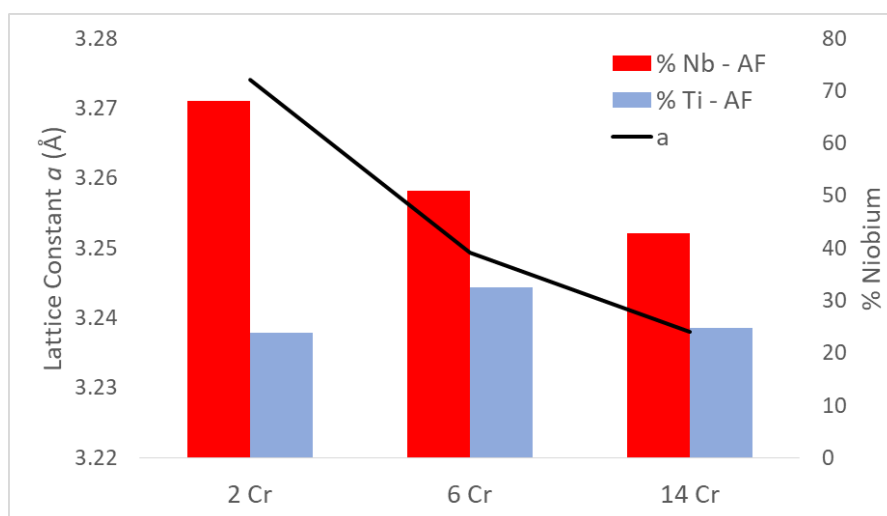


Figure 55: Relationship between lattice constant a and % Nb content in Nb_{ss} in as-formed alloys

Microstructural changes can be seen in the post-HIP alloy when comparing the backscattered images of both samples in **Figure 56**. A side-on comparison shows little change in the microstructures. A small amount of conglomeration is noticeable in the HfO_2 phase along with coarsening and “squeezing” of both Nb_5Si_3 phases. Both results are influenced by the high-pressure environment.

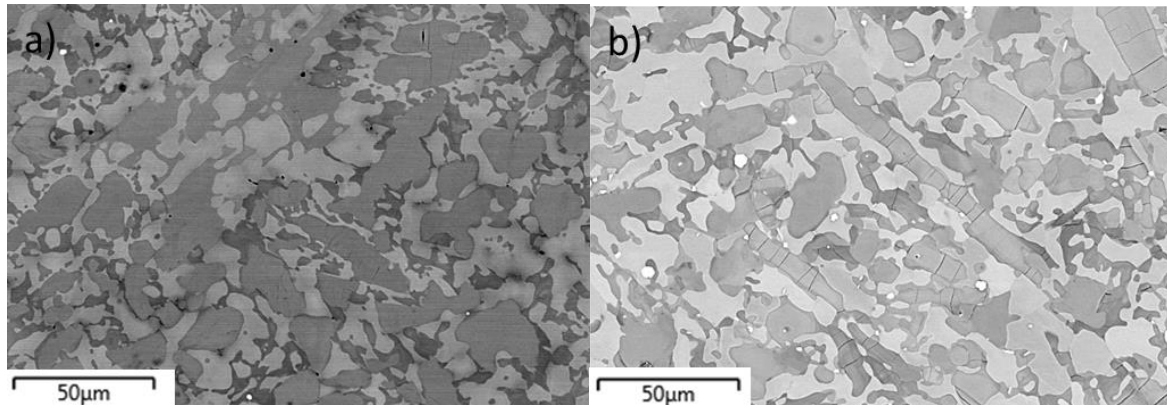


Figure 56: BEI images of Nb-22Si-26Ti-6Cr-2Al-3Hf both a) as-formed and b) post-HIP

Hot isostatic pressing has also influenced the diffractograms seen in **Figure 57**. A reduction in $\beta\text{-Nb}_5\text{Si}_3$ being absorbed into the niobium matrix noted observing $\gamma\text{-Nb}_5\text{Si}_3$, Nb_{ss} , Nb_3Si and HfO_2 .

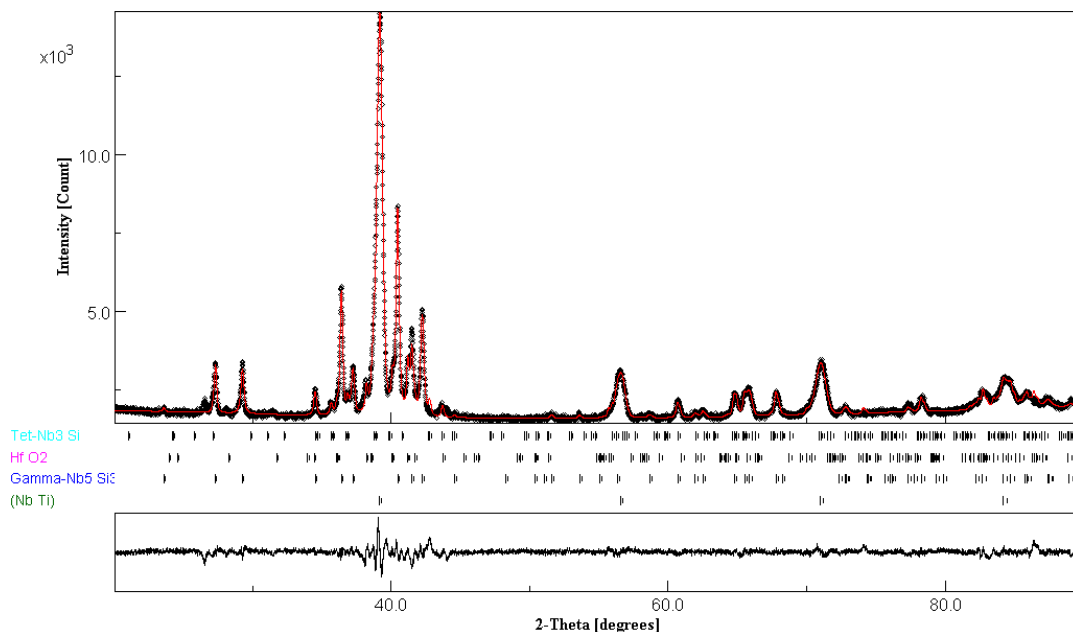


Figure 57: X-ray diffractogram of Nb-22Si-26Ti-2Al-6Cr-3Hf post-HIP modelled using MAUD

Nb_3Si was not discerned on the BEI images but its presence in small quantities in the HIP specimen suggests that it is formed as an intermediate between $\beta\text{-Nb}_5\text{Si}_3 \rightarrow \text{Nb}_{ss} + \gamma\text{-Nb}_5\text{Si}_3$. An asymmetric peak shift in $\gamma\text{-Nb}_5\text{Si}_3$ and some HfO_2 peaks suggests both an orientation shift

and lattice constant increase has occurred in both phases. The lattice constant expansion can be observed in the appendix. This change is likely due to compositional changes observed in **Table 18** for each phase.

Table 18: EDS data for Nb-22Si-26Ti-6Cr-2Al-3Hf post-HIP

	Nb	Si	Ti	Al	Cr	Hf	O	Volume Fraction (%)
Nb_{SS}	51.72	--	32.76	3.01	11.34	1.19	--	42.34
γ-Nb₅Si₃	39.04	35.17	20.7	1.23	1.04	2.83	--	56.17
γ-(Nb,Ti)₅Si₃	30.34	33.79	28.04	1.26	1.74	4.83	--	
HfO₂	0.6	--	0.08	--	--	32.77	66.55	1.4
Nb₃Si	--	--	--	--	--	--	--	0.09

Results indicate that gamma is spread in all areas of the microstructure. EDS of each phase indicates that a range of titanium concentrations is present. Evidence from G. H. Cao (2015) suggests that Ti₅Si₃ may be formed at high Ti concentrations, a model including this was attempted but not observed.^[129, 131]

The BEI images of Nb-22Si-26Ti-2Al-6Cr-3Hf post heat treatment (5 hr, 1500°C) are presented in **Figure 58 a)**. Porosity is noted in low magnification suggesting that “closed” porosity may have been hiding gas-filled pockets of argon post-HIP rather than consolidating existing cracks. The microstructure presents coarsening of the silicide phase, the contrasting light and dark silicides are difficult to discern. Hafnia inclusions are noted on the surface as noted in previous hafnium containing alloys.

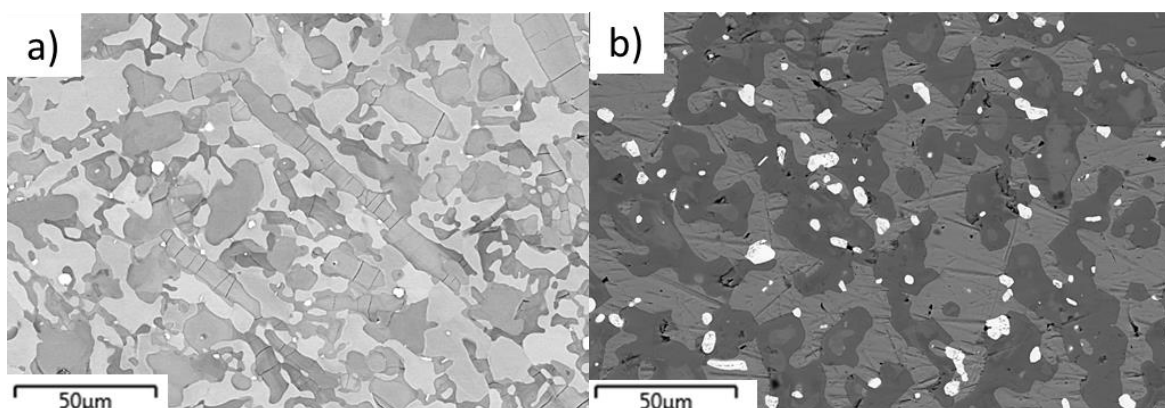


Figure 58: BEI image of Nb-22Si-26Ti-6Cr-2Al-3Hf at a) Post-HIP and b) Post-HT

The diffractogram in **Figure 59** presents with four phases. The Nb_{ss} matrix, HfO_2 and $\gamma\text{-Nb}_5\text{Si}_3$, all have been discussed previously, $\alpha\text{-Nb}_5\text{Si}_3$ is now noted and the volume fractions of this may be seen in **Table 18**. Quantitative analysis suggests the volume fraction of HfO_2 has increased marginally post-HT, likely from residual oxygen in the chamber and crucible similar to 2Cr.

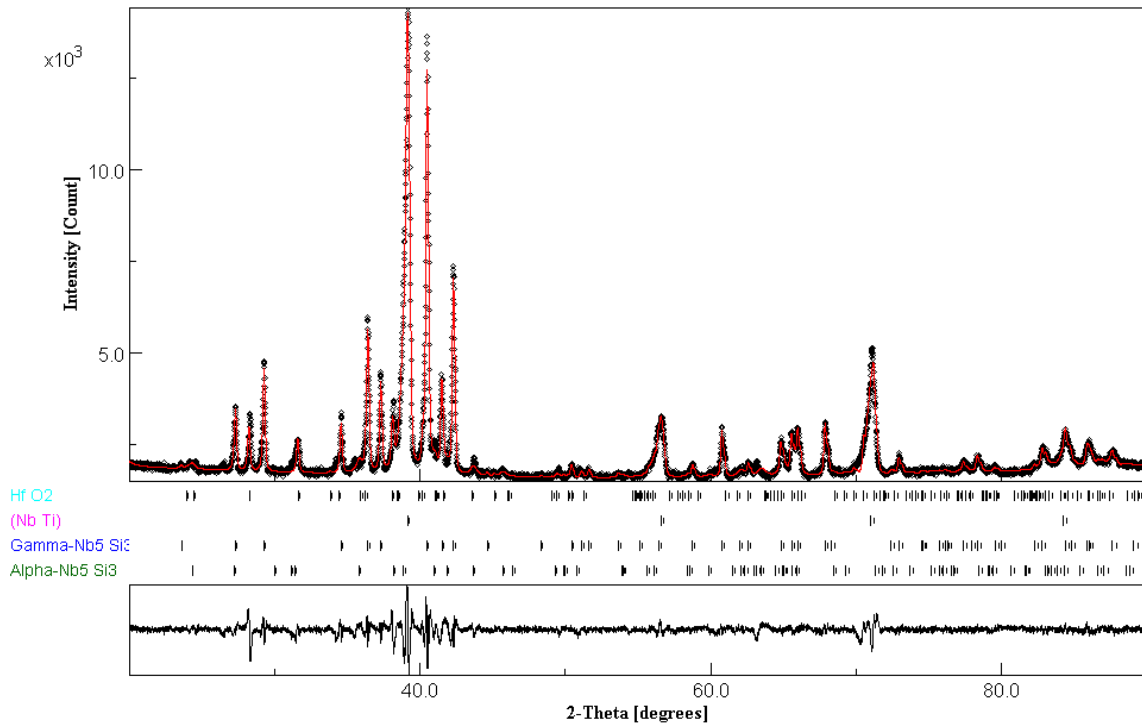


Figure 59: X-ray diffractogram of Nb-22Si-26Ti-2Al-6Cr-3Hf post-HT modelled using MAUD

The lattice parameter of Nb_{ss} can be observed in **Table 19**. It shows little changed during post-processing, which is indicative of the stability in this phase. **Table 20** shows that little has diffused in and out of the phase except small amounts of Nb and Si. The diffractogram suggests it appears to have remained stable.

Table 19: Change in Lattice parameter over processing steps of Nb-22Si-26Ti-2Al-6Cr-3Hf

Process Stage	Lattice Constant (\AA)
As-Formed	3.249415
Post-HIP	3.251266
Post-HT	3.250043

An increase in the peak $\sim 70^\circ$ suggests a change in HfO_2 as other modelled Nb_{ss} peaks do not change. Further inspection of **Table 20** presents little diffusion in other phases. $\alpha\text{-Nb}_5\text{Si}_3$ has a similar constitution as observed in the as-formed sample, what is noted is a decrease of Hf within the silicide systems which may be the source of the HfO_2 increases observed.

Table 20: Showing element and volume distribution for each phase in Nb-15Si-22Ti-6Cr-2Al-3Hf post-HT, all values in at.% unless otherwise stated

	Nb	Si	Ti	Al	Cr	Hf	V	O	Volume Fraction (%)
Nb_{ss}	54.28	1.12	29.44	2.43	11.83	0.65	0.25	--	15.95
$\alpha\text{-Nb}_5\text{Si}_3$	41.45	35.75	19.58	0.68	0.68	1.60	0.25	--	26.64
$\gamma\text{-Nb}_5\text{Si}_3$	29.84	35.45	28.65	1.26	1.42	3.16	0.22	--	53.66
HfO_2	0.99	0.50	0.72	0.70	0.15	30.25	--	66.69	3.75

Hafnium is noted to stabilise $\gamma\text{-Nb}_5\text{Si}_3$, the loss from the silicide system may have allowed for the formation of the observed $\alpha\text{-Nb}_5\text{Si}_3$, a graph summarising the phases present at each stage of the samples treatment can be seen in **Figure 60**.

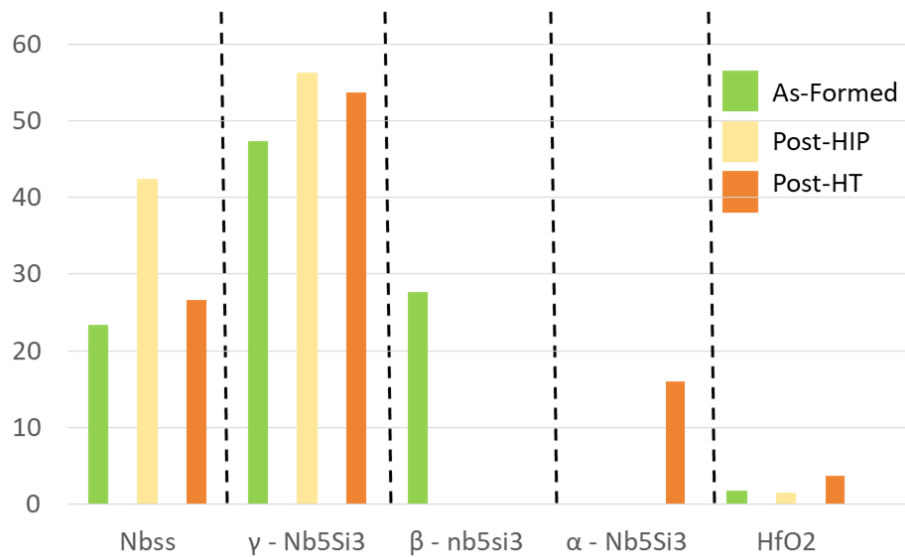


Figure 60: Comparison graph of 6Cr at each stage of production

4.5 Evaluation of Elemental Additions of Chromium and Hafnium

The aim of this chapter was to reproduce 4th generation Nb-Si-Ti alloys using DLD, HIP and HT. The inclusion of Cr and Hf to Nb-Si-Ti alloy systems aimed to produce an alloy with increased oxidation resistance, and chemistries were based on works by Songming Zhang (2015) and Dicks R. (2009).

Varied quantities of Cr had a great effect on the produced microstructure. Low quantities of Cr favoured the production of γ -Nb₅Si₃, whereas increased concentrations of Cr promoted the formation of α -Nb₅Si₃ but noted the formation of Laves phase at 14 at.% Cr. The Laves phase produced was dissimilar to reported structures. A C15 cubic structure was observed in this thesis instead of the C14 hexagonal Laves phase, potentially due to elemental differences altering the electron density of the phase.

The inclusion of Hf in all samples examined has produced HfO₂. These inclusions, as in other materials, will likely have implications on the machinability of the materials, due to the stabilisation of NbSi₃ as suggested by Qu S.^[132, 133] HfO₂ acts as an excellent O₂ getter, and also helps to stabilise α -Nb₅Si₃ but also become stress concentration points, increasing the chances of brittle fracture along the surrounding silicide. It may be wise to stop using Hf in LAM Nb-Si alloys until parameters of DLM cooling can be controlled.

5 Effects of Mo additions on Phase Evolution in Direct Laser Melting of Nb-Si Alloys

5.1 Introduction

The previous chapter discussed the effects of Hf addition in the microstructure, with the combination of stabilising γ -Nb₅Si₃ and its detrimental effects to mechanical properties from hafnia inclusions, future work removed this element. 4th generation alloys based on Nb-Ti-Si-Al-Cr systems have been reported by Jie Geng (2006) with the effects of Mo additions to the Nb-Si system. Reduction of the metastable β -Nb₅Si₃ to α -Nb₅Si₃, was observed. Whilst it is only partially soluble in the silicide it can be readily dissolved into the niobium solid solution.^[134] A paper by Kim WY (2002) attributes a solid solution hardening effect from the molybdenum and this significantly increased the yield stress of the alloy.^[134]

This section aims to discuss a different strategy in alloy production. Chemistries in the previous chapter contained small amounts of Hf and varying levels of Cr. The presence of Hf produced HfO₂ in all instances in the previous chemistry, it is surmised that these would act as crack initiator sites or de-bond themselves from the matrix interface propagating cracks as discussed in **section 4.3**. The following chapter replaces Hf with Mo to both increase oxidation resistance and improve the mechanical properties as a solid solution strengthener.^[46, 135, 136]

The Cr content was chosen based on prior experiments and knowledge. High Cr levels observed in **section 4.2** produced the Laves phase, and Cr levels too low would not provide Nb with resistance to oxygen diffusion and solubility.

5.2 Nb-18Si-24Ti-5Cr-5Al-2Mo (2Mo)

The microstructure of the as-formed sample Nb-18Si-24Ti-5Cr-5Al-2Mo (2Mo) can be seen in **Figure 61**. The low magnification shows primary grey phases suspected to be either Nb₅Si₃ or Nb₃Si surrounded by a lighter grey (likely Nb_{ss}). A third, darker grey phase (phase 3) can also be observed under high magnification.

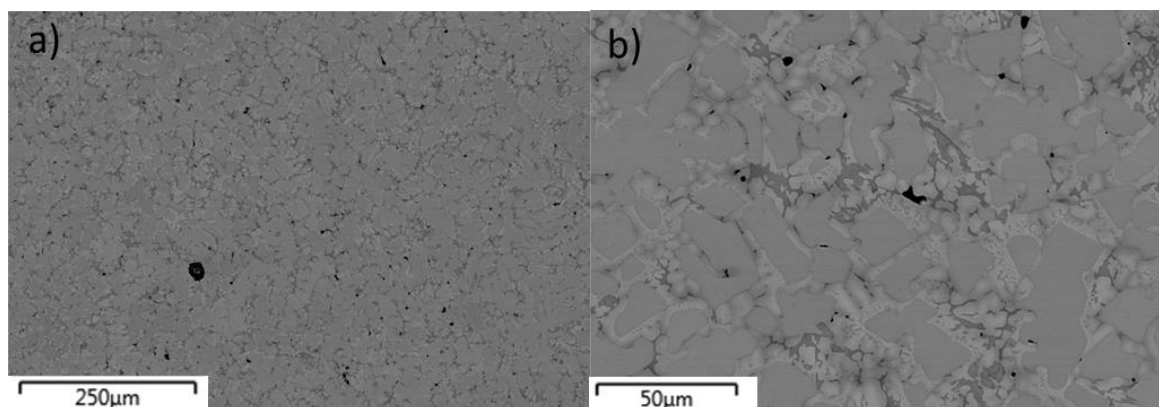


Figure 61: BEI of Nb-18Si-24Ti-5Cr-5Al-2Mo at a) Low and b) High magnification. Image taken at centre of scan sample.

The use of EDS analysis allows elemental abundance to be discovered in each ‘phase’. The results are shown in **Table 21**. The solid solution can be identified from the large Nb/Si ratio, which also contains a significant quantity of titanium. To reflect this, the phase will be described as (Nb, Ti)_{ss}. Like the phases in previous sections, Al has shown segregation to the solid solution phase with the majority favouring the low Si environment. This is equally true with Cr and Mo which show segregation to (Nb, Ti)_{ss}. The combination of these three elements is 12 at.%, previous works have suggested they contribute to the suppression of Nb₃Si and promote Nb₅Si₃. As discussed previously, Cr contributed to Laves formation in **section 4.2** but is not observed here, with most Cr being distributed in Nb_{ss}.

Table 21: Showing element distribution in phases of as formed Nb-18Si-24Ti-5Cr-5Al-2Mo, all values in at.% unless otherwise stated

	Nb	Si	Ti	Al	Cr	Mo	Volume Fraction (%)
Nb _{ss}	46.39	6.65	28.36	6.98	8.82	2.81	33.73
γ-Nb ₅ Si ₃	45.42	32.35	17.31	3.03	1.00	0.88	35.38
γ-Nb ₅ Si ₃	34.85	28.30	28.84	4.45	2.76	0.79	30.89

Unlike the Nb_{SS}, the primary phase contains a high amount of both Nb, Ti and Si. Previous studies noted only one Nb₅Si₃ formation but do not detail EDS data of each phase until after oxidation experiments.^[46] The two different silicide phases can be differentiated when comparing EDS maps in **Figure 62**. The high Ti silicide is only noted within the eutectic between the primary silicide. Ti₅Si₃ formation is noted under high Ti, though this is not observed in the diffractogram in **Figure 63** and therefore Ti is substituted for Nb within the crystal lattice.

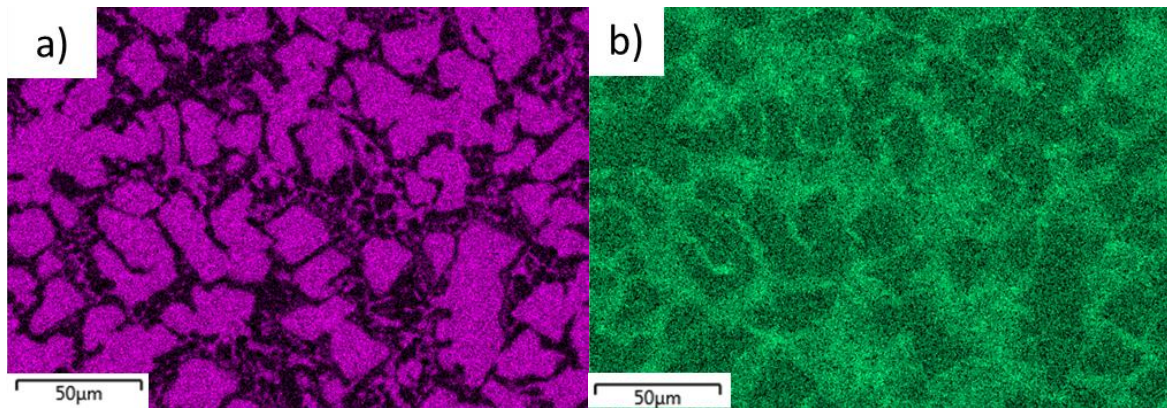


Figure 62: EDS map highlighting different elemental distributions in Nb-18Si-24Ti-5Cr-5Al-2Mo showing

a) Si distribution, b) Ti distribution

When modelled, only hexagonal Nb₅Si₃ is confirmed (**Figure 63**). Multiple structures were attempted including β-Nb₅Si₃ and Nb₃Si, which were two structures observed in original experiments by Jie Geng (2006), but a sufficient goodness of fit was not achieved.^[46]

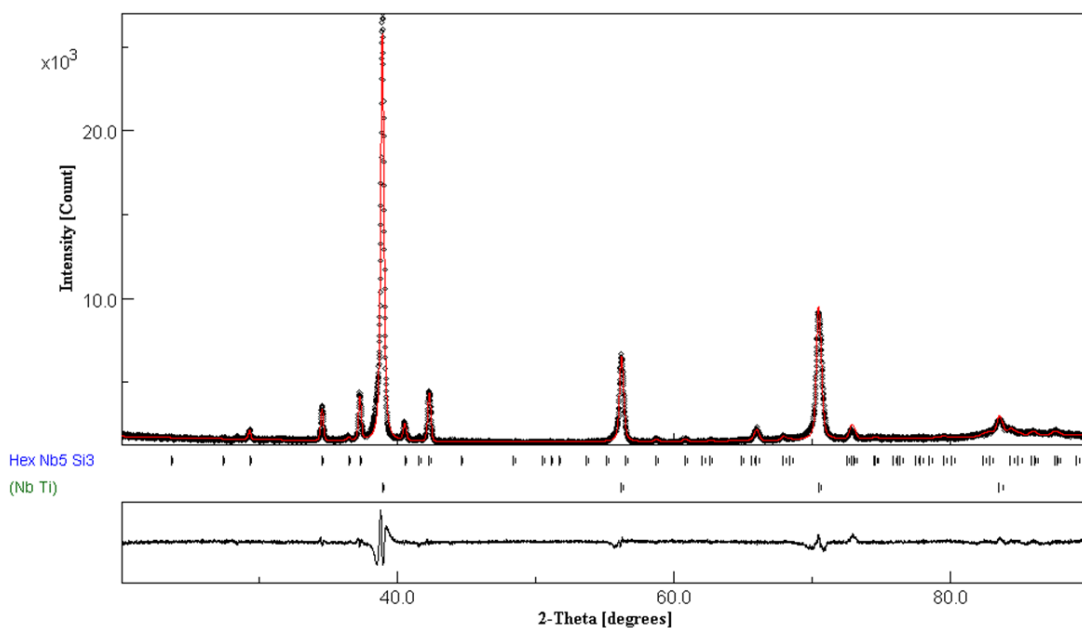


Figure 63: X-ray diffractogram of as-formed Nb-18Si-24Ti-5Cr-5Al-2Mo

The difference in observed crystal structure allows the following to be surmised;

- 1) γ - Nb_5Si_3 may contain a range of Ti concentrations
- 2) Formation methods greatly effect crystal structure formation of Nb_5Si_3

Evidence from **Figure 62** and **Figure 63** suggests that Nb_5Si_3 may exist with different ratios of Ti, with titanium atoms substituting niobium atoms, based on constant ratio of (Nb/Ti):Si throughout both phases. The modelled crystal lattice for γ - Nb_5Si_3 is smaller than expected; modelled: $a, c = 7.5202 \text{ \AA}, 5.1875 \text{ \AA}$, versus recorded: $a, c = 7.536 \text{ \AA}, 5.249 \text{ \AA}$. This shrinkage of crystal size represents the relaxation of the crystal lattice due to smaller substitutions of Ti for Nb.

Formation speed may have a significant impact on crystal formation. Work by Jie Geng (2006) used arc-melting to produce samples that were re-melted 5 times before final solidification. This is a much slower process with phases being mixed multiple times, areas of concentrated Ti were noted within the paper but not in significant amounts. As a result, Geng produced a system containing Nb_{55} , β - Nb_5Si_3 and Nb_3Si . The sample presented in this data was formed by additive manufacturing and thus cooled rapidly. A “layer” was re-melted multiple times as the laser passed over to produce the next section, promoting homogeneity. This rapid cooling may be one reason why only γ - Nb_5Si_3 is observed on solidification.

Plotting the individual phases on the ternary Nb-Si-Ti diagram in **Figure 64**, including the Ti saturated Nb_5Si_3 phase, we can observe a range where Nb_5Si_3 may solidify.

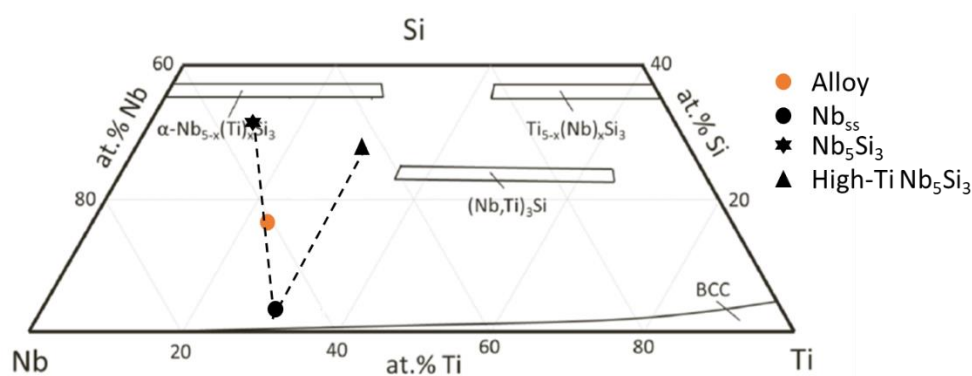
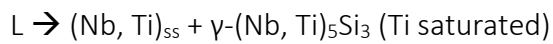
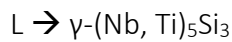


Figure 64: Ternary phase diagram of Nb-Si-Ti with respective phases plotted

Finally, the solidification can be solved as:



It is speculated that as the $\gamma\text{-Nb}_5\text{Si}_3$ phase solidified during the primary stage, during which it ejected excess titanium into the melt pool, thus saturating it. Secondly a eutectic was formed from the liquid resulting in Ti-rich $\gamma\text{-Nb}_5\text{Si}_3$ as well as $(\text{Nb, Ti})_{ss}$.

Methods of calculating phase % in 2Mo were compared to determine a difference between the surface and bulk of a sample. **Table 22** displays the volume fraction of each phase using different techniques. The bulk sample originates from the modelled diffractogram, the edge and centre sections are averaged analysis of several BEI images.

Table 22: Comparison table of phase % distribution in XRD diffractogram and BEI images

Phase	XRD	Edge	Centre
$(\text{Nb, Ti})_{ss}$	58.28	18.56	19.93
$\gamma\text{-Nb}_5\text{Si}_3$	41.71	68.25	70.49

A difference in phase quantity is seen when comparing the two measurements, noticeably with Nb_{ss} and $\gamma\text{-Nb}_5\text{Si}_3$.

These discrepancies can be the result of one of two factors:

- 1) The areas analysed using BEI had an atypical ratio of phases- not representative of the bulk material.
- 2) Penetration depth plays a larger factor than expected.

The likely answer is penetration depth, as BEI images were taken from a range of areas on a sample, averaging out should represent an accurate image of the surface. SEM analysis has a smaller penetration distance when compared to XRD, for this reason it is possible that the surface analysed under SEM may not represent a complete picture of the sample. Macroseggregation may have occurred during solidification, resulting in a shift in $\text{Nb}_{ss}/\text{Nb}_5\text{Si}_3$ volume ratios.

The BEI of Nb-18Si-24Ti-5Cr-5Al-2Mo post-HIP can be seen in **Figure 65**. Small amounts of consolidation are seen in the eutectic but the primary Nb₅Si₃ phase appears smaller. Four distinct phases can be seen in the post-HIP sample, the three noted from previous stages and a fourth black phase at the boundary of Nb₅Si₃ and Nb_{SS}.

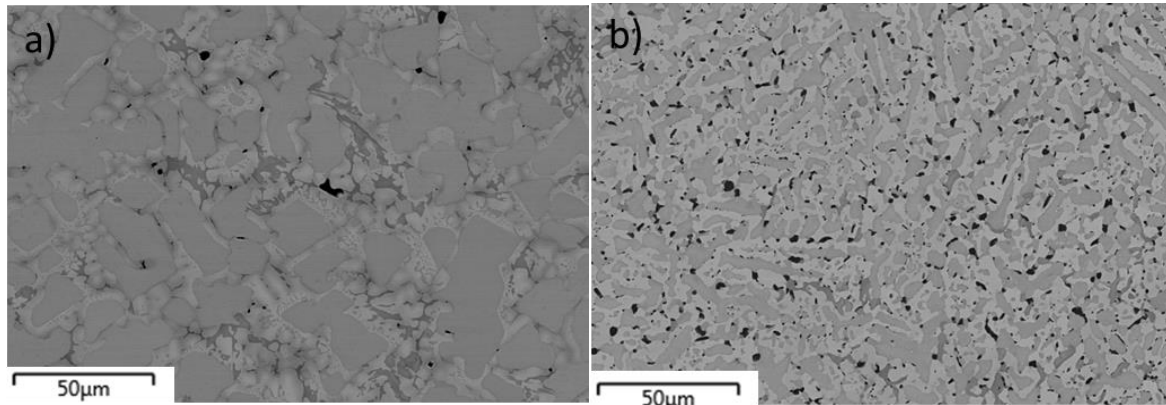


Figure 65: BEI of Nb-18Si-24Ti-5Cr-5Al-2Mo post-HIP at a) as-formed b) post-HIP. Images taken at centre of scan sample.

The new phase, localised on the boundary of Nb_{SS} and Nb₅Si₃ suggests it formed via phase boundary diffusion, its proximity to Nb₅Si₃ suggests it was expelled from this phase. The diffractogram of Nb-18Si-24Ti-5Cr-5Al-2Mo post-HIP in **Figure 66** suggests three phases are present, Nb_{SS}, γ -Nb₅Si₃ and β -Nb₅Si₃, suggesting a partial $\gamma \rightarrow \beta$ transformation.

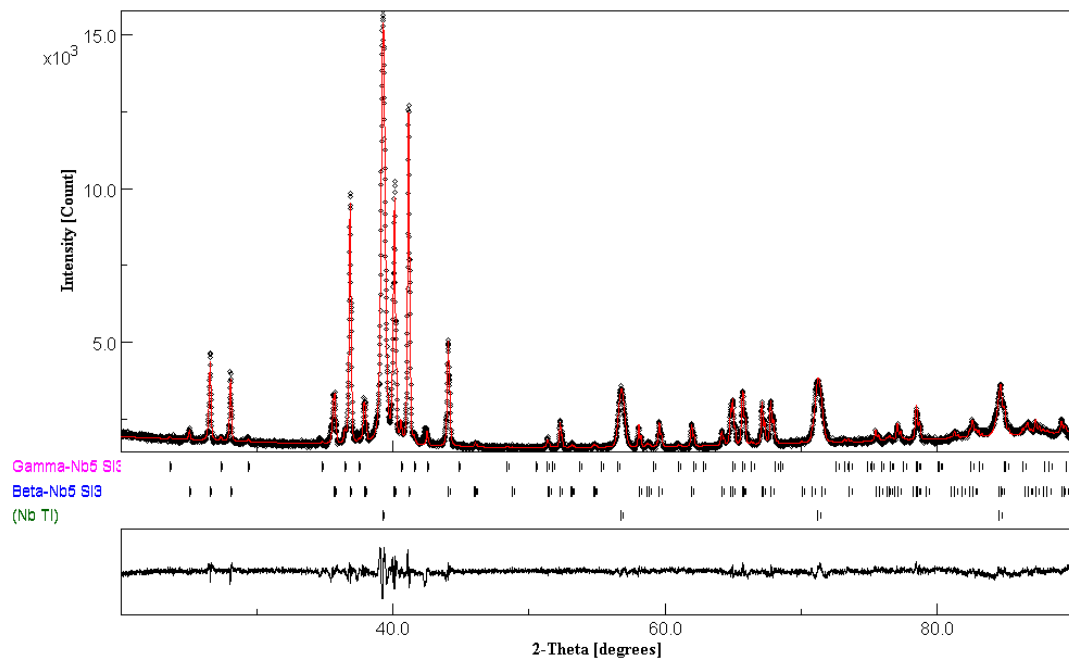


Figure 66: X-ray diffractograms of post-HIP Nb-18Si-24Ti-5Cr-5Al-2Mo

Although only three crystal structures are suggested on the diffractogram, four were noted in the BEI image, their composition has been analysed in **Table 23**. The Nb_{ss} phase is easily identified from the diffractogram and retains a similar distribution of elements, with ejection of Si suggesting the as-formed solid solution cooled too rapidly to eject it, trapping it within vacancies of the Nb_{ss} lattice, Si partially diffused out during post-processing. Work by Tsakirooulos (2018) suggests that Nb_{ss} exists with either 0 % Si or 1.5 % Si, dependant on other alloying elements, suggesting further diffusion may be required to reach equilibrium.^[129]

Table 23: Showing element distribution in phases of post-HIP Nb-18Si-24Ti-5Cr-5Al-2Mo, all values in at.% unless otherwise stated

	Nb	Si	Ti	Al	Cr	Mo	Volume Fraction (%)
Nb _{ss}	49.34	3.62	28.43	6.83	8.97	2.82	49.55
β-Nb ₅ Si ₃	45.36	32.18	17.40	3.15	1.00	0.92	38.41
γ-Nb ₅ Si ₃	51.81	26.57	17.65	1.94	1.20	0.82	12.03
Ti _{ss}	28.12	4.30	61.70	1.82	2.47	1.59	--

The two silicide phases have a very similar composition. As the XRD model suggests, β-Nb₅Si₃ is present in a larger quantity and so is labelled according to the modelled volume fraction. The contrast in the BEI image is likely the marginal difference of Nb/Si content results. Titanium levels in both phases are similar, confirming the hypothesis that the Nb₅Si₃ phase was saturated with Ti.

The fourth phase identifies with a high Ti content. No new peaks were observed in the diffractogram suggesting the material is either non-crystalline or has overlapping peaks within the sample. Ti_{ss} is a likely candidate with an Im-3m crystal structure, the same observed in Nb_{ss} as discussed in **section 3.3.4** making it difficult to model within the larger Nb_{ss} peaks. It has also been previously noted to appear in electron beam surface melted samples in work by Dicks (2008).^[9, 137, 138] The table above shows that Ti concentrations have reduced to ~17.5% in both phases, It is possible that the ejection of Ti resulted in the formation of Ti_{ss} on the Nb₅Si₃ boundary, further experiments were required to determine the origins of Ti_{ss} and are discussed later in **8**.

The heat-treated sample may be seen in **Figure 67**. It presents a microstructure similar to the post-HIP sample, this initially suggests either that the HIP stage sample was under equilibrium or the time was not long enough to promote any significant morphology changes.

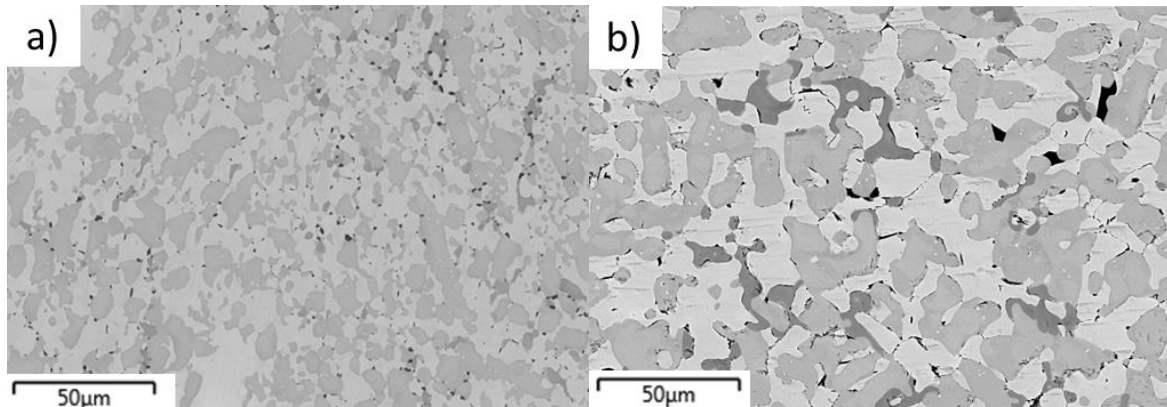


Figure 67: BEI of Nb-18Si-24Ti-5Cr-5Al-2Mo at a) Post-HIP and b) Post-HT. Images taken at centre of scan sample.

Similar to previous steps, two contrasting Nb_5Si_3 phases are observed in the BEI images, inspection of the diffractogram for this sample in **Figure 68** shows three phases. Nb_{ss} continues as previous, $\gamma-Nb_5Si_3$ is still detected and $\beta-Nb_5Si_3$ is now replaced with $\alpha-Nb_5Si_3$.

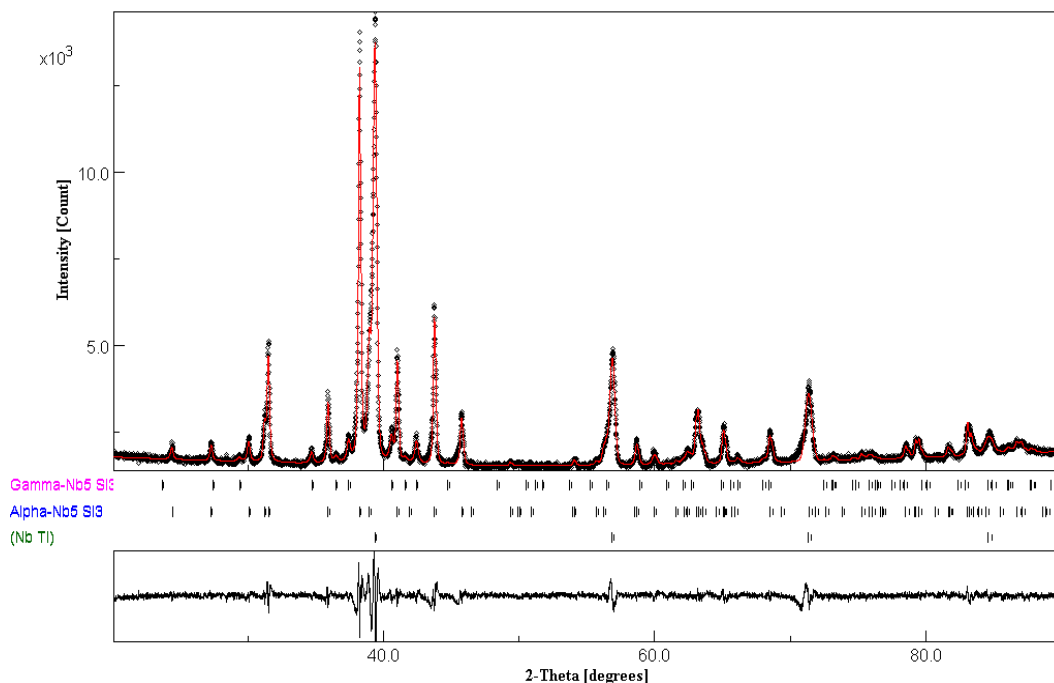


Figure 68: X-ray diffractogram of post-HT Nb-18Si-24Ti-5Cr-5Al-2Mo post-HT performed for 5 h at 1500°C

The presence of $\alpha-Nb_5Si_3$ within the 5 h heat treatment suggests its transformation may occur via a mechanism not involving Nb_3Si decomposition. Indeed, its absence from the

diffraction pattern suggests it was not formed. Alluding to another mechanism converting $\beta\text{-Nb}_5\text{Si}_3 \rightarrow \alpha\text{-Nb}_5\text{Si}_3$. The presence of $\gamma\text{-Nb}_5\text{Si}_3$ proposes the transformation is in this material incomplete. It is possible the eutectoid $\beta\text{-Nb}_5\text{Si}_3 \rightarrow \alpha\text{-Nb}_5\text{Si}_3 + \text{NbSi}_2$ reaction occurred but NbSi_2 could not be modelled successfully.^[129] Another heat treatment of 1200°C was also performed for 100 h. The modelled diffraction pattern observed in **Figure 69** of the 100 h HT shows a fully transformed crystal structure with no Nb_3Si present.

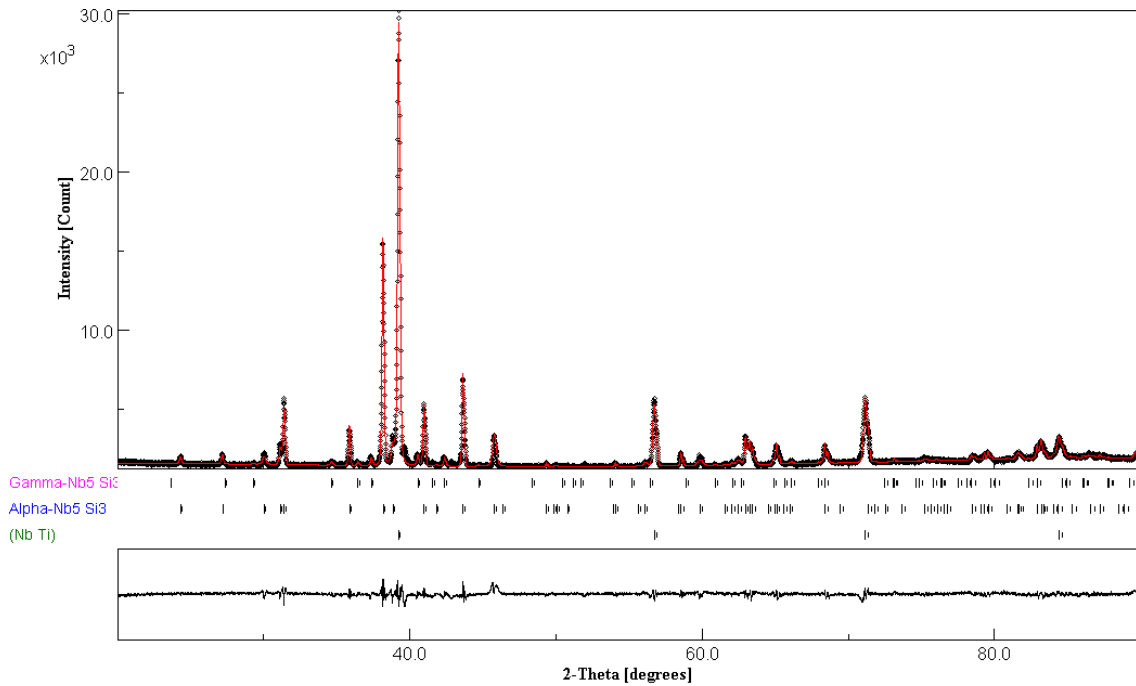


Figure 69: X-ray diffraction pattern of post-HT Nb-18Si-24Ti-5Cr-5Al-2Mo – HT performed for 100 h at 1200°C

The HT temperature was not as high as the previous experiment, it does show transformation of $\beta\text{-Nb}_5\text{Si}_3$ to $\alpha\text{-Nb}_5\text{Si}_3$ with no some $\gamma\text{-Nb}_5\text{Si}_3$ noted at small quantities within the pattern. The volume % distribution can be seen below in **Table 24**.

Table 24: Volume fraction of two different HT parameters

Phase	Volume Fraction %	
	5 h	100 h
Nb_{ss}	30.14	51.92
$\alpha\text{-Nb}_5\text{Si}_3$	43.81	42.95
$\gamma\text{-Nb}_5\text{Si}_3$	26.05	5.13

The 5 h sample shows a much lower volume fraction of solid solution and it is likely that further HT to 100 h would result in the decomposition of $\gamma\text{-Nb}_5\text{Si}_3$ into Nb_{ss} and $\alpha\text{-Nb}_5\text{Si}_3$. The peaks at 40.98° and 43.65° are different between 5 h and 100 h. To provide a better fit, arbitrary texturing model was removed suggesting that an orientation change has occurred, reducing

preferred orientation of α -Nb₅Si₃ during the 100 h HT. Note that this is a supposition, complete texture analysis of both samples would be required.

The BEI in **Figure 70** shows the microstructure of 2Mo at three different stages of post-processing, the observed volume% of Ti_{ss} is greatest immediately post-HIP and reduces started from 5 h, with 100 h containing the least. This also coincides with a diffusion of Ti into the solid solution.

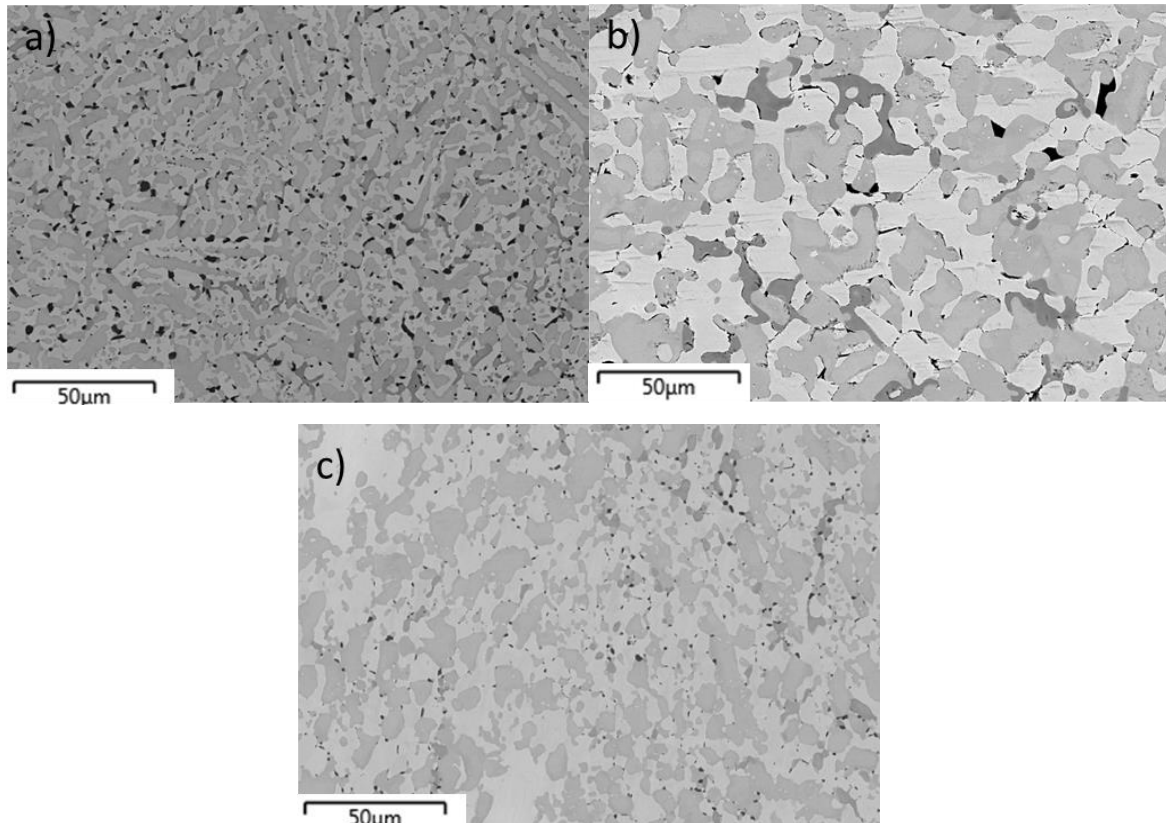


Figure 70: BEI of Nb-18Si-24Ti-5Cr-5Al-2Mo at a) Post-HIP, b) Post-HT (5 h, 1500°C) and c) Post-HT (100 h, 1200°C), showing different levels of Ti_{ss}

Table 25 presents the elemental distribution in each phase in the 5 h and 100 h HT samples. It is noted that Si decreases as heat treatment time persists and is no longer present in Nb_{ss} after 100 h. Slow homogenisation between Nb_{ss} and Ti_{ss} is evident, observing a 2 % Cr switch. Diffusion also appears from Ti_{ss} towards γ -Nb₅Si₃ with concentrations of titanium increasing to as-formed levels.

Table 25: Showing element distribution in phases of post heat treatment Nb-18Si-24Ti-5Cr-5Al-2Mo, all values in at.% unless otherwise stated

		Nb	Si	Ti	Al	Cr	Mo
Nb _{ss}	5 h	50.08	1.07	28.00	6.92	10.55	3.39
	100 h	56.14	--	28.45	6.49	8.92	--
α-Nb ₅ Si ₃	5 h	44.89	31.73	18.76	2.37	1.22	1.03
	100 h	46.07	32.54	17.37	3.60	1.25	--
α-(Nb,Ti) ₅ Si ₃	5 h	33.45	32.44	28.51	3.22	1.72	0.67
	100 h	33.19	32.27	30.49	3.28	1.15	--
Ti _{ss}	5 h	6.26	0.27	92.20	0.41	0.66	0.29
	100 h	20.58	7.95	68.95	1.58	2.42	--

A comparison of all these changes can be seen in **Figure 71** along with transformations during all post-treatment stages.

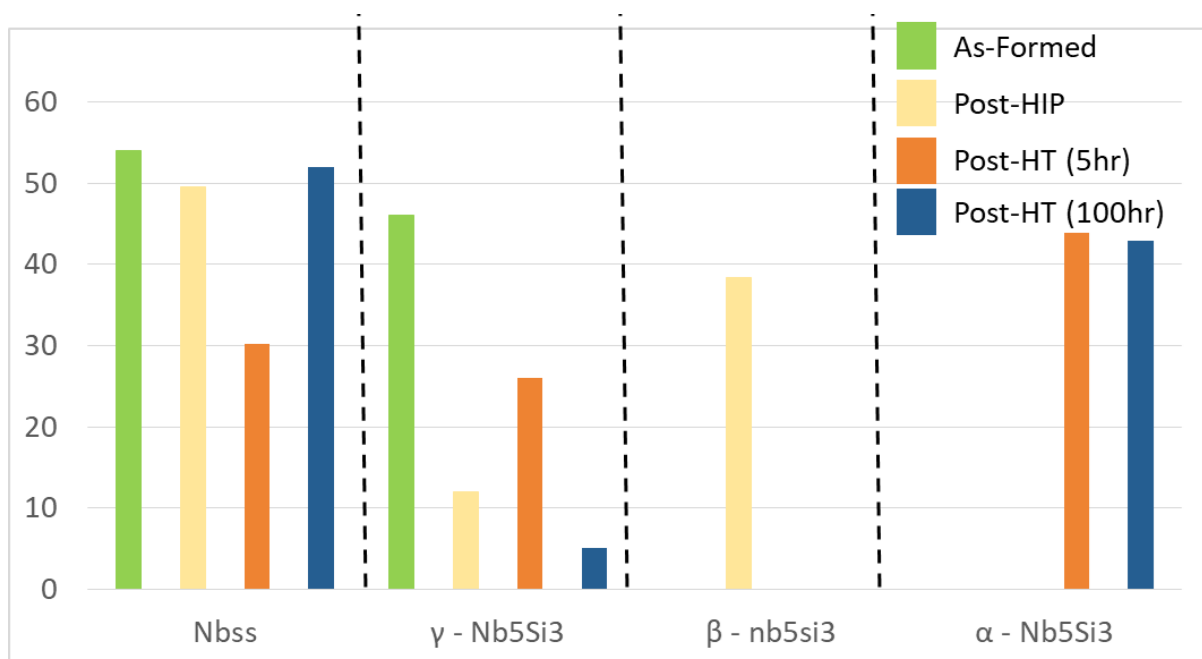


Figure 71: Comparison graph of 2Mo at each stage of production

5.3 Evaluation of Elemental Additions

This chapter aimed to replicate work conducted by Jie Geng (2006). The phase evolution of 4th generation Nb-Si-Ti alloys produced by directional solidification and additive manufacturing were compared.

Work in the previous chapter established the effects of Cr and Hf on alloy systems. Hf was removed to prevent HfO₂ formations within the system. The quantity of chromium was decided based on phases produced in the reported paper and knowledge acquired in **4**. The addition of Mo to the Nb-Si-Ti alloy systems aimed to produce an alloy with increased oxidation resistance and strengthen the solid solution.

Titanium concentration was based on the chemistry reported by Jie Geng (2006) and microsegregation of Ti was noted on formation. During HIP post-processing Ti_{ss} was produced epitaxially to Nb₅Si₃ structures. During heat-treatment these reabsorbed into Nb_{ss} and Nb₅Si₃ phases, suggesting a diffusion mechanism. Further discussion of this phenomena may be seen in **section 8.3**.

6 Effects of Zr and Y Additions in 4th Generation Nb-Si Alloys

6.1 Introduction

The oxidation resistance of current niobium silicide alloys is poor at approximately 700°C. It was discussed earlier in **section 2.4.2**. It is suspected that oxygen propagates through existing cracks and pores within the sample. Pesting can also occur in some alloys, where a non-protective oxide layer peels from a components surface.^[139] The elemental additions of the previous chapter (Al, Ti and Cr) are known to be beneficial to oxidation resistance, although the target oxidation resistance of 23 $\mu\text{m}\cdot\text{h}^{-1}$ has not been reached.^[31, 140] The previously discussed chemistry 2Mo (Nb-24Ti-18Si-5Al-5Cr-2Mo) was constructed under LAM and shows unique microstructure compared to arc-melting performed by Jie Geng (2006). Separate work by Douglas A. showed that this alloy was shown to have greater oxidation resistance after LAM construction followed by HIP and 100 h HT at 1200°C.^[141]

The primary oxide of Nb-Si-Ti alloys is Nb₂O₅ and several conformation changes occur when temperature is increased, each of which results in a volumetric change.^[142] This change in volume is likely to be responsible for the pesting phenomenon observed in Nb-Si-Ti oxides.

One consideration for oxidation improvement is the addition of zirconium which has a thermodynamically stable oxide; ZrO₂ (zirconia). At high temperatures it is more stable than Al₂O₃, as with Nb₂O₅, it also undergoes conformation changes seen below in **Figure 72**. Zr and Y have been shown to improve oxidation resistance in other materials, a study has found improved oxidation resistance in Nb-Si-Ti.^[143] Little is known of the effect of Zr on the microstructure and phase stabilisation of Nb-Si-Ti alloys.^[143, 144] Zr, like Ti, is a group IV metal with a hexagonal close packed (HCP) crystal lattice, this suggests it may also stabilise γ -Nb₅Si₃, though the extent of stabilisation is unknown.^[129, 145] Some work suggests that Zr improves mechanical properties of Nb-Si alloys by increasing dislocation mobility.^[144]

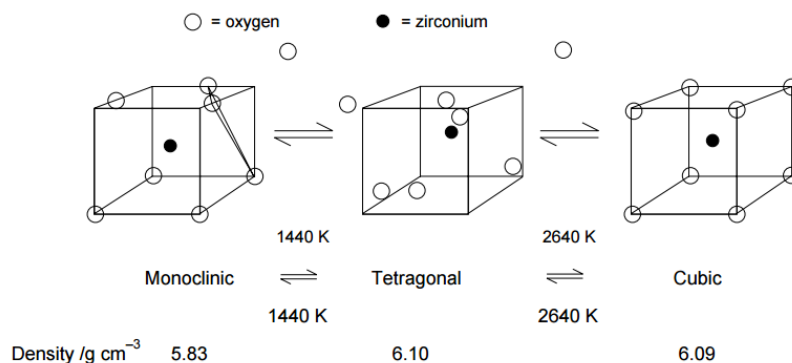


Figure 72: Conformational changes in ZrO₂ as a result of thermal changes^[146]

Figure 72 also presents density changes within the crystal structure, suggesting that the conformer transformation is not beneficial. Studies have shown that ZrO₂ can be stabilised by additions of yttrium oxide. Y₂O₃ has been shown to partially stabilise ZrO₂ in the tetragonal form or sometimes fully stabilise the cubic phase.^[147]

It is hypothesised that the addition of Zr and Y will enhance oxidation resistance by producing a stable conformer. The lack of conformer change will ideally form a non-porous oxide layer which would be less prone to peeling.

Yttrium also influences the thermal coefficient of expansion, for example 4 at.% yttria has a similar value to niobium in stabilised ZrO₂.^[7, 148] As mentioned, the difference in volume (and therefore thermal expansion) is one of the factors leading to peeling of the oxide layer. Yttrium has been shown to decrease the grain boundary size of NiAl alloys, improving oxidation resistance. This has also been shown by Yueling Guo (2018) to refine microstructures, the result being a smaller oxide which can modify the growth and stress produced and prevent peeling.^[149, 150] At high temperatures it also produces a more stable oxide than hafnium, niobium and titanium, meaning it acts as a potential oxygen sink, similar to the HfO₂ discussed in **Chapter 4** Yttrium will be added to reduce the change in volume, and therefore thermal expansion in the oxidation layers.

6.2 Nb-18Si-24Ti-5Cr-5Al-2Mo-5Zr-0.4Y (CoZy5)

The addition of Zr produces a very fine, regular microstructure as can be seen in **Figure 73 a)**. When inspecting at high magnification **b)** we can see a microstructure containing 3 distinct formations. The predominant lighter phase (likely Nb_{ss}) contains a mixture of two grey phases. The larger grey phase appears blocky with a “lathlike” H shaped formation, highlighted, whilst a smaller eutectic structure can also be observed within the Nb_{ss}.

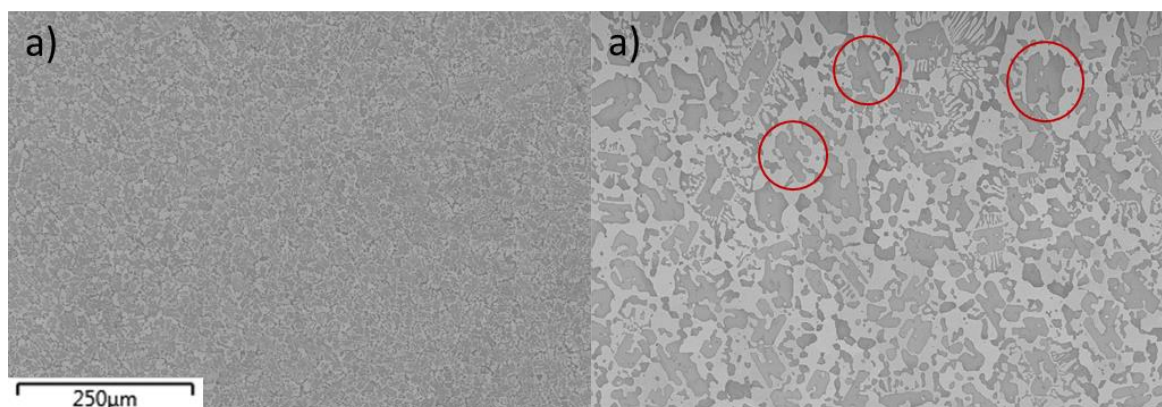


Figure 73: BEI image of Nb-18Si-24Ti-5Cr-5Al-2Mo-5Zr-0.4Y as-formed at a) Low and b) High magnification

The added Zr and Y have altered the microstructure significantly. Previously, large consolidated γ -Nb₅Si₃ dendrites were present, surrounded by Nb_{ss} and small quantities of high-Ti γ -Nb₅Si₃ as seen in **Figure 74**. The high-Ti Nb₅Si₃ phase remains but the average size of the silicide's is smaller.

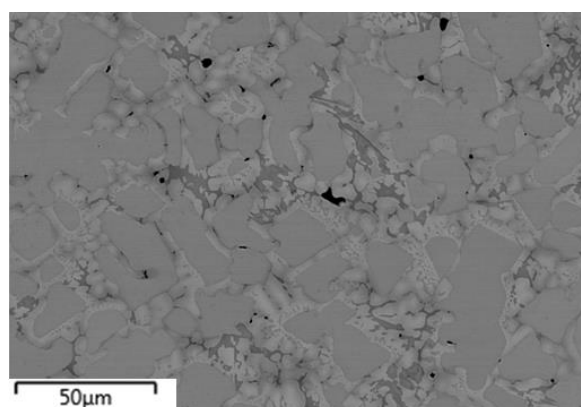


Figure 74: BEI image of 2Mo as-formed at high magnification

Closer examination of the microstructures produced using EDS (**Figure 75**) allows the elemental distribution to be observed, below is the comparison of 2Mo and CoZy5. The niobium concentration remains mostly homogeneous, with a higher concentration in the solid solution areas.

As expected, the silicon distribution is non-homogeneous, segregating to the darker grey microstructures seen in the BEI images. A notable difference is seen between the titanium maps; the Ti originally prefers the solid solution but becomes more homogenous with the chemistry alterations.

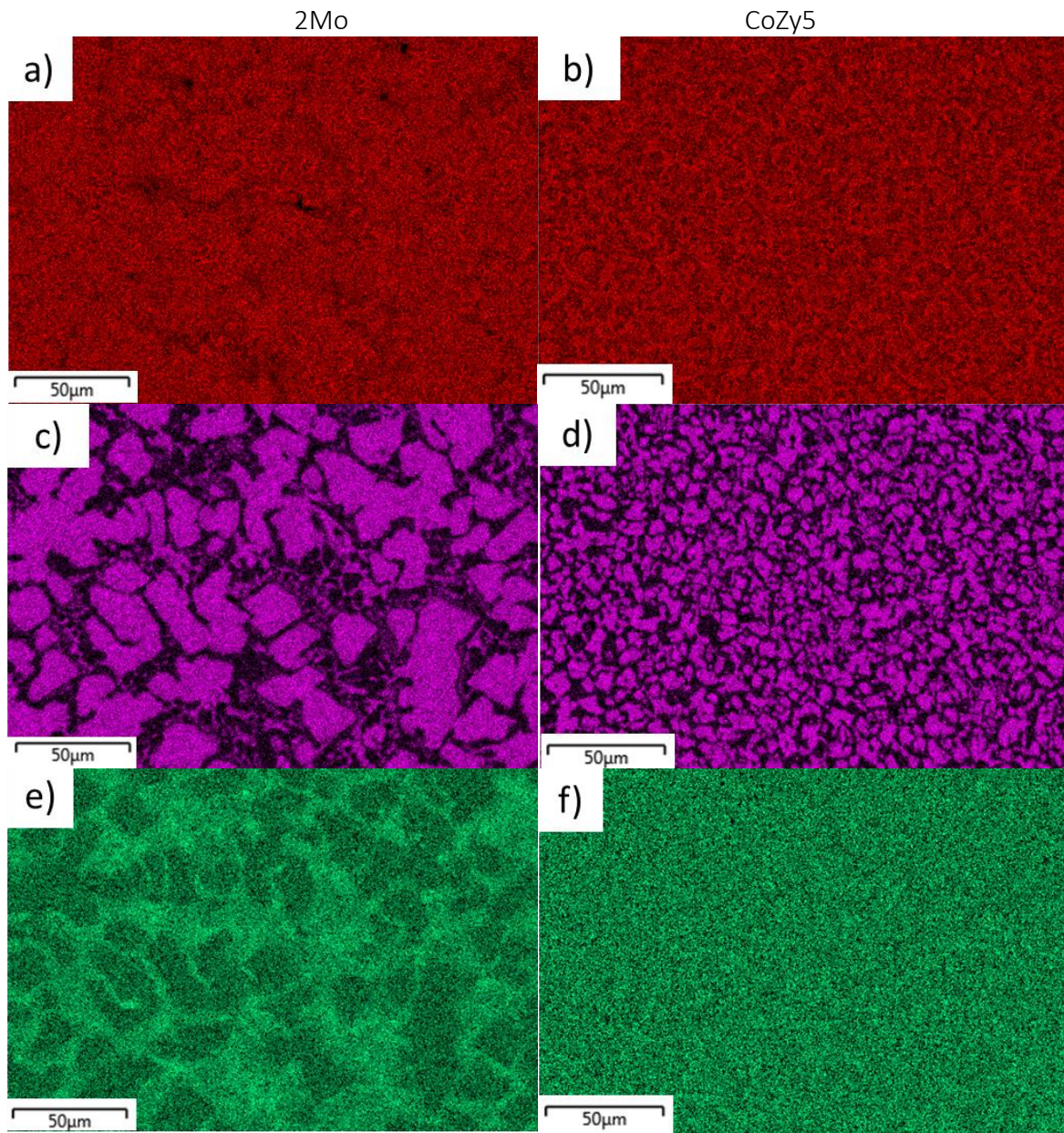


Figure 75: EDS map of Nb-18Si-24Ti-5Cr-5Al-2Mo (a, c, e) and Nb-18Si-24Ti-5Cr-5Al-2Mo-5Zr-0.4Y (b, d, f) showing distribution of Red) Nb, Purple) Si and Green) Ti

This size reduction maybe due to:

- 1) The addition of Zr and Y reducing the size of the microstructure
- 2) Processing parameters played a role in changing the microstructure shape

Scan speed, heat density and scan pattern have been noted to change the size and shape of microstructures, for this reason all parameters remained the same for this study. Focal point distance is also known to also effect LAM, drift does occur during printing and the beam required periodic re-alignment to prevent major microstructure changes. The more likely scenario is the added Zr and Y acts to reduce precipitated phases, causing distortions in the crystal structure which allows increased solubility. The alloy composition is new, with little work on microstructural effects of Zr and Y.^[144, 149] An evaluation of elemental additions will be discussed in **section 6.4**.

Table 26 displays the elemental composition of both phases, the names of phases have been preliminarily added based on knowledge of previous samples. As in the previous chemistries, Al and Cr were found predominantly in both the solid solution phase and “phase 3”. Unlike previous samples, molybdenum was only detected within the solid solution phase, as with the alloy 2Mo.

This alloy was designed to add Zr to the solid solution to increase oxygen resistance. Unfortunately, however, in the as-formed component only a trace concentration could be found in the solid solution, with the majority located in the silicide.

Table 26: Showing element distribution in phases of as-formed Nb-18Si-24Ti-5Cr-5Al-2Mo-5Zr-0.4Y, all values in at.% unless otherwise stated

	Nb	Si	Ti	Al	Cr	Mo	Zr	Y	Volume Fraction
(Nb, Ti)_{ss}	58.98	1.86	20.95	7.85	6.52	2.64	0.81	0.42	51.60
Nb₅Si₃	36.61	32.79	17.31	3.69	1.00	0.08	9.49	0.14	48.40

The significance of the element segregation is not appreciated until its parent alloy, 2Mo, is considered. The original was a Nb_{ss}/γ-Nb₅Si₃ alloy with varied Ti concentration in the silicide producing contrasting Nb₅Si₃ phases. The elemental distribution of these phases is compared in **Table 27**.

Table 27: Comparison of elements from 2Mo and CoZy5

Phases	Nb		Ti		Si	
	2Mo	CoZy5	2Mo	CoZy5	2Mo	CoZy5
Nb _{ss}	46.39	58.98	28.36	20.95	6.65	1.86
γ -Nb ₅ Si ₃	45.42	36.61	17.31	17.31	32.35	32.79
γ -(Nb, Ti) ₅ Si ₃	34.85	--	28.84	--	28.3	--

The silicide noted in CoZy5 relates to the low Ti-silicide with similar Ti and Si concentrations, a lower Nb concentration is noted, replaced by Zr. As stated previously, the concentration of Nb is greater in the solid solution but is almost 30% more concentrated in CoZy5 than 2Mo. Also noted is the concentration of Si is lower in CoZy5, appearing closer 2Mo at the post-HIP stage.

Modelling of the XRD spectrum in **Figure 76** confirms two phases present, the (1,1,0) Nb_{ss} may be seen at 39.03° and the previously noted (1,1,2) γ -Nb₅Si₃ peak at 41.88°. This represents a shift in the solid solution from 38.909° in 2Mo, indicating a decrease in lattice parameter. Conversely, the opposite is seen with γ -Nb₅Si₃, inclusions of Zr show an increase in lattice constants. Further comparison of both chemistries in this chapter will be discussed in **section 6.4**. Yanqiang Qiao (2017) showed the opposite trend based on the difference in atomic size ($r_{\text{Nb}}=215$ pm and $r_{\text{Zr}}= 230$ pm), expanding the matrix.

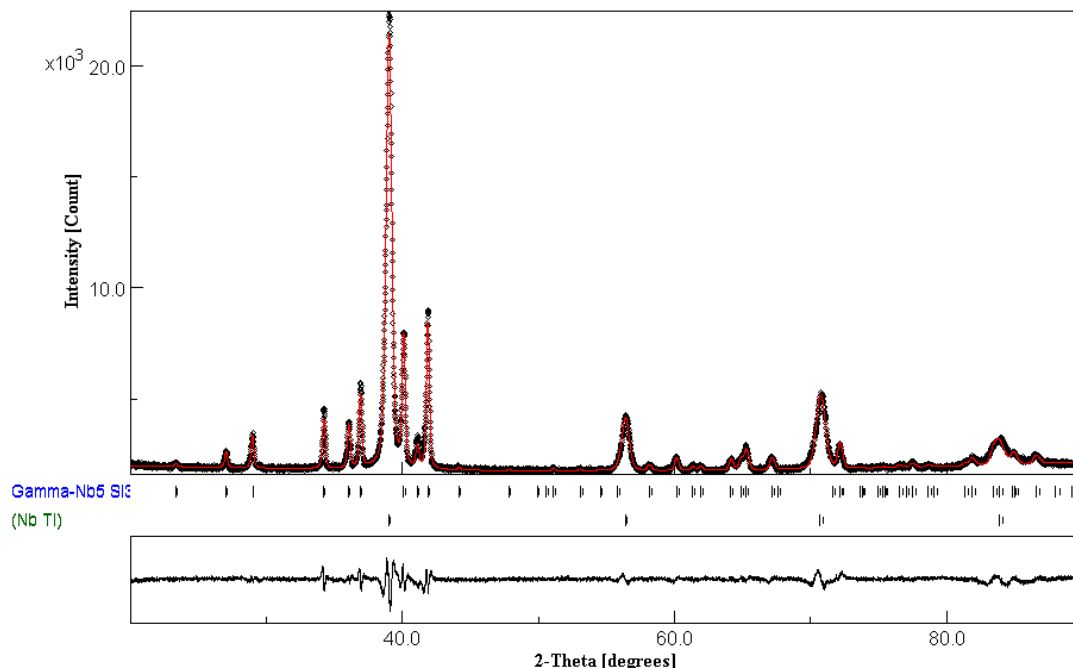
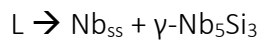
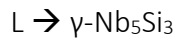


Figure 76: X-ray diffractograms of as-formed Nb-18Si-24Ti-5Cr-5Al-2Mo-5Zr-0.4Y

Based on the information above, the suggested sequence of formation is given:



The shape of the phases in the microstructure and their plot on the ternary diagram suggest that $\gamma\text{-Nb}_5\text{Si}_3$ is the primary phase, forming a lathlike microstructure followed by the invariant $L \rightarrow \text{Nb}_{\text{ss}} + \gamma\text{-Nb}_5\text{Si}_3$ eutectic. Unlike 2Mo, the final $\gamma\text{-Nb}_5\text{Si}_3$ formed with similar concentration of Ti.

The BEI of Nb-18Si-24Ti-5Cr-5Al-2Mo-5Zr-0.4Y can be seen in **Figure 77**. Little consolidation has occurred in the post-HIP sample; the dark Nb_{ss} present in the as-formed sample is still observed after HIP treatment. The $\text{Nb}_{\text{ss}}/\text{Nb}_5\text{Si}_3$ eutectic which is detected in **Figure 77 a)** is also still present, suggesting temperature and pressures were not high enough to initiate diffusion, or the phase presented is stable in the P6₃/mcm formation. As phase transformations have been observed in previous works it is unlikely that the addition of Zr would suppress this.

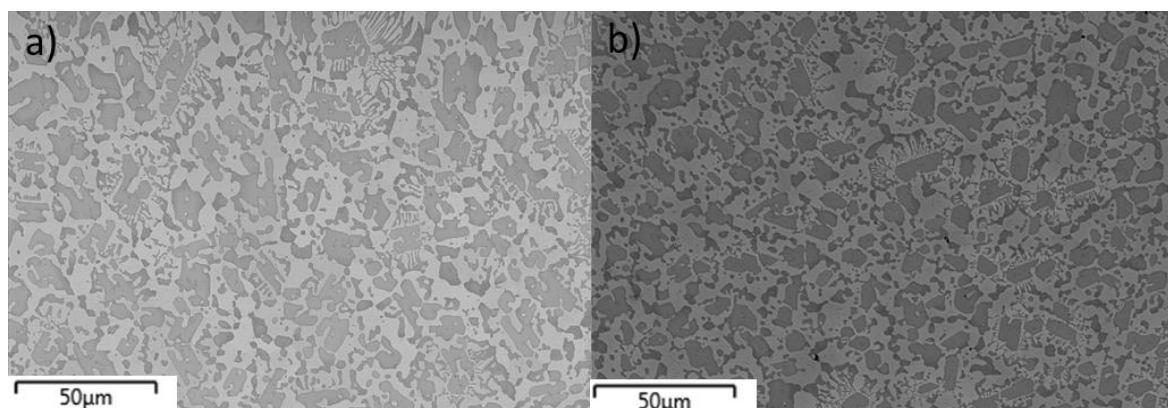


Figure 77: BEI of Nb-18Si-24Ti-5Cr-5Al-2Mo-5Zr-0.4Y at a) As-formed and b) Post-HIP stages. Images taken at centre of scan sample.

The diffractogram of Nb-18Si-24Ti-5Cr-5Al-2Mo-5Zr-0.4Y post-HIP in **Figure 78** shows no phase transformation. The volume fraction of $\gamma\text{-Nb}_5\text{Si}_3$ is increased to 50% which coincides with the BEI images.

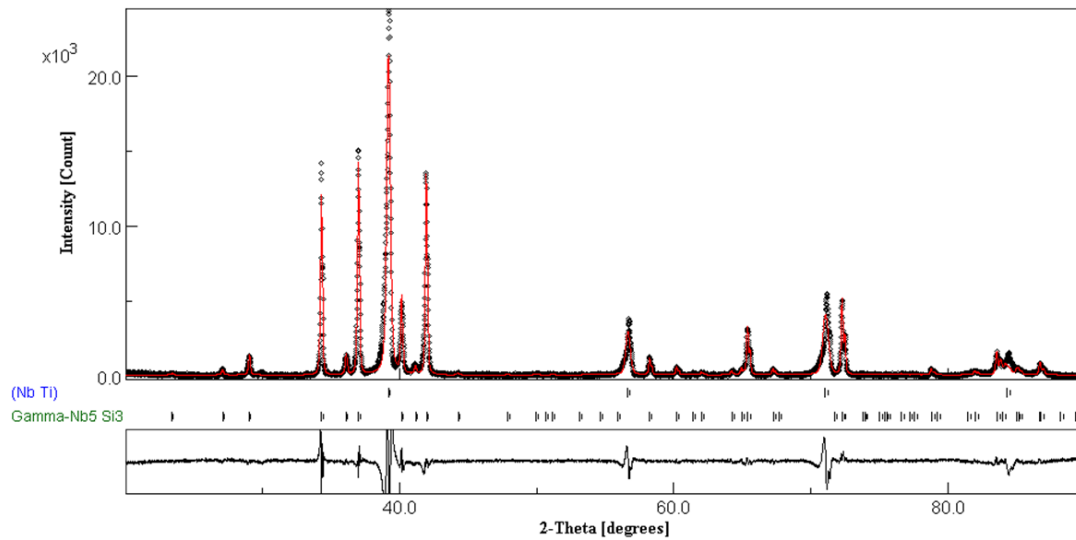


Figure 78: X-ray diffractograms of Nb-18Si-24Ti-5Cr-5Al-2Mo-5Zr-0.4Y at a) Post-HIP diffractogram modelled using MAUD

The change in volume fraction in the post-HIP sample may be due to difficulties fitting the models. Diffraction peaks shifted during HIP which is seen in **Figure 80**. These shifts are representative of physical changes within the sample, for example a shift of 2θ would represent sample misalignment and is not observed. What is observed, however, is non-uniform peak heights changes at different 2θ , which is indicative of an orientation change. It was understood that there may be orientation preference when the sample was manufactured, during post-processing it appears that $\gamma\text{-Nb}_5\text{Si}_3$ re-orientated. This may explain the slight contrast difference in the silicide phases observed in **Figure 73**. The equipment used was unable to perform full texture analysis, so an in-depth study was not performed.

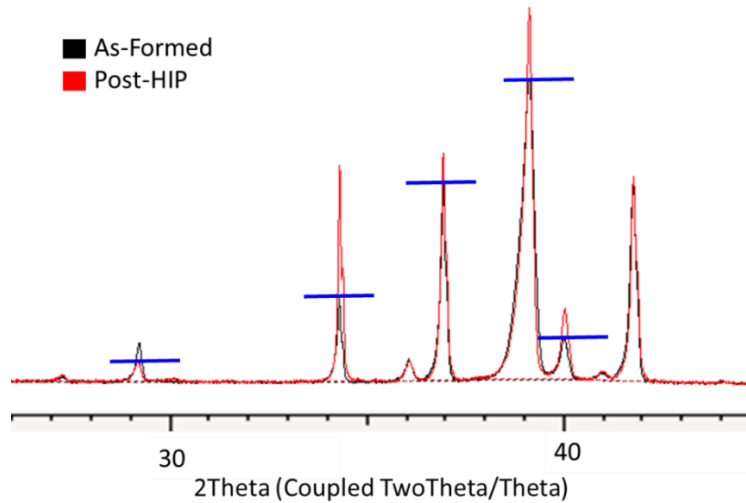


Figure 79: Combined X-ray diffractograms of Nb-18Si-24Ti-5Cr-5Al-2Mo-5Zr-0.4Y at Blue) Post-HIP Black) As-formed. Heights of as-formed peak are indicated in red

Examination of **Figure 79** suggests the material was not under thermodynamic equilibrium. The high temperature and pressure environment have caused the two phases in the as-formed sample to each undergo diffusion, typically between Nb and Ti. Minor elements like Al and Cr undergo diffusion, Cr diffuses from the silicide towards the solid solution, Al appears to reduce in both cases but is likely due to small sections of inhomogeneity within the solid solution.

Table 28: EDS data for Nb-18Si-24Ti-5Cr-5Al-2Mo-5Zr-0.4Y for both as formed and HIP showing distribution of elements

		Nb	Si	Ti	Al	Cr	Mo	Zr	Volume Fraction (%)	GOF
Nb _{ss}	AF	58.98	1.86	20.95	7.85	6.52	2.64	0.81	75.9	2.042
	HIP	52.02	1.99	26.88	5.51	9.41	2.53	1.52	52.2	3.32
γ -Nb ₅ Si ₃	AF	36.61	32.79	17.31	3.69	1.00	0.08	8.40	24.1	2.042
	HIP	36.36	33.12	19.82	2.41	0.62	0.00	7.67	47.8	3.32

No crystallographic transformation is noted in the modelled XRD diffractogram seen previously in **Figure 47**, although quantitative analysis of both diffractograms using MAUD suggests the quantity of each phase has changed from Nb_{ss} = 76% in AF to Nb_{ss} = 52% in the post-HIP sample (γ -Nb₅Si₃ fills in the remaining). This may be explained by the goodness of fit value = 3.32. The GOF will be affected by peak broadening and discussed texture of samples, preventing the pattern from being modelled correctly. As a solid solution, the peaks of Nb_{ss} may become

broader than expected due to saturation of unexpected elements. The GOF for the as-formed sample is also very low. Considering the noted problems in calibration, it is possible that the GOF is artificially lowered due to a high background noise, so it should be considered. As atom sites were not modelled in this diffractogram it is difficult to determine its effects on the results. Future work may be able to establish a more successful modelling route.

The 5 h heat-treated microstructure of Nb-18Si-24Ti-5Cr-5Al-2Mo-5Zr-0.4Y in **Figure 80** shows coarsening in the eutectic which now appears globular, further enhancement of H-shaped primary silicide is highlighted below.

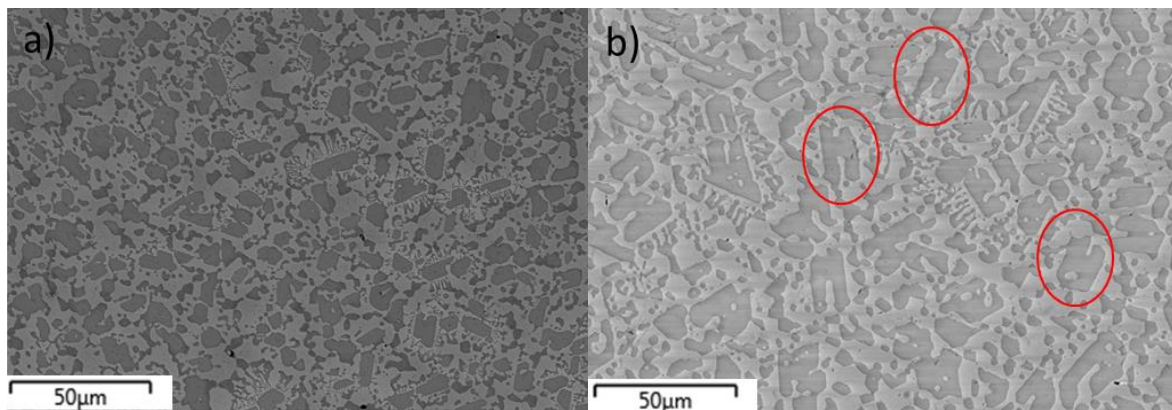


Figure 80: BEI of Nb-18Si-24Ti-5Cr-5Al-2Mo-5Zr-0.4Y at a) Post-HIP and b) Post-HT stage. Images taken at centre of scan sample.

Again the diffractogram of Nb-18Si-24Ti-5Cr-5Al-2Mo-5Zr-0.4Y post-HT seen in **Figure 81** shows no significant changes. γ -Nb₅Si₃ peak heights are smaller after heat treatment, this change is proportional and not a sign of the orientation change observed in HIPping.

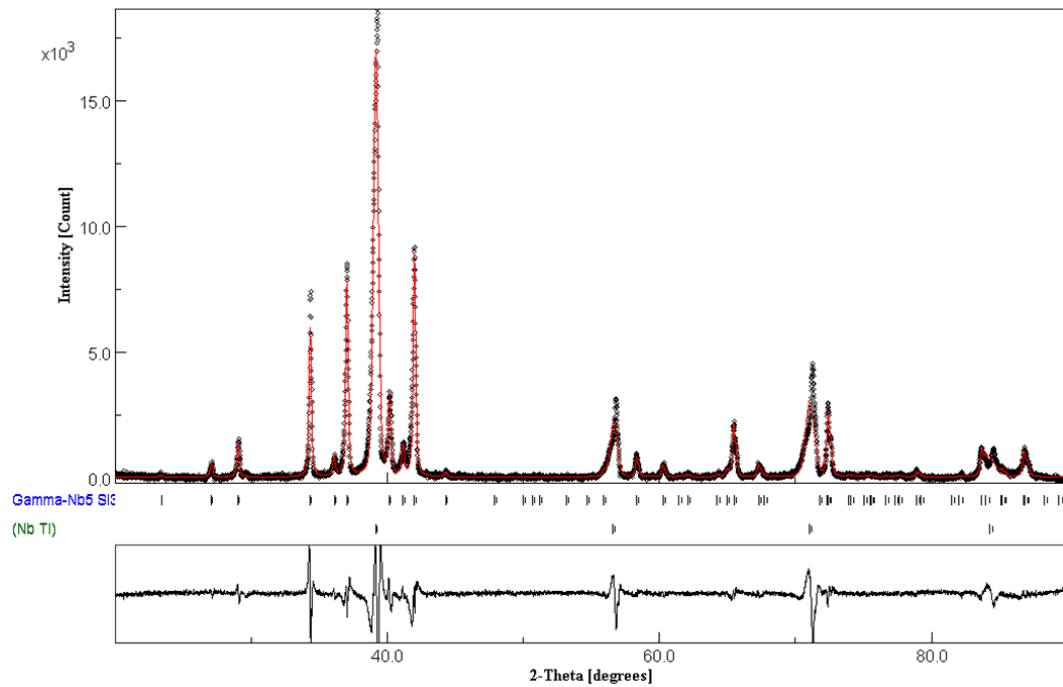


Figure 81: X-ray diffractograms of post-HT Nb-18Si-24Ti-5Cr-5Al-2Mo-5Zr-0.4Y

As with the post-HIP diffractogram, the GOF is relatively high at 3.90 seen in Table 29. The volume fraction calculated is similar to post-HIP samples. There should be consideration of the high GOF as the high value reduces accuracy of the calculated volume fraction.

Table 29: EDS data for Nb-18Si-24Ti-5Cr-5Al-2Mo-5Zr-0.4Y for both HIP and HT stages, showing distribution of elements and modelled volume fraction

		Nb	Si	Ti	Al	Cr	Mo	Zr	Volume Fraction (%)	GOF
Nbss	HIP	52.02	1.99	26.88	5.51	9.41	2.53	1.52	52.2	3.32
	HT	54.17	2.71	24.20	5.87	8.48	3.21	0.94	51.7	3.90
γ -Nb ₅ Si ₃	HIP	36.36	33.12	19.82	2.41	0.62	0.00	7.67	47.8	3.32
	HT	36.53	24.93	24.46	3.39	2.84	1.53	6.83	48.3	3.90

Slight changes in the composition are noted with Zr decrease in the solid solution and γ -Nb₅Si₃ being most notable, observed in Table 29, this can be seen graphically in Figure 82.

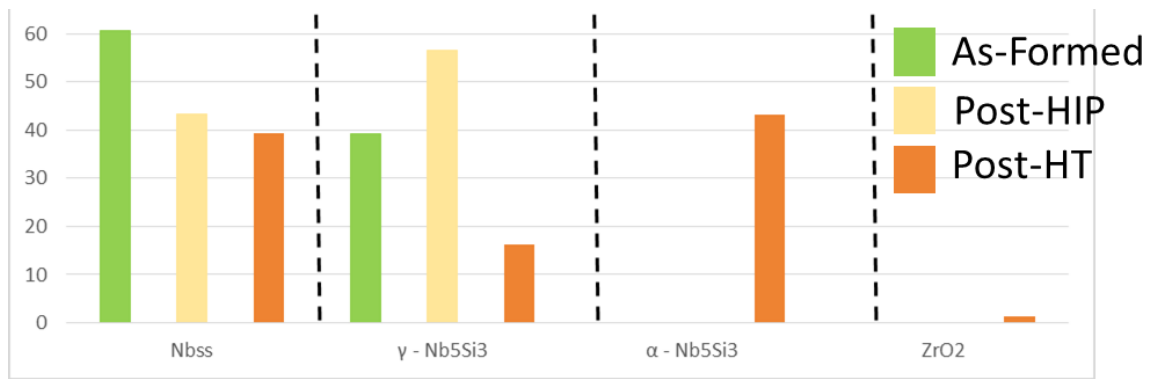


Figure 82: Comparison graph of CoZr5 at each stage of production

Increased Ti is observed in the silicide phase, likely replacing expelled Zr from the solid solution due to its increased mobility. Thus the decreased Zr is then localised epitaxially to the silicide's as seen in Figure 83.

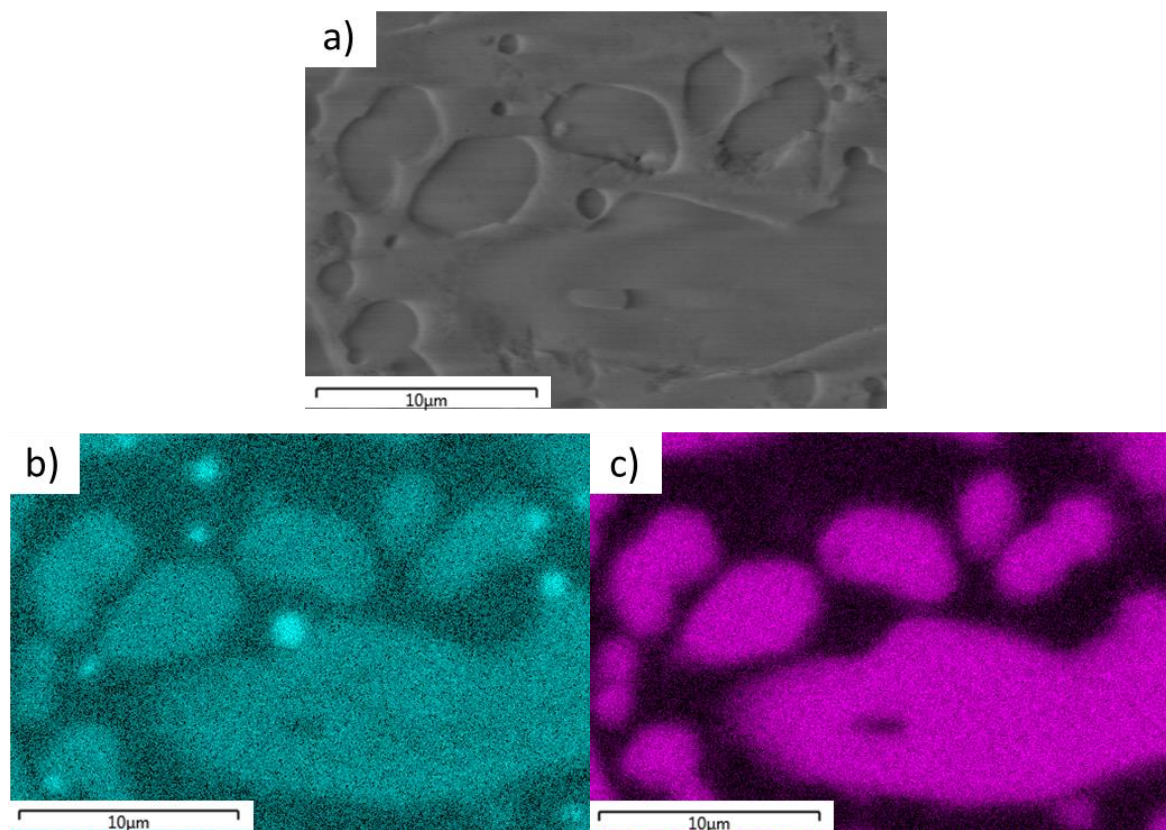


Figure 83: BEI and EDS map of Nb-18Si-24Ti-5Cr-5Al-2Mo-5Zr-0.4Y showing a) High magnification, b) Zr map and c) Si map. Images taken at centre of scan sample.

6.3 Nb-18Si-24Ti-5Cr-5Al-2Mo-1Zr-0.08Y (CoZy1)

Figure 84 a) shows that the reduction in zirconium produces a larger silicide microstructure than seen in CoZy5 but smaller than in 2Mo. The lighter phase is nominally named Nb_{ss}, multiple darker phases are denoted as silicide's in the as-formed phase. It may be noted in **Figure 84 b)** the darkest is seen in multiple areas, both adjacent to the Nb₅Si₃ as well as in the centre of Nb_{ss} formations, suggesting they formed separately.

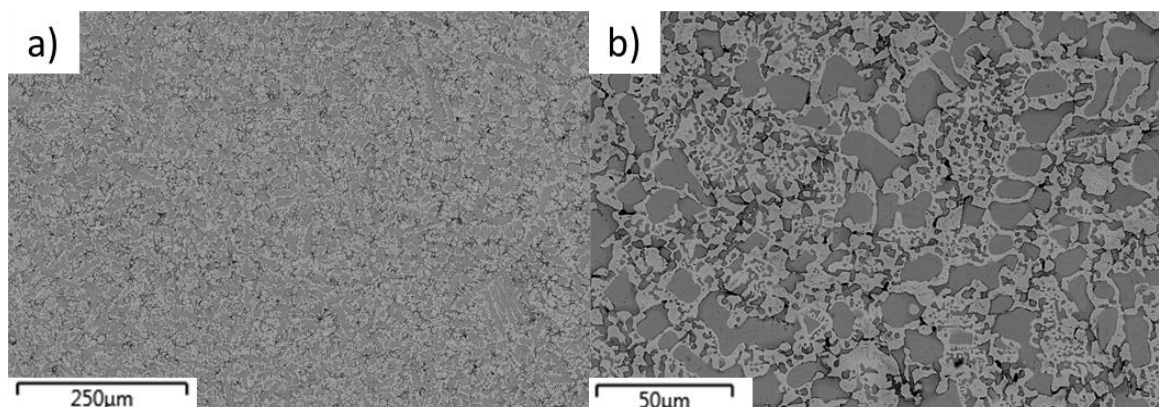


Figure 84: BEI of Nb-18Si-24Ti-5Cr-5Al-2Mo-1Zr-0.08Y as-formed at a) Low and b) High magnification. Images taken at centre of scan sample.

The EDS maps in **Figure 85** show element distributions in the as-formed sample; **a)** and **b)** show Si and Ti concentrations and the combination in **c)** highlights three phases. Dark green shows the high concentrations of Ti in Nb_{ss}, the dark purple shows low Ti silicide, from image analysis and XRD comparison. The levels of Nb, Si and Ti with within the range observed in 2Mo and CoZy5. Further discussion will occur on this trend in **section 6.4**.

It is suggested from the EDS maps in **Figure 85** that Ti is ejected during initial silicide formation with high-Ti Nb₅Si₃ often being found encapsulated by Nb_{ss}, volume fraction distribution of each phase can be found in **Table 30** and elemental analysis in **Table 31**.

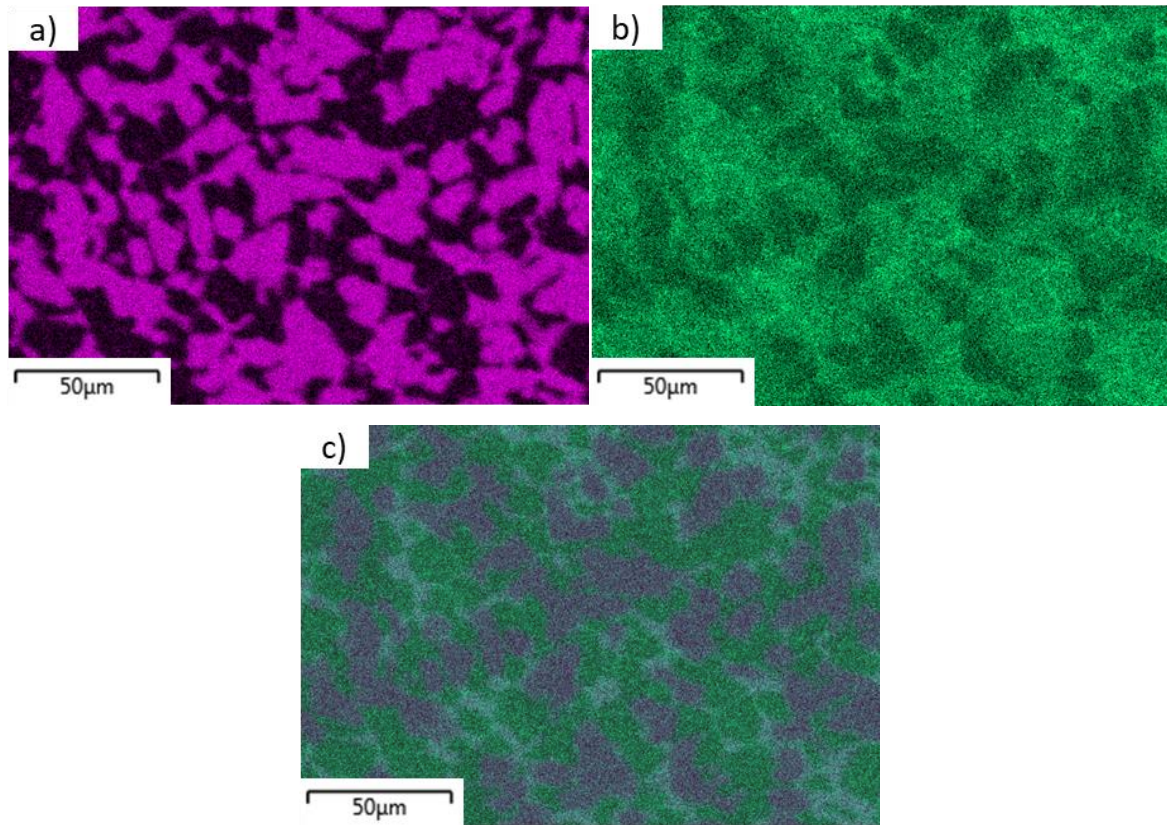


Figure 85: EDS map of Nb-18Si-24Ti-5Cr-5Al-2Mo-1Zr-0.08Y a) Si b) Ti c) Si, Ti combined

The modelled diffractogram seen below in **Figure 86**, suggests the presence of four phases; Nb_{ss} as well as all crystal structures of Nb₅Si₃, β, α and γ. Quantitative analysis shows β-Nb₅Si₃ to be present in the highest volume fraction with the full list seen in **Table 30**.

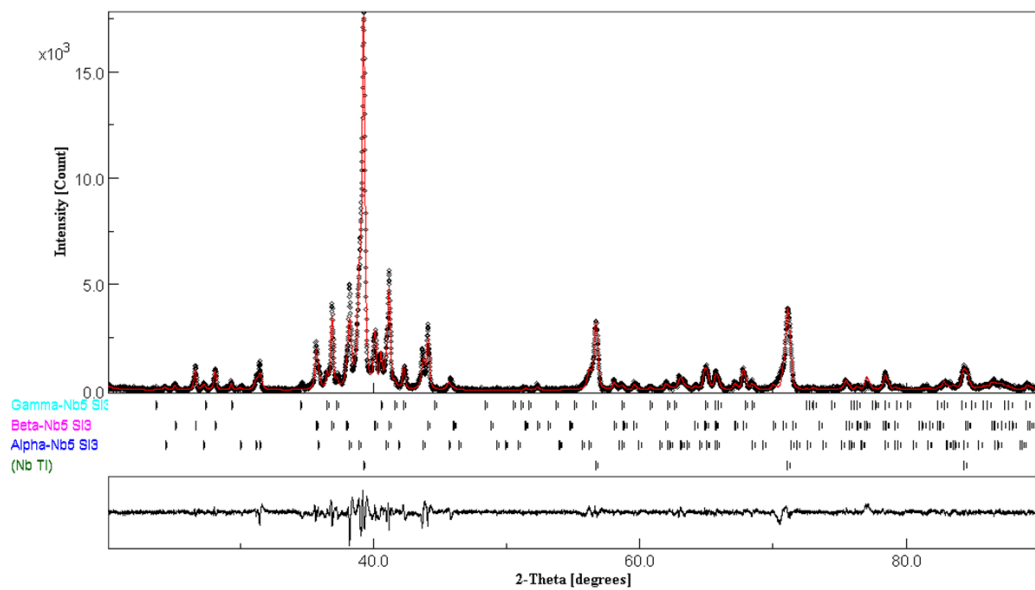


Figure 86: X-ray diffractograms of Nb-18Si-24Ti-5Cr-5Al-2Mo-1Zr-0.08Y as-formed, modelled using MAUD

Table 30: Volume Fraction distribution of CoZy1 as-formed

Phase	Volume Fraction (%)
Nb _{ss}	26.40
α-Nb ₅ Si ₃	30.38
β-Nb ₅ Si ₃	35.77
γ-Nb ₅ Si ₃	7.45

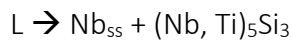
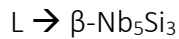
The position of (1,1,0) peak of Nb_{ss} in CoZy1 is shifted to a higher 2θ. This coincides with less Zr within the solid solution compared to CoZy5, fitting with the observed changes by Sankar et al (2018).^[144] γ-Nb₅Si₃ was noted in small quantities but was not observable in the BEI images, for this reason no elemental composition is noted in **Table 31**. A combination of EDS and EBSD could have been implemented to identify the different phases but was not performed due to time restraints. For this reason, phases are simply referred to as β-Nb₅Si₃ or (Nb, Ti)₅Si₃ to represent high concentrations of Ti. It is surmised that β-Nb₅Si₃ has the lowest Si content based on comparison of XRD and EDS data and its high temperature stability.

Table 31: Showing element distribution in phases of as-formed Nb-18Si-24Ti-5Cr-5Al-2Mo-1Zr-0.08Y, all values in at.% unless otherwise stated

	Nb	Si	Ti	Al	Cr	Mo	Zr	Y
(Nb, Ti) _{ss}	53.36	1.11	27.2	5.95	8.36	3.44	0.19	0.38
(Nb, Ti) ₅ Si ₃	32.93	29.99	29.19	3.06	1.89	0.68	2.16	0.10
β-Nb ₅ Si ₃	46.17	31.88	15.94	3.19	0.95	1.14	0.41	0.32

From **Table 31** the inhomogeneity of CoZy1 can be observed, similar to 2Mo, with Ti being mostly rejected from the primary silicide and present mostly in Nb_{ss} as well as the secondary silicide.

From the data provided a solidification route can be suggested:



During solidification, Ti is ejected into the melt as seen in **Figure 65**. The next stage observes Nb_{ss} formation with Si ejected to the melt front. When the Si concentration reaches a critical point further silicide formation begins, this time with a higher concentration of Ti. This is most likely a combination of $\gamma-Nb_5Si_3$ and $\alpha-Nb_5Si_3$, promoted by the high Ti and rapid solidification respectively. The formation of $\alpha-Nb_5Si_3$ in an as-formed sample is rare, the decomposition from Nb_3Si in the binary Nb-Si alloy is slow, requiring long heat treatments. It is suggested that the addition of Zr in substitution of Nb destabilises the Nb_3Si phase resulting in a rapid transformation into $\alpha-Nb_5Si_3$.^[144] This is contrary to the work of Yanqiang Qiao (2017) who has shown that addition of Zr breaks down Nb_3Si observed in common Nb-Si binary alloys, forming only the $Nb_{ss}/\gamma-Nb_5Si_3$ binary as a result. At low Zr concentrations $\gamma-Nb_5Si_3$ was formed, while at higher concentrations $\alpha-Nb_5Si_3$ was observed. This leads to the paper's conclusion that high quantities of Zr stabilise $\alpha-Nb_5Si_3$ formation. Alloy design has been discussed by Tsakiroopoulos (2018), wherein $\gamma-Nb_5Si_3$ promotion is discussed. The closer Nb:Ti+Hf is to 1 the increase in likely $\gamma-Nb_5Si_3$ formation. As Zr is another potential $\gamma-Nb_5Si_3$ stabiliser it is important to consider this element as well. The small quantities of γ -silicide noted may be due to microsegregation of Ti. During solidification Ti is ejected into the melt pool, this high Ti may result in a ratio of Nb/(Ti+Zr) reaching close to 1 and result in the small quantity noted. It was not noted in the BEI but is likely found on the boundary of $\alpha-Nb_5Si_3$. This would likely be difficult to distinguish without EBSD or TEM.

The post-HIP microstructure in **Figure 87** shows a small amount of coarsening throughout, with islands of silicide within the Nb_{ss} . Comparing **a)** and **b)** still shows three phases, the smaller dark silicide phases previously found on the edges of $\alpha-Nb_5Si_3$ are no longer observed and the previous eutectic has coarsened into one phase (indicated with an arrow).

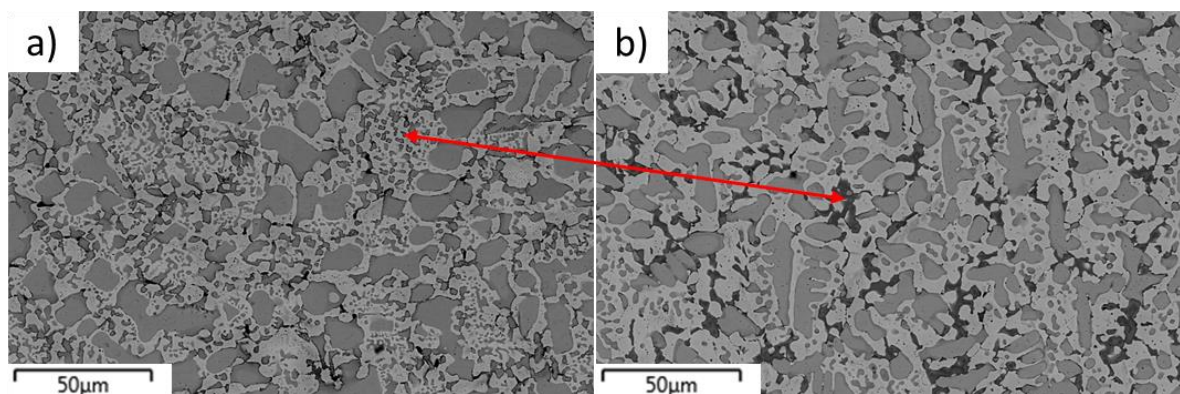


Figure 87: BEI of Nb-18Si-24Ti-5Cr-5Al-2Mo-1Zr-0.08Y as-formed at a) As-formed and b) Post-HIP. Images taken at centre of scan sample.

Coarsening is more easily viewed in **Figure 88** where Ti and Si both show up different phases similar to **Figure 85 c)**. Along with general coarsening, Ti has also been noted to homogenise during hot isostatic pressing, with more Ti being absorbed into both silicides. Silicon content appears lower in β -Nb₅Si₃, this may be due to the energy and pressure from HIP forcing a grain boundary diffusion mechanism such as vacancy diffusion. This was observed in **8** although it is difficult to fully determine from the data collected.

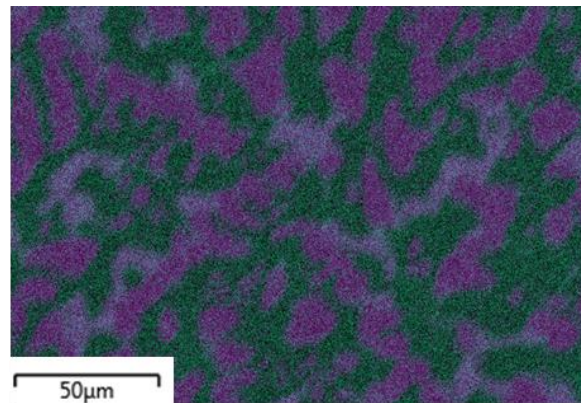


Figure 88: EDS map of Nb-18Si-24Ti-5Cr-5Al-2Mo-1Zr-0.08Y post-HIP Purple) Si, Green) Ti

Collected EDS samples seen in **Table 32** show a stable amount of Si in Nb_{ss} and β -Nb₅Si₃, but highlights the much-reduced amount in (Nb, Ti)₅Si₃. An increase in Cr and Al into the β -silicide suggests that rather than a vacancy diffusion, an exchange of smaller elements may occur.

Table 32: Showing element distribution in phases of post-HIP Nb-18Si-24Ti-5Cr-5Al-2Mo-5Zr-0.4Y, all values in at.% unless otherwise stated

	Nb	Si	Ti	Al	Cr	Mo	Zr	Y
(Nb, Ti) _{ss}	51.48	1.88	28.66	6.05	8.30	2.90	0.51	0.23
β -Nb ₅ Si ₃	43.70	32.19	17.80	3.19	1.11	1.05	0.60	0.37
(Nb, Ti) ₅ Si ₃	37.32	21.37	30.08	3.99	4.00	1.36	1.63	0.26

The microstructure and elemental distributions observed in **Figure 87** and **Table 32** should not be considered in isolation. Quantitative analysis of the diffractogram in **Figure 89** shows a large shift in phase composition, showing that HIP had effects other than phase diffusion.

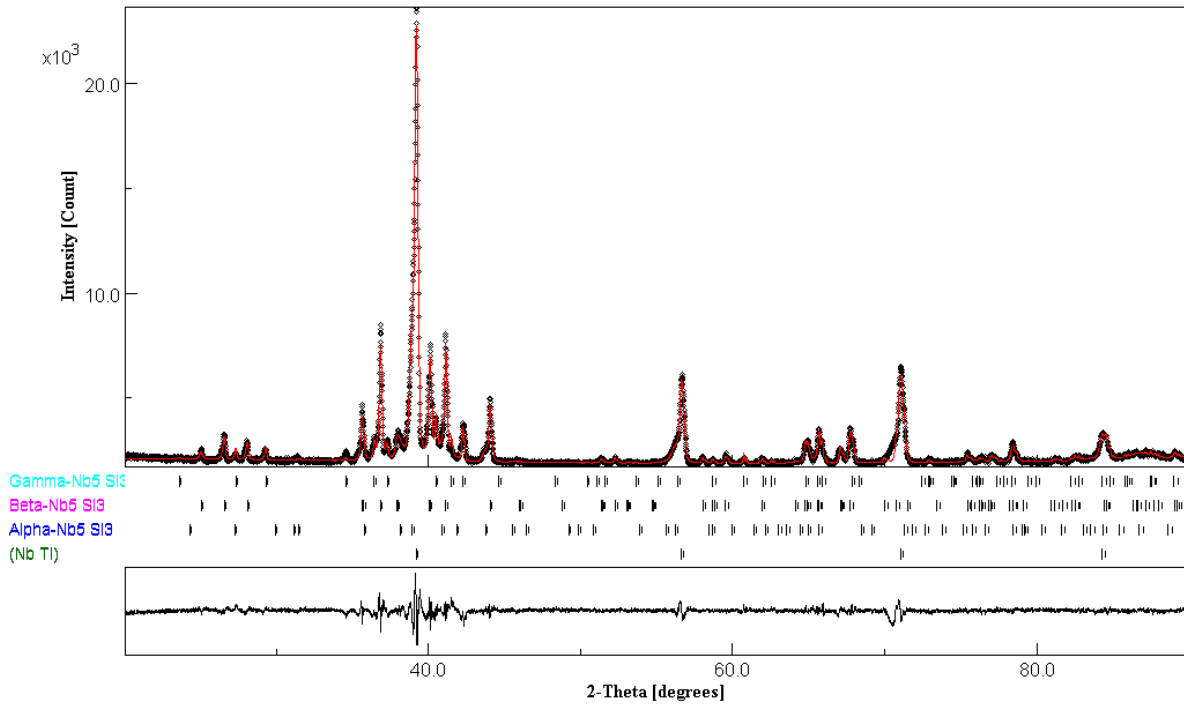


Figure 89: X-ray diffractograms of Nb-18Si-24Ti-5Cr-5Al-2Mo-1Zr-0.08Y post-HIP, modelled using MAUD

All phases are present in the post-HIP sample, volume analysis in **Table 33** shows all phases still present with a slight decrease in β -Nb₅Si₃ with an increase noted for α -Nb₅Si₃ and Nb_{SS}.

Table 33: Volume % distribution of phases in as-formed CoZy1

Phase	Volume % - AF	Volume % - HIP
Nb _{SS}	26.41	29.41
α -Nb ₅ Si ₃	30.38	34.87
β -Nb ₅ Si ₃	35.77	28.36
γ -Nb ₅ Si ₃	7.42	7.56

This is unexpected as γ -Nb₅Si₃ is considered metastable and should disappear during post-processing it increases marginally. As noted in the CoZy5 alloy in **section 6.2**, the increase of Zr resulted in γ -Nb₅Si₃ being stabilised at all stages, with HIP presenting with a binary Nb_{SS}/ γ -Nb₅Si₃ microstructure. The quantity of Zr in each phase is similar in as-formed and post-HIP samples in all phases but is higher in the secondary silicide (assumed α -Nb₅Si₃ and γ -Nb₅Si₃). Ti, similarly to Zr and Hf, is noted to play a role in producing metastable γ -Nb₅Si₃, in high concentrations it can cause conventional casting melts to stabilise the hexagonal-silicide to room temperature.^[44, 123, 151]

Similar to the allotropic forms of ice or carbon, the use of high pressure in HIP provided enough energy to allow the crystal structure of high-Ti β -Nb₅Si₃ to become strained and re-arrange into

α -Nb₅Si₃ and Nb_{ss}, (Nb may be replaced by a transition metal such as Ti). The transition metal may be the cause of Ti_{ss}. A similar pattern occurs with Nb₃Si formation under varied pressures and temperatures.^[152] Modelling was also performed to establish if Nb₃Si or NbSi₂ was-formed, neither fit the diffractogram. Without in-situ XRD analysis or further HIP experiments performed at different parameters it is difficult to provide certainty. Note this transformation was minimal, noting a 4% increase in α -Nb₅Si₃.

The BEI of post-HT samples in **Figure 90 b)** present a much greater contrast than the previous post-HIP stage **a)**.

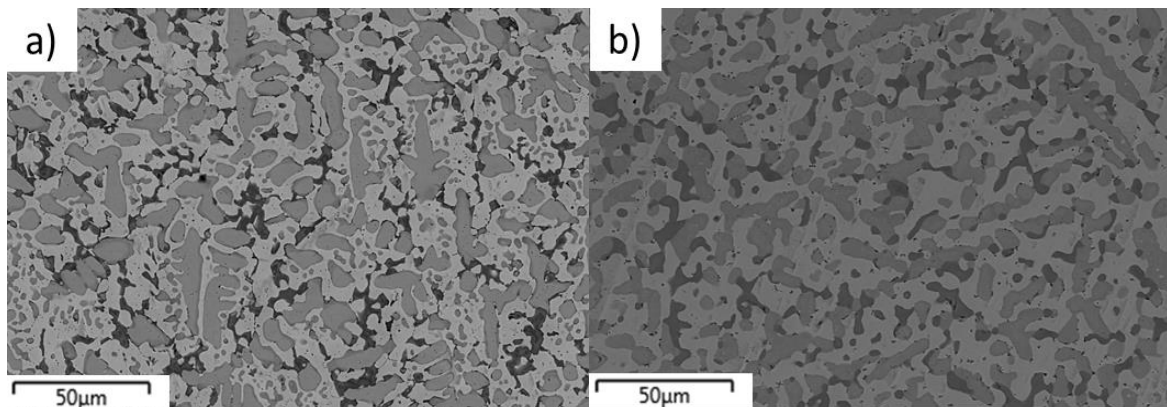


Figure 90: BEI of Nb-18Si-24Ti-5Cr-5Al-2Mo-1Zr-0.08Y post-HT at a) post-HIP and b) post-HT. Images taken at centre of scan sample.

Further coarsening has occurred in the Nb_{ss} with a globular silicide presented throughout. As with previous processing steps, two silicide phases may be observed with different contrasts. There appears to be no pattern to their arrangement with light silicide's being found encapsulated within the darker silicide as well as adjacent to one another.

The diffractogram in **Figure 91** presents three phases, with a disappearance of β -Nb₅Si₃. The smaller fourth phase noted above was likely too small to be within detection limits of the XRD.

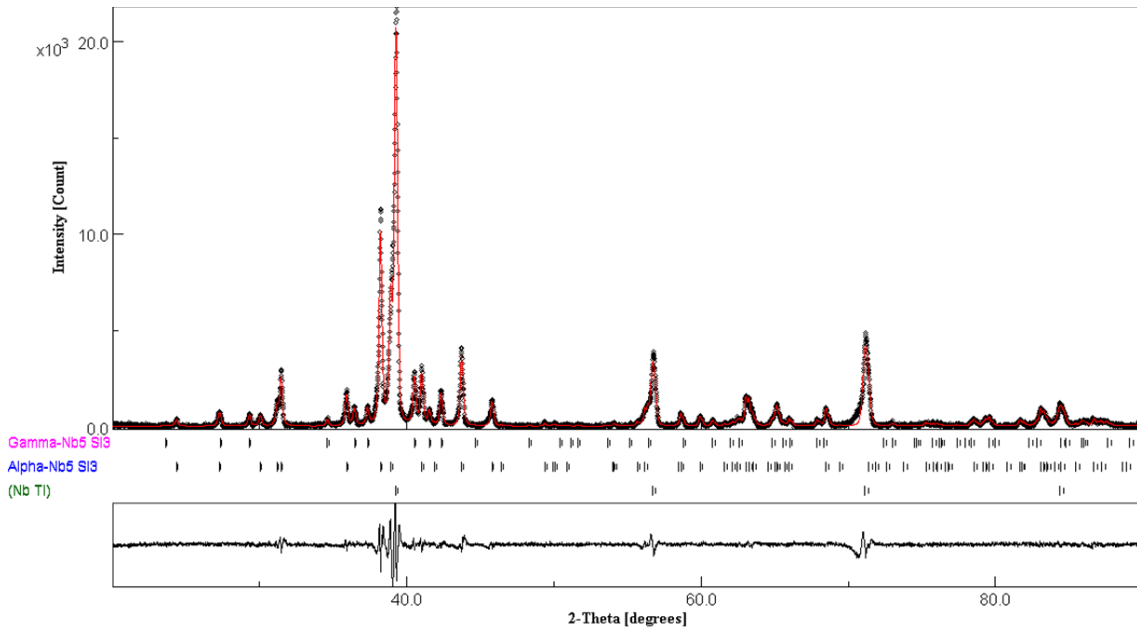


Figure 91: X-ray diffractograms of Nb-18Si-24Ti-5Cr-5Al-2Mo-1Zr-0.08Y post-HT, modelled using MAUD

Quantitative analysis of the modelled diffractogram may be seen in **Table 34** and shows an absence in β -Nb₅Si₃ as well as an increase in α -Nb₅Si₃, a graphical version of this may be seen in **Figure 92**.

Table 34: Volume % distribution of phases in CoZy1 at different stages of development

Phase	Volume Fraction (%)		
	AF	HIP	HT
Nb _{ss}	26.41	36.94	44.73
α -Nb ₅ Si ₃	30.38	16.89	45.65
β -Nb ₅ Si ₃	35.77	36.09	--
γ -Nb ₅ Si ₃	7.42	10.09	9.62

The heat treatment at 1500°C resulted in a large volumetric change in the tetragonal silicide's, presenting with the expected transformation seen in **section 5.2** with β -Nb₅Si₃ re-arranging to α -Nb₅Si₃. The change in γ and Nb_{ss} are small and likely due to the GOF of the diffractogram and the limitations of the previously discussed XRD calibration. The diffractogram was also modelled with NbSi₂ to determine if the eutectoid transformation β -Nb₅Si₃ \rightarrow α -Nb₅Si₃ + NbSi₂ occurred. The results were insignificant, either a breakdown of NbSi₂ had occurred or the pathway was different.

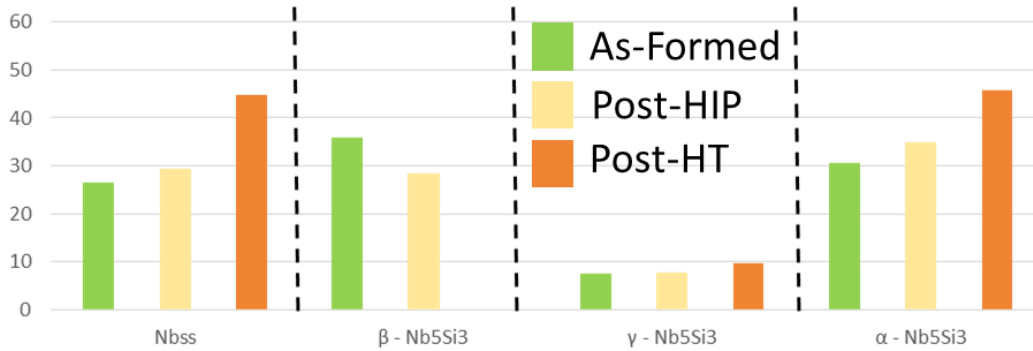


Figure 92: Comparison graph of CoZy1 at each stage of production

Small quantities of concentrated Ti can be observed on the edges of silicide samples in **Figure 93**. As the chemistry is similar to 2Mo, it may be as a result of a similar ejection during heat treatment. Ti quantities are marginally lower in the transition from β -Nb₅Si₃ → α -Nb₅Si₃ so this may be the origin.

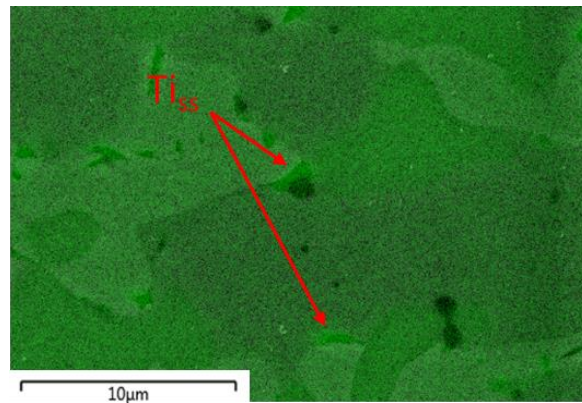


Figure 93: BEI of Nb-18Si-24Ti-5Cr-5Al-2Mo-1Zr-0.08Y post-HT with EDS map of Ti overlaid, highlighting areas of high Ti concentration.

Elemental distribution displayed in **Table 35** shows little change in the chemistry between the notable phases, relaxation through HT allows further segregation of Si out of the Nb_{ss} throughout the sample. A small phase may be noted in some areas of the sample presenting increased Zr concentration.

Table 35: Showing element distribution in phases of post-HT Nb-18Si-24Ti-5Cr-5Al-2Mo-1Zr-0.08Y, all values in at.% unless otherwise stated

	Nb	Si	Ti	Al	Cr	Mo	Zr	Y
(Nb, Ti) _{ss}	52.72	0.69	27.28	6.45	8.94	3.43	0.09	0.40
α -Nb ₅ Si ₃	45.35	33.48	16.83	1.93	0.51	0.81	0.63	0.45
γ -Nb ₅ Si ₃	32.11	32.21	28.51	3.08	1.40	0.48	2.12	0.10
(Nb, Ti, Zr) ₅ Si ₃	37.95	21.78	25.42	2.39	1.49	0.96	7.27	2.73

6.4 Evaluation of Elemental Additions

Work by Jie Geng (2006) and knowledge obtained in **5** was built upon with the addition of Zr and Y. Increases in Zr content inversely reduced the size of the primary silicide.

Work by M. Sankara (2018) suggested a stabilisation of α -Nb₅Si₃ with additions of 4 - 6 Zr at.%. This was not observed in this work, with high concentrations of Zr (5 at.%) presented with a binary Nb_{ss}/γ-Nb₅Si₃ alloy system.

At low concentration (1 at.%) α -Nb₅Si₃ was observed after heat treatment. Microsegregation of Ti also occurred similarly to the alloy in **5** resulting in stable γ-Nb₅Si₃ at all stages. Ti_{ss} was also observed in CoZr1 during post-processing, which was likely the result of microsegregation.

7 Effects of Ta Additions in 4th Generation Nb-Si Alloys

7.1 Chapter Introduction

Zr was discussed in the previous chapter regarding how it can improve the oxidation properties of the material and prevent the formation of Nb₃Si. A literature review of Zr additions in Nb-Si alloys suggest it can have a positive effect on the material's physical properties.^[153, 154]

The aim is to further improve this by adding small quantities of tantalum, it was previously noted that Ta provides a strengthening effects when combined with Zr <6 at.%.^[40, 139] Ta has also been shown to increase the Si concentration in Nb_{ss}, restricting the ejection of Si in the melt during solidification, contributing less to micro segregation. It has also been noted that Ta can decrease oxygen solubility in Nb₅Si₃.^[139]

High quantities of Ta may be detrimental to the β- to α-Nb₅Si₃ transition as it may restrict diffusion, de-accelerating the solid-state transformation and reducing homogenisation during heat treatment, for this reason small quantities of Ta will be used.^[31]

The following chapter will examine the addition of Ta to both CoZy1 and CoZy5 to observe the microstructural evolution. Back scattered electron images will be used to look at the microstructural changes throughout processing and X-ray diffraction will determine the phases present.

7.2 Nb-18Si-24Ti-5Cr-5Al-2Mo-5Zr-0.4Y-2Ta (TCoZy5)

The microstructure of Nb-18Si-24Ti-5Cr-5Al-2Mo-5Zr-0.4Y-2Ta (TCoZy5) seen in **Figure 94 a)** produces phases very similar to CoZy5. The primary silicide phases are larger than previous and contain a much higher quantity of eutectic. The high magnification images in **b)** reveal the 2 distinct phases. As before, the predominant lighter phase (likely Nb_{ss}) contains a mixture of two grey phases with the lightest grey phase appearing lathlike as noted in previous alloys. A eutectic can also be seen formed within the Nb_{ss}.

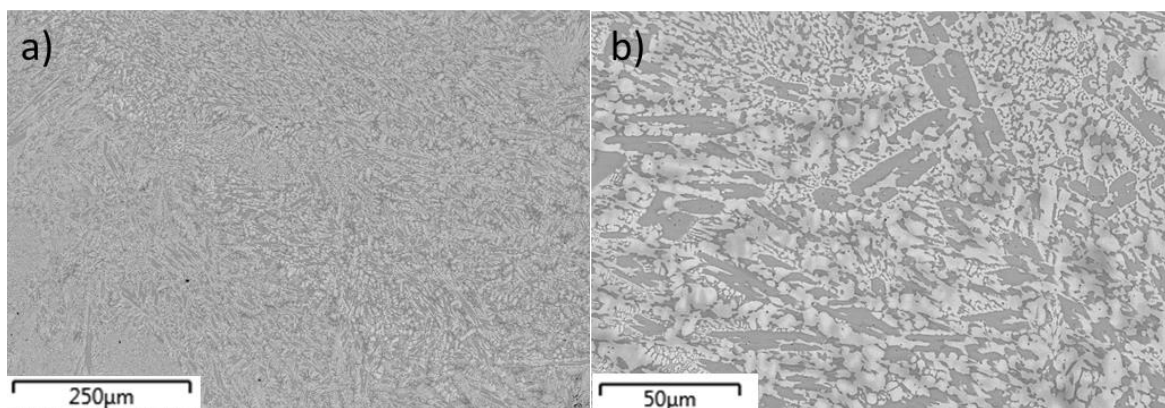


Figure 94: BEI image of Nb-18Si-24Ti-5Cr-5Al-2Mo-5Zr-0.4Y-2Ta as-formed at a) Low and b) High magnification

The added Ta has altered the microstructure, the quantity of eutectic has increased greatly and the large silicide's have reduced in quantity but increased in size. In CoZy5 the large silicides were identified as γ -Nb₅Si₃ surrounded by Nb_{ss} and a eutectic of the same phases

In CoZy1 and 2Mo the solidification path resulted in the ejection of Ti into the melt pool during solidification, resulting in saturated zones of Ti-rich Nb₅Si₃. This phenomenon is less pronounced in TCoZy5 and Si distribution is inhomogeneous, with segregation to the silicide phase. Si concentration is higher in the silicide phase than in 2Mo and CoZy5. With the inclusion of Ta, the Nb_{ss} matrix was expected to be larger allowing for a higher percentage of Si inclusions.

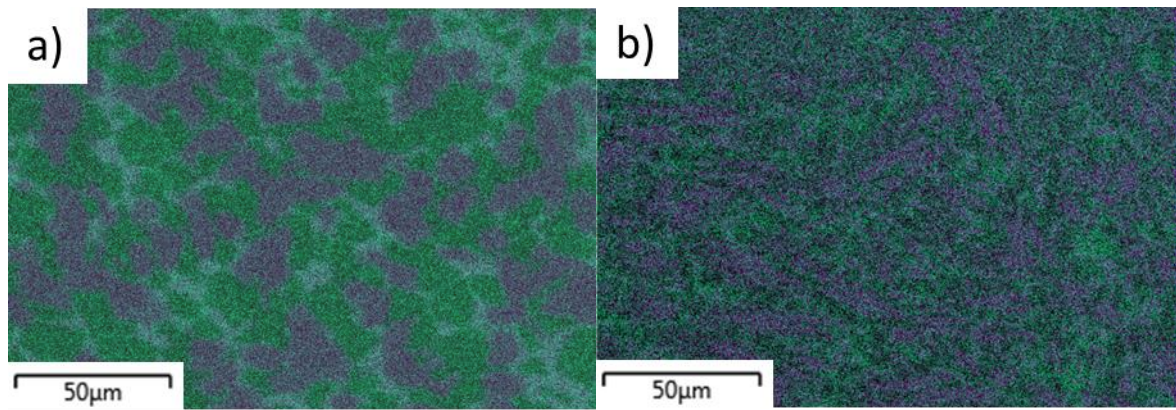


Figure 95: EDS map of Ti comparing a) CoZy1 and b) Nb-18Si-24Ti-5Cr-5Al-2Mo-5Zr-0.4Y-2Ta showing change on homogeneity of elements.

A detailed breakdown of phase distributions can be seen below in **Table 36**. Whilst initial inspection suggests a two-phase alloy. The element distribution below shows Y being localised to small sections of microstructure labelled as “(Nb,Zr,Y)₅Si₃” in the table below. The BEI of the phase can be observed in **Figure 96**.

Table 36: Showing element distribution in phases of as-formed Nb-18Si-24Ti-5Cr-5Al-2Mo-5Zr-0.4Y-2Ta, all values in at.% unless otherwise stated

	Nb	Si	Ti	Al	Cr	Mo	Zr	Y	Ta
(Nb, Ti) _{ss}	46.97	2.97	28.86	4.41	9.56	2.12	1.68	0.32	2.86
Nb ₅ Si ₃	33.26	34.23	19.3	2.52	0.58	--	8.37	--	1.73
(Nb, Zr, Y) ₅ Si ₃	33.59	20.76	18.91	2.23	1.97	--	10.4	10.74	1.39

This high concentration yttrium area could be explained by either:

- 1) A new phase brought about by localised Y during solidification
- 2) The same Nb₅Si₃ phase but with the high Y concentration replacing the other elements.

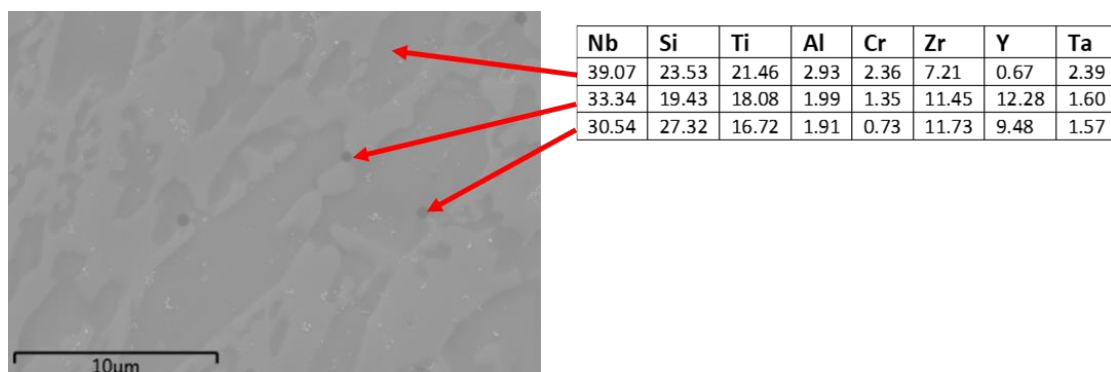


Figure 96: BEI image showing Y concentration in Nb-18Si-24Ti-5Cr-5Al-2Mo-5Zr-0.4Y-2Ta

The diffractogram in **Figure 97** models only two phases: Nb_{ss} and γ -Nb₅Si₃. With a GOF = 2.029542 this is a close approximation for the model, suggesting that yttrium concentrations in the silicide did not alter it to produce β - or α -Nb₅Si₃. It is noted that Y concentration increases the concentration of Zr in a phase, as can be seen when the two phases of high zirconium are compared. Note that Mo was removed from this table as it is present in negligible quantities in all cases (0 – 0.3%) and is not worthy of consideration.

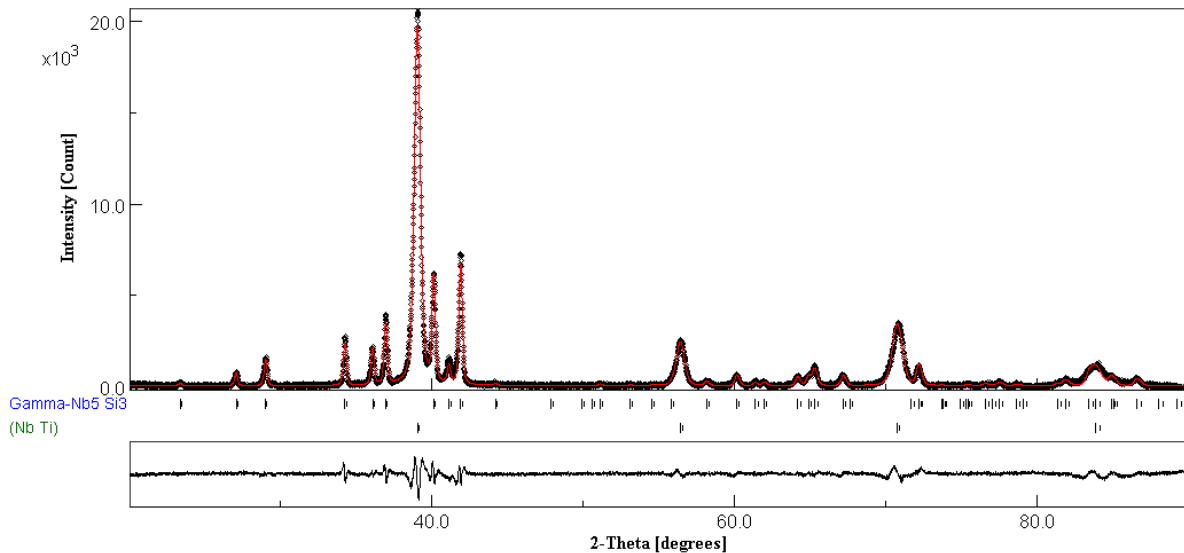
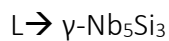


Figure 97 : X-ray diffractogram of as-formed Nb-18Si-24Ti-5Cr-5Al-2Mo-5Zr-0.4Y-2Ta

Using the information above, a suggestion for the thermodynamic route of formation can be created:



Initially the globular γ -Nb₅Si₃ is likely formed by ejecting Y from the melt, concentrated areas noted in **Figure 96** are all epitaxial, this acts as a nucleation point for the γ -silicide as the liquid melt reaches its eutectic point. Beyond this, flowers of γ -Nb₅Si₃ and Nb_{ss} are formed in the second stage until the melt is used up.

During hot isostatic pressing, consolidation of the TCoZy5 eutectic microstructure can be seen in **Figure 98**. The microstructure has different contrasting silicide's suggesting that the process has not reached equilibrium, with different levels of consolidation in the eutectic.

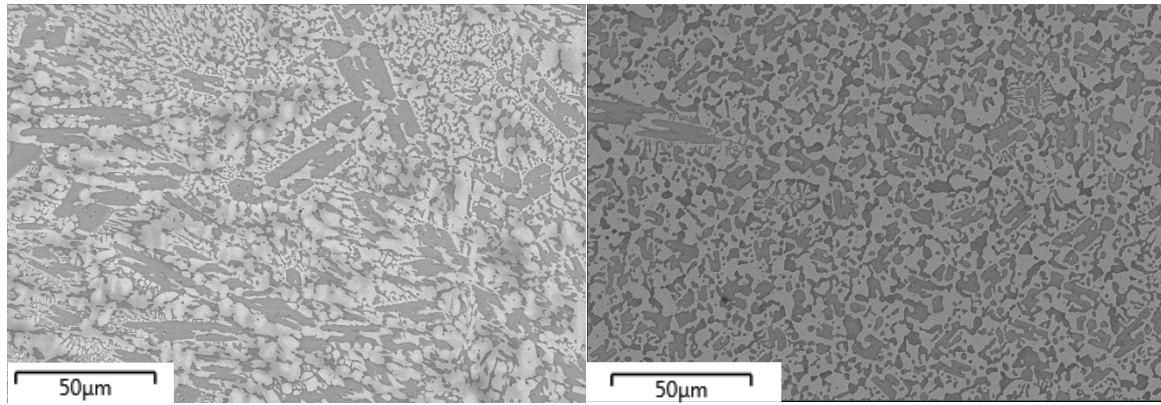


Figure 98: BEI images of Nb-18Si-24Ti-5Cr-5Al-2Mo-5Zr-0.4Y-2Ta at a) as-formed b) post-HIP both samples represent edge of piece

Table 37 shows a disparity between the two contrasting Nb_5Si_3 . The darker silicide appears with a higher Ti content and a slightly higher Zr increase. Ti has been noted to have a higher diffusion rate than Nb in the binary alloy system.^[155] The difference in diffusion rates may encourage a Kirkendall style effect, with Ti diffusing towards the silicide, would result from this change and leave an altered elemental change and Kirkendall porosity. The porosity is not seen however, which may be because temperatures were not high enough to initiate it. What is observed is an exchange of 8-9% of Nb and Ti, occurring between the boundaries of Nb_{ss} and $\gamma-Nb_5Si_3$. The increase in Ti within the silicide leads to an attraction of Zr from the solid solution matrix. This is due to their similar co-ordination numbers and the preference for Zr to be in $\gamma-Nb_5Si_3$'s HCP formation over the BCC formation of Nb_{ss} .

Table 37:EDS data for Nb-18Si-24Ti-5Cr-5Al-2Mo-5Zr-0.4Y for both AF and HIP showing distribution of elements

		Nb	Si	Ti	Al	Cr	Zr	Y	Ta
Nb_{ss}	AF	46.97	2.97	28.86	4.41	9.56	1.68	0.32	2.86
	HIP	52.16	2.35	24.99	5.24	8.17	0.85	0.41	3.29
Nb_5Si_3	AF	33.26	34.23	19.30	2.52	0.58	8.37	0	1.73
	HIP	33.05	33.34	20.22	2.65	0.73	8.03	0.40	1.60
$(Nb, Ti)_5Si_3$	HIP	24.67	31.61	28.37	3.14	0.96	10.47	0.06	0.72

The phases in the X-ray diffractogram in Figure 99 suggests that no phase change has occurred, although the ratio of phases supports the information provided by the BEI scans. An orientation change is noted however in $\gamma-Nb_5Si_3$, this is similar to the change in $CoZr_5$ where peaks change anisotropically.

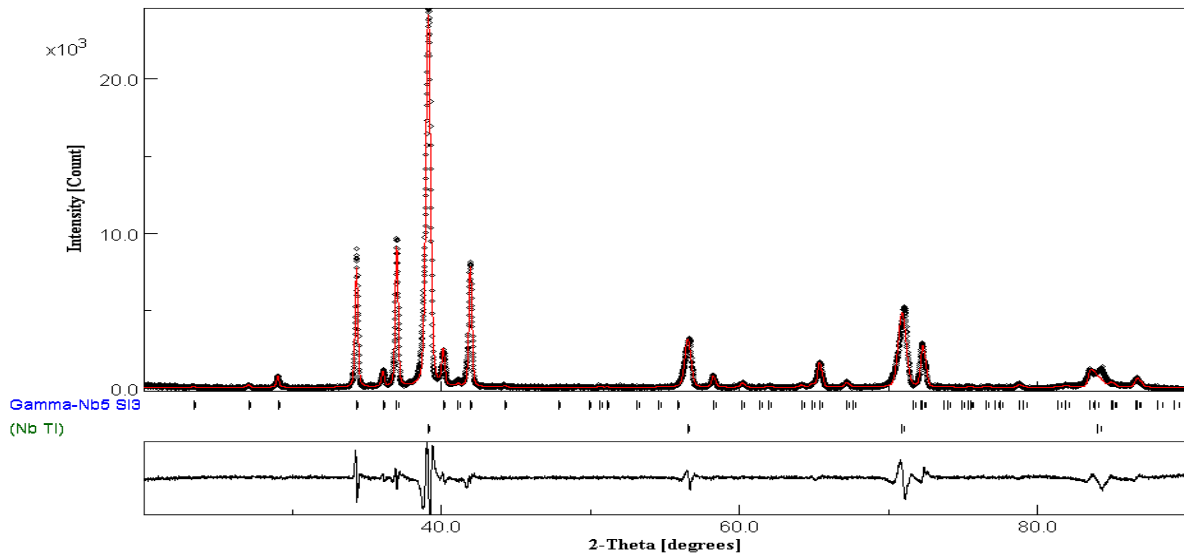


Figure 99 : X-ray diffractogram of post-HIP Nb-18Si-24Ti-5Cr-5Al-2Mo-5Zr-0.4Y-2Ta

The Y-concentrated silicide's would explain the broadening of the γ -Nb₅Si₃ peaks seen in Figure 99, these are not observed due to their low concentration. They can be observed in post-HIP BEI images in Figure 100 and they are commonly located on the phase boundary of most silicide's.

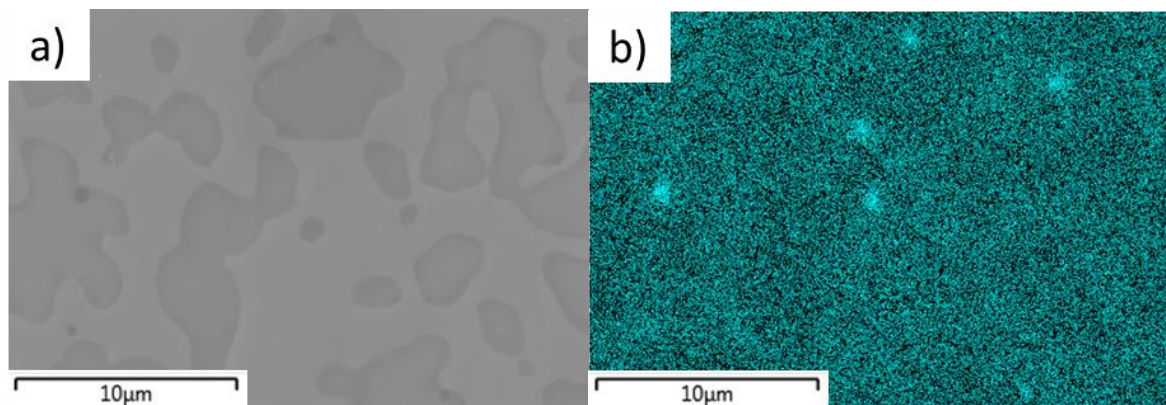


Figure 100: BEI images of Nb-18Si-24Ti-5Cr-5Al-2Mo-5Zr-0.4Y-2Ta at a) 16,000 magnification b) EDS map highlighting Y concentration of same area. Both samples represent edge of sample piece

EDS analysis shows little change in the composition except for an increase of Zr and Si, with some Y dissolving into the surrounding areas.

Table 38: EDS data for Nb-18Si-24Ti-5Cr-5Al-2Mo-5Zr-0.4Y for both AF and post-HIP highlighting Y concentration

		Nb	Si	Ti	Al	Cr	Mo	Zr	Y	Ta
Y High Nb ₅ Si ₃	AF	33.59	20.76	18.91	2.23	1.97	0	10.40	10.74	1.39
	HIP	27.96	26.99	19.12	2.30	0.85	0	14.75	6.72	1.32

The 5 h HT microstructure of Nb-18Si-24Ti-5Cr-5Al-2Mo-1Zr-0.08Y is seen in **Figure 101 b)** where it may be compared to the adjacent post-HIP BEI image. It shows that a significant coarsening has occurred in all phases post-HT. Large globular silicide phases may be noted throughout the microstructure with smaller silicide's appearing to grow epitaxially on the phase boundary.

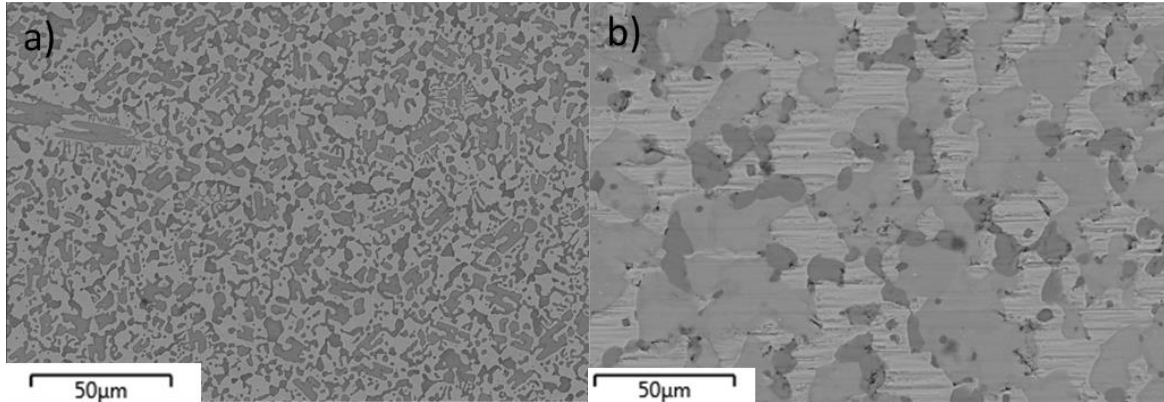


Figure 101: BEI image of Nb-18Si-24Ti-5Cr-5Al-2Mo-5Zr-0.4Y-2Ta at a) Post-HIP and b) Post-HT. Image taken at centre of sample

The post-HT diffractogram was modelled in **Figure 102**. It notes a decrease in γ -Nb₅Si₃ along with the appearance of α -Nb₅Si₃ denoting a transformation of the former to the latter. It is also noted that Nb_{ss} decreases within the system. In the EDS phase analysis, it is possible to see a large diffusion of Ti from the α -Nb₅Si₃ (~7 %), this likely occurred during transformation from $\gamma \rightarrow \alpha$ silicide, accounting for the location of γ -Nb₅Si₃ on the boundary of α -Nb₅Si₃. The lattice size of both Nb_{ss} and γ -Nb₅Si₃ reduces, which coincides with **Figure 101 b)** showing the expulsion of the larger Zr and Y atoms from both phases.

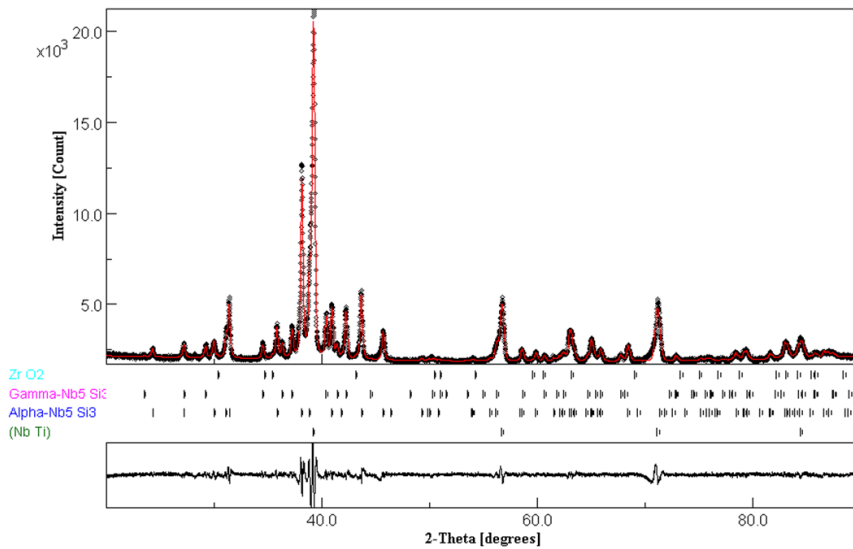


Figure 102 : X-ray diffractogram of post-HT Nb-18Si-24Ti-5Cr-5Al-2Mo-5Zr-0.4Y-2Ta

Visual inspection of the material noted a white coating around the sample, denoting the presence of an oxide formation on the materials surface. Ti and Zr are both possible candidates to produce a white oxide. On consulting an Ellingham diagram of both materials in **Figure 103**, the minor increase in Zr reactivity is noted. A further increase in temperature would likely have resulted in a TiO_2 formation.

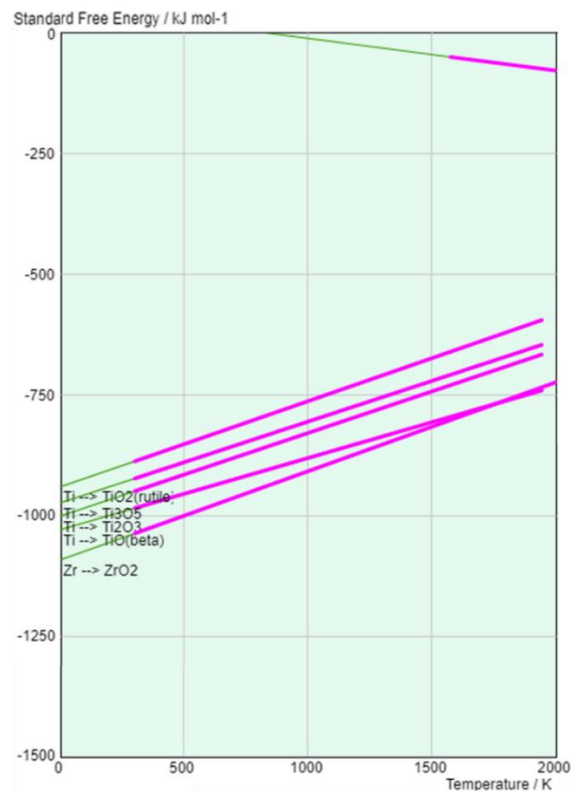


Figure 103: Ellingham diagram of Zr and Ti oxides[126]

When modelling the diffractogram a tetragonal ZrO_2 with the crystal definition P42/nmc matched closest. This further establishes the observed peak shifts of both Nb_{ss} and $\gamma-Nb_5Si_3$. **Table 39** shows the majority has left, leaving 1-3% within the silicide, further indicating it has preferentially oxidised over Ti.

Table 39: Showing element distribution in phases of post-HT Nb-18Si-24Ti-5Cr-5Al-2Mo-5Zr-0.4Y-2Ta, all values in at.% unless otherwise stated

	Nb	Si	Ti	Al	Cr	Mo	Zr	Y	Ta	O
$(Nb, Ti)_{ss}$	50.05	2.66	23.75	6.79	9.29	3.41	0.00	0.38	3.69	--
Nb_5Si_3	43.10	34.65	14.56	2.38	0.61	0.75	1.33	0.27	2.34	--
$(Nb, Zr, Ti)_5Si_3$	31.33	32.45	25.81	3.91	1.44	0.43	3.03	0.13	1.44	--
ZrO_2	3.79	1.98	2.91	0.32	0.26	0.00	27.61	3.30	0.16	59.66

Figure 104 highlights ZrO_2 located on the silicide boundary. The location suggests it was both ejected from the silicide and preferentially oxidised during HT. The previously noted Zr, Y concentrations in **Figure 100** are also oxidised. The appearance of oxygen was unexpected, as HT was performed under an argon atmosphere so residual oxygen from the ceramic dish used is likely the cause.

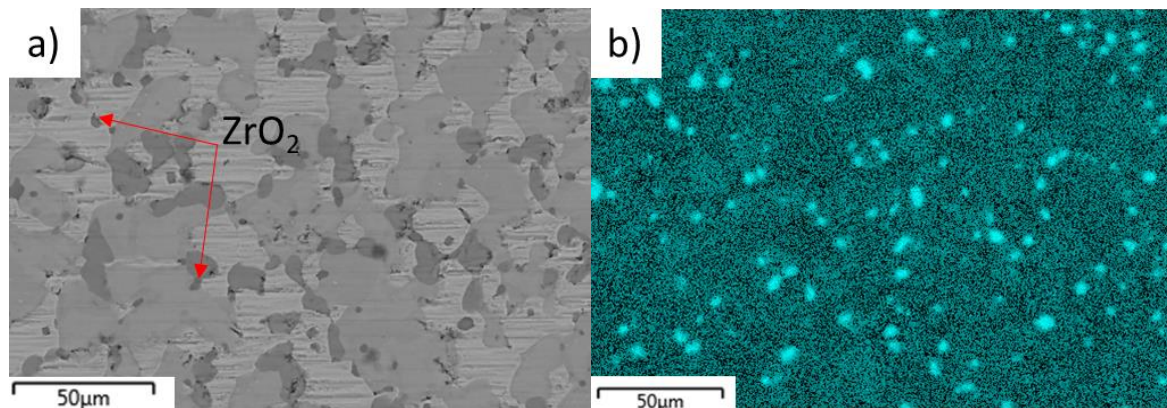


Figure 104: BEI and EDS map of Nb-18Si-24Ti-5Cr-5Al-2Mo-5Zr-0.4Y showing a) High magnification b) Zr map. Images taken at centre of scan sample.

The volume fraction described in **Table 40** post-HT shows a large change in phases, with Nb_{ss} decreasing significantly along with the transition of $\gamma-Nb_5Si_3 \rightarrow \alpha-Nb_5Si_3$, this can be seen graphically in **Figure 105**. The transformation is incomplete with significant quantities of γ -silicide present.

Table 40: Showing volume distribution of phases of post-HT Nb-18Si-24Ti-5Cr-5Al-2Mo-5Zr-0.4Y-2Ta modelled using MAUD. Note GOF added for accuracy reference

Phase	Volume Fraction As-Formed	Volume Fraction Post-HIP	Volume Fraction Post-HT
GOF	2.023	3.323	2.152
Nb _{ss}	60.80	43.32	39.40
α-Nb ₅ Si ₃	--	--	43.20
γ-Nb ₅ Si ₃	39.20	56.68	16.20
ZrO ₂	--	--	1.30

The transformation of $\gamma\text{-Nb}_5\text{Si}_3 \rightarrow \alpha\text{-Nb}_5\text{Si}_3$ coincides with the reduction of Zr from the silicide. Work by M. Sankara (2018) has shown that high levels of Zr stabilised $\alpha\text{-Nb}_5\text{Si}_3$, which is contrary to the work in this thesis where high Zr content is indicative of stabilised $\gamma\text{-Nb}_5\text{Si}_3$. The presence of ZrO₂ may have coincidentally reduced the level of Zr and allowed for the transformation to occur.^[144]

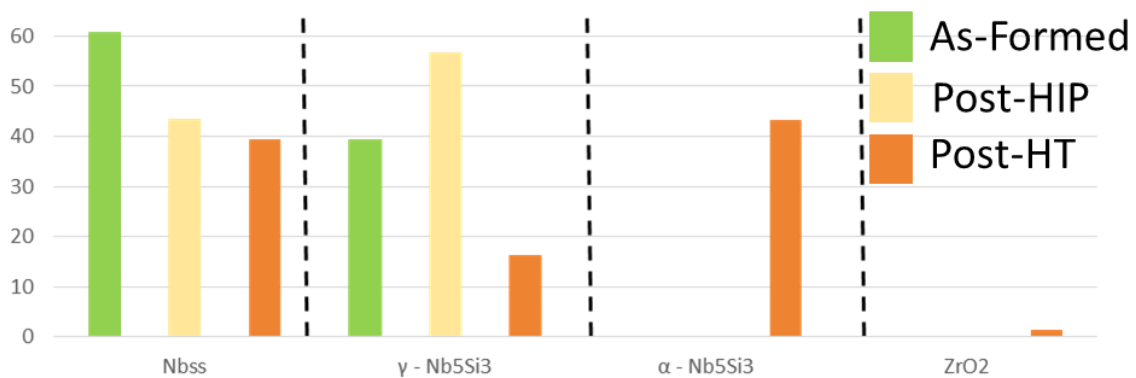


Figure 105: Comparison graph of TCoZy5 at each stage of production

The presence of concentrated Y and Zr is unexpected in the post-HIP samples. Its ejection may be to release increased lattice strain induced by its inclusion in the solid solution matrix. **Figure 106** correlates the expulsion of Zr from the Nb_{ss} matrix and Nb₅Si₃ along with the size of their respective crystal lattice. The concentration of Zr remained stable within the $\gamma\text{-Nb}_5\text{Si}_3$, only dropping during heat treatment as Zr reacted with oxygen as discussed above. The Nb_{ss} displayed less Zr as post-processing occurred, along with a decrease in lattice constant. From this evidence it is suggested that initial Zr levels were too high on formation, resulting in a strained lattice which expanded to compensate. Diffusion occurred during post-processing, whereby Zr was removed, allowing the crystal to relax. The result is concentrated regions of Zr which formed long phase boundaries. Concentrations of other elements in the region suggest

a small silicide region with high Zr is formed. This may explain why a small amount of lattice increase is observed, the $(\text{Nb, Zr})_5\text{Si}_3$ would have the same lattice structure and orientation but a slightly different lattice constant and replicate diffraction line broadening.

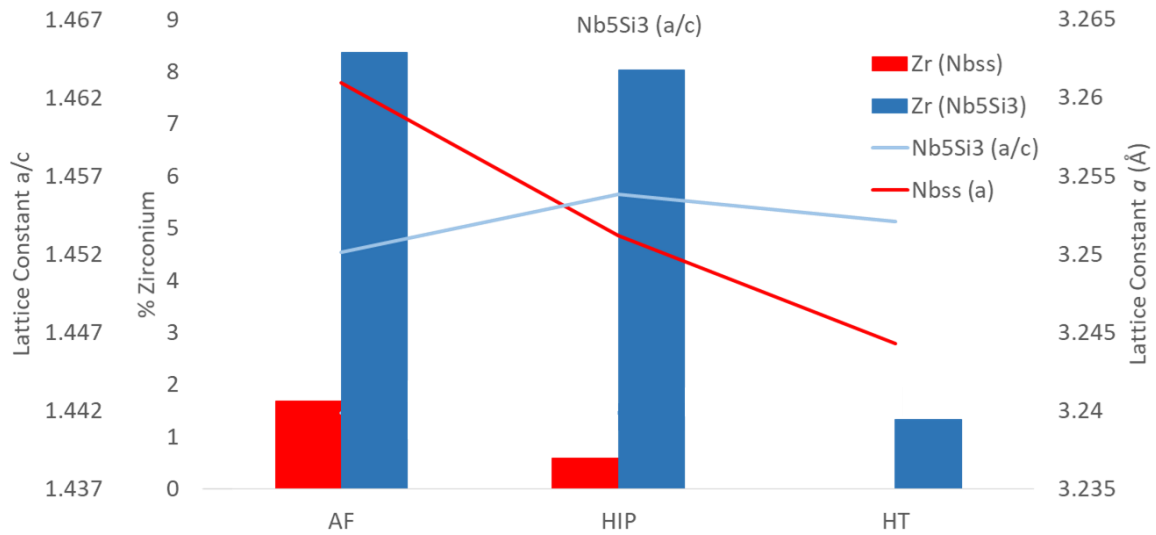


Figure 106: Shows the change in Zr concentration v. Lattice constant in phases during post-processing

7.3 Nb-18Si-24Ti-5Cr-5Al-2Mo-1Zr-0.08Y-2Ta (TCoZy1)

The microstructure of Nb-18Si-24Ti-5Cr-5Al-2Mo-5Zr-0.4Y-2Ta seen in **Figure 107 a)** observes a globular microstructure, with a large matrix (assumed to be Nb_{ss}) seen surrounding a darker secondary phase. With higher magnification, shown in **b)**, evidence of coring on this phase is shown. Both the lighter sections in the centre and the dark edges suggest diffusion was not completed during formation. A eutectic can also be seen within the solid solution matrix.

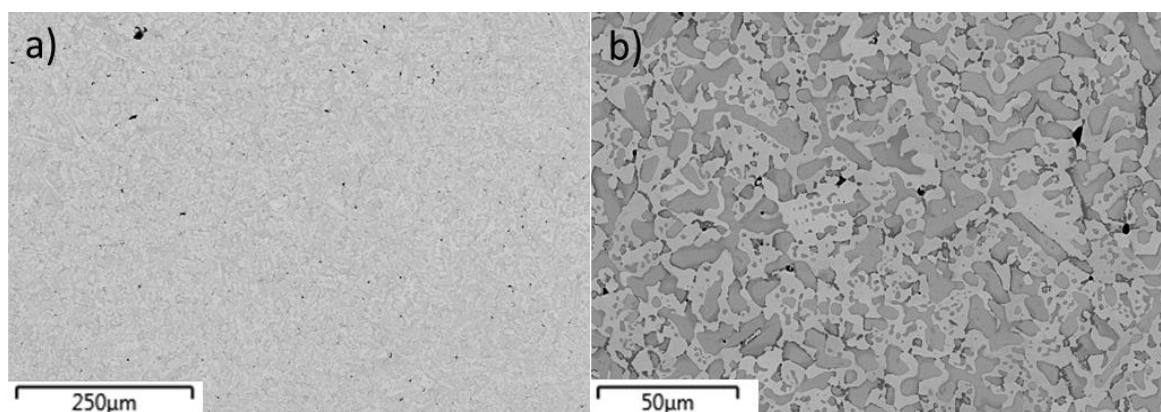


Figure 107: BEI image of Nb-18Si-24Ti-5Cr-5Al-2Mo-1Zr-0.08Y-2Ta as-formed at a) Low and b) High magnification

A small amount of porosity is seen on the surface of the sample (see **Figure 108**). An image analysis calculates the porosity to be ~0.30% at the centre and ~2.70% at the edge of the sample. This discrepancy could be due to less re-melting of the area and a faster cooling, allowing gasses to become trapped on solidification. Porosity in Nb-Si alloys will be discussed in more detail in **section 8.2**.

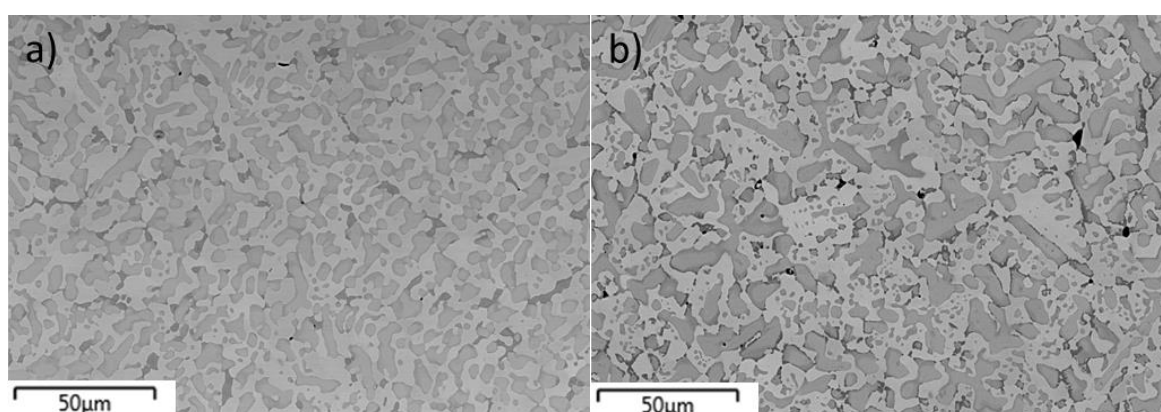


Figure 108: BEI image of Nb-18Si-24Ti-5Cr-5Al-2Mo-1Zr-0.08Y-2Ta as-formed at a) Edge and b) Centre

EDS analysis was conducted (**Table 41**) and shows an elemental distribution similar to the parent sample, 2Mo with a composition that is markedly close. It is expected that γ -silicide is the primary phase of the material.

Table 41: Showing element distribution in phases of as-formed Nb-18Si-24Ti-5Cr-5Al-2Mo-1Zr-0.08Y-2Ta, all values in at.% unless otherwise stated

		Nb	Si	Ti	Al	Cr	Mo	Zr	Y	Ta
TCoZy1	(Nb, Ti) _{ss}	53.00	1.14	31.06	4.65	6.95	2.68	0.28	0.26	2.16
2Mo	(Nb, Ti) _{ss}	46.39	6.65	28.36	6.98	8.82	2.81			
TCoZy1	(Nb, Ti) ₅ Si ₃	45.21	32.63	17.54	2.56	0.92	0.67	0.29	0.03	--
2Mo	γ -Nb ₅ Si ₃	45.42	32.35	17.31	3.03	1.00	0.88			
TCoZy1	High Ti (Nb, Ti) ₅ Si ₃	34.14	32.48	29.33	2.26	1.23	0.3	0.22	0.04	--
2Mo	β -Nb ₅ Si ₃	34.85	28.30	28.84	4.45	2.76	0.79			

The new as-formed chemistry also has an even distribution of Zr within all phases unlike CoZy1 (**Table 31**). Ta, however, shows segregation to the solid solution phase with none detected in any of the silicides. As with CoZy1, the small amounts of Zr and Y appears to have reduced the overall size of the microstructure by allowing the melt to flow.

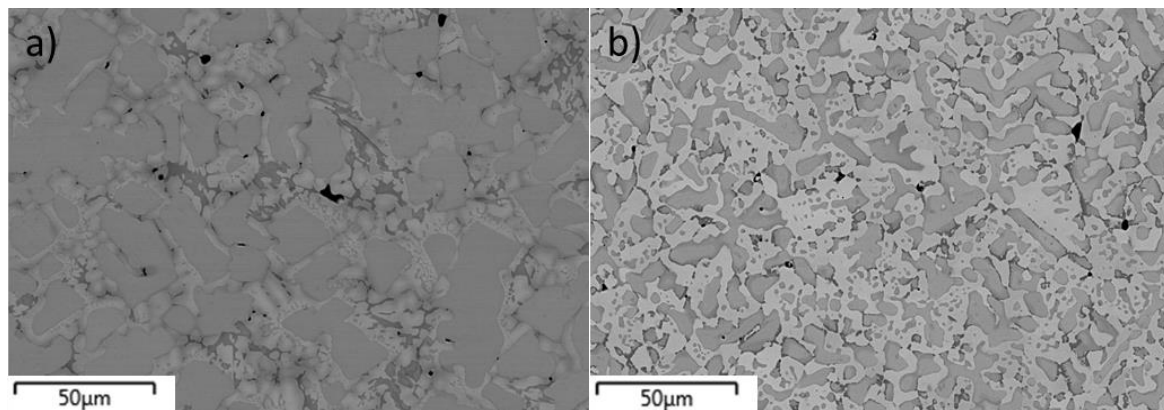


Figure 109: BEI image of as-formed samples a) Nb-18Si-24Ti-5Cr-5Al-2Mo and b) Nb-18Si-24Ti-5Cr-5Al-2Mo-1Zr-0.08Y-2Ta

XRD was used to determine if γ -silicide was present, this was modelled using MAUD to calculate the volume fraction of phases. Where an ideal diffraction fit would be ~ 2 , the diffractogram was modelled with a GOF of 2.856 as peak intensities were not completely modelled. One reason could be a large amount of texturing in the sample. As mentioned previously, texture analysis is beyond the scope of this PhD so was not analysed using MAUD. The volume distribution can be seen in **Table 42** and the diffractogram may be viewed in **Figure 110**.

Table 42: Showing volume distribution of phases of as-formed Nb-18Si-24Ti-5Cr-5Al-2Mo-1Zr-0.08Y-2Ta

	Volume Fraction (%)	
	TCoZy1 AF	CoZy1 AF
Nb _{ss}	43.93	24.40
α-(Nb, Ti) ₅ Si ₃	19.46	30.38
β-(Nb, Ti) ₅ Si ₃	27.64	35.77
γ-Nb ₅ Si ₃	8.96	7.42

The phases suggested quantitatively by MAUD are seen in the **Table 42**. As observed in CoZy1, all forms of Nb₅Si₃ (α-, β- and γ-silicide) were present on initial construction. The volume fractions show less α-Nb₅Si₃ with Ta additions but similar γ-Nb₅Si₃. It is possible that the microsegregation noted in **Figure 109** resulted in areas of high Ti and Zr. The preference of both these elements is hexagonal close packed (HCP) and thus promoted the formation of γ-Nb₅Si₃.

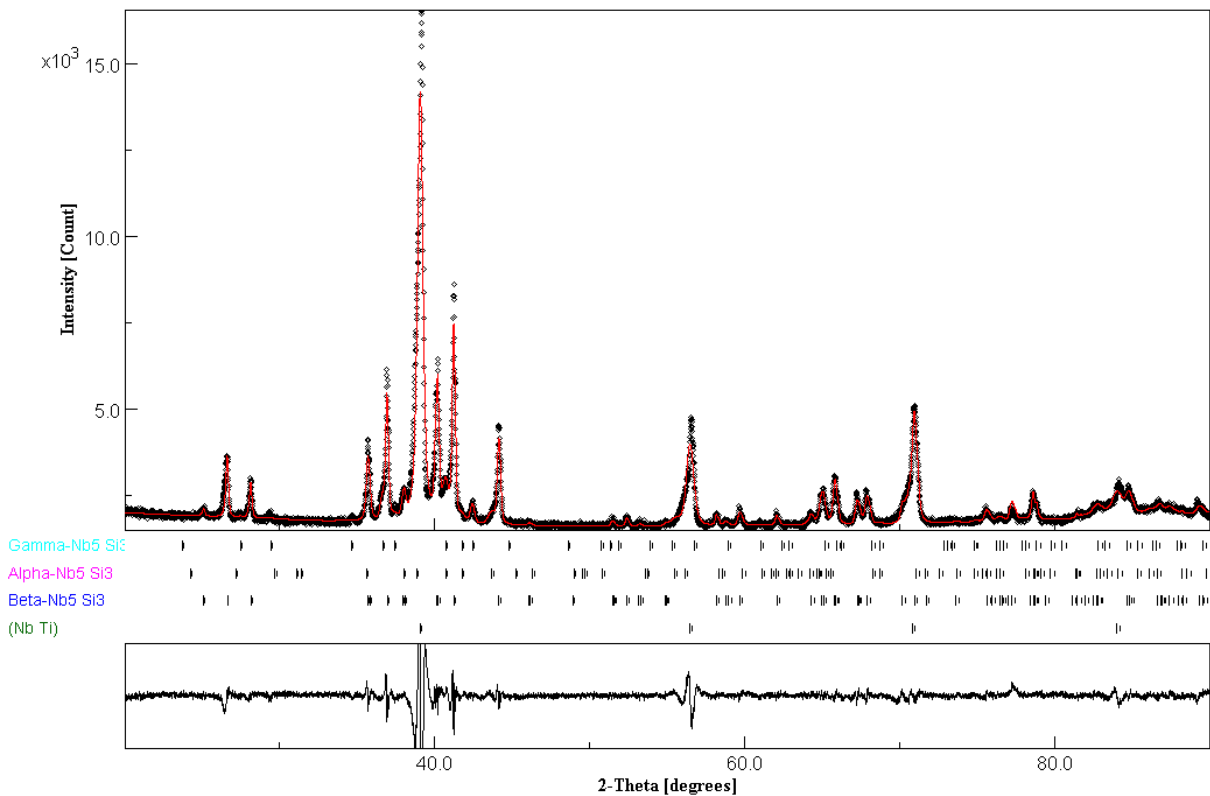
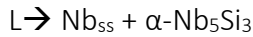
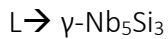


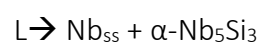
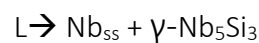
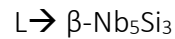
Figure 110 : X-ray diffractogram of as-formed Nb-18Si-24Ti-5Cr-5Al-2Mo-1Zr-0.08Y-2Ta

Using the EDS, XRD and BEI images collected, it is possible to suggest potential solidification routes:

1)



2)



The second option is ruled out because α -silicide would be isolated in Nb_{ss} rather than adjacent to the $\beta\text{-Nb}_5\text{Si}_3$. The solidification process involved melting and re-melting, giving opportunity for restructuring to occur. Evidence of coring in the β -silicide suggests the initial solidification occurred rapidly, leaving an inhomogeneous structure. It is possible that during the melting and re-melting stages, areas of the silicide near the edge were less viscous. Zr and Ta have been known to increase the fluidity of the melt and the high concentration of Ti may have allowed transformation to $\gamma\text{-Nb}_5\text{Si}_3$ during this short time period.

The BEI of Nb-18Si-24Ti-5Cr-5Al-2Mo-1Zr-0.08Y2Ta after hot isostatic pressing can be seen in **Figure 65**. Consolidation has occurred with the β -silicide eutectic, and the evidence of coring is reduced. Large areas can be seen showing a black phase. This could be either porosity or another example of Ti_{ss} and will be investigated further.

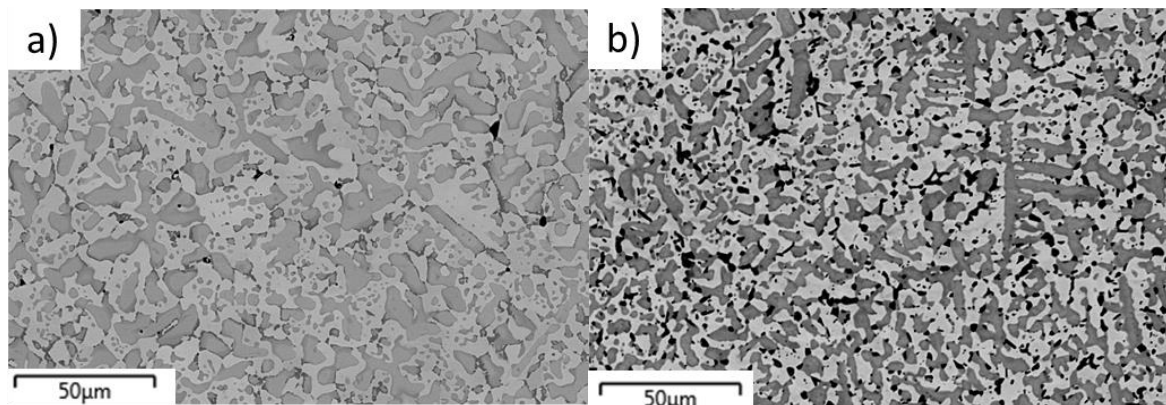


Figure 111: BEI of Nb-18Si-24Ti-5Cr-5Al-2Mo-1Zr-0.08Y2Ta at a) As-formed b) Post-HIP. Images taken at centre of scan sample.

XRD analysis of **Figure 111** shows that the homogenisation of the silicide phase has resulted in an overall phase change. The result is a diffractogram that only models Nb_{ss} and $\alpha\text{-Nb}_5\text{Si}_3$.

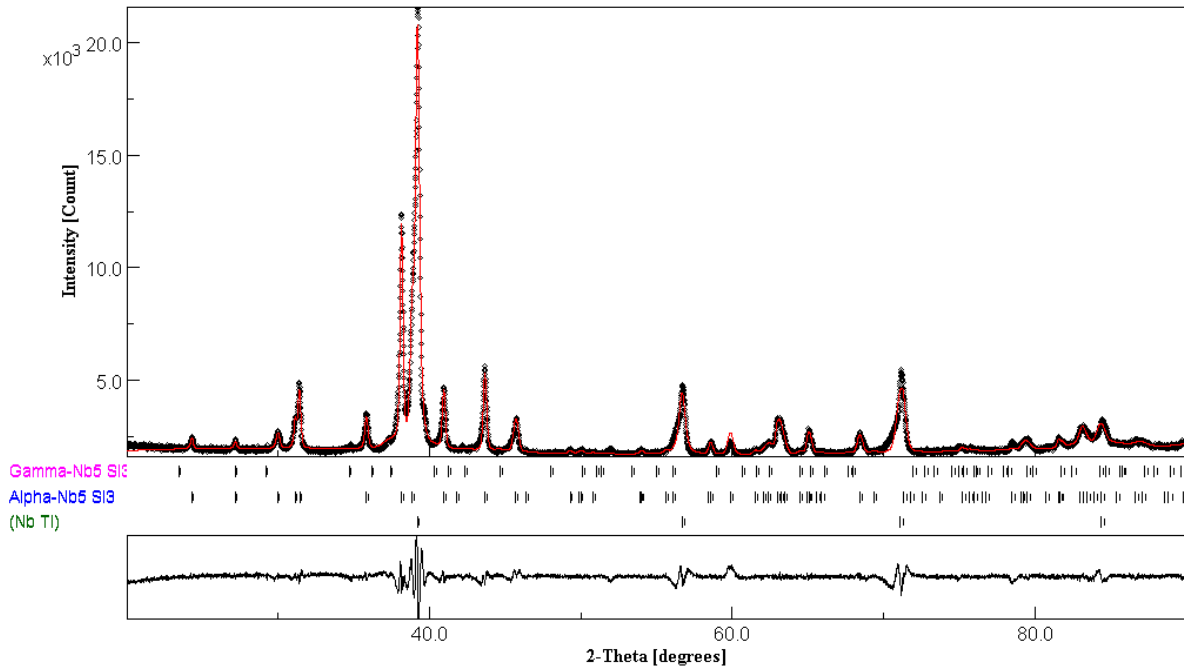


Figure 112: X-ray diffractogram of Nb-18Si-24Ti-5Cr-5Al-2Mo-1Zr-0.08Y2Ta post-HIP, modelled using MAUD

This does not fit with the information presented in **Figure 65**. The BEI suggests that there are either three phases in the post-HIP microstructure, or two phases and a large amount of porosity. Whilst both are possible, it is unlikely that HIP versions of a sample would produce porosity in this quantity due to the nature of the process.

Table 43 displays the volume fraction of post HIP. Quantitative analysis was performed using MAUD on the diffractogram as seen in **Figure 112** obtaining a modelled GOF = 2.649. The model suggests that the volume fraction of Nb_{ss} is 59.33% whereas image analysis of the same sample suggests it is ~46%. This discrepancy can be explained when considering the presence of Ti_{ss}, which has the same cubic structure as Nb_{ss} and thus would disrupt any values given, as previously discussed in **section 5.2**. γ -Nb₅Si₃ is observed in a similar fraction as the as-formed sample suggesting it is stable despite hot isostatic pressing. Coring is not noted in the post-HIP sample and so it is expected that silicide's that formed as γ -Nb₅Si₃ did not re-arrange due to diffusion of larger elements destabilising them.

Table 43: Showing volume distribution of phases of post-HIP Nb-18Si-24Ti-5Cr-5Al-2Mo-1Zr-0.08Y-2Ta

Phase	Volume Fraction (%)
Nb _{ss}	59.33
α -Nb ₅ Si ₃	29.25
γ -Nb ₅ Si ₃	11.42

For further clarification, an EDS map for Ti was overlaid onto the same image in **Figure 113**, highlighting the increased Ti concentrations on the darkened areas. Small areas of precipitated Zr, similarly ejected from $\beta\text{-Nb}_5\text{Si}_3$ during the phase transformation of $\beta\text{-Nb}_5\text{Si}_3 \rightarrow \alpha\text{-Nb}_5\text{Si}_3$.

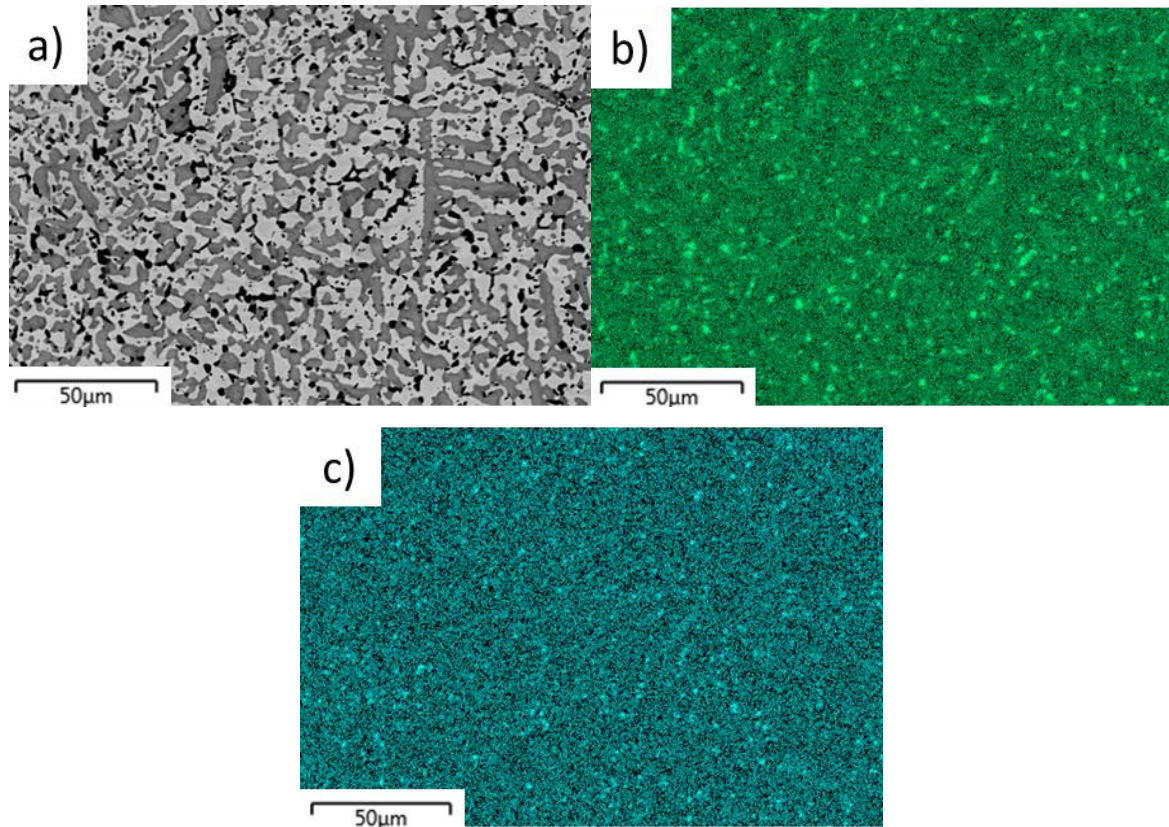


Figure 113: BEI of Nb-18Si-24Ti-5Cr-5Al-2Mo-1Zr-0.08Y2Ta a) post-HIP and EDS maps of b) Ti, c) Zr

Comparison of the microstructural changes of post-HIP and post-HT Nb-18Si-24Ti-5Cr-5Al-2Mo-1Zr-0.08Y2Ta can be seen in **Figure 114**. Multiple differences are observed, the most notable of which is the large amount of coarsening of Nb_{ss} , as well as a disappearance of the previously seen Ti_{ss} . The silicide phase has also coarsened, with the appearance of a darker Nb_5Si_3 phase growing from the main silicide phase.

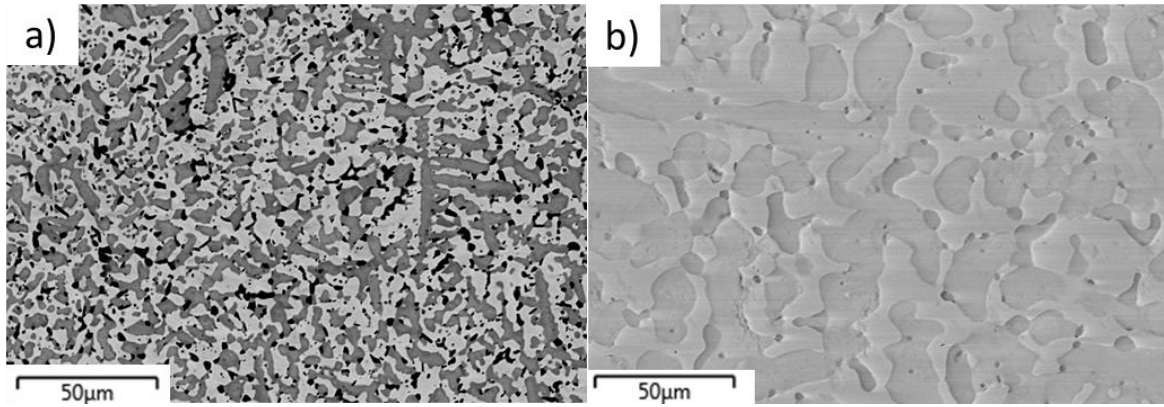


Figure 114: BEI of Nb-18Si-24Ti-5Cr-5Al-2Mo-1Zr-0.08Y2Ta a) Post-HIP and b) Post-HT

These two contrasting phases are modelled as α - and γ -Nb₅Si₃ as seen in **Figure 115**. Other phases were modelled to discern if intermediate silicide's (NbSi₂, Nb₃Si etc.) were present to suggest a possible mechanism but none were detected.

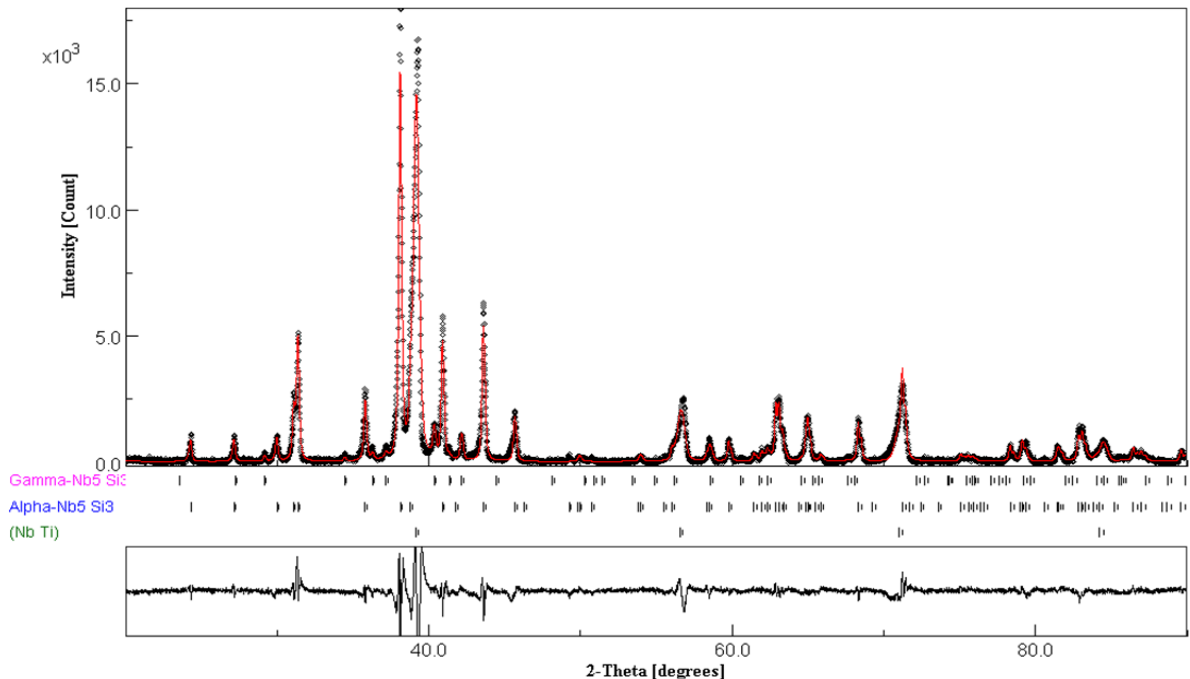


Figure 115: X-ray diffractogram of Nb-18Si-24Ti-5Cr-5Al-2Mo-1Zr-0.08Y2Ta post-HT, modelled using MAUD

The presence of γ -Nb₅Si₃ is unexpected in a heat-treated sample, due to it being a low temperature metastable phase. Although unexpected, both quantitative analysis of XRD and image analysis of the BEI suggest the darker phase is γ -Nb₅Si₃. If the distribution of Ti in the post-HT sample is considered we can observe in **Figure 116 b)** that during the coarsening of the HT sample the Ti has been re-absorbed into the silicide phase.

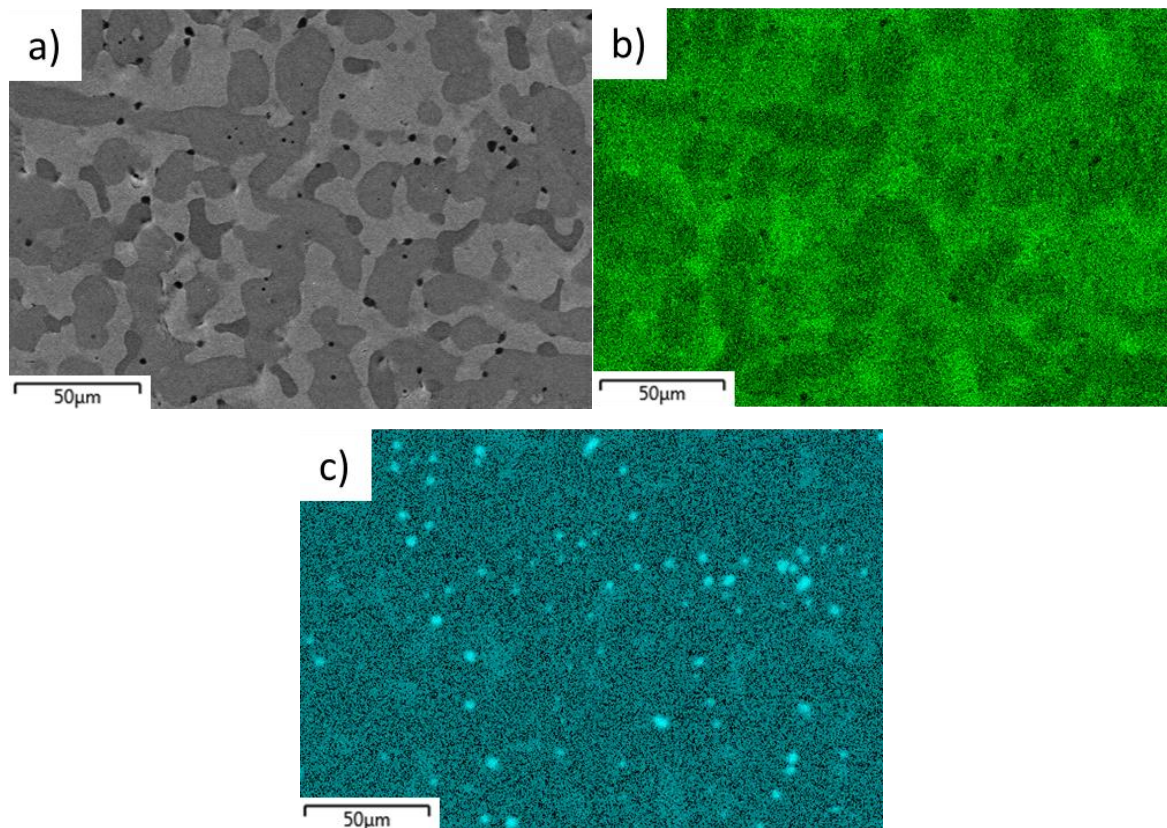


Figure 116: SE and EDS maps of Nb-18Si-24Ti-5Cr-5Al-2Mo-1Zr-0.08Y2Ta a) Post-HT and b) EDS map of Ti c) EDS map of Zr

This is counter intuitive if the previous alloy, 2Mo, is considered, as Ti_{ss} was observed in both stages of post-processing. The key difference in this case is the segregated Zr distributed throughout the microstructure on the boundary of Nb_5Si_3 . It is this difference which has allowed the re-formation of $\gamma-Nb_5Si_3$ either through:

- 1) Presence of Zr stabilising the surrounding $\alpha-Nb_5Si_3$
- 2) The combination of both highly concentrated elements in close proximity during HT
- 3) Highly concentrated Ti re-absorbing into adjacent $\alpha-Nb_5Si_3$

The likely reason is 2). If one considers that the EDS of the post-HT sample still contains many highly concentrated precipitates of Zr. These remained despite the coarsening of the other phases in solution, suggested their absorption is slow. This may be due to the larger size and lower mobility of Zr within the Nb_{ss} .^[156] If Zr was involved in the $\gamma-Nb_5Si_3$ transformation then it would likely be absorbed into one or both of the silicide's. From **Table 44** it can be seen that the $\gamma-Nb_5Si_3$ phase appears with much more Zr than the other phases (ignoring Zr precipitates).

The EDS map in **Figure 116 b)** showed the microsegregation separating Ti into the three phases under different concentrations. A similar occurrence was noted with 2Mo, where the Ti showed segregation into highly concentrated Nb₅Si₃ phases. The diffractogram of this sample showed stable levels of γ -Nb₅Si₃ throughout each phase of processing, suggesting that whilst Ti concentration was high, it was not significant enough for α -Nb₅Si₃ to be transformed and stabilised into γ -Nb₅Si₃. **Figure 116 c)** shows the largest amount of Zr within the darkest silicide. Estimates of the quantity of dark silicide present in the microstructure through image analysis are in line with XRD results.

Table 44: Showing element distribution in phases of post-HT Nb-18Si-24Ti-5Cr-5Al-2Mo-5Zr-0.4Y-2Ta, all values in at.% unless otherwise stated

	Nb	Si	Ti	Al	Cr	Mo	Zr	Y	Ta
(Nb, Ti) _{ss}	55.77	2.07	19.66	7.05	10.63	1.96	0.10	0.47	2.29
α -Nb ₅ Si ₃	48.43	33.86	10.89	2.52	0.80	0.74	0.74	0.40	1.62
(Nb, Zr, Ti) ₅ Si ₃	35.01	31.82	22.55	4.14	1.76	0.05	3.63	0.06	0.97
Zr	29.21	16.62	11.83	1.75	2.37	0.03	33.17	4.23	0.80

For this reason, it is theorised that the combination of coarsening of highly concentrated Ti_{ss} and Zr on the boundary of α -Nb₅Si₃ resulted in its absorption. The change in phases throughout each stage can be seen in **Figure 117** and shows the transformation towards α -Nb₅Si₃ from as-formed to post-HT. β -Nb₅Si₃ is present in the as-formed stage but disappears on hot isostatic pressing.

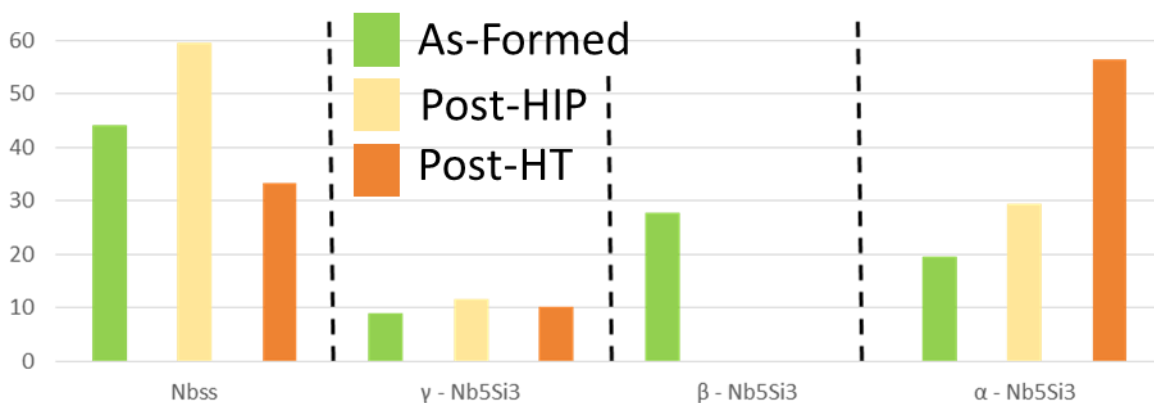


Figure 117: Comparison graph of TCoZy1 at each stage of production

7.4 Evaluation of Elemental Additions

The previous chapter discussed the addition of Zr and Y to improve phase stabilisation and promote the low temperature α -Nb₅Si₃. At high concentrations of Zr a binary alloy of Nb_{ss} and γ -Nb₅Si₃ was observed. Additions of Ta were designed to improve the mechanical properties of these materials and promote α -Nb₅Si₃.

Ta showed preferential substitution to the solid solution matrix with some diffusion into the silicide during post-processing. As observed with CoZy1 and CoZy5, the size of the silicide phase decreased as Zr levels were increased

At low levels of Ta (1 at.%) initial formations showed all combinations of Nb₅Si₃, post-processing realised a Nb_{ss}/ α -Nb₅Si₃ structure. Similar to CoZy1 and 2Mo, coring and microsegregation during formation produced small amounts of γ -Nb₅Si₃ throughout all stages. Ejection of Ti_{ss} was also noted during heat treatment forming epitaxially to the α -silicide.

TCoZy5 observed γ -Nb₅Si₃ on both formation and post-HIP. Upon heat treatment a breakdown occurred from γ -Nb₅Si₃ → α -Nb₅Si₃. Ejection of Zr was noted within the microstructure as ZrO₂, suggesting a reaction with residual oxygen in the furnace chamber.

8 Effects of Hot Isostatic Pressing on Direct Laser Melted Nb-Si Alloys

8.1 Chapter Introduction

The majority of this thesis has focused on different elemental additions in the Nb-Si alloy. At most stages' porosity was detected due to the nature of the additive manufacturing technique. This chapter will investigate the effects of hot isostatic pressing on consolidation of these pores and discuss a possible mechanism for pore reduction. HIP also promoted the formation of Ti_{ss} , and part of this chapter will be dedicated to proposing its formation path using different pressures and phase evolution as evidence.

8.2 Densification of Laser Additive Manufactured Nb-Si-Ti-(2,14)Cr Alloys During Hot Isostatic Pressing

Studies have been undertaken in this thesis to analyse laser additive manufacturing (LAM) as a novel method for Nb-Si alloy production. Using DLM techniques, thin walled objects have been successfully created and have a similar microstructure to those which are formed using casting methods.^[157] This leads to other challenges however, highlighting porosity as one of the main defects present in additively manufactured (AM) materials.^[54]

The rapid solidification experienced during construction leads to the formation of cavities as the melt solidifies and shrinks, dendrite formation and successive layers of solidifying material also leads to the trapping of pores.^[158] These processing pores are often irregular in shape. Spherical porosity is likely the cause of gases dissolved within the melt which get trapped upon solidification, as the spherical shape has the smallest surface area and as such requires least energy. Rapidly solidified materials may exhibit non-uniform gas-filled pores which on subsequent heat treatments may be dissolved into the matrix and diffuse towards regions of lower pressure (either surface or larger pores). The result is larger pores spherodising due to the driving force to reduce surface area and added gas.^[91]

Traditionally, porosity is reduced using plastic deformation in cast materials such as hot working methods. An alternative is to use a consolidation method such hot isostatic pressing (HIP). This is a densification process similar to sintering, used for both densification and a near net shape manufacturing of metals, ceramics and glasses. Pressure is applied in all directions to the alloy using non-reactive gas, such as argon, which is at high temperature. **Figure 118** shows the typical stages to hot isostatic pressing.

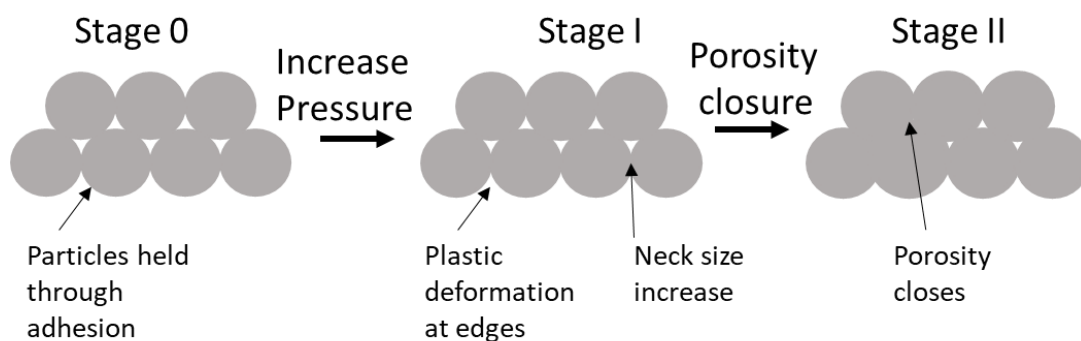


Figure 118: Schematic showing densification through hot isostatic pressing

In the initial stages, particles are in contact with no bonding forces other than adhesion. Plastic deformation occurs as pressure is applied, causing rearrangement of particles and densification. During stage II, grain boundary and lattice diffusion consolidates particles with the application of temperature which increases the neck size of particles. When neck size expands large enough, open porosity begins to close, shifting into stage III of sintering. The trapped pores increase in internal pressure, the application of external pressure leads to further densification through two main methods: diffusional creep and solution of gas into the metal lattice.^[159] Pre-cast components start at either stage I or II and will vary depending on if porosity is closed or linked to the surface (therefore effectively open). Powder metallurgy however begins at stage 0. As mentioned previously HIP is becoming more common as a near net shape manufacturing technique partially for financial reasons.^[91] Yuan *et al* suggests that healing of pre-cast Ni-based alloys occurs in two steps; (i) plastic diffusion via creep and (ii) diffusion.^[160] Chmiela *et al* shows the negative effects of HIP and its general requirement for a post heat treatment. As HIP is usually performed at $>70\% T_m$ (melting temperature) and involves diffusion and plastic deformation, the microstructure generally refines and becomes irregular and misshapen resulting in areas of higher micro-strain and slightly lower mechanical properties.^[161, 162]

Other research has examined the use of HIP to create Nb-Si alloys from powders, reporting that it improves the high cycle fatigue limit, an important failure mechanism in high temperature turbine blades.^[9] This failure path is normally caused by the number of crack initiation sites, for which a large number of pores contributes. Counter-intuitively the size of pores does not alter the stress concentration factor, only the quantity. Coarsening is a common side-effect of HIP treatments, studies have found that the larger grains can increase crack propagation resistance and increased fatigue strength.^[138, 163]

Two Nb-Si-Ti alloys were produced containing varying quantities of Cr (2 and 14 at.%), both were produced via laser additive manufacturing and were used to demonstrate the effects of hot isostatic pressing on sample porosity. More information on these alloys may be found in **section 4.2** and **4.3** Successful densification has been shown in both alloys. Porosity was observed after formation and hot isostatic pressing used to reduce internal pores. The density of constructs was measured using X-ray CT software and was improved up to 99% with most

pores smaller than the detection limit of the X-ray CT. Remaining porosity is resigned to “open” pores near alloy surface as well as anomalous microstructure regions formed during laser deposition and not typical of the overall structure. Porosity close to the surface remains after hot isostatic pressing due to connecting micro-cracks linking pores to surface.

Microstructure and microscale porosity

Microstructural analysis presents a high ratio of brittle silicide as well as presence of Laves phase, which makes it susceptible to cracks. These originate at both the phase boundary and pore boundary (Figure 119 a) and c) respectively) and propagate along the phase boundary between the Nb_{ss} and Nb_5Si_3 . These appear closed up after HIP has occurred with none being evident in either alloy as shown in Figure 119. Densification occurs with small-sized “process” porosity being closed and cracks are healed beyond the detection limit of the microscope.

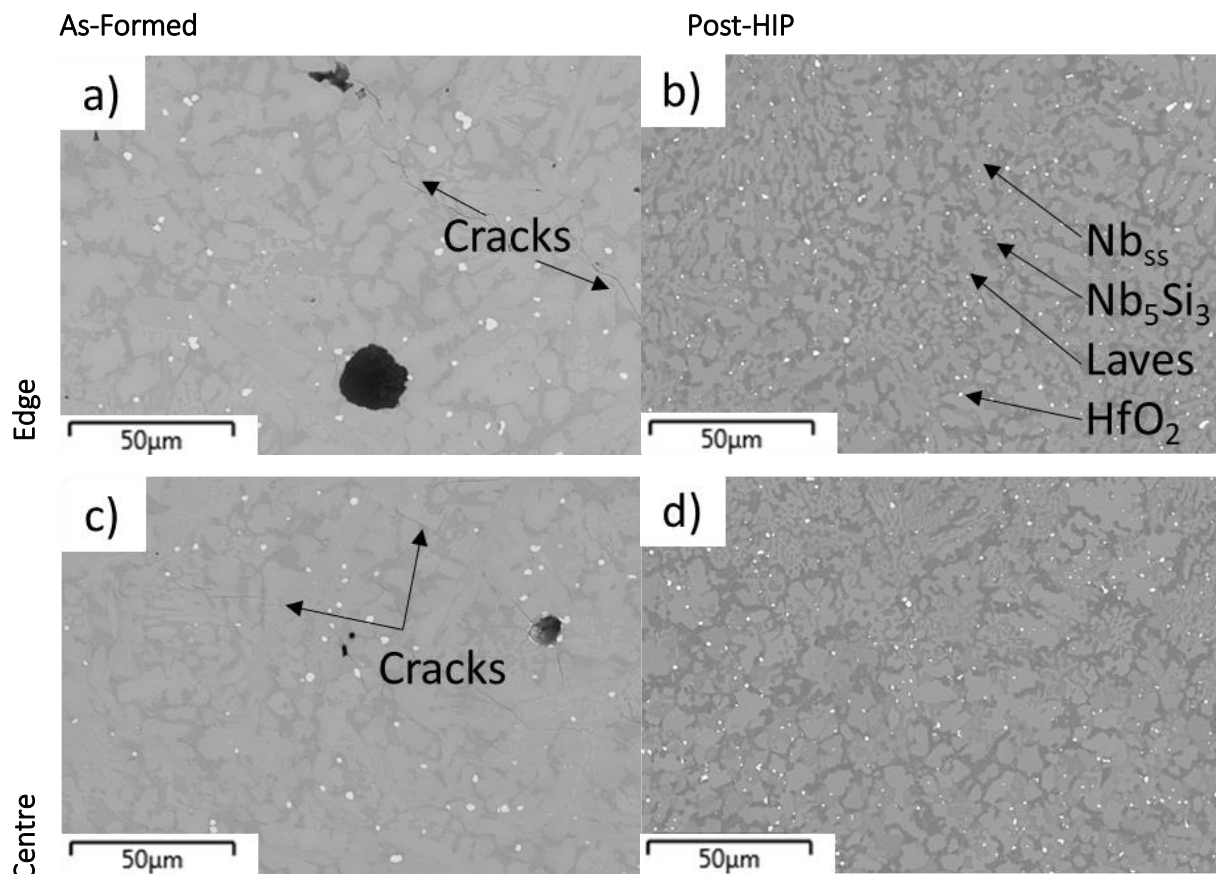


Figure 119: BSE microstructure images of 14Cr - A + B) Edge C + D) Centre

Figure 120 shows the microstructure of 2Cr containing predominantly Nb_{ss} (light) with small quantities of Nb_5Si_3 (darker). Figure 120 a) and c) compare as-formed samples at different sections to post-HIP specimens. The microstructure of the as-formed metal presents a large quantity of pores throughout the sample in the Nb_{ss} phase, the majority of these pores are non-spherical and suggest that they are caused during solidification rather than trapping of gaseous argon. Cracks were not observed at either stages and is attributed to the larger concentration of soft Nb_{ss} .

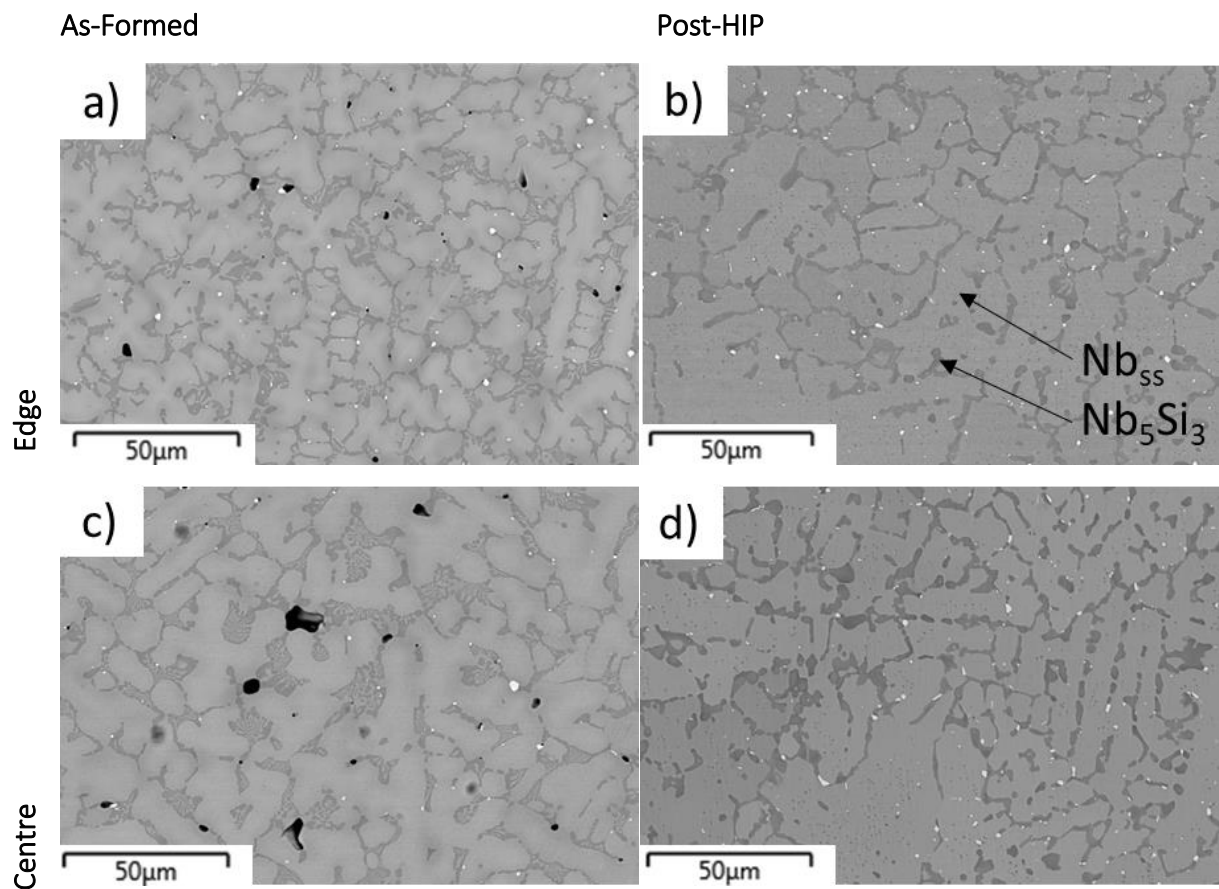


Figure 120: BSE microstructure images of 2Cr - A + B) Edge C + D) Centre

The microstructure of 14Cr (Figure 119) presents a lower ratio of solid solution compared with 2Cr due to the lower ratio of Nb in the Nb-Si-Ti alloy. A greater quantity of large spherical porosity is presented compared to 2Cr suggesting they contain argon.

The overall porosity reduction can be seen in Table 45 showing porosity is not detectable in post-HIP. Average porosity was calculated based on image analysis of multiple back scattered electron images. Only a small area noted porosity after HIP, this is an exception and is discussed later in the chapter.

Table 45: Changes in phase % before and after HIP of both chemistries observed using BSE imaging

	% Phase in 14Cr				% Phase in 2Cr			
	As-Formed		Post-HIP		As-Formed		Post-HIP	
	Edge	Centre	Edge	Centre	Edge	Centre	Edge	Centre
Nb _{ss}	35.03	38.80	45.34	45.10	80.77	86.00	82.40	80.10
Nb ₅ Si ₃	32.48	33.39	27.03	27.21	18.42	13.25	17.10	19.58
Cr ₂ Nb	29.80	26.46	26.36	26.52	--	--	--	--
HfO ₂	0.82	0.83	1.27	1.17	00.49	1.30	0.50	0.32
Porosity	1.87	0.52	--	--	0.32	0.62	--	--

The driving force for densification during hot isostatic pressing is the release of mechanical stress and the reduction in surface area.^[91] Non-gaseous porosity is likely removed due to a combination of lattice and grain boundary diffusion. It can be noted from **Figure 121** that multiple types of pores can be seen sharing different environments, those found on the interior of a grain and those sharing a boundary with two or three different grains. The challenge of closing porosity increases as pores share more grain boundaries.

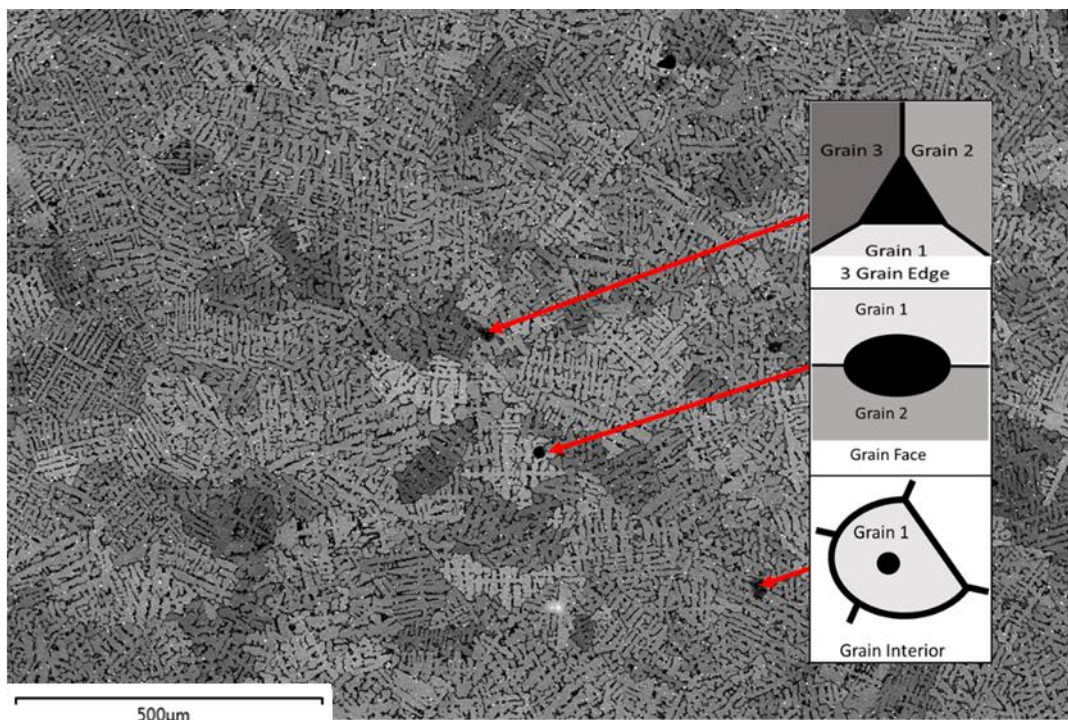


Figure 121: BSE of 2Cr (as formed) , highlighting 3° (Grain Edge), 2° (Grain Face) and 1° (Grain Interior) on sample surface

14Cr alloy shows less pores localised inside a single phase and instead most pores are on the boundaries of two or three different grains. In both chemistries however, lattice diffusion is likely the dominant mechanism due to the small grain sizes present in both samples.

3D Distribution of Porosity

X-ray CT results in **Figure 122** show a variation in porosity in each alloy chemistry, with the 2Cr alloy containing the most porosity. In steels gaseous porosity is commonly associated with hydrogen embrittlement.^[164] This alloy was constructed under an argon atmosphere at standard pressure, therefore it is likely that any spherical shaped pores result from argon encapsulation. Problems arise when HIP densification is attempted. In contrast to hydrogen, argon is too large to diffuse through materials, even at high temperatures and pressures.

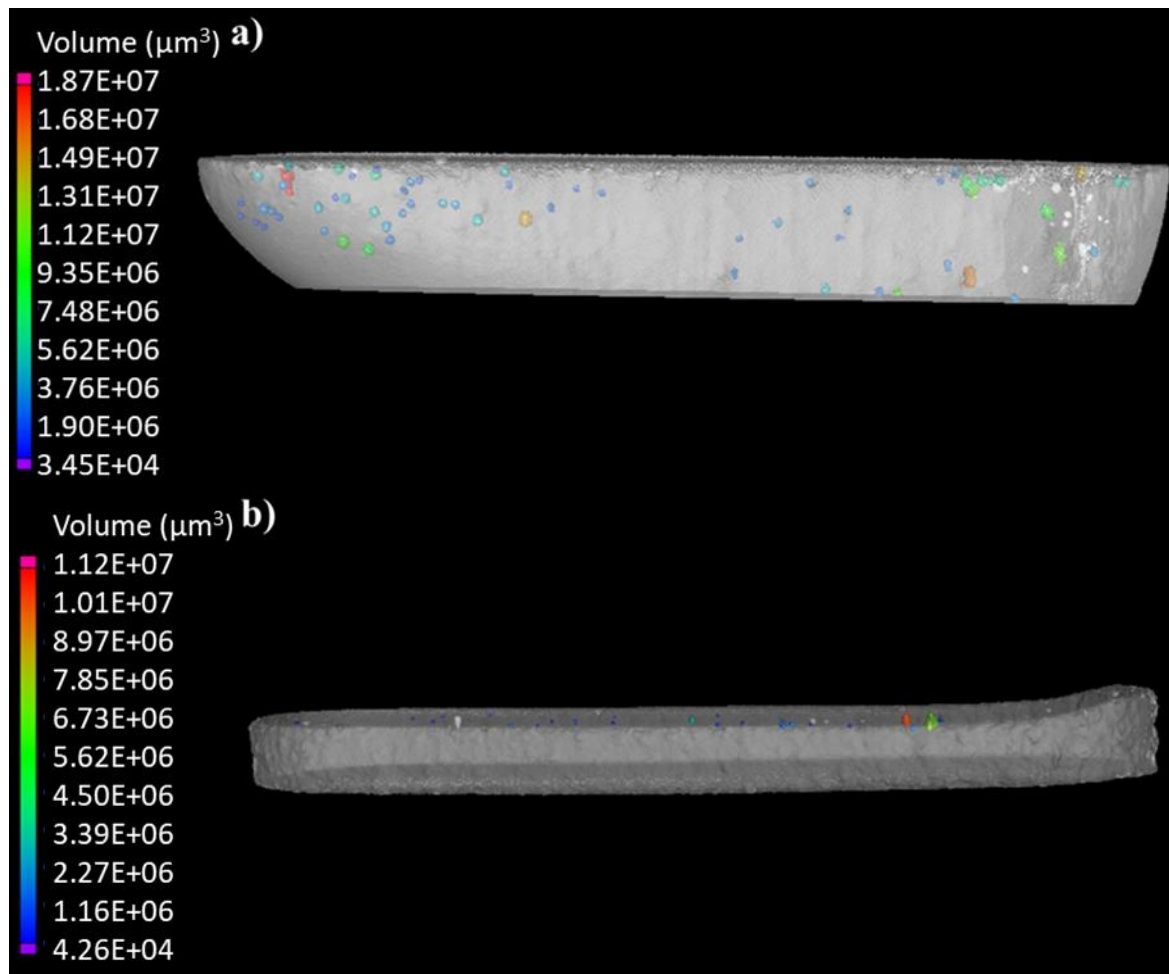


Figure 122: Shows the change in porosity from a) as-formed to b) HIP for sample 2Cr

Small areas of pure Nb can be observed in **Figure 123 a)**. These sections are both rare and found close to the edge of both alloys and is likely a result of poor mixing during printing. Defects may be noticed in the as-formed sample, these are likely due from SiC during polishing.

A boundary is presented around the Nb anomaly in **a)** and has grown post-HIP in **b)**, using elemental analysis it is theorised that the Kirkendall effect has occurred. The high temperature and pressure environment of the HIP process has set up a diffusion couple between the concentrated Nb and $(\text{Nb, Ti})_{ss}$ allowing interdiffusion to occur. This effect has been previously noted as a source of porosity during heat treatments as vacancy diffusion. Unlike substitutional diffusion, a net movement of vacancies occurs which may result in the formation of voids. These are not observed in this case as HIP will act to reduce the expansion of voids, the source of Ti from $(\text{Nb, Ti})_{ss}$ was also “infinite” relative to the anomaly effectively allowing vacancy sites to be absorbed into the bulk material.

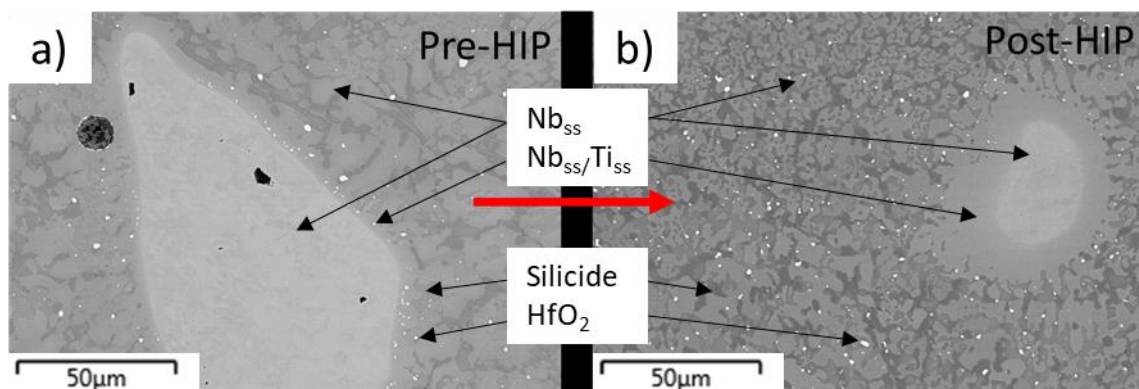


Figure 123: BSE microstructure image showing Nb_{ss} concentrations of a) 14Cr as-formed b) 14Cr post-HIP

It was not expected for gaseous porosity to be removed, but to be shrunk beyond the detection limit of the X-ray-CT. Analysis seen in **Figure 122** agrees with this hypothesis. Most spherical porosity disappeared upon post-processing, though larger enclosed porosities

close to the edge of the sample are still present. The only remaining porosity is in a single plane, it is proposed that micro cracks connected these pores to the surface.

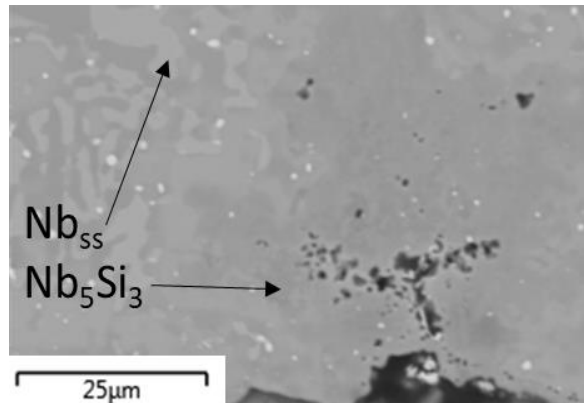


Figure 124: BSE microstructure of 14Cr post-HIP showing edge porosity contained within Nb₅Si₃ phase. Samples were HIPped without a canister and/or a surface coating, which effectively linked these “enclosed” pores to the surface. An example of this phenomenon can be observed in Figure 124, showing porosity trapped within the Nb₅Si₃ phase, likely caused by micro cracks and tunnelling defects.^[165] HIP is unable to consolidate and remove this type of porosity. A schematic diagram of this problem can be seen in Figure 125. To reduce surface porosity, it is important to consider surface coatings before commencing HIP post-processing on pre-fabricated samples.

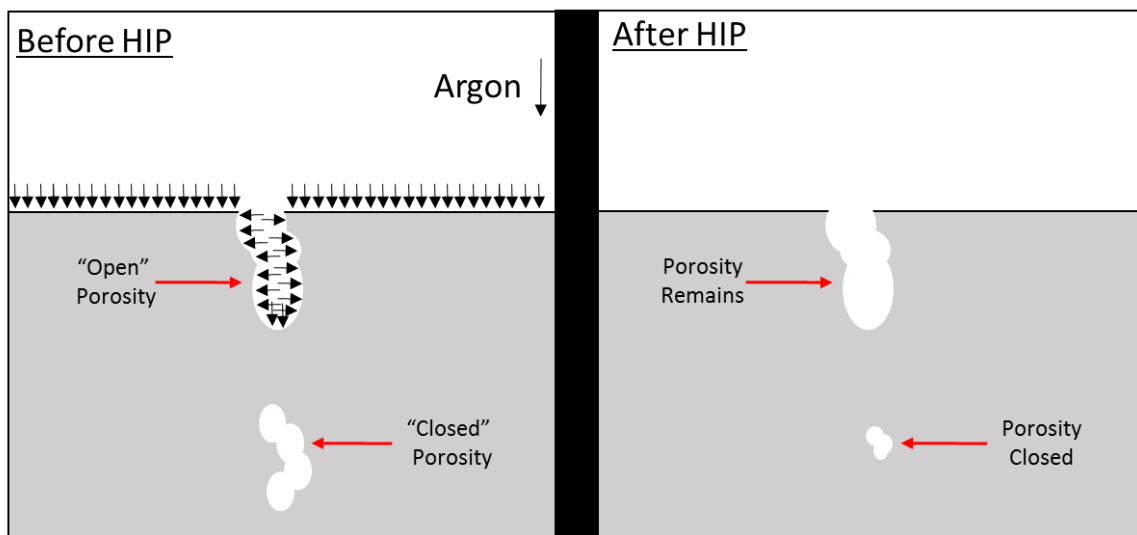


Figure 125: Schematic diagram showing difference in “Open” and “Closed” porosity both before and after HIP

8.3 Phase Transformation of Alloys During Hot Isostatic Pressing

During this work multiple alloy systems have shown evidence of Ti_{ss} precipitates. Multiple articles have observed these phenomena but the reason for its formation is unknown. The three alloys exhibiting Ti_{ss} expulsion are; 2Mo, CoZy1 and TCoZy1 from sections 5.2, 6.3 and 7.3 respectively. The microstructures are observed in **Figure 126**, and two things are notable;

- 1) The silicide structure is smaller with 1 at.% additions of Zr
- 2) Microsegregation is present in all samples

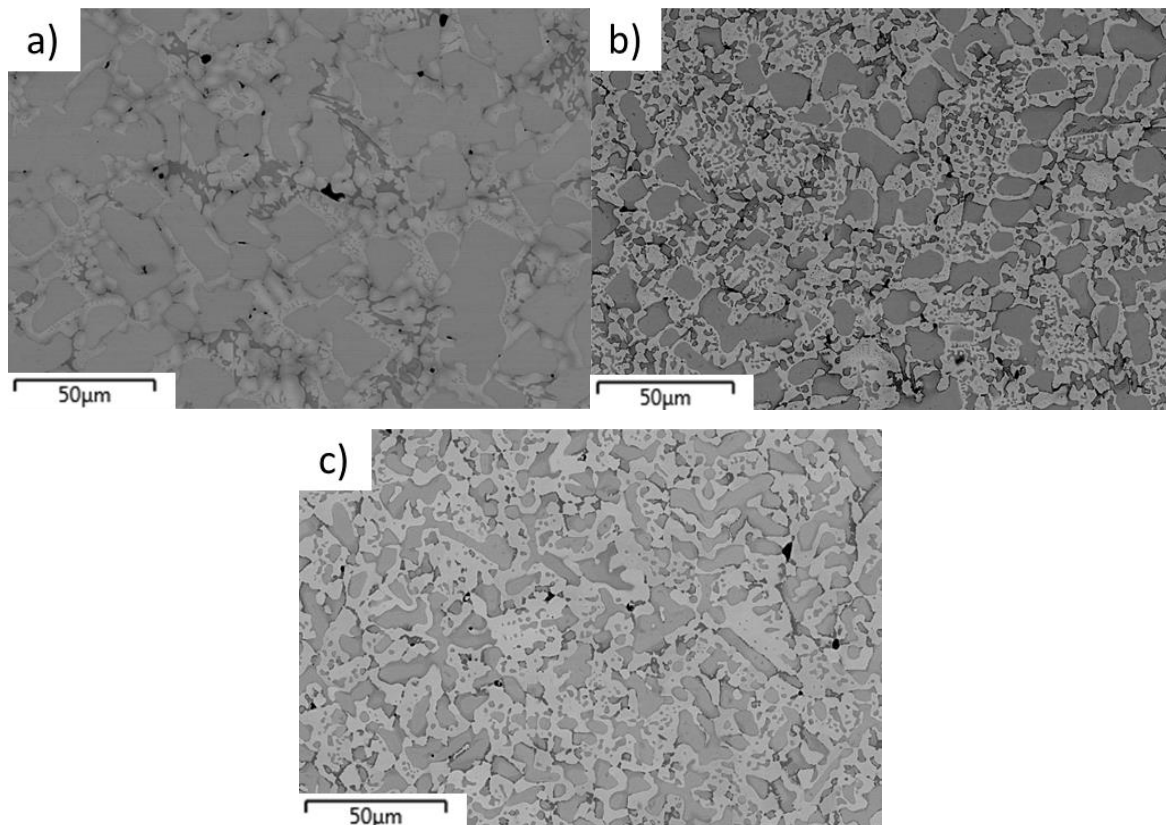


Figure 126: BEI image of as-formed a) 2Mo, b) CoZy1, c) TCoZy1

Both of these phenomena have been discussed in more detail in their respective sections. Zr additions to the alloy system sometimes presented highly concentrated $(Nb, Zr)_5Si_3$ systems during post-processing.

Low Zr additions (1 at.%) decreased the amount of $\gamma-Nb_5Si_3$ present in the as-formed samples from 46% (2Mo) to 7-8% (CoZy1, TCoZy1). The low additions did not prevent microsegregation, which was observed in the contrasting silicide phases. Evidence presented in **section 6.2** and **7.2** suggest that high concentrations do prevent microsegregation during initial construction, although the exact value was not determined during this experiment.

It was hypothesised that the Ti-saturated Nb_5Si_3 phases ejected titanium during post-processing to establish Ti_{ss} as observed in **Figure 127**.

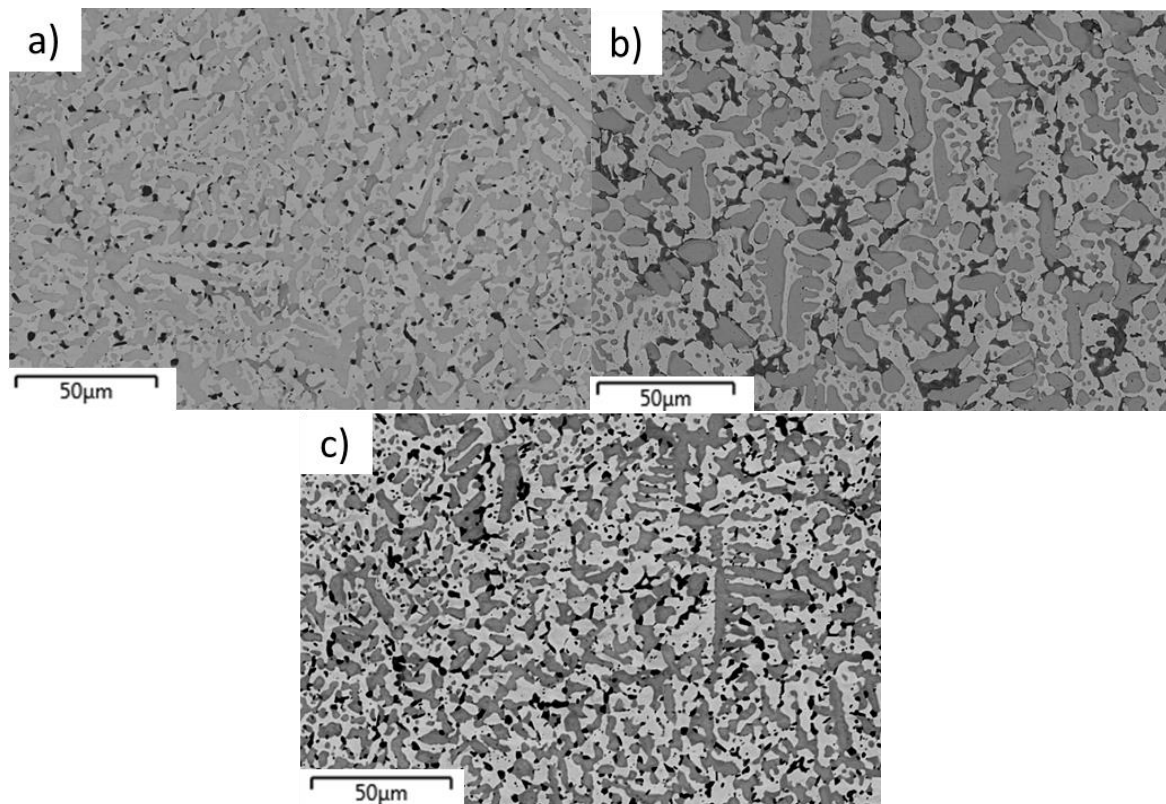


Figure 127: BEI image of post-HIP a) 2Mo, b) CoZy1, c) TCoZy1

The post-processed microstructure of all alloys contained small quantities of Ti_{ss} ejected from its surrounding phases, this was present in the post-HT samples of CoZy1. It was not observed at any stage of CoZy5's development, however. CoZy5 presented a $\text{Nb}_{\text{ss}}/\gamma\text{-Nb}_5\text{Si}_3$ system throughout each post-processing step. This suggests that the appearance of Ti_{ss} is the result of a phase change rather than standard diffusion in the material.

A phase transformation was noted during the post-processing of each alloy system discussed.

$\gamma\text{-Nb}_5\text{Si}_3 \rightarrow \beta\text{-Nb}_5\text{Si}_3$ was noted in 2Mo

$\beta\text{-Nb}_5\text{Si}_3 \rightarrow \alpha\text{-Nb}_5\text{Si}_3$ was noted in CoZy1 and TCoZy1.

It is hypothesised that during the high-pressure environment of HIP a transformation of phases ($\gamma\text{-Nb}_5\text{Si}_3 \rightarrow \beta\text{-Nb}_5\text{Si}_3 \rightarrow \alpha\text{-Nb}_5\text{Si}_3$) a release of Nb occurs under standard conditions. It has been discussed throughout this work that many atoms substitute Nb within the Nb_5Si_3 lattice. Ti, Cr, Hf are all elements known to do this. The reason Ti_{ss} forms so readily during these transformations may be due to a difference in diffusion rate.

The diffusion coefficients of Ti and Nb in an Nb-Ti alloy were discussed by Pontauet *al.* (1979), the results are seen in **Table 46**.

Table 46: Diffusion rates of Ti and Nb in Nb-Ti binary alloy[155]

Nb (at.%)	Temperature (°C)	D_{Ti} (cm ² .s ⁻¹)	D_{Nb} (cm ² .s ⁻¹)
0	1511	7.7×10^{-8}	4.9×10^{-8}
5.4	959	5.9×10^{-10}	2.8×10^{-10}
19.6	1292	4.9×10^{-9}	3.6×10^{-9}
35.7	1384	4.1×10^{-9}	2.0×10^{-9}

The results show that Ti is more mobile in pure titanium than in Nb-doped titanium alloy compared to Nb. With this to consider it is logical to suggest that Ti will have greater diffusivity than Nb in the alloy systems used in this thesis, especially when larger atoms such as Zr or Y expand the Nb_{ss} lattice, providing a lower energy pathway. Increasing temperature also positively affects the diffusivity. Whilst pressure was not considered in this thesis, it is logical to predict that an increase in pressure would also facilitate greater diffusivity due to the extra energy provided. Such a finding would agree with the observation in **Figure 127**.

The additive manufacturing process introduced a growth direction, and texturing has been noted at various points in this thesis. This may introduce mismatched lattices and vacancy sites into the matrix allowing ample sites for transition metals to diffuse through or along phase boundaries. The combination of some Nb₅Si₃ being saturated with titanium leads a re-arrangement to occur. It has a higher diffusion rate than Nb and thus is more likely to be the ejected transition metal.

The transition metal likely leaves the silicide through vacancy diffusion before being replaced by an atom from the solid solution. Due to the increased pressure and temperature there is a pull for ejected titanium atoms to segregate, forming their own Ti_{ss} phase to reduce interfacial energies.^[166] A phase split occurs as discussed by V. Chandrasekaran (1972). During aging treatment of Ti-Mo alloys, a new solid solution precipitate was noted. This new phase had an identical crystal structure to the original matrix but altered compositions resulted in slightly varied lattice parameters.^[167, 168] During heat treatment the volume fraction of Ti_{ss} reduces, suggesting that gradual diffusion into the Nb_{ss} matrix occurred.

The alloys presented **section 5.2** were based on similar work from Jie Geng (2006).^[46] The work presented a progression of $\text{Nb}_3\text{Si} + \beta\text{-Nb}_5\text{Si}_3 \rightarrow \alpha\text{-Nb}_5\text{Si}_3$ microstructure throughout the HT process. This was not observed in the above data, mostly likely due to the rapid solidification observed in LAM over traditional arc-melting. Instead a transition from $\gamma \rightarrow \beta \rightarrow \alpha$ is noted from as-formed \rightarrow HIP \rightarrow HT. The transformation to $\alpha\text{-Nb}_5\text{Si}_3$ occurred only after the second post-processing stage (heat treatment), suggesting that the parameters of pressure, time or temperature may have been a factor preventing the α -silicide formation post-HIP. Experiments were performed on 2Mo to understand the effects of pressure on samples.

Different pressures were analysed to discern their effects on phase transformation of Nb-Si alloy systems. The transformation of 2Mo shows different amounts of Ti_{ss} in the post-HIP samples depending on pressure used, with fewer Ti_{ss} precipitates as pressure decreased. At high pressure $\beta\text{-Nb}_5\text{Si}_3$ was stabilised, whereas at lower pressures only $\alpha\text{-Nb}_5\text{Si}_3$ was noted. Comparison of the BEI and XRD of the post-HIP samples in **Figure 128** at different pressures shows both phase and microstructural variations.

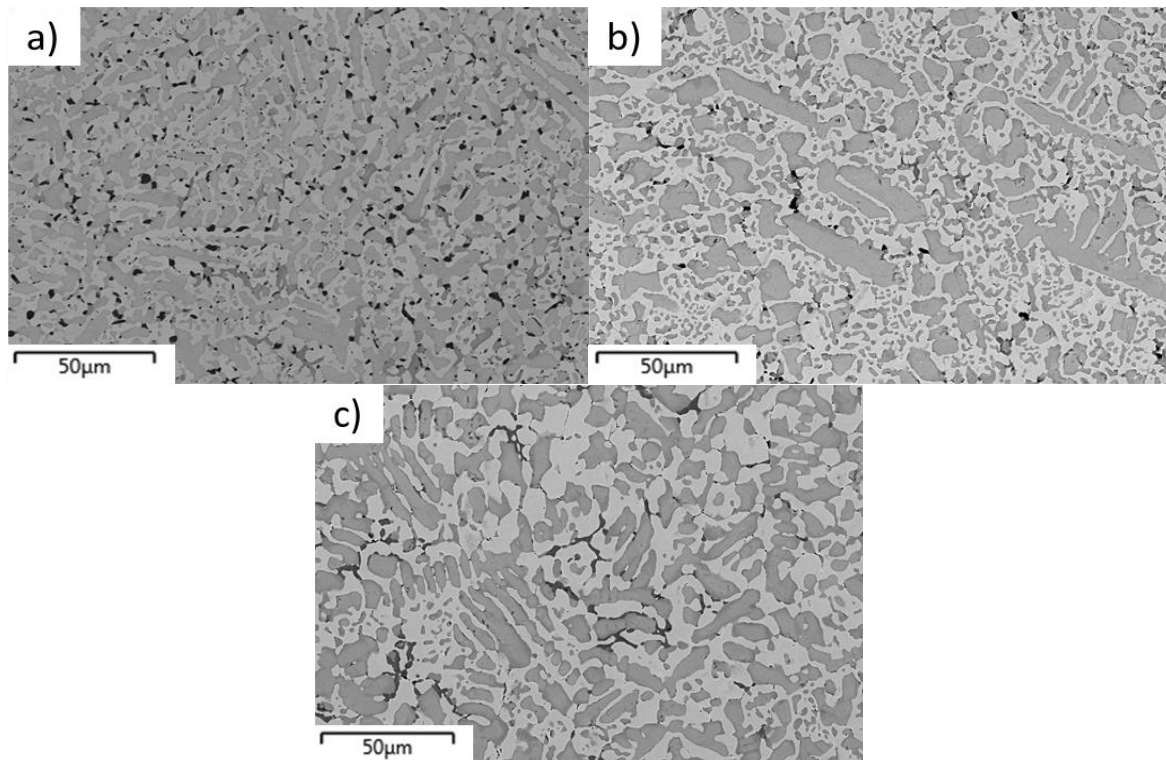
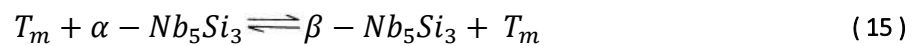


Figure 128: BEI images of Post-HIP Nb-18Si-24Ti-5Cr-5Al-2Mo, processed under different pressures
a) 150 MPa b) 100 MPa c) 50 MPa

The solidification path of 2Mo was discussed in **section 5.2**. It was modelled as $\gamma\text{-Nb}_5\text{Si}_3$ and during HIP post-processing a silicide transformation occurred, with $\gamma\text{-Nb}_5\text{Si}_3$ transforming to $\beta\text{-Nb}_5\text{Si}_3$.

Figure 129 presents the diffractogram of Nb-18Si-24Ti-5Cr-5Al-2Mo at the post-HIP stage. It shows that applied pressure plays an important role in phase evolution. **a)** 150 MPa produces the $\beta\text{-Nb}_5\text{Si}_3$ whereas the lower **b)** 100 MPa and **c)** 50 MPa both produced $\alpha\text{-Nb}_5\text{Si}_3$.

Under no pressure, Nb_3Si was presented. This suggests that the transformation from $\gamma\text{-Nb}_5\text{Si}_3$ to tetragonal-silicide occurred through an alternative reaction path. Ti_{ss} is presented in the $\beta\text{-Nb}_5\text{Si}_3 \rightarrow \alpha\text{-Nb}_5\text{Si}_3$ transformation but not in the $\gamma\text{-Nb}_5\text{Si}_3 \rightarrow \alpha\text{-Nb}_5\text{Si}_3$ reaction. It is hypothesised that during 150 MPa HIP post-processing $\gamma\text{-Nb}_5\text{Si}_3$ transformed to $\alpha\text{-Nb}_5\text{Si}_3$ then due to the high-pressure environment a re-arrangement to $\beta\text{-Nb}_5\text{Si}_3$ was encouraged, explaining the presence of Ti_{ss} in the post-processing of 2Mo. Therefore it is suggested that $\gamma\text{-Nb}_5\text{Si}_3$ follows the observed reaction path in equation (14) and (15).



T_m represents a transition metal, such as Nb, Ti, Zr, Hf or Y. The high pressure forced the β -silicide to become more stable and was observed on completion along with Ti_{ss} . It is likely that both CoZy1 and TCoZy1 transformed via equation (15). A transformation from $\gamma\text{-Nb}_5\text{Si}_3 \rightarrow \alpha\text{-Nb}_5\text{Si}_3$ was noted in TCoZy5 and did not note Ti ejection. Zr formations were noted but these were assumed to be caused by reactions with oxygen rather than through a $\gamma\text{-Nb}_5\text{Si}_3$ transformation mechanism.

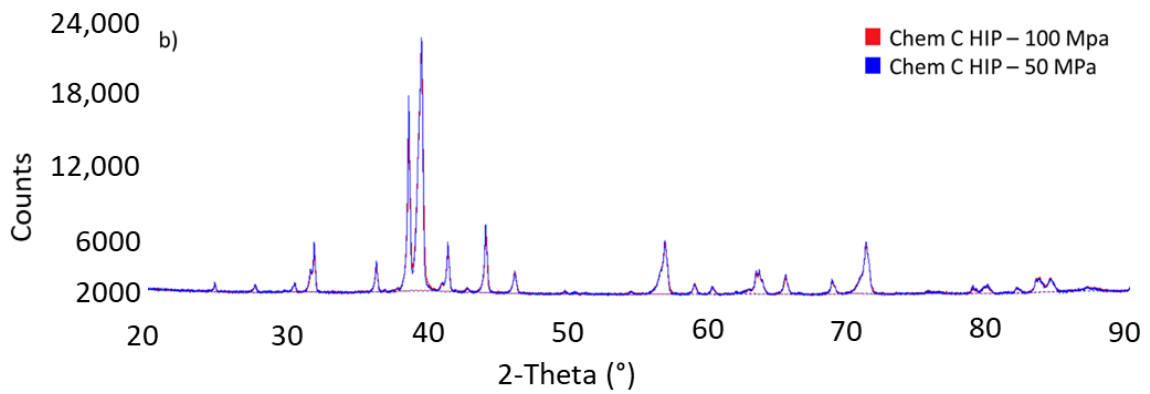
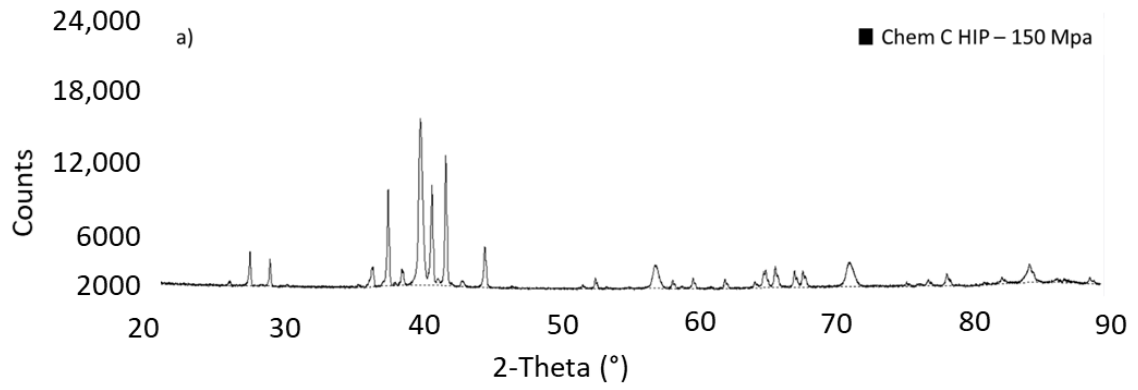


Figure 129: X-ray diffractograms of Nb-18Si-24Ti-5Cr-5Al-2Mo with HIP processes performed under different pressures a) 150 MPa b) 100 MPa and 50 MPa

8.4 Evaluation on the Effect of Hot Isostatic Pressing

The densification of Nb-Si-Ti alloys has been successfully shown to achieve near full densification from laser additive manufactured components. Three type of inclusions were observed, on grain interiors, faces and edges, increasing with closure difficulty respectively. The only remaining porosity is in a single plane, it is proposed that micro cracks connected these pores to the surface.

The density of samples was increased up to 99%, with the closing of large pores below the detection limit of the X-ray CT as well as small manufacturing defects and closing of small-scale cracks.

SEM results presented some porosity after HIPping but these were restricted to anomalous areas, likely formed as a result of mixing problems. Pores that were connected to the surface of the material via micro cracks still remained unchanged. It is suggested that adding a barrier coating to the material would isolate surface-linked porosity, allowing HIP to effectively consolidate the observed phenomenon.

Microsegregation in 2Mo, CoZy1 and TCoZy1 resulted in a phase split of γ -Nb₅Si₃ and γ -(Nb, Ti)₅Si₃ (Ti saturated). The saturation of Ti encouraged phase transformation during HIP and HT via its ejection to form a separate Ti solid solution. A reaction mechanism was suggested, resulting from the combination of high pressure and temperature. The addition of high concentrations of Zr prevented micro segregation and as a result no Ti_{ss} ejection was noted during any stage of post-processing. The added Zr has both benefits and detriments; it acts as a stabiliser for Ti and prevents its ejection, but also stabilises the γ -Nb₅Si₃ formation. For this reason, quantities of Zr must be carefully considered to prevent promotion of the poor creep resistant hexagonal-silicide.

2Mo, CoZy5 and TCoZy5 were presented, samples were HIPped at 3 different pressures and the results compared. At low pressures, 2Mo presented with α -Nb₅Si₃, during the high-pressure HIP (150 MPa) β -Nb₅Si₃ was presented instead. This suggests that pressure may have a role during the post-processing, further work some be performed to establish what reactions are occurring under different HIP pressures.

9 Overall Conclusion and Future Work

This work has shown that Nb-Si alloys may be successfully produced using additive manufacturing. A combination of hot-isostatic pressing, heat treatments and elemental additions were used to promote a desired phase combination of Nb_{ss} and α -Nb₅Si₃.

Phase identification and stabilisation was the focus of this work with and so mechanical and oxidation studies were not performed. The testing was not a focus on this work, but it can be surmised from previous literature presented within this thesis which alloy would provide the most ideal properties.

CoZy5 and 6Cr show the highest levels of γ -Nb₅Si₃ and would likely have the lowest creep resistance. 2Cr contains ~80% Nb_{ss} and would likely be the least oxidation resistant alloy within those produced. 14Cr is the only system to have both Cr₂Nb and HfO₂ and due to this, would likely be the hardest sample due to the laves phase's unique properties and thus be more prone to low temperature brittle fracture. TCozy1 produces the highest α -Nb₅Si₃ but also low Nb_{ss} (relative to other alloys produced in this study) so would likely have high oxidation resistance and a high hardness, although it may not be as brittle as 14Cr. For these reasons it is predicted that TCozy1 will show the best overall properties of the alloys in this thesis.

The notable conclusions can be made from this study:

- 1) The use of rapid solidification promoted the formation of γ -Nb₅Si₃ in most cases. Alloys noted in the literature formed different phases, suggesting additive manufacturing and rapid solidification may have an impact on alloy phases. Some γ -Nb₅Si₃ reduces on post-processing but all alloys show at least a small amount of γ -Nb₅Si₃.
- 2) The quantity of chromium used greatly affected the microstructure. A Laves phase was produced with high Cr (14 at.%). A cubic C15 Laves phase was produced over the hexagonal C14 Laves phase reported in the literature. Lower quantities showed coring and formation of Nb₃Si.
- 3) The addition of Hf promoted inclusions of HfO₂ throughout the microstructure which may cause stress concentrators within the microstructure leading to reduced mechanical properties of the material.

-
-
- 4) Increases in Ti and addition of Mo showed coring during solidification, on post-processing the formation of Ti_{ss} was noted epitaxially to Nb_5Si_3 structures. During long heat treatments the quantity of Ti_{ss} reduced, suggesting reabsorption.
 - 5) Zr and Y aimed to improve oxidation resistance by stabilising Nb_{ss} but was shown to mostly absorb into the silicide regions or form concentrated Zr and Y regions.
 - 6) Additions of Zr and Y showed stabilisation of $\gamma-Nb_5Si_3$ at high concentrations (5 at.%) but at low concentrations it had a negligible effect on its formation. Low concentrations of the elements also featured coring and produced Ti_{ss} formations during post-processing.
 - 7) Zr and Y reduced the size of observed silicide phases as concentrations of the elements were increased. Low concentrations minimised the formation of $\gamma-Nb_5Si_3$ to below 10 % in most cases.
 - 8) Ta was shown to promote the formation of $\alpha-Nb_5Si_3$ in as-formed and post-HIP phases without high concentrations of Cr, which represents a financial saving regarding the manufacturing costs of long heat treatments. Standard heat treatments are 100 hr at 1500°C reducing this to 5 hr will decrease the energy requirements and reduce costs.
 - 9) The $\gamma-Nb_5Si_3$ phase remained stable through most processes and suggests that the processing technique may play a part in its formation. It was noted to only change when long heat treatments were applied. A short heat treatment of TCoZy5 showed the unique transformation of $\gamma-Nb_5Si_3 \rightarrow \alpha-Nb_5Si_3$ however.
 - 10) Texture changes were noted in most chemistries during formation and post-processing stages.

Additive manufacturing of Nb-Si alloys has much potential, and whilst great strides have been made recently there is still much to learn. Not everything was within the scope of this work, and further experimentation is required if these alloy systems are to be successfully applied in the harsh environments of jet turbines. Further potential research topics include:

- 1) The mechanism of porosity introductions in additively manufactured Nb-Si alloys is poorly understood. Further research into varied laser parameters and scan patterns may provide better techniques which may reduce porosity.
- 2) Some pore closing mechanisms were discussed in this thesis but further investigation of the closing mechanisms of HIP, and how processing parameters effect the consolidation and phase evolution of these systems could potentially reduce manufacturing costs.
- 3) The evolution of Ti_{ss} was discussed in this thesis. A brief mechanism was suggested but further analysis may show if Ti_{ss} is involved in the decomposition of $\beta-Nb_5Si_3$ and if longer heat treatments reduce these inclusions within the matrix.
- 4) The additions of Zr and Y elements has been shown to reduce the phase size of silicide's within Nb-Si alloys. A study demonstrating how this effects oxidation resistance and if the desired stable oxide layer is produced to prevent the pesting phenomena would be beneficial to the understanding of the topic.
- 5) Low quantities of Zr and Y helped prevent the formation of $\gamma-Nb_5Si_3$, high quantities promoted it however. Microsegregation was reduced when Zr and Y concentrations were increased. The balance between preventing microsegregation and reducing $\gamma-Nb_5Si_3$ would be an important step for additive manufacturing of Nb-Si alloys.
- 6) An in-depth discussion of mechanical properties is required if these alloys are to be used in the aerospace industry and a comparative study with AM to demonstrate their viability in commercial use.

References

1. Langston, L.S., *Air Race*, in *Mechanical Engineering Magazine*, . 2010. p. 34-38.
2. Barber J. 1791.
3. Hunecke, K., *Jet Engines: Fundamentals of Theory, Design and Operation*. 1997: The Crowood Press Ltd. 224.
4. Electric, G. *7HA.01/.02 Gas turbine*. 2014 [cited 2019 20-05].
5. Alstom, *The worlds first industrial gas turbine set - GT neuchatel : A historic mechanical engineering landmark*. The American Society of Mechanical Engineers, 2007.
6. Industries, M.H., *MHI Achieves 1,600°C Turbine Inlet Temperature in Test Operation of World's Highest Thermal Efficiency "J-Series" Gas Turbine*. 2011, Mitsubishi Heavy Industries:
<https://web.archive.org/web/20130916192916/http://www.mhi.co.jp/en/news/story/1105261435.html>.
7. Bewlay BP, J.M., Gigliotti MFX,, *Niobium Silicide High Temperature In Situ Composites, in Intermetallic Compounds*, ed. W.a. Fleisher. Vol. 3. 2002: John Wiley and Sons, Ltd., 541-560.
8. Reed, R., *The Superalloys: Fundamentals and Applications*. 2006, Cambridge: Cambridge University Press.
9. Dicks, R.P., *The development of niobium-silicide based materils for high temperature applications*, in *Metallurgy and Materials*. 2008, The University of Birmingham.
10. canaday, H., *Composites vs Metals*. Aerospace america, 2015: p. 18-23.
11. plc., A.f.R.-R., *The Jet Engine*. .
12. R. Li, T.H.H., W. Sun, E.J. Williams, *Fatigue crack growth testing of the Super CMV hollow shafts under combined torsional and axial loading*. Engineering Failure Analysis, 2014. **36**: p. 173-185.
13. EO, E., *Key Improvements in the machining of difficult-to-cut aerospace alloys*. International Journal of Machine Tools and Manufacture, 2005. **45**: p. 1353-1367.
14. Kellner, T. *GE Develops Jet Engines Made From Ceramic Matrix Composite*. 2015 [cited 2019 18/04]; Available from: <https://www.ge.com/reports/post/112705004705/ge-develops-jet-engines-made-from-ceramic-matrix/>.
15. Narendernath Miriyala, J.K., and Jeffrey Price, Karren More and Peter TortoreUi, Harry Eaton, Gary Linsey, and Ellen Sun, *The evaluation of CFCC liners after field testing in a gas turbine - III*. ASME TURBO EXPO 2002 2002: p. 10.
16. TUTTLE J.H., C.M.B., MELLOR A.M., *Characteristic time correlations of emissions from conventional aircraft type flames*. 1976, Purdue University and Environmental Protection Agency. p. 1-133.
17. Andrew, P.L., *Ceramic matrix composite turbine engine*. 2012, General Electric Co: United States. p. 14.
18. Ketzer, R.D.A., *Turbine vane assembly including a low ductility vane*. 2002, General Electric Co: United States.
19. Phelps, B.S.H.C.G.G.S.A.F.T.R.R.T.S., *Ceramic matrix composite nozzle mounted with a strut*, E.P. Office, Editor. 2015. p. 27.
20. Kellner, T. *Space Age Ceramics Are Aviation's New Cup Of Tea*. 2016 [cited 2019 18/04]; Available from: <https://www.ge.com/reports/space-age-cmcs-aviations-new-cup-of-tea/>.

-
-
21. GE Successfully Tests World's First Rotating Ceramic Matrix Composite Material for Next-Gen Combat Engine 2015 [cited 2019 11-02]; Available from: http://www.geaviation.com/press/military/military_20150210.html.
 22. Kuhn, M., et al., *CMC Materials for Combustion Chamber Applications*. 2009.
 23. M. Ortelt, H.H., A. Herbertz, I. Müller *Advanced Design Concepts for Ceramic Thrust Chamber Components of Rocket Engines*, in *5th European Conference for Aeronautics and Space Sciences (EUCASS)*. 2013: German Aerospace Center.
 24. Lee, K.N., D.S. Fox, and N.P. Bansal, *Rare earth silicate environmental barrier coatings for SiC/SiC composites and Si₃N₄ ceramics*. *Journal of the European Ceramic Society*, 2005. **25**(10): p. 1705-1715.
 25. Bose S, *Engineering aspect of creep deformation of molybdenum disilicide*,. *Materials Science and Engineering A*, 1992. **155**: p. 217-225.
 26. Thorn AJ, M.M., Akinca M, KimV,, *Processing and Fabrication of Advanced Materials for High Temperature Applications*. The Minerals, Metals & Materials Society and ASM International, 1993.
 27. Jingyan Wu, W.W., Chungen Zou, *Microstructure and oxidation resistance of Mo-Si-B coating on Nb based in situ composites*. *Corrosion Science*, 2014. **87**: p. 421-426.
 28. Fang Zhang, L.Z., Jinxing Yu, Jianshen Wu, *Growth of single crystals and low temperature oxidation behaviors of MoSi₂ and NbSi₂*. *Materials Science Forum*, 2005. **475-479**: p. 729-732.
 29. Sakidja R, P.J., , , *Alloying and microstructure stability in the high temperature Mo-Si-B system*. *Journal of Nuclear Materials*, , 2007. **366-3** p. 1268-1276.
 30. Zelenitsas K, T.P., *Study of the role of Ta and Cr additions in the microstructure of Nb-Ti-Si-Al in situ composites*. *Intermetallics*, 2006. **14**: p. 639-659.
 31. B.P. Bewlay, M.R.J., and H.A. Lipsitt, *The balance of mechanical and environmental properties of a multielement niobium-niobium silicide-based In Situ composite*. *METALLURGICAL AND MATERIALS TRANSACTIONS A*, 1996. **27A**: p. 3801.
 32. Sha JB, Y.-M.Y., Harada H, , *Microstructural evolution and mechanical properties of Ir-Hf-Zr ternary alloys at room and high temperature*,. *Intermetallics*, , 2006. **14**: p. 1364-1369.
 33. B.P. Bewlay, M.R.J., and H.A. Lipsitt,, *Metall. Trans.*, 1996. **27A**: p. 3801.
 34. Fairbank, G.B., *Development of Platinum Alloys for High-Temperature Service*, in *Department of Materials Science and Metallurgy*. 2003, Cambridge. p. 138.
 35. Ira M. Wolff, P.J.H., *Platinum Metals-Based Intermetallics for High-Temperature Service*. *Platinum Metals Rev*, 2000. **44**: p. 158-166.
 36. B.P. Bewlay, M.R.J., and M.F.X. Gigliotti,, *Intermetallic Compounds—Principles and Practice*, . Vol. 3. 2001: John Wiley & Sons,.
 37. P.R. Subramanian, M.G.M., D.M. Dimiduk, and M.A. Stucke, , *Mater. Sci. Eng.*, 1997. **A239–240**
 38. B.P. Bewlay, M.R.J., P.R. Subramanian, *Processing High-Temperature Refractory-Metal Silicide in-situ Composites*. *JOM*, 1999: p. 32-36.
 39. B.P. Bewlay, J.J.L., and M.R. Jackson,, *JOM*, 1997. **49** p. 46.
 40. B.P. BEWLAY, M.R.J., J.-C. ZHAO, and P.R. SUBRAMANIAN, *A Review of Very-High-Temperature Nb-Silicide-Based Composites*. *METALLURGICAL AND MATERIALS TRANSACTIONS A*, 2003. **34**: p. 2043-2052.
 41. J.H. Schneibel, M.J.K., O. Unal, and R.N. Wright, *Intermetallics*, 2001. **9**: p. 25.
-
-

-
-
42. Mendiratta MG, D.D., *Phase relations and transformation kinetics in the high Nb region of the Nb-Si system*. Scripta Metallurgica and Materialia,, 1991. **25**: p. 237-242.
 43. ONERA. *Nb-Si Binary Phase Diagram*. 2006 [6 July 2016].
 44. Zhao JC, B.B., Jackson MR,, *Determination of Nb-Hf-Si Phase Equilibria*. Intermetallics, 2001. **9** p. 681-689.
 45. Bewlay BP, J.M., Briant CL, , *Deformation mechanisms in Niobium-Silicide based Composites*. 2001a.
 46. Jie Geng, P.T., Guosheng Shao, *Oxidation of Nb-Si-Cr-Al in situ composites with Mo, Ti and Hf additions*. Materials Science and Engineering, 2006. **441**: p. 26-38.
 47. Kim. J.-H., T.T., Hirai H., Kitahara A., Handa S., *Mechanical Properties of Nb-18Si-5Mo-5Hf-2C In-Situ Composite Prepared by Arc-Casting Method*. Materials Transactions, 2002. **43**(9): p. 2201-2204.
 48. S. Kashyap, C.S.T., K. Chattopadhyay*, *Effect of Gallium on microstructure and mechanical properties of Nb-Si eutectic alloy*. Intermetallics, 2011. **19**: p. 1943-1952.
 49. Nobuaki Sekido, Y.K., Seiji Miura and Yoshinao Mishima, *Solidification Process and Mechanical Behavior of the Nb/Nb₅Si₃ Two Phase Alloys in the Nb-Ti-Si System*. Materials Transactions, 2004. **45**(12): p. 3264 - 3271.
 50. Songming Zhang, X.S., Jiangbo Sha, *Microstructural evolution and mechanical properties of as-cast and directionally solidified Nb-15Si-22Ti-2Al-2Hf-2V-(2,14) Cr alloys at room and high temperatures*. Intermetallics, 2015(56): p. 8.
 51. Jie Geng, P.T., Guosheng Shao, *A study of the effects of Hf and Sn additions on the microstructure of Nbss/Nb₅Si₃ based in situ composites*. Intermetallics, 2007(15): p. 69-76.
 52. Nobuaki Sekido, Y.K., Seiji Miura, Fu-Ga Wei, Yoshinao Mishima, *Fracture toughness and high temperature strength of unidirectionally solidified Nb-Si binary and Nb-Ti-Si ternary alloys*. Journal of Alloys and Compounds, 2006(425): p. 223-229.
 53. M. F. Ashby, F.J.B.a.M.B., Acta Metall. Mater, 1989. **37**: p. 1847-1757.
 54. Feitosa, L., et al., *MICROSTRUCTURE EVOLUTION OF THE Nb-18Si-24Ti-5Cr-5Al-2Mo ALLOY PRODUCED VIA LASER ADDITIVE MANUFACTURING*. Metal 2017: 26th International Conference on Metallurgy and Materials. 2017, Slezska: Tanger Ltd. 1613-1618.
 55. Subramanian PR, M.M., Dimiduk DM, Stucke MA,, *Advanced intermetallic alloys - beyond gamma titanium aluminides*. Materials Science and Engineering A, 1997: p. 239-240.
 56. Jin-Hak Kim, T.T., Hisatoshi Hirai, Akira Kitahara, *Mechanical Properties of Nb-18Si-5Mo-5Hf-2C In-Situ Composite prepared by Arc-Casting Method*. Materials Transactions, 2002. **43**(9): p. 2201- 2204.
 57. AA Pauzi, M.A.G., SY Chang, GP Ng, S Husin, *A study on tensile deformation at room temperature and 650 °C in the directional solidified Ni-base superalloy GTD-111, in International Conference on Materials Physics and Mechanics*. 2017.
 58. Tsakiroopoulos, P., *On the Alloying and Properties of Tetragonal Nb₅Si₃ in Nb-Silicide Based Alloys*. Materials, 2018. **11**(69).
 59. Bewlay BP, B.C., Jackson MR, Subramanian PR,, *Recent advances in Nb silicide in-situ composites*. Proceedings to Plansee Seminar, 2001: p. 1-15.
 60. Bewlay, B.P.J., M.R. , *High temperature in situ composites: Processing and properties*. 2003, In Comprehensive Composite Materials: Elsevier: Amsterdam, The Netherlands.
-
-

-
-
61. Subramanian, P.R., et al., *Compressive creep behavior of Nb₅Si₃*. Scripta Metallurgica et Materialia, 1995. **32**(8): p. 1227-1232.
 62. F. Zhang, L.T.Z., A.D. Shan, J.S. Wu, *Microstructural effect on oxidation kinetics of NbSi₂ at 1023K*. Alloys and Compounds, 2006(422): p. 308-312.
 63. Subramanian PR, M.M., Dimiduk DM, *The Development of Nb-Based Advanced Intermetallic Alloys for Structural Applications*. Journal of Materials Processing Technology, 1996(48): p. 33-38.
 64. Yongping Wang, S.L., Chungen Zhou, Shiyu Qu, Ligu Song, Yafang Han, *Oxidation resistant silicide coatings for Nbss/Nb₅Si₃ in-situ composites*. Materials Science forum, 2005. **475-479**: p. 741-744.
 65. Neil Birks, G.H.M., , Frederick S. Pettit, *Introduction to the High Temperature Oxidation of Metals*. 2009.
 66. Guo, Y.J., Lina & Kong, Bin & Zhang, Fengxiang & Liu, Jinhui & Zhang, Hu., *Improvement in the oxidation resistance of Nb-Si based alloy by selective laser melting*. Corrosion Science., 2017.
 67. Geng J, T.P., Shao G,, *Oxidation of Nb-Si-Cr-Al in situ composites with Mo, Ti and Hf additions*. Materials Science and Engineering A, 2006. **441**: p. 26-38.
 68. Wan Wang, B.Y., Chungen Zhou, *Formation and oxidation resistance of germanium modified silicide coating on Nb based in situ composites*. Corrosion Science, 2014. **80**: p. 164-168.
 69. P. Rodhammer, W.K., C. semprimoschning., *International journal of refractory metals and hard materials*, 1993-1994. **12**: p. 283-293.
 70. Chougen Zhou, H.X., Shengkai Gong, Kyoo Young Kim, *Materials Science and Engineering*, 2003. **A341**: p. 169-173.
 71. R.T. Haasch, S.K.T., S. Sircar., *Metallurgical transactions*, 1992. **A**(23): p. 2631-2639.
 72. P. Ritt, R.S., J.H. Perepezko, , , *Mo-Si-B based coating for oxidation protection of SiC-C composites*. Surf. Coat. technol., 2012. **206** p. 19-20.
 73. Movchan, B.A. and G.S. Marinski, *Gradient protective coatings of different application produced by EB-PVD*. Surface and Coatings Technology, 1998. **100-101**: p. 309-315.
 74. Koçak, A., *MATERIALS SCIENCE AND ENGINEERING #Thin Film Preparation, Particle Size and Thickness Analysis Experimental Report*. 2018.
 75. Wei Li, H.Y., Aidang Shan, Lanting Zhang and Wu Jiansheng, *Microstructure and properties of directionally solidified NbSi₂/Nb₅Si₃ composites*. Materials Science forum, 2005. **475-479**: p. 733-736.
 76. su, Y., et al., *Lamellar orientation control in directionally solidified TiAl intermetallics*. Vol. 11. 2014. 219-231.
 77. J.A. Suttiff and B.P. Bewlay. in *53rd Annual Meeting of the Microscopy Society of America*. 1995. San Francisco, CA: San Francisco Press.
 78. Sinha, M., S. Deb, and U. Dixit, *Design of a multi-hole extrusion process*. Vol. 30. 2009. 330-334.
 79. JIANGBO SHA, H.H., TATSUO TABARU, AKIRA KITAHARA, HIDETOSHI UENO, and SHUJI HANADA, *Toughness and Strength Characteristics of Nb-W-Si Ternary Alloys Prepared by Arc Melting*. METALLURGICAL AND MATERIALS TRANSACTIONS A, 2003. **34A**: p. 2861-2871.
 80. Melgaard, D., R. L. Williamson, and J. Beaman, *Controlling remelting processes for superalloys and aerospace Ti alloys*. Vol. 50. 1998. 13-17.
-
-

-
-
81. A. Kostov, B.F., Computational Material, 2006. **38**: p. 374.
 82. Limin Ma, X.t., Bin Wang, Lina Jia, Sainan Yuan and Hu Zhang, *Purification in the interaction between yttria mould and Nb-silicide-based alloy during rdirectional solidification: A novel effect of yttrium*. Scripta Materialia, 2012(67): p. 4.
 83. Westman, A.-K., *Hot isostatic pressing of ceramics and influence of glass encapsulation*, in *Doctoral thesis / Luleå University of Technology 1 jan 1997 → ...*. 1998, Luleå tekniska universitet: Luleå. p. 152.
 84. Nekkanti EM, D.D., *Ductile-phase toughening in niobium-niobium silicide powder processed composites*. Materials Research Society Proceedings, 1999. **104**: p. 175-182.
 85. Dicks R., W.F., Wu X., *The manufacture of a niobium/niobium-silicide-based alloy using direct laser fabrication*. Journal of Materials Processing Technology, 2009. **209**: p. 1752-1757.
 86. Sai, P.C., Yeole, Shivraj. . *Fused Deposition Modeling - Insights*. . (2014).
 87. Paulo Jorge Ba'rtolo, I.G., *Stereolithography: Materials, Processes and Applications*, 2011: Springer Science & Business Media.
 88. Yap, C.Y., et al., *Review of selective laser melting: Materials and applications*. Vol. 2. 2015. 041101.
 89. Wang, Q. and M. Xing Zhang, *Review on Recent Research and Development of Cold Spray Technologies*. Vol. 533. 2012. 1-52.
 90. Pathak, S. and G. C Saha, *Development of Sustainable Cold Spray Coatings and 3D Additive Manufacturing Components for Repair/Manufacturing Applications: A Critical Review*. Vol. 7. 2017.
 91. DAVIES, H.V.A.a.S., *Fundamental Aspects of Hot Isostatic Pressing: An Overview*. METALLURGICAL AND MATERIALS TRANSACTIONS A, 2000. **31A**: p. 2981-3000.
 92. Birmingham, U.o. [Image] 2018 [cited 2018 26-09]; Available from: <https://www.birmingham.ac.uk/research/activity/irc-materials-processing/themes/AMPLab/AMPLab-Facilities.aspx>.
 93. Day N., M.-R.P. *Crystallographic Open Database*. [cited 2018; Available from: <http://www.crystallography.net/cod/>].
 94. Lutterotti, L.S., P, *Simultaneous structure and size-strain refinement by the Rietveld method*. Journal of Applied Crystallography, 1990. **23**: p. 246-252.
 95. Baden, W. and A. Weiss, *X-ray and 1 H-NMR studies on niobium-titanium-hydrides*. Zeitschrift fuer Metallkunde, 1983. **74**(2): p. 89-93.
 96. Parthe, E., B. Lux, and H. Nowotny, *Der Aufbau der Silizide M 5 Si 3*. Monatshefte für Chemie und verwandte Teile anderer Wissenschaften, 1955. **86**(5): p. 859-867.
 97. Aronsson, B., *The crystal structure of Mo5 Si3 and W5 Si3*. Acta Chemica Scandinavica, 1955. **9**: p. 1107-1110.
 98. Schachner, H., E. Cerwenka, and H. Nowotny, *Neue Silizide vom M 5 Si 3-Typ mit D 8 8-Struktur*. Monatshefte fuer Chemie und verwandte Teile anderer Wissenschaften, 1954. **85**(1): p. 245-254.
 99. Galasso, F., B. Bayles, and S. Soehle, *Superconducting Alloys of the Nb3SnxM1-x Type*. Nature, 1963. **198**(4884): p. 984.
 100. Waterstrat, R.M., Flack, H.D., Yvon, K.; Parthe, E., *Refinement of Nb3Si Nb3As*. Acta Crystallographica B, 1975. **24**(31): p. 2765-2769.
 101. Kubiak, R., et al., *Refinement of the crystal structure of NbSi 2, NbGe 2 and TaGe 2*. Bulletin de l'Academie Polonaise des Sciences. Serie des Sciences Chimiques, 1972. **20**.
-
-

-
-
102. Laves, F. and H. Wallbaum, *Die Kristallstruktur von Ni₃Ti und Si₂Ti*. Zeitschrift für Kristallographie-Crystalline Materials, 1939. **101**(1-6): p. 78-93.
 103. Kornilov, I.I.B., P.B.; Alisova, S.P., *Isothermal section of the Mo - Zr - Cr constitution diagram at 1500 C*. Izvestiya Akademii Nauk SSSR, Neorganicheskie Materialy, 1965. **1**: p. 2205-2207.
 104. Wyckoff, R., *Interscience Publishers, New York, New York rocksalt structure*. Crystal structures, 1963. **1**: p. 85-237.
 105. Whittle, K., G. Lumpkin, and S. Ashbrook, *Neutron diffraction and MAS NMR of Cesium Tungstate defect pyrochlores*. Journal of Solid State Chemistry, 2006. **179**(2): p. 512-521.
 106. Chateigner, D., *Combined Analysis*. John Wiley & Sons, Inc., 2013.
 107. Lutterotti L. *Introduction to Crystallography and Diffraction Techniques*. 2018.
 108. Lutterotti L., C.D., Peponi G. *Introduction to MAUD*. in *9th Maud school on combined analysis by X-ray and neutron scattering*. 2018. Caen.
 109. Fultz, B., Howe, J., *Diffraction and the X-Ray Powder Diffractometer in Transmission Electron Microscopy and Diffractometry of Materials*. Berlin, Heidelberg: Springer Berlin Heidelberg., 2013.
 110. Cherin, P., *Determination of Composition of Solid Solutions Using X-Ray Diffraction Techniques*, in *Applications of the newer techniques of analysis*. 1973, Springer. p. 103-122.
 111. Chateigner D., *Structure Refinement by Diffraction Profile Adjustment (Rietveld Method)*. Combined Analysis, John Wiley & Sons, Inc., 2013.
 112. *NIST 2015a. Certificate of Analysis Standard Reference Material 1976b Instrument Response Standard for X-Ray Powder Diffraction*. [cited 2018 07-08]; Available from: <https://www.nist.gov/publications/certification-standard-reference-material-1976b>.
 113. *NIST 2015b. Certificate Standard Reference Material 660c Line Position and Line Shape Standard for Powder Diffraction (Lanthanum Hexaboride Powder)*. [cited 2018 07-08]; Available from: <https://www-s.nist.gov/srmors/certificates/660c.pdf>.
 114. L., L., *MAUD: Materials Analysis Using Diffraction*. 2018.
 115. Watkinson E.J., *Space Nuclear Power Systems: Enabling Innovative Space Science and Exploration Missions*, in *Physics and Astronomy*. 2017, University of Leicester.
 116. Lutterotti, L., Bortolotti, M., Ischia, G., Lonardelli, I. & Wenk, H. R., *Rietveld Texture analysis from Diffraction Images*. Zeitschrift für Kristallographie, 2007. **1**: p. 125-130.
 117. Chateigner D. , *Quantitative Texture Analysis in Combined Analysis*. John Wiley & Sons, Inc., 2013.
 118. Fong, R., *Phase Transformation, Texture and Mechanical Anisotropy in Zirconium Alloys*. 2013, Carleton University.
 119. Metrology, N. *Detector Reference Page*. 2018 [cited 2018 05-11]; Available from: www.nikonmetrology.com/en-us/product/xt-h-225.
 120. TB, M., *Binary Alloy Phase Diagrams*. 1986, ASM, Ohio.
 121. Zhao JC, J.M., Peluso LA,, *Determination of the Nb-Cr-Si Phase Diagram using Diffusion Multiples*, *Acta Materialia*. 2003(51): p. 6395-6405.
 122. Zhao JC, P.L., Jackson MR, Tan L,, *Phase Diagram of the Nb-Al-Si ternary system*. Alloys of Compounds, 2003. **360**: p. 183-188.
 123. Zhao JC, B.B., Jackson MR, Peluso LA, , , *Alloying and Phase Stability in Niobium Silicide In-situ Composites*. GE Technical Report no. 2001 CRD090, 2001a.
-
-

-
-
124. Tsakiroopoulos, P., *Alloying and Hardness of Eutectics with Nbss and Nb5Si3 in Nb-silicide Based Alloys*. Materials, 2018. **11**(592).
 125. Feitosa L., *Solidification Behaviour and Microstructure Evolution of Refractory Metals-Based Alloys Under Rapid Solidification*. 2018, University of Leicester.
 126. Cambridge, U.o. *Interactive Ellingham Diagram*. [cited 2018; Available from: https://www.doitpoms.ac.uk/tlplib/ellingham_diagrams/interactive.php].
 127. Jacob, A., *Thermochemical Modeling of Laves Phase Containing Ferritic Steels*. 2015: Research Center Jülich GmbH. Publisher, Central Library.
 128. M. Takeyama, C.T.L., *Microstructure and mechanical properties of Laves-phase alloys based on Cr2Nb*. Materials Science and Engineering, 1991: p. 61-66.
 129. Tsakiroopoulos, P., *On Nb Silicide Based Alloys: Alloy Design and Selection*. Materials, 2018. **11**(844).
 130. K. Zelenitsas, P.T., *Study of the role of Al and Cr additions in the microstructure of Nb–Ti–Si in situ composites*. Intermetallics, 2005. **13**: p. 1079-1095.
 131. G. H. Cao, G.Y.J., N. Liu, W. H. Zhang, Alan M. Russell, and D. Gerthsen, *Microstructure and mechanical properties of an ultrafine Ti–Si–Nb alloy*. Materials Chemistry and Physics, 2015. **163**: p. 512-517.
 132. Ånmark N., K.A., Jönsson PG., *The Effect of Different Non-Metallic Inclusions on the Machinability of Steels*. Materials, 2015. **8**: p. 751-783.
 133. Qu, S., Y. Han, and L. Song, *Effects of alloying elements on phase stability in Nb–Si system intermetallics materials*. Vol. 15. 2007. 810-813.
 134. Kim WY, T.H., Hanada S., *Microstructure and High-Temperature Strength at 1773K of Nbs/Nb-Si, Composites Alloyed with Molybdenum*. Intermetallics, 2002. **10**: p. 625-634.
 135. Uemura, T. and K. Asano, *Effects of Ti, Mo and Cr Addition on Microstructure and Mechanical Properties of Nb-Si Based Alloy*. Vol. 2018.93. 2018. P015.
 136. Won-Yong Kim, I.-D.Y., Mok-Soon Kim, Shuji Hanada, *Effect of Cr Addition on Microstructure and Mechanical Properties in Nb-Si-Mo Base Multiphase Alloys*. Materials Transactions, 2002. **43**(12): p. 3254-3261.
 137. Koji Hagihara, T.N., Masahiro Suzuki, Takuya Ishimoto, Suyalatu, Shi-Hai Sun, *Successful additive manufacturing of MoSi2 including crystallographic texture and shape control*. Journal of Alloys and Compounds, 2017. **696**: p. 67-72.
 138. Luca Facchini, E.M., Pierfrancesco Robotti, Alberto Molinari, *Microstructure and mechanical properties of Ti-6Al-4V produced by electron beam melting of pre-alloyed powders*. Rapid Prototyping Journal, 2009. **15**(3): p. 171-178.
 139. Douglass D., *The thermal expansion of niobium pentoxide and its effect on the spalling of niobium oxidation films*. Journal of the Less Common Metals, 1963. **5**(2): p. 151-157.
 140. Drawin S, J.J., *Advanced Lightweight Silicide and Nitride Based Materials for Turbo-Engine Applications*. Aerospace Lab., 2011. **3**: p. 1-13.
 141. Andrew Douglas, A.A., Leandro M. Feitosa, Huan Qian, Jun Li, Hongbiao Dong, Moataz Attallah, Xin Lin, Weidong Huang, *Oxidation of additively manufactured Nb-Si-Ti-Cr-Al-Mo alloys*. 2019.
 142. Reisman A, H.F., *Nb2O5 and Ta2O5 Structure and Physical Properties. High Temperature Oxides Part II - Oxides of Rare Earths, Titanium, Zirconium, Hafnium, Niobium and Tantalum.*, ed. A. A. 1970: Academic Press Inc;.
-
-

-
-
143. Yanqiang Qiao, X.G., Yuxiang Zeng, *Study of the effects of Zr addition on the microstructure and properties of Nb-Ti-Si based ultrahigh temperature alloys*. Intermetallics, 2017. **88**: p. 19-27.
 144. M. Sankara, G.P., Vajinder Singha, V.V. Satya Prasada, *Effect of Zr additions on microstructure evolution and phase formation of Nb-Si based ultrahigh temperature alloys*. Intermetallics, 2018. **101**: p. 123-132.
 145. Jean-Pierre Brog, C.-L.C., Aurelien Crochet, Katharina M. Fromm, *Polymorphism, what it is and how to identify it: a systematic review*. RSC Advances, 2013.
 146. Hannink R, K.P., Muddle B., *Transformation toughening in Zirconia-Containing ceramics*. Journal of the American Ceramic Society, 2004. **83**(3): p. 461-487.
 147. Basu B, B.K., *Advanced Structural Ceramics*. 2011, Chichester: John Wiley and Sons.
 148. Hayashi H, S.T., Maruyama N, Inaba H, Kawamura K, Mori M., *Thermal expansion coefficient of yttria stabilized zirconia for various yttria contents*. Solid State Ionics, 2005. **176**(5-6): p. 613-619.
 149. Yueling Guo, L.J., Huarui Zhang, Fengxiang Zhang, Hu Zhang, *Enhancing the oxidation resistance of Nb-Si based alloys by yttrium addition*. Intermetallics, 2018. **101**: p. 165-172.
 150. Wang C., *Influence of yttrium on microstructure and properties of Ni-Al alloy coatings prepared by laser cladding*. Defence Technology, 2014. **10**(1): p. 22-27.
 151. Jing, B., et al., *Liquid-Solid Phase Equilibria of Nb-Si-Ti Ternary Alloys*. Chinese Journal of Aeronautics, 2008. **21**(3): p. 275-280.
 152. Léger, J.-M. and H.T. Hall, *Pressure and temperature formation of A3B compounds I. Nb₃Si and V₃Al*. Journal of the Less Common Metals, 1973. **32**(2): p. 181-187.
 153. Miura, S., et al., *Effect of microstructure on the high-temperature deformation behavior of Nb-Si alloys*. Vol. 510. 2009. 317-321.
 154. Sankar, M., G. Phanikumar, and V.V. Satya Prasad, *Effect of Zr addition on the mechanical properties of NbSi based alloys*. Materials Science and Engineering: A, 2019. **754**: p. 224-231.
 155. Pontau, A.E. and D. Lazarus, *Diffusion of titanium and niobium in bcc Ti-Nb alloys*. Physical Review B, 1979. **19**(8): p. 4027-4037.
 156. Tiwari G. P., S.B.D., Raghunathan V. S., Patil R. V.,, *Self and Solute Diffusion in Dilute Zr-Nb Alloys in B-phase*. Journal of Nuclear Materials,, 1973. **46**: p. 35-40.
 157. Zhonghua Li, R.X., Zhengwen Zhang, Ibrahim Kucukko, *The influence of scan length on fabricating thin-walled components in selective laser melting*. Elsevier, 2018. **126**: p. 12.
 158. Edouard Chauvet, P.K., Eric A. Jagle, Baptiste Gault, Dierk Raabe, Catherine Tassin, Jean-Jacques Blandin, Remy Dendievel, Benjamin Vayre, Stephane Abed, Guilhem Martin, *Hot cracking mechanism affecting a non-weldable Ni-based superalloy produced by selective electron Beam Melting*. Acta Materialia, 2018. **142**: p. 82-94.
 159. Broeckmann, C., *Hot isostatic pressing of near net shape components – process fundamentals and future challenges*. Powder Metallurgy, 2012. **55**(3): p. 176-179.
 160. Chao Yuan, J.L., Kai-Xin Dong and Jian-Ting Guo, *On Healing Mechanism of Cast Porosities in Cast Ni-Based Superalloy by Hot Isostatic Pressing*. The Minerals, Metals & Materials Society, 2017: p. 265-275.
 161. B. CHMIELA, B.K., J. CWAJNA, *EFFECT OF HOT ISOSTATIC PRESSING ON THE MICROSTRUCTURE OF TURBINE BLADE AIRFOIL MADE OF NICKEL-BASE SUPERALLOY*. Arch. Metall. Mater., 2017. **62**(1): p. 241-245.
-
-

-
-
162. R. Kaiser, K.W., C. O'Brien², S. Ramirez-Garcia and D. J. Browne, *Effects of hot isostatic pressing and heat treatment on cast cobalt alloy*. Institute of Materials, Minerals and Mining, 2014: p. 1-7.
 163. J.M. Larson, S.F., *Metallurgical Factors Affecting the Crack Growth Resistance of a Superalloy*. METALLURGICAL AND MATERIALS TRANSACTIONS A, 1977. **8A**.
 164. Timing Zhang, W.Z., Qiushi Deng, Wei Jiang, Yonglin Wang, Yong Wang, Wenchun Jiang, *Effect of microstructure inhomogeneity on hydrogen embrittlement susceptibility of X80 welding HAZ under pressurized gaseous hydrogen*. International Journal of Hydrogen Energy, 2017. **42**: p. 25102-25113.
 165. Tammas-Williams, S., et al., *The Effectiveness of Hot Isostatic Pressing for Closing Porosity in Titanium Parts Manufactured by Selective Electron Beam Melting*. Metallurgical and Materials Transactions A, 2016. **47**(5): p. 1939-1946.
 166. Tan, L., et al., *Effects of temperature and pressure of hot Isostatic pressing on the grain structure of powder metallurgy superalloy*. Materials, 2018. **11**(2): p. 328.
 167. V. Chandrasekaran, R.T., D.H. Polonis,, *Phase Separation Processes in the Beta Phase of Ti-Mo Binary Alloys*. Metallography, 1972. **5**: p. 393-398.
 168. Leineweber, A. and E.J. Mittemeijer, *Diffraction line broadening due to lattice-parameter variations caused by a spatially varying scalar variable: its orientation dependence caused by locally varying nitrogen content in [epsilon]-FeNO.433*. Journal of Applied Crystallography, 2004. **37**(1): p. 123-135.

Appendix

Below is a tabulated record of modelled diffractograms for the reader's convenience.

Sample		R_{wp}	R_{exp}	GoF
14Cr	AF	5.839873	2.227893	2.621253803
	HIP	6.0847197	2.3578827	2.580586261
	HT	4.3502617	2.2833264	1.905229887
2Cr	AF	6.3480663	2.2359498	2.839091602
	HIP	4.6496677	2.3148081	2.008662273
	HT	3.8360615	2.3287451	1.647265517
6Cr	AF	3.7412906	2.2779996	1.642357883
	HIP	3.8965123	2.2125533	1.761093077
	HT	4.2454786	2.2123895	1.918956224
2Mo	AF	5.371409	2.3314633	2.303878856
	HIP	3.8579571	2.2198312	1.73795066
	5 h HT	4.536609	2.2595766	2.007725253
	100 h HT	6.0330625	2.335558	2.583135379
CoZy1	AF	4.4535794	2.1088526	2.111849543
	HIP	4.9890065	2.0844374	2.393454704
	HT	4.6990795	2.089863	2.248510788
CoZy5	AF	4.2973685	2.1044867	2.042003164
	HIP	6.884588	2.0736494	3.320034718
	HT	8.244903	2.1163144	3.895878136
TCoZy1	AF	6.251613	2.1887684	2.856224076
	HIP	5.640362	2.1295035	2.648674679
	HT	6.4940376	2.044244	3.176742894
TCoZy5	AF	4.2721214	2.1049683	2.029541918
	HIP	6.8970537	2.0754366	3.323182072
	HT	4.436261	2.0611057	2.152369478

14Cr	Phase 1	Volume %	a			
AF	Nb _{SS}	56.39	3.238029			
HIP	Nb _{SS}	61.81	3.2730634			
HT	Nb _{SS}	46.55	3.249673			
	Phase 2	Volume %	a	c		
AF	γ - Nb ₅ Si ₃	4.21	7.553306	5.052107		
HIP	γ - Nb ₅ Si ₃	4.54	7.5495358	5.2108254		
HT	γ - Nb ₅ Si ₃	10.06	7.518278	5.1803784		
	Phase 3	Volume %	a			
AF	Cr ₂ Nb	21.283	7.0793			
HIP	Cr ₂ Nb	14.486973	7.1217227			
HT	Cr ₂ Nb	8.451478	7.0793			
	Phase 4	Volume %	a	c		
AF						
HIP	Nb ₃ Si	2.52	10.354015	5.218813		
HT	Nb ₃ Si	12.43	10.122092	5.253095		
	Phase 5	Volume %	a	c		
AF	α - Nb ₅ Si ₃	16.73	6.5457892	11.919201		
HIP	α - Nb ₅ Si ₃	13.21	6.5754514	11.9569645		
HT	α - Nb ₅ Si ₃	16.45	6.5341406	11.953238		
	Phase 6	Volume %	a	b	c	β°
AF	HfO ₂	1.38	5.1636615	5.178123	5.285664	99.37139
HIP	HfO ₂	4.07	5.180752	5.1857	5.2841	99.352
HT	HfO ₂	6.06	5.118	5.1857	5.2841	99.352

2Cr	Phase 1	Volume %	a			
AF	Nb _{SS}	90.95	3.2753026			
HIP	Nb _{SS}	76.07	3.274465			
HT	Nb _{SS}	80.36	3.2723465			
	Phase 2	Volume %	a	c		
AF						
HIP	γ - Nb ₅ Si ₃	4.77	7.5227804	5.1823897		
HT	γ - Nb ₅ Si ₃	12.91	7.529867	5.178558		
	Phase 3	Volume %	a	c		
AF	Nb ₃ Si	8.822	10.009906	5.138286		
HIP	Nb ₃ Si	16.233086	10.486571	5.19036		
HT						
	Phase 6	Volume %	a	b	c	β°
AF	HfO ₂	0.25	5.167692	5.1968555	5.313422	99.524536
HIP	HfO ₂	2.92	5.113	5.1857	5.2861	99.353
HT	HfO ₂	6.74	5.074755	5.1835303	5.312434	99.55821

6Cr	Phase 1	Volume %	a			
AF	Nb _{SS}	23.31	3.249415			
HIP	Nb _{SS}	42.34	3.2512662			
HT	Nb _{SS}	26.63	3.2500434			
	Phase 2	Volume %	a	c		
AF	γ - Nb ₅ Si ₃	47.32	7.525966	5.1916213		
HIP	γ - Nb ₅ Si ₃	56.17	7.533652	5.192956		
HT	γ - Nb ₅ Si ₃	53.67	7.530762	5.184173		
	Phase 3	Volume %	a	c		
AF	β - Nb ₅ Si ₃	27.64	10.020879	5.036573		
HIP	Nb ₃ Si	0.09	10.38491	5.1645284		
HT	α - Nb ₅ Si ₃	15.953	6.5471883	11.882059		
	Phase 6	Volume %	a	b	c	β°
AF	HfO ₂	1.74	5.008621	5.279519	5.2871	99.432
HIP	HfO ₂	1.40	5.046088	5.27468	5.28076	99.6054
HT	HfO ₂	3.75	5.059817	5.292844	5.27111	99.1989

2Mo	Phase 1	Volume %	a	
AF	Nb _{SS}	53.97	3.2708664	
HIP	Nb _{SS}	49.55	3.239759	
5 h HT	Nb _{SS}	30.14	3.2367413	
100 h HT	Nb _{SS}	51.92	3.2432191	
	Phase 2	Volume %	a	c
AF	γ - Nb ₅ Si ₃	46.03	7.5208254	5.187607
HIP	γ - Nb ₅ Si ₃	12.03	7.516	5.149
5 h HT	γ - Nb ₅ Si ₃	26.06	7.520325	5.170445
100 h HT	γ - Nb ₅ Si ₃	5.13	7.5296817	5.1744914
	Phase 3	Volume %	a	c
AF				
HIP	β - Nb ₅ Si ₃	38.41503	10.034266	5.032905
5 h HT	α - Nb ₅ Si ₃	43.8058	6.5399113	11.894876
100 h HT	α - Nb ₅ Si ₃	42.9488	6.5517473	11.880418

CoZy1	Phase 1	Volume %	a	
AF	Nb _{SS}	26.41	3.2448664	
HIP	Nb _{SS}	29.20	3.2473593	
HT	Nb _{SS}	44.73	3.2433774	
	Phase 2	Volume %	a	c
AF	γ - Nb ₅ Si ₃	7.42	7.53	5.182
HIP	γ - Nb ₅ Si ₃	7.56	7.528464	5.188712
HT	γ - Nb ₅ Si ₃	9.62	7.5284257	5.180227
	Phase 3	Volume %	a	c
AF	β - Nb ₅ Si ₃	35.77	10.037985	5.033319
HIP	β - Nb ₅ Si ₃	28.36443	10.04259	5.0364065
HT				
	Phase 4	Volume %	a	c
AF	α - Nb ₅ Si ₃	30.38	6.538037	11.925896
HIP	α - Nb ₅ Si ₃	34.87	6.5403786	11.939951
HT	α - Nb ₅ Si ₃	45.65	6.5429816	11.883644

CoZy5	Phase 1	Volume %	a	
AF	Nb _{SS}	75.92	3.2613337	
HIP	Nb _{SS}	42.61	3.2513392	
HT	Nb _{SS}	51.67	3.249037	
	Phase 2	Volume %	a	c
AF	γ - Nb ₅ Si ₃	24.09	7.6024117	5.232522
HIP	γ - Nb ₅ Si ₃	57.39	7.594718	5.2167306
HT	γ - Nb ₅ Si ₃	48.33	7.5896707	5.216257

TCoZy1	Phase 1	Volume %	a	
AF	Nb _{SS}	43.93	3.2569995	
HIP	Nb _{SS}	59.33	3.2457852	
HT	Nb _{SS}	33.37	3.249123	
	Phase 2	Volume %	a	c
AF	γ - Nb ₅ Si ₃	8.96	7.4871407	5.17364
HIP	γ - Nb ₅ Si ₃	11.42	7.570266	5.158568
HT	γ - Nb ₅ Si ₃	10.09	7.5529637	5.1994276
	Phase 3	Volume %	a	c
AF	β - Nb ₅ Si ₃	27.63872	10.017094	5.0262556
HIP				
HT				
	Phase 4	Volume %	a	c
AF	α - Nb ₅ Si ₃	19.46	6.5485272	12.016495
HIP	α - Nb ₅ Si ₃	29.25	6.5497217	11.898888
HT	α - Nb ₅ Si ₃	56.53	6.558302	11.907208

ToZy5	Phase 1	Volume %	a	
AF	Nb _{ss}	60.75	3.2609513	
HIP	Nb _{ss}	43.32	3.2511973	
HT	Nb _{ss}	39.38	3.2442935	
	Phase 2	Volume %	a	c
AF	γ - Nb ₅ Si ₃	39.25	7.598956	5.2329493
HIP	γ - Nb ₅ Si ₃	56.68	7.5942297	5.216441
HT	γ - Nb ₅ Si ₃	16.18	7.544364	5.1884933
	Phase 3	Volume %	a	c
AF				
HIP				
HT	α - Nb ₅ Si ₃	43.168	6.5487547	11.9023695
	Phase 4	Volume %	a	c
AF				
HIP				
HT	ZrO ₂	1.27	3.5781	5.1623